

University of Texas Rio Grande Valley

ScholarWorks @ UTRGV

Theses and Dissertations

5-2016

Design of three-dimensional near-zero refractive index metamaterials

David Flores III

The University of Texas Rio Grande Valley

Follow this and additional works at: <https://scholarworks.utrgv.edu/etd>



Part of the [Mechanical Engineering Commons](#)

Recommended Citation

Flores, David III, "Design of three-dimensional near-zero refractive index metamaterials" (2016). *Theses and Dissertations*. 34.

<https://scholarworks.utrgv.edu/etd/34>

This Thesis is brought to you for free and open access by ScholarWorks @ UTRGV. It has been accepted for inclusion in Theses and Dissertations by an authorized administrator of ScholarWorks @ UTRGV. For more information, please contact justin.white@utrgv.edu, william.flores01@utrgv.edu.

DESIGN OF THREE-DIMENSIONAL NEAR-ZERO
REFRACTIVE INDEX METAMATERIALS

A Thesis

by

DAVID FLORES III

Submitted to the Graduate College of
The University of Texas Rio Grande Valley
In partial fulfillment of the requirements for the degree of

MASTER OF SCIENCE

May 2016

Major Subject: Electrical Engineering

DESIGN OF THREE-DIMENSIONAL NEAR-ZERO
REFRACTIVE INDEX METAMATERIALS

A Thesis
by
DAVID FLORES III

COMMITTEE MEMBERS

Dr. Nantakan Wongkasem
Chair of Committee

Dr. Heinrich D. Foltz
Committee Member

Dr. Yoonsu Choi
Committee Member

May 2016

Copyright 2016 David Flores III
All Rights Reserved

ABSTRACT

Flores III, David, Design of Three-Dimensional Near-Zero Refractive Index Metamaterials.

Master of Science (MS), May, 2016, 160 pp., 14 tables, 124 figures, references, 76 titles.

Near-zero refractive index metamaterials exhibit remarkable electromagnetic properties which can and will be applied in the near future. From the known methods of achieving near-zero refractive index, this work primarily focuses on the design of 3D metamaterials whose permittivity and permeability are both close to zero while maintaining relatively low loss factor. The design of the metamaterials is based on the chiral shape “omega” and designed to weave periodically as a fishnet. Theoretical analysis, computer modeling and simulation are steps taken in the design of metamaterials. A computational tool based on the robust method for effective parameter extraction is successfully developed and validated in order to examine the effective material parameters. This tool is also employed as a preliminary test for the design of metamaterials. Novel two-dimensional and three-dimensional metamaterial designs which exhibit desirable near-zero refractive index with relatively low loss are developed.

DEDICATION

To the Spirit and to the bride, who both say, Come!

For I am able to do all things in Christ who empowers me. Amen!

ACKNOWLEDGMENTS

In the period of the completion of this thesis and the work leading it, I give my sincerest gratitude to those who helped and prayed for me, supplying me with your rich fellowship. Thank you dearest saints!

I owe many thanks to my advisor, Dr. Wongkasem, for her guidance, support, patience and remarkable mentorship all throughout this research. I also give thanks to the people whom I had the pleasure to work with on a near day-to-day basis, such as these professors, in no particular order: Dr. Foltz, Dr. Wilson, Dr. Ben Ghalia, Dr. Choi, and to my classmates and graduate lab mates: Andy, Mario, Edwardo, Justin, Edni, Eric and Gerika. I will value their input and encouragement throughout the semesters.

My family also helped and cheered me, with their love, Má, Pá, El vú and Lanlanlo. Furthermore, the dear brothers and sisters who supported me through prayer and yummy nourishment, both physical and spiritual. Truly a double portion!

Lastly, I would not have accomplished this work without the continued support and aid of my Chulita, my true counterpart and Love.

Thank you everyone! Words are not enough to express my eternal gratitude.

TABLE OF CONTENTS

	Page
ABSTRACT	iii
DEDICATION	iv
ACKNOWLEDGMENTS	v
TABLE OF CONTENTS.....	vi
LIST OF TABLES.....	viii
LIST OF FIGURES	x
CHAPTER I. INTRODUCTION.....	1
1.1: Background and Rational of Study	1
1.2: Objectives	2
1.2.1: Study electromagnetic properties of near-zero refractive index metamaterials... ..	2
1.2.2: Design near-zero refractive index metamaterials with low loss in the X-band microwave regimes	2
1.3: Scope and Limitations	2
1.4: Anticipated Outcomes.....	3
CHAPTER II. THEORIES AND LITERATURE REVIEWS	4
2.1: History of Metamaterials	4
2.2: Metamaterial Classifications.....	6
2.3: Electromagnetic Material Parameters Extraction	8
2.4: Near-Zero Refractive Index Metamaterials	15
CHAPTER III. RESEARCH METHODOLOGY	41
3.1: Design of Near-Zero Refractive Index Metamaterials (NZRIM).....	41
3.2: Simulation Setup.....	44
3.2.1: 2D with Substrate.....	44
3.2.2: 3D Structure.....	65

3.3: Metamaterial Structure Validation.....	71
CHAPTER IV. DESIGN AND NUMERICAL STUDIES.....	79
4.1: Introduction.....	79
4.2: Circular Closed-Ring Resonator (CCRR) Structures	80
4.2.1: CCRRs in 4 mm × 4 mm Unit Cell.....	82
4.2.2: CCRRs in 5 mm × 5 mm Unit Cell.....	85
4.2.3: CCRRs in 6 mm × 6 mm Unit Cell.....	88
4.2.4: CCRRs in 8 mm × 8 mm Unit Cell.....	91
4.3: Split-Ring Resonator (SRR) Structures	94
4.3.1: SRRs in 6 mm × 6 mm Unit Cell.....	98
4.3.2: SRRs in 8 mm × 8 mm Unit Cell.....	101
4.4: Omeganet and Omega MTM Structures.....	104
4.4.1: Omeganet MTM Structures Over Arlon Di 880 (lossy) Substrate	107
4.4.2: Omega MTM Structures Over Arlon Di 880 (lossy) Substrate	116
4.4.3: Omeganet MTM Structures Over FR-4 (lossy) Substrate	124
4.4.4: Omega MTM Structures Over FR-4 (lossy) Substrate	127
4.4.5: Hexagonal Two-Dimensional Omeganet Over FR-4 (lossy) Substrate	130
4.4.6: Select Cases Derived from 2D Hexagonal Omeganet Over FR-4 (lossy) Substrate.....	137
4.5: Three-Dimensional Omeganet Metamaterial Structures	143
CHAPTER V. CONCLUSIONS AND DISCUSSION	151
5.1: Conclusion	151
5.2: Discussion.....	152
5.3: Future Work.....	152
5.3.1: Fabrication and Measurements	153
5.3.2: Further Optimizations	153
5.3.3: Application Approach.....	153
REFERENCES	154
BIOGRAPHICAL SKETCH	160

LIST OF TABLES

	Page
Table 2.4.1: Comparison of Literature Review Near-Zero Refractive Index Metamaterials (NZRIM).....	17
Table 4.2.1: CCRR Structure Linewidth and Spacing Variations for 4 mm × 4 mm Unit Cell.....	83
Table 4.2.2: CCRR Structure Linewidth and Spacing Variations for 5 mm × 5 mm Unit Cell.....	85
Table 4.2.3: CCRR Structure Linewidth and Spacing Variations for 6 mm × 6 mm Unit Cell.....	88
Table 4.2.4: CCRR Structure Linewidth and Spacing Variations for 8 mm × 8 mm Unit Cell.....	91
Table 4.3.1: Ring Split Variations for 6 mm × 6 mm Unit Cell (Boundary Range: 1 – 40 GHz).....	98
Table 4.3.2: Ring Split Variations for 8 mm × 8 mm Unit Cell (Boundary Range: 1 – 30 GHz).....	101
Table 4.4.1: Summary of Low Loss NZRIM Bands for 2D Omeganet Structures in Arlon Di 880 Substrate	115
Table 4.4.2: Summary of Low Loss NZRIM Bands for 2D Omega Structures in Arlon Di 880 Substrate	123
Table 4.4.3: Summary of Low Loss NZRIM Bands for 2D Omeganet Structures in FR-4 Substrate.....	127
Table 4.4.4: Summary of Low Loss NZRIM Bands for 2D Omega Structures in FR-4 Substrate.....	130

Table 4.4.5: Summary of Low Loss NZRIM Bands for 2D Hexagonal Omeganet Structures in FR-4 Substrate	136
Table 4.4.6: Summary of Low Loss NZRIM Bands for Select 2D Hexagonal Omeganet Structures in FR-4 Substrate	142
Table 4.5.1: Summary of Low Loss NZRIM Bands for 3D Omeganet Structures.....	149

LIST OF FIGURES

	Page
Fig 2.1.1: Li, Y. et al [2.5]: Zero-Index MTM Composed of Silicon Pillar Arrays Embedded in a Polymer Matrix and Clad in Gold Film Produces a Constant Phase of Light Which Stretches out in Infinitely Long Wavelengths.	4
Fig 2.1.2: D. R. Smith <i>et al.</i> [2.16]: First <i>LH</i> Structure Consisting of Split-Ring Resonators Fabricated by Smith’s group in UCSD.	6
Fig 2.2.1: Classification of Materials in the $\epsilon\mu$ -plane in terms of their sign for permittivity and permeability [2.17].	7
Fig. 2.2.2: Classification of Extreme-Magnitude Materials in the $\epsilon\mu$ -plane [2.17].	8
Fig. 2.3.1: Flowchart of Robust Method for Extracting Complex Effective Parameters [2.19].	11
Fig. 2.3.2: Location of the Two Effective Boundaries of a Two-Cell MTM [2.19].	13
Fig. 3.1.1: Illustration of Negative Refractive Index (NRI).	41
Fig. 3.1.2: Illustration of Zero Refraction Index (ZRI).	42
Fig. 3.2.1: Step 1 – Run CST STUDIO SUITE. Once loaded, this is the start screen.	44
Fig. 3.2.2: Step 2 – Click “Create a new project” button.	45
Fig. 3.2.3: Step 3 – From the “Create a new template” screen, select “MW & RF & Optical”.	45
Fig. 3.2.4: Step 4 – Select the “Periodic Structures” workflow.	46
Fig. 3.2.5: Step 5 – Select “Phase Reflection Diagram” workflow.	46
Fig. 3.2.6: Step 6 – Select “Frequency Domain” solver.	47
Fig. 3.2.7: Step 7 – Select the appropriate units. The default settings are set for microwave applications.	47


Fig. 3.2.8: Step 8 – Configure additional settings such as frequency range and monitors (optional at this point).....	48
Fig. 3.2.9: Step 9 – Name template appropriately for future use.	48
Fig. 3.2.10: CST Microwave Studio Workspace.	49
Fig. 3.2.11: “Modeling” tab ribbon.	49
Fig. 3.2.12: Step 10 – Click the “Modeling” tab at the top, then click the “Brick”  button.....	50
Fig. 3.2.13: Step 11 – After clicking the “Brick” button, press the Tab key on the keyboard. Although one may manually select the points for the structure, it is more efficient to assign aptly-named variables for these. This prompt is for the x -max and y -max coordinates of the structure.	50
Fig. 3.2.14: Step 12 – After clicking OK on the previous step, this “New Parameter” window will pop up. In our case, the Unit Cell is 6×6 mm. Don’t forget the description (optional).....	51
Fig. 3.2.15: Step 13 – Next, just as in Step 11, this window prompts for the x -min and y -min coordinates of the structure.....	51
Fig. 3.2.16: Step 14 – After entering the coordinates for the length and width of the structure, CST will prompt for the “height” of the structure. By default, the software allows the user to manually select the points in the Workspace. Simply hit the Tab key to enter a variable name instead as shown.....	51
Fig. 3.2.17: Step 15 – After clicking OK on the previous step, this “New Parameter” window will pop up. In our case, the substrate thickness for FR-4 is 1.6 mm. Don’t forget the description (optional).	52
Fig. 3.2.18: Step 15 – Once finished with the size parameters, this confirmation window will pop up. Here you may name this structure, readjust parameters, and select the material. Click the drop-down for the “Materials” and select either from the default materials or, in our case, “[Load material from library...]” to select FR- 4.	52

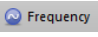
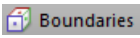
Fig. 3.2.19: Step 16 – Select the desired material from the Material Library, in our case, FR-4 (lossy) was selected.	53
Fig. 3.2.20: Step 17 –CST will prompt the user to confirm all the parameters for the structure.	53
Fig. 3.2.21: FR-4 (lossy) substrate structure in CST Workspace.....	54
Fig. 3.2.22: Components for the design will be displayed at the top-left column under “Navigation Tree.”	54
Fig. 3.2.23: Step 18 – (optional) In case the design requires different values for ϵ_r and μ_r , these may be modified by right-clicking the structure from the component list, then select “Material Properties”.	55
Fig. 3.2.24: Step 19 – (optional) From the “Material Parameters” General tab, one may change the value for Epsilon, Mue, color, etc.	55
Fig. 3.2.25: Step 20 – (optional) From the “Material Parameters” Conductivity tab, one may change the value for loss tangent, etc.	56
Fig. 3.2.26: Substrate and MTM structure CAIII. The same steps for apply for the MTM structure.	56
Fig. 3.2.27: Step 21 – From the “Simulation” tab, select the Frequency  button.	57
Fig. 3.2.28: Step 22 – Input the desired frequency range min and max values to be simulated.....	57
Fig. 3.2.29: Step 23 – From the “Simulation” tab, once more, select the “Boundaries”  button.....	57
Fig. 3.2.30: Step 24 – Since we are working with periodic structures, set x -min, y -min, x -max, y -max to “unit cell”, and z -min and z -max (the propagation direction) set to “open (add space)” which allows for CST to evaluate the best spacing for the location of Port-1 and Port-2 with respect to the MTM structure “slab.”	58
Fig. 3.2.31: MTM structure in Unit Cell configuration with Bounding Box, which appears after setting Boundary Conditions.	59

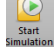

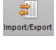
Fig. 3.2.32: Step 25 – From the “Simulation” tab, click “Setup Solver.”	59
Fig. 3.2.33: Step 26 – From the Frequency Solver, click the “Select...” button to configure the excitation.	60
Fig. 3.2.34: Step 27 – Select excitation source from z-min, and TE(0,0) mode.	60
Fig. 3.2.35: Step 28 – To start the simulation, you may either click “Start”  from within the Frequency Solver, or from the “Home” tab, click the “Start Simulation” button.	60
Fig. 3.2.36: Step 28 – After the simulation has completed, you may view the various results by selecting 1D, 2D/3D Results in the Navigation Tree. In our case, we are interested in the <i>S</i> -Parameters for further investigation, so click on “1D Results”, then “S-Parameters”, where you may view either individual <i>S</i> -Parameters or all at once.	61
Fig. 3.2.37: Step 29 – In order to export the <i>S</i> -Parameter data, you must click on the individual <i>S</i> -Parameter, (which will enable the “1D plot” tab to appear), then select the “Polar”  button (which contains frequency, magnitude and phase data of each of the samples).	62
Fig. 3.2.38: Step 30 – Once the <i>S</i> -Parameter is set to Polar, select the “Post Processing” tab.	63
Fig. 3.2.39: By default, CST labels the S_{11} and S_{21} <i>S</i> -Parameters SZmin(1),Zmin(1) and SZmax(1),Zmin(1), respectively, according to the configured excitation and ports from Step 27.	63
Fig. 3.2.40: Step 31 – From the “Post Processing” tab, click the “Import/Export”  button, then select “Plot Data (ASCII)...”	64
Fig. 3.2.41: Step 32 – The user is prompted to select a location and filename for the <i>S</i> -Parameter data. It is highly encouraged to properly name the data with case names, etc., rather than “ <i>S21.txt</i> ”	64
Fig. 3.2.42: ASCII representation of the exported <i>S</i> -Parameter data.	65

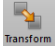
Fig. 3.2.43: Step 1 – Building from the foundation for Section 3.2.1, we start with our 2D MTM structure. Click to select the MTM structure name under the “Components” folder, top-left column. In our case, the MTM is called “CAIII.”	66
Fig. 3.2.44: Step 2 – Once the MTM structure is selected, click on the “Modeling” tab.	67
Fig. 3.2.45: Step 3 – From the “Modeling” tab, select the “Transform”  button.	67
Fig. 3.2.46: The Transform button will prompt to either Translate (Move), Scale, Rotate or Mirror the selected structure.	68
Fig. 3.2.47: Step 4 – Since we are designing a “cube” structure from the 2D MTM selected, click the “Copy” box, and fill the desired length to copy the 2D structure in the desired direction.	68
Fig. 3.2.48: “Front” and “Back” sides of the cube in the z-direction. After “copying” and moving the 2D MTM structure, we have two structures under “component1.”	69
Fig. 3.2.49: Step 5 – Select both the original and new 2D structures, then click the “Transform” button once again.	69
Fig. 3.2.50: Step 6 – Select to “Rotate” the structure, check the “Copy” box, fill the Rotation angle 90° in the y-axis, and choose the Origin to be the center of the shape.	70
Fig. 3.2.51: Step 7 – We repeat Steps 5 and 6, however, select the Rotation angle 90° in the x-axis to complete the cube structure.	70
Fig. 3.2.52: Completed 3D CAIII MTM Structure.	71
Fig. 3.3.1: From Katsarakis et al. [3.3], the left-hand side depicts the MTM structure studied. The right-hand side shows the four orientations for the SRR with respect to the “triad” k, E, and H of the incident EM field.	72
Fig. 3.3.2: From Katsarakis et al. [3.3], the top plot shows the measured transmission spectra of a lattice of SRRs for the four different orientations shown in Fig. 3.3.1. The bottom plot demonstrates the plotted (MATLAB) transmission spectra from the S-Parameter data obtained from CST simulation to validate CST setup.	72

Fig. 3.3.3:	CST simulation of cases $a - d$ from Katsarakis study Fig. 3.3.1 [3.3], to validate CST setup.....	74
Fig. 3.3.4:	From Kafesaki et al. [3.4], (a). – (b). corresponding designs studied square and circular single SRR, (c). transmission, (T , in dB) as a function of frequency (GHz) for the structures (a) and (b), (d). magnetic permeability as a function of frequency for structures (a) and (b).	75
Fig. 3.3.5:	CST simulation of Single-ring SRR structures from Kafesaki’s study Fig. 3.3.2 [3.4], in order to validate Robust Method for Extraction of Effective Parameters MATLAB code: (a). squared, (b). circular.	76
Fig. 3.3.6:	Comparison of extraction for magnetic permeability as a function of frequency for structures square and circular SRR [3.4], in order to validate Robust Method for Extraction of Effective Parameters MATLAB code: (a). Kafesaki’s result for $\text{Re}(\mu)$, (b). Extracted $\text{Re}(\mu)$ using Robust Method.....	77
Fig. 3.3.7:	Comparison of transmission (T , in dB) as a function of frequency: (a). Kafesaki’s result [3.4], (b). obtained S_{21} data from CST simulation and plotted via MATLAB.....	78
Fig. 4.1.1:	Progression of 3D Omega-net MTM Design from its Fundamental Structure to the End Product: (a) Circular Closed-Ring Resonator (CCRR), (b) Circular Split-Ring Resonator (CSRR), (c) Omeganet structure derived from the CSRR, (d) Hexagonalized Omeganet, (e)-(h) Selected Optimizations Performed on Hexagonal Omeganet, (i) “Single Shell” Cubic Hexagonal Omeganet derived from Optimized Hexagonal Omeganet Structure, (j) “Octahedral Double-Shell” Cubic Hexagonal Omeganet derived from Optimized 2D Hexagonal Omeganet Structure.....	80

Fig. 4.2.1:	Circular Closed-Ring Resonator (CCRR) Structure: (a). CCRR in unit cell with parameters g (unit cell size), lw (structure linewidth), sp (spacing between periodic structures), (b). Representation of periodic array with 2×2 CCRR unit cells, (c). CCRR in unit cell with propagation direction in the z -direction.	81
Fig. 4.2.2:	CCRR Designs for Unit Cell Size $4 \text{ mm} \times 4 \text{ mm}$ Varying Parameters for Linewidth, lw , and Spacing Between Periodic Structures, sp : (a). $lw = 1 \text{ mm}$, $sp = 2 \text{ mm}$, (b). $lw = 1 \text{ mm}$, $sp = 1 \text{ mm}$, (c). $lw = 0.5 \text{ mm}$, $sp = 1 \text{ mm}$, (d). $lw = 0.5 \text{ mm}$, $sp = 0.5 \text{ mm}$, (e). $lw = 0.25 \text{ mm}$, $sp = 0.5 \text{ mm}$, (f). $lw = 0.125 \text{ mm}$, $sp = 0.25 \text{ mm}$, (g). $lw = 0.0625 \text{ mm}$, $sp = 0.125 \text{ mm}$, (h). $sp = 0.03125 \text{ mm}$, $sp = 0.0625 \text{ mm}$	83
Fig. 4.2.3:	Effective Parameter Extraction from Simulation Results for $4 \text{ mm} \times 4 \text{ mm}$ Unit Cell CCRR Cases 1 – 8: (a) S -Parameters, (b) Real and imaginary parts of n , (c) Real and imaginary parts of ϵ , (d) Real and imaginary parts of μ , (e) Loss Factor.	84
Fig. 4.2.4:	CCRR Designs for Unit Cell Size $5 \text{ mm} \times 5 \text{ mm}$ Varying Parameters for Linewidth, lw , and Spacing Between Periodic Structures, sp : (a). $lw = 1 \text{ mm}$, $sp = 2 \text{ mm}$, (b). $lw = 1 \text{ mm}$, $sp = 1 \text{ mm}$, (c). $lw = 0.5 \text{ mm}$, $sp = 1 \text{ mm}$, (d). $lw = 0.5 \text{ mm}$, $sp = 0.5 \text{ mm}$, (e). $lw = 0.25 \text{ mm}$, $sp = 0.5 \text{ mm}$, (f). $lw = 0.125 \text{ mm}$, $sp = 0.25 \text{ mm}$, (g). $lw = 0.0625 \text{ mm}$, $sp = 0.125 \text{ mm}$, (h). $lw = 0.03125 \text{ mm}$, $sp = 0.0625 \text{ mm}$	86
Fig. 4.2.5:	Effective Parameter Extraction from Simulation Results for $5 \text{ mm} \times 5 \text{ mm}$ Unit Cell CCRR Cases 1 – 8: (a) S -Parameters, (b) Real and imaginary parts of n , (c) Real and imaginary parts of ϵ , (d) Real and imaginary parts of μ , (e) Loss Factor.	87

Fig. 4.2.6:	CCRR Designs for Unit Cell Size $6\text{ mm} \times 6\text{ mm}$ Varying Parameters for Linewidth, lw , and Spacing Between Periodic Structures, sp : (a). $lw = 1\text{ mm}$, $sp = 2\text{ mm}$, (b). $lw = 1\text{ mm}$, $sp = 1\text{ mm}$, (c). $lw = 0.5\text{ mm}$, $sp = 1\text{ mm}$, (d). $lw = 0.5\text{ mm}$, $sp = 0.5\text{ mm}$, (e). $lw = 0.25\text{ mm}$, $sp = 0.5\text{ mm}$, (f). $lw = 0.125\text{ mm}$, $sp = 0.25\text{ mm}$, (g). $lw = 0.0625\text{ mm}$, $sp = 0.125\text{ mm}$, (h). $lw = 0.03125\text{ mm}$, $sp = 0.0625\text{ mm}$.	89
Fig. 4.2.7:	Effective Parameter Extraction from Simulation Results for $6\text{ mm} \times 6\text{ mm}$ Unit Cell CCRR Cases 1 – 8: (a) S -Parameters, (b) Real and imaginary parts of n , (c) Real and imaginary parts of ϵ , (d) Real and imaginary parts of μ , (e) Loss Factor.	90
Fig. 4.2.8:	CCRR Designs for Unit Cell Size $8\text{ mm} \times 8\text{ mm}$ Varying Parameters for Linewidth, lw , and Spacing Between Periodic Structures, sp : (a). $lw = 1\text{ mm}$, $sp = 2\text{ mm}$, (b). $lw = 1\text{ mm}$, $sp = 1\text{ mm}$, (c). $lw = 0.5\text{ mm}$, $sp = 1\text{ mm}$, (d). $lw = 0.5\text{ mm}$, $sp = 0.5\text{ mm}$, (e). $lw = 0.25\text{ mm}$, $sp = 0.5\text{ mm}$, (f). $lw = 0.125\text{ mm}$, $sp = 0.25\text{ mm}$, (g). $lw = 0.0625\text{ mm}$, $sp = 0.125\text{ mm}$, (h). $lw = 0.03125\text{ mm}$, $sp = 0.0625\text{ mm}$.	92
Fig. 4.2.9:	Effective Parameter Extraction from Simulation Results for $8\text{ mm} \times 8\text{ mm}$ Unit Cell CCRR Cases 1–8: (a) S -Parameters, (b) Real and imaginary parts of n , (c) Real and imaginary parts of ϵ , (d) Real and imaginary parts of μ , (e) Loss Factor.	93
Fig. 4.3.1:	SRR Reference Studies on EM Response and Equivalent-Circuit: (a) From [4.5], permeability as a function of frequency for a square SRR. Solid dark lines correspond to the real and imaginary parts of the permeability determined using transfer matrix method (TMM) from simulation data; (b) From [4.6], SRR topology (left) and its equivalent-circuit model (right) (ohmic losses can be taken into account by including series resistance in the model).	94

Fig. 4.3.2:	Circular Split Ring Resonator (CSRR) Metamaterial Structure: (a). CSRR in unit cell with varying parameters linewidth of structure lw , spacing between periodic structures sp , and horizontal ring split rs_h , (b). Representation of periodic array with 2×2 CSRR unit cells, (c). CSRR in unit cell with propagation in the z -direction.	96
Fig. 4.3.3:	Effective Parameter Extraction from Simulation Results for $6 \text{ mm} \times 6 \text{ mm}$ Unit Cell CSRR Cases 1–8: (a) S -Parameters, (b) Real and imaginary parts of n , (c) Real and imaginary parts of ϵ , (d) Real and imaginary parts of μ , (e) Loss Factor.	99
Fig. 4.3.4:	Effective Parameter Extraction from Simulation Results for $6 \text{ mm} \times 6 \text{ mm}$ Unit Cell CSRR Cases 9–12: (a) S -Parameters, (b) Real and imaginary parts of n , (c) Real and imaginary parts of ϵ , (d) Real and imaginary parts of μ , (e) Loss Factor.	100
Fig. 4.3.5:	Effective Parameter Extraction from Simulation Results for $8 \text{ mm} \times 8 \text{ mm}$ Unit Cell CSRR Cases 1–8: (a) S -Parameters, (b) Real and imaginary parts of n , (c) Real and imaginary parts of ϵ , (d) Real and imaginary parts of μ , (e) Loss Factor.	102
Fig. 4.3.6:	Effective Parameter Extraction from Simulation Results for $8 \text{ mm} \times 8 \text{ mm}$ Unit Cell CSRR Cases 9 –12: (a) S -Parameters, (b) Real and imaginary parts of n , (c) Real and imaginary parts of ϵ , (d) Real and imaginary parts of μ , (e) Loss Factor.	103
Fig. 4.4.1:	From [4.5], (a). Real part of the permittivity as a function of frequency for a wire medium, (b). Real part of permeability and real part of permittivity as a function of frequency for the combination of SRR/wire medium.	104
Fig. 4.4.2:	From [4.9], an LC circuit model for the fishnet structure where L_s and L_n denote the loop inductances at the slabs and necks, respectively, and C the capacitance of the structure.	106

Fig. 4.4.3:	Progression of the 2D Omeganets (top row) and Omegas (bottom row) in FR-4 Substrate varying the location of the ECB: (a). Omeganet Right ECB Case, (b). Omeganet Right-Middle ECB Case, (c). Omeganet Middle ECB Case, (d). Omeganet Left-Middle ECB Case, (e). Omeganet Left ECB Case, (f). Omega Right ECB Case, (g). Omega Right-Middle ECB Case, (h). Omega Middle ECB Case, (i). Omega Left-Middle ECB Case, (j). Omega Left ECB Case.....	106
Fig. 4.4.4:	Modified CSRR 6 mm \times 6 mm “Omega” Metamaterial Structure with the <i>Epsilon</i> -Controlling Bar (ECB) at the Right Side Position with parameters $lw = rs_h = 1$ mm, $sp = 0.5$ mm, and variable dx : (a) Omeganet Unit Cell with Connected End-to-End ECB, (b) Omega Unit Cell with Disconnected ECB.	108
Fig. 4.4.5:	Omeganet MTM Structure in 6 mm \times 6 mm Unit Cell Size: (a). Omeganet Structure displaying the design dimensions in unit cell with fixed parameters linewidth, $lw = 1.0$ mm, spacing between structures, $sp = 0.5$ mm, and the ECB is located on the Right case ($dx = 2.25$), (b). Representation of periodic array with 2×2 Omeganet unit cells, (c). Omeganet Structure in Unit Cell with propagation in the z -direction.	109
Fig. 4.4.6:	Omeganet MTM Structure in 6 mm \times 6 mm Unit Cell Size: (a). Omeganet Structure displaying the design dimensions in unit cell with fixed parameters linewidth, $lw = 1.0$ mm, spacing between structures, $sp = 0.5$ mm, and the ECB is located on the Right-Middle case ($dx = 1.125$), (b). Representation of periodic array with 2×2 Omeganet unit cells, (c). Omeganet Structure in Unit Cell with propagation in the z -direction.	110

Fig. 4.4.7:	Omeganet MTM Structure in 6 mm × 6 mm Unit Cell Size: (a). Omeganet Structure displaying the design dimensions in unit cell with fixed parameters linewidth, $lw = 1.0$ mm, spacing between structures, $sp = 0.5$ mm, and the ECB is located on the Middle case ($dx = 0$), (b). Representation of periodic array with 2×2 Omeganet unit cells, (c). Omeganet Structure in Unit Cell with propagation in the z-direction.	111
Fig. 4.4.8:	Omeganet MTM Structure in 6 mm × 6 mm Unit Cell Size: (a). Omeganet Structure displaying the design dimensions in unit cell with fixed parameters linewidth, $lw = 1.0$ mm, spacing between structures, $sp = 0.5$ mm, and the ECB is located on the Left-Middle case ($dx = -1.125$), (b). Representation of periodic array with 2×2 Omeganet unit cells, (c). Omeganet Structure in Unit Cell with propagation in the z-direction.	112
Fig. 4.4.9:	Omeganet MTM Structure in 6 mm × 6 mm Unit Cell Size: (a). Omeganet Structure displaying the design dimensions in unit cell with fixed parameters linewidth, $lw = 1.0$ mm, spacing between structures, $sp = 0.5$ mm, and the ECB is located on the Left case ($dx = -2.25$), (b). Representation of periodic array with 2×2 Omega unit cells, (c). Omeganet Structure in Unit Cell with propagation in the z-direction.	113
Fig. 4.4.10:	Effective Parameter Extraction from Simulation Results for 6 mm × 6 mm Unit Cell 2D Omeganet in Arlon Di 880 Substrate: (a) S-Parameters, (b) Real and imaginary parts of n , (c) Real and imaginary parts of ϵ , (d) Real and imaginary parts of μ , (e) Loss Factor.	114

Fig. 4.4.11: Omega MTM Structure in 6 mm \times 6 mm Unit Cell Size: (a). Omega Structure displaying the design dimensions in unit cell with fixed parameters linewidth, $lw = 1.0$ mm, spacing between structures, $sp = 0.5$ mm, and the ECB is located on the Right case ($dx = 2.25$), (b). Representation of periodic array with 2×2 Omega unit cells, (c). Omega Structure in Unit Cell with propagation in the z -direction.	117
Fig. 4.4.12: Omega MTM Structure in 6 mm \times 6 mm Unit Cell Size: (a). Omega Structure displaying the design dimensions in unit cell with fixed parameters linewidth, $lw = 1.0$ mm, spacing between structures, $sp = 0.5$ mm, and the ECB is located on the Right-Middle case ($dx = 1.125$), (b). Representation of periodic array with 2×2 Omega unit cells, (c). Omega Structure in Unit Cell with propagation in the z -direction.	118
Fig. 4.4.13: Omega MTM Structure in 6 mm \times 6 mm Unit Cell Size: (a). Omega Structure displaying the design dimensions in unit cell with fixed parameters linewidth, $lw = 1.0$ mm, spacing between structures, $sp = 0.5$ mm, and the ECB is located on the Middle case ($dx = 0$), (b). Representation of periodic array with 2×2 Omega unit cells, (c). Omega Structure in Unit Cell with propagation in the z -direction.	119
Fig. 4.4.14: Omega MTM Structure in 6 mm \times 6 mm Unit Cell Size: (a). Omega Structure displaying the design dimensions in unit cell with fixed parameters linewidth, $lw = 1.0$ mm, spacing between structures, $sp = 0.5$ mm, and the ECB is located on the Left-Middle case ($dx = -1.125$), (b). Representation of periodic array with 2×2 Omega unit cells, (c). Omega Structure in Unit Cell with propagation in the z -direction.	120

Fig. 4.4.15: Omega MTM Structure in $6\text{ mm} \times 6\text{ mm}$ Unit Cell Size: (a). Omega Structure displaying the design dimensions in unit cell with fixed parameters linewidth, $lw = 1.0\text{ mm}$, spacing between structures, $sp = 0.5\text{ mm}$, and the ECB is located on the Left case ($dx = -2.25$), (b). Representation of periodic array with 2×2 Omega unit cells, (c). Omega Structure in Unit Cell with propagation in the z -direction.	121
Fig. 4.4.16: Effective Parameter Extraction from Simulation Results for $6\text{ mm} \times 6\text{ mm}$ Unit Cell 2D Omega in Arlon Di 880 Substrate: (a) S -Parameters, (b) Real and imaginary parts of n , (c) Real and imaginary parts of ϵ , (d) Real and imaginary parts of μ , (e) Loss Factor.	122
Fig. 4.4.17: Progression of the 2D Omeganets (top row) and Omegas (bottom row) in FR-4 Substrate: (a). Omeganet Right Case, (b). Omeganet Right-Middle Case, (c). Omeganet Middle Case, (d). Omeganet Left-Middle Case, (e). Omeganet Left Case, (f). Omega Right Case, (g). Omega Right-Middle Case, (h). Omega Middle Case, (i). Omega Left-Middle Case, (j). Omega Left Case.	124
Fig. 4.4.18: 3×3 Unit Cells Array View of the 2D Omeganets (left column.) and 2D Omegas (right column.) in FR-4 (lossy) Substrate.	125
Fig. 4.4.19: Effective Parameter Extraction from Simulation Results for $6\text{ mm} \times 6\text{ mm}$ Unit Cell 2D Omeganet in FR-4 (lossy) Substrate 5 Cases: (a) S -Parameters, (b) Real and imaginary parts of n , (c) Real and imaginary parts of ϵ , (d) Real and imaginary parts of μ , (e) Loss Factor.	126
Fig. 4.4.20: 3×3 Unit Cells Array View of the 2D Omegas in FR-4 (lossy) Substrate: (a). Omega Right Case, (b). Omega Right-Middle Case, (c). Omega Middle Case, (d). Omega Left-Middle Case, (e). Omega Left Case.	128

Fig. 4.4.21: Effective Parameter Extraction from Simulation Results for 6 mm × 6 mm Unit Cell 2D Omega FR-4 (lossy) 5 Cases: (a) <i>S</i> -Parameters, (b) Real and imaginary parts of <i>n</i> , (c) Real and imaginary parts of ϵ , (d) Real and imaginary parts of μ , (e) Loss Factor.	129
Fig. 4.4.22: Progression of the 2D Hexagonal Omeganets in FR-4 Substrate: (a). Hex. Omeganet Right Case, (b). Hex. Omeganet Right-Middle Case, (c). Hex Omeganet Middle Case, (d). Hex. Omeganet Left-Middle Case, (e) Hex. Omeganet Left Case.....	131
Fig. 4.4.23: Hexagonal 2D Omeganet MTM Structure in 6 mm × 6 mm Unit Cell with the <i>Epsilon</i> -Controlling Bar (ECB) at the Right Side Position and structure parameters $lw = 1$ mm, $rs_h = 0.75$ mm, $sp = 0.5$ mm, and variable dx	132
Fig. 4.4.24: 3 × 3 Unit Cells Array View of the 2D Hexagonal Omeganets Five Cases in FR-4 (lossy) Substrate.....	133
Fig. 4.4.25: Effective Parameter Extraction from Simulation Results for 6 mm × 6 mm Unit Cell 2D Hexagonal Omeganet in FR-4 (lossy) Substrate: (a) <i>S</i> -Parameters, (b) Real and imaginary parts of <i>n</i> , (c) Real and imaginary parts of ϵ , (d) Real and imaginary parts of μ , (e) Loss Factor.....	134
Fig. 4.4.26: Comparison and Evaluation of Effective Parameter Extraction for 6 mm × 6 mm Unit Cell 2D Hexagonal Omeganet in FR-4 (lossy) Substrate: (a). Refractive index and (b) Loss Factor of the Hexagonal Omeganet Structures Focusing on the NNZ Frequency Range.....	135
Fig. 4.4.27: Selected Designs Derived from Hexagonal Omeganet MTM Structure with Optimization Design Names: (a). C3, (b). C3a, (c). C3ai, (d). C3aiii.	137
Fig. 4.4.28: MTM Design “C3a” Hexagonal 2D Omeganet Structure in 6 mm × 6 mm Unit Cell with the <i>Epsilon</i> -Controlling Bar (ECB) Position $dx = 0$ and structure parameters $lw = 1$ mm, $rs_h = 0.75$ mm, $rs_v = 0.3$ mm, $sp = 0.5$ mm.....	138

Fig. 4.4.29: MTM Design “C3ai” Hexagonal 2D Omeganet Structure in 6 mm × 6 mm Unit Cell with the <i>Epsilon</i> -Controlling Bar (ECB) Position $dx = 0$ and structure parameters $lw = 1$ mm, $rs_h = 0.75$ mm, $rs_v = 0.3$ mm, $sp = 0.5$ mm.....	138
Fig. 4.4.30: MTM Design “C3aiii” Hexagonal 2D Omeganet Structure in 6 mm × 6 mm Unit Cell with the <i>Epsilon</i> -Controlling Bar (ECB) Position $dx = dy = 0$ and structure parameters $lw = 1$ mm, $rs_h = rs_v = 0.3$ mm.....	139
Fig. 4.4.31: 2D Hexagonal Omeganet MTM Design “C3aiii” Derivation from Design “C3ai” by 90-degree rotation and overlaying.....	139
Fig. 4.4.32: 3 × 3 Unit Cells Array Configuration of the Selected 2D Hexagonal Omeganets MTM Design Optimizations: (a). C3, (b). C3a, (c). C3ai, (d). C3aiii.	140
Fig. 4.4.33: Effective Parameter Extraction from Simulation Results for 6 mm × 6 mm Unit Cell Select Optimizations for 2D Hexagonal Omeganet in FR4 (lossy) Substrate: (a) <i>S</i> -Parameters, (b) Real and imaginary parts of n , (c) Real and imaginary parts of ϵ , (d) Real and imaginary parts of μ , (e) Loss Factor.	141
Fig. 4.4.34: Select 2D Omeganet MTM Structure: (a). Refractive index and (b) Loss Factor of the Hexagonal Omeganet Structures Focusing on the NNZ Frequency Range.....	142
Fig. 4.5.1: Synthesized 3D Omeganet Structures Derived from the Select Optimized 2D Hexagonal Omeganet Structure CAIII: (a). Single-Shell (SS), (b). Double-Shell (DS), (c). Diamond Double-Shell (DDS), (d). Octahedral Double-Shell (ODS).....	144
Fig. 4.5.2: Inner View of the Double-Shell 3D Omeganet Designs: (a). Double-Shell (DS), (b). Diamond Double-Shell (DDS), (c). Octahedral Double-Shell (ODS).....	144
Fig. 4.5.3: 3 × 3 Unit Cells Array View of the 3D Hexagonal Omeganets where Left Colum are in Perspective View and Right Colum are Frontal View: (a) & (b). Single-Shell (SS), (c) & (d). Double-Shell (DS), (e) & (f). Diamond Double-Shell (DDS), (g) & (h). Octahedral Double-Shell (ODS).....	145

Fig. 4.5.4:	Effective Parameter Extraction from Simulation Results for 3D Hexagonal Omeganet MTM Structures: (a) Magnitude [dB] of S -Parameters, (b) Real and imaginary parts of n , (c) Real and imaginary parts of ϵ , (d) Real and imaginary parts of μ , (e) Loss Factor.....	146
Fig. 4.5.5:	Evaluation of Effective Parameter Extraction Results for 3D Hexagonal Omeganet MTM Structures Focusing on the NNZ Frequency Range in General: (a). Magnitude [dB] of S -Parameters, (b). Refractive index and (c) Loss Factor....	147
Fig. 4.5.6:	Evaluation of Effective Parameter Extraction Results for 3D Hexagonal Omeganet MTM Structures Focusing on the NNZ Frequency Range in the X -band Frequency Range: (a). Magnitude [dB] of S -Parameters, (b). Refractive index and (c) Loss Factor.....	148

CHAPTER I

INTRODUCTION

1.1: Background and Rational of Study

Ever since the first humans walked on the earth several thousand years ago, there has been an ongoing search and desire for the improvement of human living by modifying and bending the available natural materials to perform and behave in ways that make useful tools. Today, numerous scientific literature is available which describe various characteristics of materials under different physical environments. With such resources available, scientists and engineers may choose a particular material with its known characteristics for a specific application. Nevertheless, it is innately human to strive and go above and beyond the current state. We are always looking for new materials with novel characteristics which excel and exceed our expectations.

Metamaterials (from the Greek word “meta-“, *μετά*- meaning “to go beyond”) are synthetic composite materials with specific structures engineered to have properties not found in natural materials [1.1]. In general, metamaterials are designed as periodic structures in such a way that extraordinary electromagnetic novel properties sought after emerge such as negative refractive index, double negative refractive index, extreme chirality, and zero refractive index. Each periodic element within the structure is referred to as a unit cell. The periodicity of these unit cells are of scales much smaller than the wavelength of particular interest.

Just like naturally existing materials, the properties of metamaterials are intrinsically derived from the selected components and the design and arrangements of such. Once a designer finds a basis for a system, then the next step is to design the structure from the components with specific patterns such that the dominant electromagnetic resonances may be easily “tuned” or controlled. These unit cell components are arranged in a periodic fashion in one-, two- or three-dimensional arrays. Sandwiching or coupling together such arrangement of these components will modify and have a significant impact on the properties of the overall metamaterial design.

This research is primarily focused on near-zero refractive index metamaterials with low loss, where permittivity and permeability are both close to zero. Their main drawback is that there is a significant loss, which is generally described by the loss factor (LF) or figure of merit (FOM) As the real part of a refractive index is very small or close to zero, LF increases dramatically, starting high loss. It is important to design NZRIM where the imaginary part of refractive index is low. Several approaches to design broad NZRIM bandwidth with low loss have been proposed and discussed.

1.2: Objectives

1.2.1: Study electromagnetic properties of near-zero refractive index metamaterials.

1.2.2: Design near-zero refractive index metamaterials with low loss in the X-band microwave regimes.

1.3: Scope and Limitations

Design and optimize near-zero refractive index metamaterials (NZRIM) in the *X*-band microwave regimes.

1.4: Anticipated Outcomes

This research benefits the antenna components in telecommunication systems, microwave lens, etc. The aim of this research is to design near-zero refractive index metamaterials that exhibits relatively low losses.

CHAPTER II

THEORIES AND LITERATURE REVIEWS

2.1: History of Metamaterials

Electromagnetic (EM) metamaterials (MTMs) are artificial EM media with specific structures engineered to have remarkable and exciting properties which transcend across the entire EM spectrum. For the past decade, scientific breakthroughs in MTMs research have demonstrated the tremendous potential MTMs have in vast fields of science and engineering. Such achievements include negative refractive index (NRI) media [2.1–2.3], EM invisibility [2.4], perfect lens [2.2], infinite phase velocity and wavelength applications in integrated optics [2.5] (Fig. 2.1.1), chiral metamaterials [2.6,2.7], EM tunneling [2.8], enhanced antennas, enhanced absorbers, EM shielding and wave blocking [2.9], lighter and more efficient X-Ray shielding, enhanced solar cells, sensors, polarizers and zero refractive index [2.10].

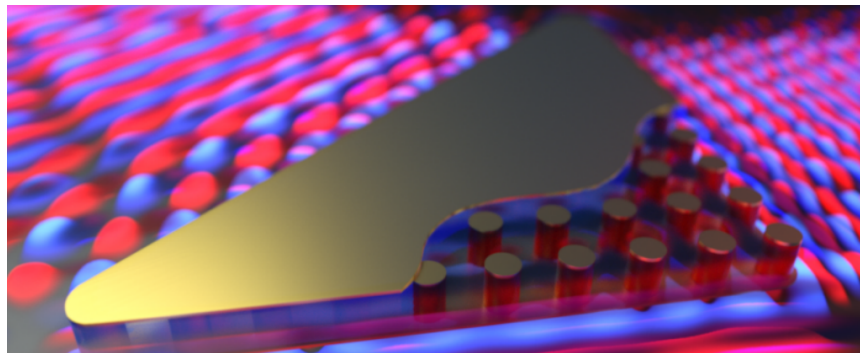


Fig. 2.1.1: Li, Y. et al [2.5]: Zero-Index MTM Composed of Silicon Pillar Arrays Embedded in a Polymer Matrix and Clad in Gold Film Produces a Constant Phase of Light Which Stretches out in Infinitely Long Wavelengths.

The history of EM MTMs begins at the turn of the twentieth century running almost parallel with the history of radio. To the best of our knowledge, the first ever attempt to experiment with artificial materials has its roots back to the late part the nineteenth century when in 1898 Jagadis Chunder Bose conducted the first microwave (MW) experiment on twisted structures whose geometries were essentially artificial chiral media by today's terminology [2.11]. From 1914 and into the 1920s, Karl F. Lindman studied artificial chiral media formed by embedding a collection of randomly oriented small wire helices in a host medium. [2.12]. In 1948, Winston E. Kock, a researcher for Bell Laboratories, pioneered works in MW engineering involving artificial dielectrics. He made lightweight MW lenses by employing particles which varied arranged conducting spheres, disks and strips in a periodic fashion and noticed that the permittivity ϵ and permeability μ can be purposely tuned, but not independently, effectively tailoring the refractive index of the artificial media [2.13].

The theory of left-handed (LH) materials, which have a negative refractive index (NRI), was first introduced by Russian scientist V. G. Veselago in 1968 [2.14]. He theoretically investigated plane-wave propagation in a material having simultaneously negative ϵ and μ , concluding that the refractive index of a material should be revised and expressed as $n = \sqrt{\epsilon\mu}$. However, Veselago's theoretical work on NRI MTMs did not advanced into practical applications due to the lack of the ability to produce a material possessing simultaneous negative ϵ and μ . In the 1990s, John B. Pendry and his colleagues were the first research group to demonstrate that a three-dimensional array of intersecting thin wires could be utilized to create negative values of ϵ [2.15] and negative μ [2.16]. This work leads the way to a new research domain of what we now know as metamaterials.



<http://esperia.iesl.forth.gr/~ppm/Research.html>

Fig. 2.1.2: D. R. Smith *et al.* [2.16]: First *LH* Structure Consisting of Split-Ring Resonators Fabricated by Smith's group in UCSD.

In 2000, David R. Smith [2.16] and his research group proposed and later produced the first MTM processing simultaneous negative ϵ and μ with the aid of copper split-ring resonator (SRR) structures on circuit boards and standing wires as periodic elements seen in Fig. 2.1.2. Once the first MTM demonstrating NIR prototype was materialized, it encouraged and motivated the rapid development of new experiments and theories of MTMs.

2.2: Metamaterial Classifications

Materials can be classified into four categories which depend on the real part of the effective complex permittivity (ϵ , *epsilon*) and effective complex permeability (μ , *mu*) [2.17]: double positive (DPS), double negative (DNG), epsilon negative (ENG) and mu negative (MNG). Fig. 2.2.1 shows a graph of μ vs. ϵ where Quadrant I (QI) are ordinary materials with

$(+)\epsilon$ and $(+)\mu$ which produce forward EM waves. Since these materials are on the right side of the μ -axis, they are referred to as right-handed (RH) materials or media, having a positive refractive index (PRI), $(+)n$. In Quadrant III (QIII) are the left-handed media (LHM), the type of materials from Veselago's theoretical work sometimes referred to as *Veselago media*, which possess both $(-)\epsilon$ and $(-)\mu$ and produce backward EM waves. These materials have a negative refractive index (NRI), $(-)n$.

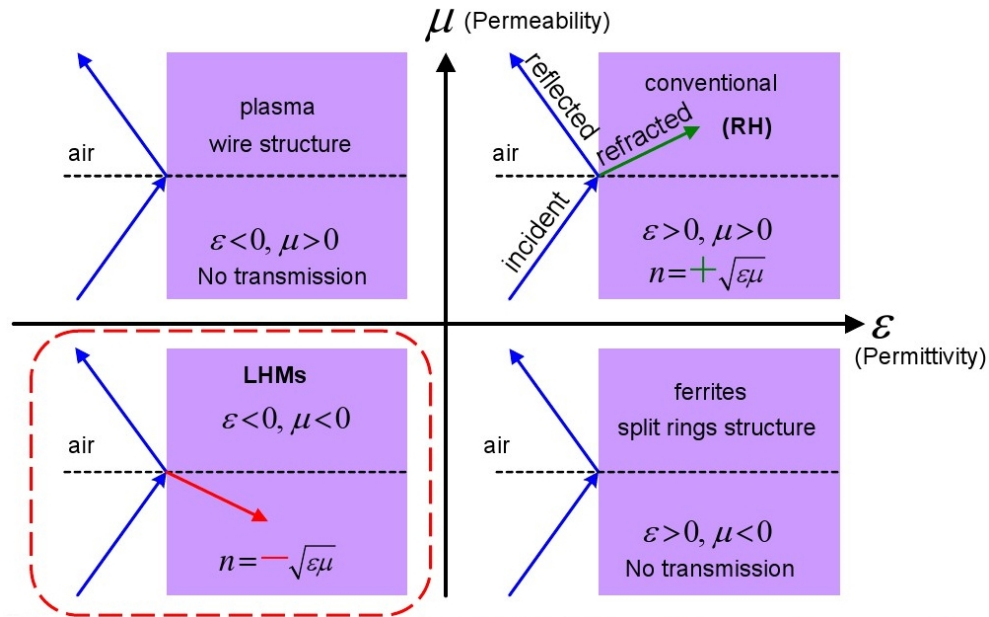


Fig. 2.2.1: Classification of Materials in the $\epsilon\mu$ -plane in terms of their sign for permittivity and permeability [2.17].

The materials in Quadrant II (QII) are referred to as *epsilon* negative (ENG), having $(-)\epsilon$ and $(+)\mu$, and the materials on Quadrant IV (QIV) as *mu* negative (MNG), with $(+)\epsilon$ and $(-)\mu$. The materials from QII and QIV are both plasmonic media, metals or metal-like, which can exploit interface waves or surface plasmons. Plasmonic media cannot support propagation of EM waves.

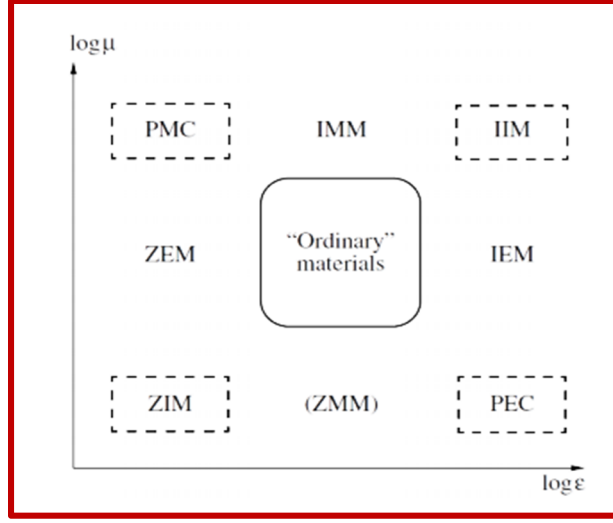


Fig. 2.2.2: Classification of Extreme-Magnitude Materials in the $\epsilon\mu$ -plane [2.17].

Plane waves propagating in homogenous dielectric-magnetic media can be analyzed with refractive index $n = \sqrt{\epsilon\mu}$ and with wave impedance $z = \sqrt{\frac{\mu}{\epsilon}}$. In the ideal EM case, the perfect electric conductor (PEC) corresponds to $\epsilon \rightarrow \infty, \mu \rightarrow 0$, and the perfect magnetic conductor (PMC) has $\epsilon \rightarrow 0, \mu \rightarrow \infty$. Therefore, PEC possesses an extremely small impedance, (zero-impedance material), while PMC processes an extremely large impedance (infinite-impedance material). Combinations of either very large of very small values for the four parameters ϵ, μ, z and n are possible which are basis for drawing the classification of Fig. 2.2.2. The remaining abbreviations are IIM: infinite-index media; IMM: infinite-magnetic material; ZEM: zero-electric material; ZIM: zero-index material; ZMM: zero-magnetic material; IEM: infinite-electric material.

2.3: Electromagnetic Material Parameters Extraction

After Veselago's work [2.14] where the first systematic study on LH material parameters was performed, several methods [2.18-2.22] for the extraction of effective material parameters have been proposed in order to retrieve the effective complex permittivity, permeability,

impedance and refractive index of the material under test. The effective material parameters for complex permittivity

$$\varepsilon = \varepsilon' + j\varepsilon'' \quad (2.1)$$

and complex permeability

$$\mu = \mu' + j\mu'' . \quad (2.2)$$

Therefore, the complex effective refractive index is

$$n = n' + jn'' . \quad (2.3)$$

The method presented by Nicolson, Ross and Weir [2.20] enable the calculation of the complex permittivity and permeability of a material sample over a broad frequency range by utilizing the S -parameters, from which the effective refractive index n and impedance z are first obtained. The values for ε and μ are then calculated directly from equations:

$$\mu = nz \quad (2.4)$$

$$\varepsilon = \frac{n}{z} \quad (2.5)$$

However, this extraction method may fail in certain conditions such as then the thickness of the effective slab is not accurately estimated [2.21] or when the reflection (S_{11}) and

transmission (S_{21}) data are very small in magnitude [2.24]. The theoretical retrieval equations presented by Chen, Grzegorzczuk, Pacheco and Kong [2.19] present a robust and effective method and address the aforementioned issues. This robust method to retrieve constitutive effective parameters of a slab of MTMs characterizes such slab as an effective homogenous slab. In such case, one may retrieve ϵ and μ directly from S_{11} and S_{21} . In order to extract these complex material parameters, we must consider the unit element of the MTM with lattice vectors in the x -, y - and z - directions. Appropriate boundary conditions and excitations are applied to the various surfaces of the three-dimensional unit element to simulate the periodic MTM and its excitation in order to acquire the S -parameters S_{11} and S_{21} [2.25].

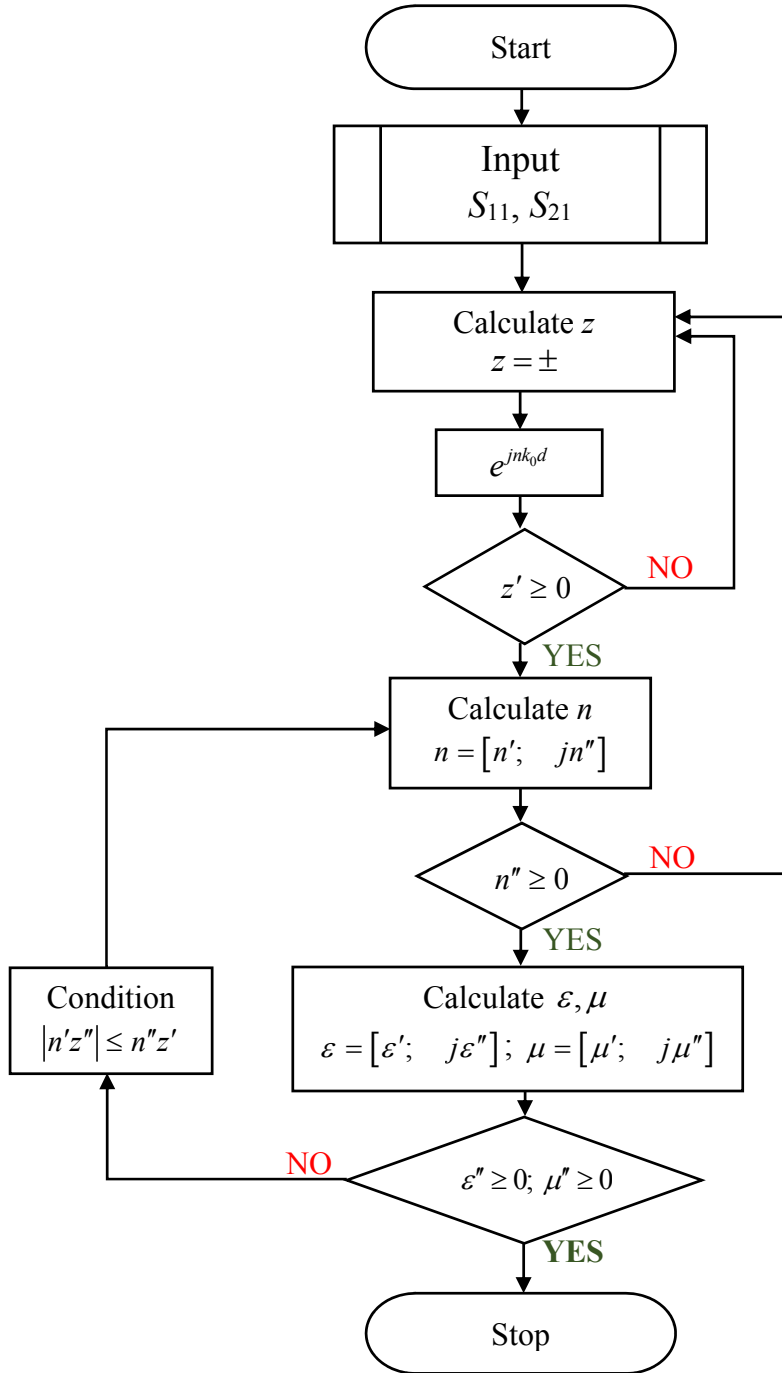


Fig. 2.3.1: Flowchart of Robust Method for Extracting Complex Effective Parameters [2.19].

Fig. 2.3.1 is a representation of the algorithm which the robust method follows systematically. The S parameters can be represented as [2.19],

$$S_{11} = \frac{R_{01}(1 - e^{j2nk_0d})}{1 - R_{01}^2 e^{j2nk_0d}}, \quad (2.6a)$$

$$S_{21} = \frac{(1 - R_{01})e^{jnk_0d}}{1 - R_{01}^2 e^{j2nk_0d}}, \quad (2.6b)$$

where $R_{01} = \frac{z-1}{z+1}$.

As indicated in [2.21,2.22], the refractive index and the impedance are obtained by solving for the impedance z by inverting the above Equations 2.6a and 2.6b yields,

$$z = \pm \sqrt{\frac{(1 + S_{11})^2 - S_{21}^2}{(1 - S_{11})^2 - S_{21}^2}}, \quad (2.7a)$$

$$e^{jnk_0d} = X \pm j\sqrt{1 - X^2}, \quad (2.7b)$$

Where $X = \frac{1}{2S_{21}(1 - S_{11}^2 + S_{21}^2)}$.

Since MTMs are passive media, the signs in Equations 2.7a and 2.7b are determined by the requirements

$$z' \geq 0 \quad (2.8a)$$

and

$$n'' \geq 0 \quad (2.8b)$$

where $(\cdot)'$ and $(\cdot)''$ denote the real and imaginary parts respectively. From Eqn. (2.7b), the complex refractive index n can be determined

$$n = \frac{1}{k_0 d} \left\{ \left(\left[\ln \left(e^{jnk_0 d} \right) \right]'' + 2m\pi \right) - j \left[\ln \left(e^{jnk_0 d} \right) \right]' \right\}, \quad (2.9)$$

where “ m ” is an integer related to the branch index of n' . The imaginary part n'' is uniquely determined, yet the real part n' is complicated by the branches of the logarithm function. Eqs. (2.7a) and (2.7b) can be directly applied in a homogenous slab which:

- i. The boundaries of the slab are well defined, and
- ii. S parameters are accurately known.

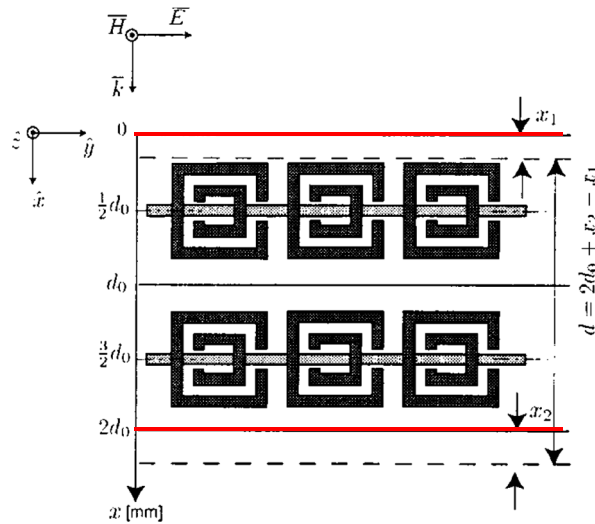


Fig. 2.3.2: Location of the Two Effective Boundaries of a Two-Cell MTM [2.19].

The locations of the two boundaries may be observed in Fig. 2.3.2 (solid red lines). One characteristic of a homogenous slab of material is the fact that its impedance does not depend on its thickness [2.19]. Furthermore, optimization model to minimize the impedance mismatch of different numbers of MTM cells is given by

$$\min f(\bar{x}) = \frac{1}{N_f} \sum_{i=1}^{N_f} \frac{|z_1(f_i, \bar{x}) - z_2(f_i, \bar{x})|}{\max\{|z_1(f_i, \bar{x})|, |z_2(f_i, \bar{x})|\}}, \quad (2.10)$$

where N_f denotes the total number of sample frequencies and $z_j(f_i)$ represents the impedance of the slab j (where $j = 1, 2$) at frequency f_i . When utilizing the EM commercial software CST Microwave Studio[®] to simulate “unit cells” for periodic structures, the ports are automatically set, thus employing the most optimal boundaries. S parameters obtained from numerical computation and measurements are noisy. This is since the impedance and refractive index are sensitive to small variations of S_{11} and S_{21} as both z and n are related [2.24], and for this matter Chen suggests to exploit their relationship in order to determine the signs in Equations 2.7a and 2.7b. The signs of real part of the impedance and the imaginary part of the refractive index are then changed so that both satisfy $z' \geq 0$ and $n'' \geq 0$, or equivalently $|e^{jnk_0d}| \leq 1$. From the relationship of z and n , n is derived from Equations 2.7a and 2.7b to obtain

$$e^{jnk_0d} = \frac{S_{21}}{1 - S_{11} \frac{z-1}{z+1}}. \quad (2.11)$$

In order to determine the branch index m of the real part of the refractive index at the initial frequency is determined from Equations 2.4 and 2.5, we have the imaginary part of the complex permeability defined by the equation

$$\mu'' = n'z'' + n''z', \quad (2.12a)$$

and the complex permittivity defined by the equation

$$\varepsilon'' = \frac{1}{|z|^2} (-n'z'' + n''z'). \quad (2.12b)$$

The requirements which must be satisfied to determine m are that $\varepsilon'' \geq 0$ and $\mu'' \geq 0$ or $n'' \geq 0$.

This leads to

$$|n'z''| \leq n''z'. \quad (2.13)$$

In this iterative method, if there is only one solution, it is the correct branch. In case there are multiple solutions, for each candidate branch index m the value of n' must be determined at all subsequent frequencies to check the validity of n' at all frequencies produced by the candidate initial branch [2.19].

2.4: Near-Zero Refractive Index Metamaterials

In recent years, many remarkable designs of NZRIM have been achieved, all which have diverse prospective applications. Table 2.4.1 contains a tabulation of the collected literature reviewed for this research and a comparison of operating frequency as well as structure design and materials. One thing to note is that although all of these designs present NZRIM, some of the designs are engineered to be either *epsilon* near-zero (ENZ), *mu* near-zero (MNZ) and *epsilon* and *mu* near-zero (EMNZ) to achieve NZRIM for their specific goal and application. For instance, designs such as [2.5, 2.29,2.30,2.33] are ENZ. which would essentially yield high electric losses due to high impedance. For our research, the goal is to have both ENZ and MNZ simultaneously in order to minimize electric and magnetic losses. We see the designs listed in Table 2.4.1[2.43, 2.47, 2.50, 2.53, 2.62] which claim to design their NZRIM with this goal in mind. In Chapter 3, we will further discuss these conditions in more detail.

Jang et. al. [2.37] proposed an antenna design they claim has been designed with a realized increased gain of about 5 dB by introducing a single layer MTM superstrate with

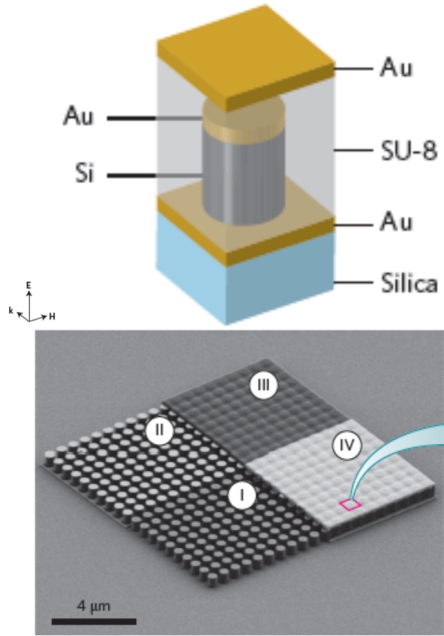
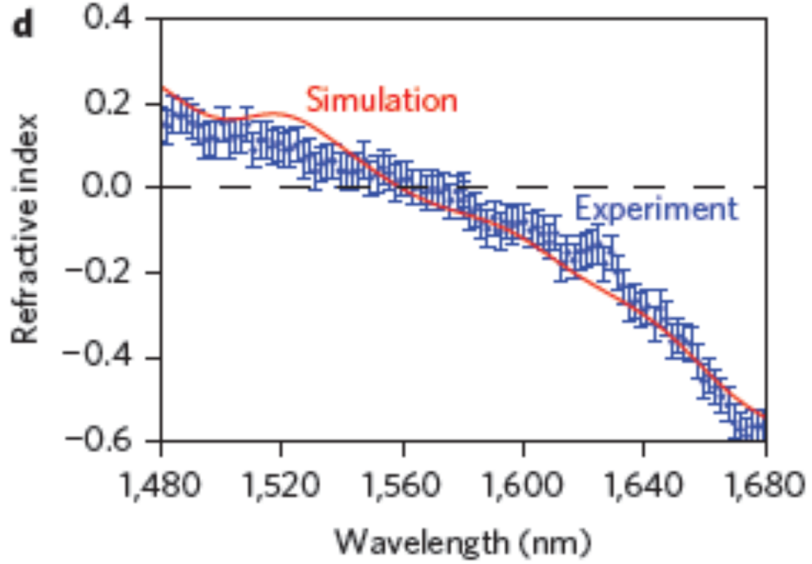
NZIRM. Their design is based on the concept of fractal geometry which was introduced to the antenna field as a new and innovative design which have demonstrated good performances.

Navarro-Cía et al. [2.47] report on a structure designed for directivity enhancement by a short-focal-length plano-concave lens. Their design is engineered by stacked subwavelength circular hole arrays in a fishnet-like fashion. They claim to have achieved pencil-like radiation by utilizing NZIRM lens based on stacked extraordinary optical transmission layers at millimeter waves with high gain.

Soemphol et al. [2.62] claim to have achieved a broader near-zero band by stacking layers of fishnet MTM structures. They also pointed out that the near-zero band is not only broader, but located at a lower frequency as more layers are added. This is due to the impact of the total capacitance and the couplings among the additional structures.

The research from groups such as these will prove to be very useful in our design of NZIRM with low loss.

TABLE 2.4.1
 Comparison of Literature Review Near-Zero Refractive Index Metamaterials (NZRIM) [pp. 17– 40]

Ref. #	MTM Structure	Operating Freq. [GHz]
[2.5]		

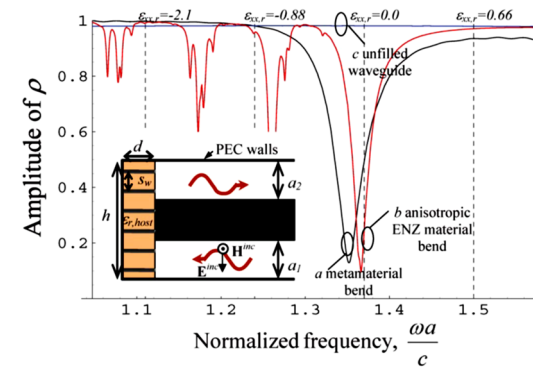
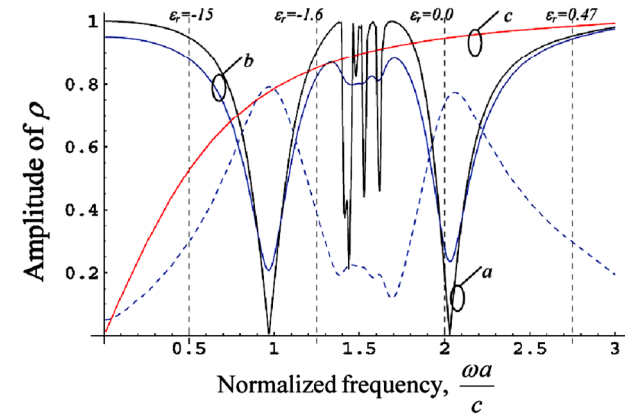
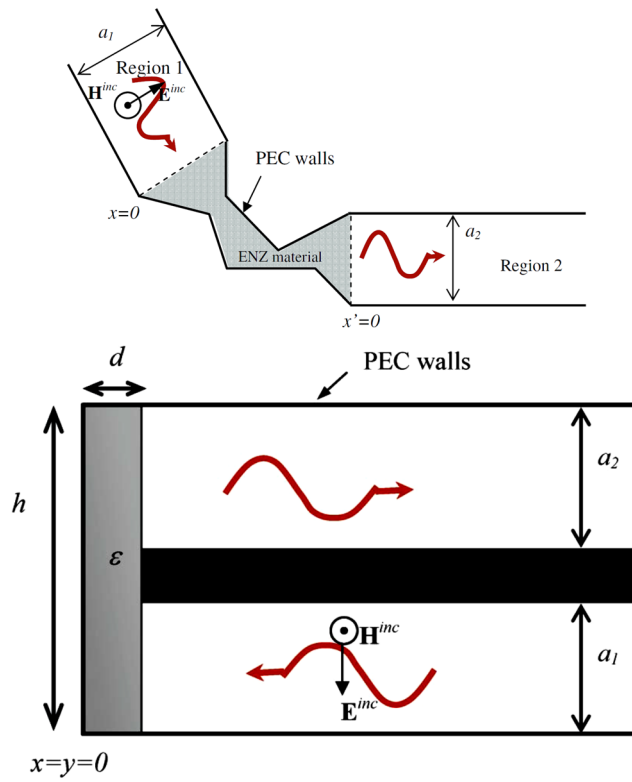
Ref. #

MTM Structure

Operating Freq.

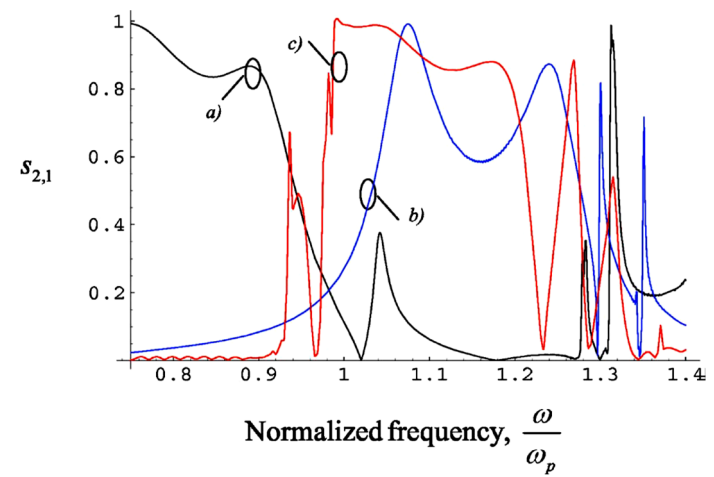
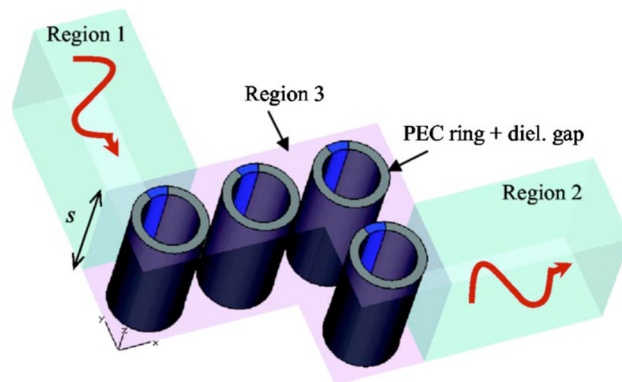
[GHz]

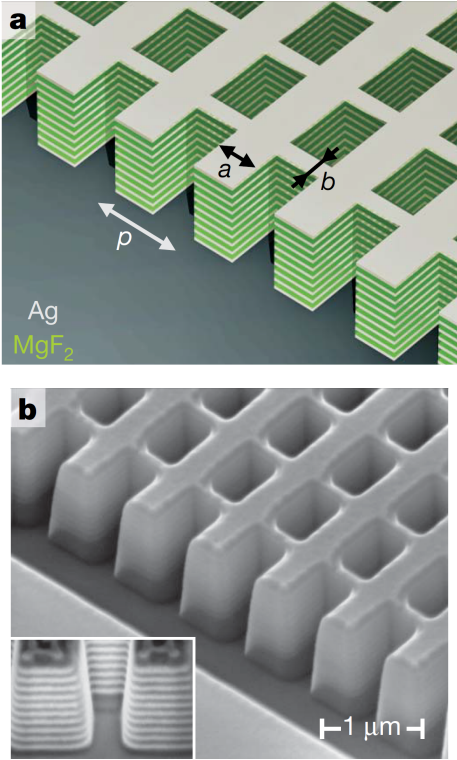
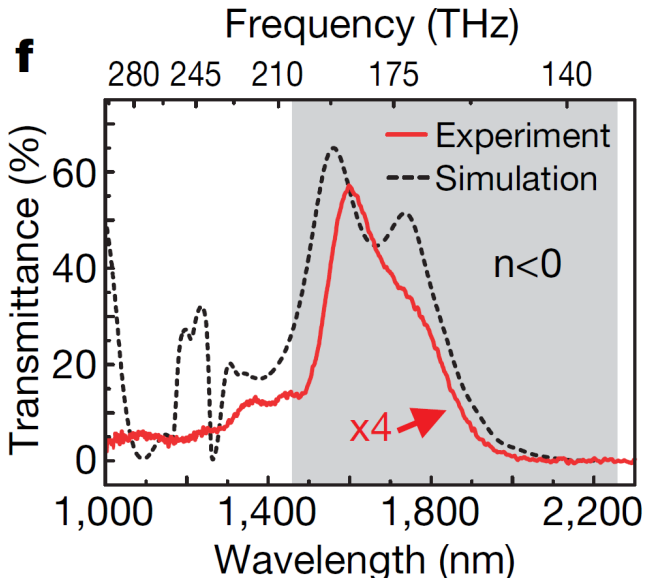
[2.29]

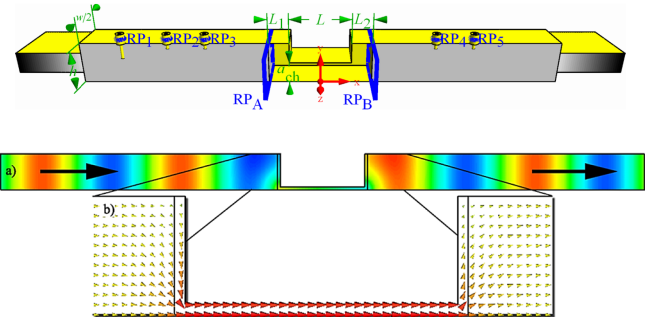
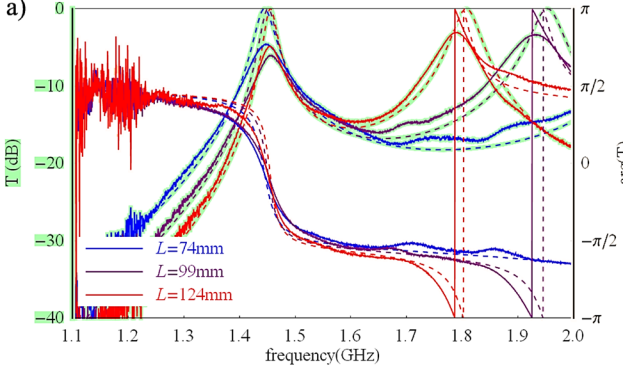
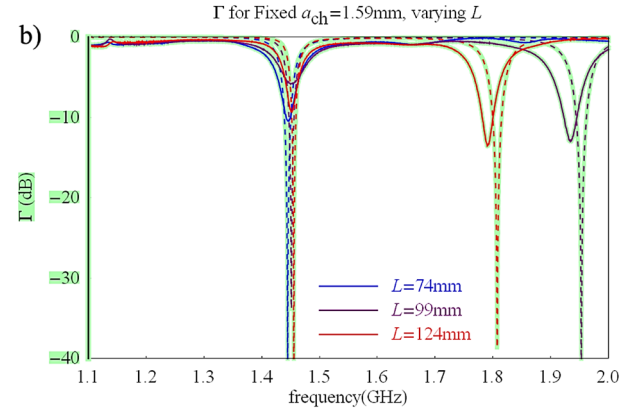


Ref. #	MTM Structure	Operating Freq. [GHz]
--------	---------------	--------------------------

[2.30]



Ref. #	MTM Structure	Operating Freq. [GHz]
[2.31]	 <p>Figure (a) is a 3D schematic of the MTM structure, showing a cross-hatched pattern of layers. The layers are labeled Ag (green) and MgF₂ (grey). Dimensions a, b, and p are indicated. Figure (b) is a scanning electron micrograph (SEM) of the structure, showing the physical realization of the cross-hatched pattern. A scale bar of 1 μm is provided.</p>	 <p>Figure (f) is a plot of Transmittance (%) versus Frequency (THz) and Wavelength (nm). The top x-axis shows Frequency (THz) from 280 to 140. The bottom x-axis shows Wavelength (nm) from 1,000 to 2,200. The y-axis shows Transmittance (%) from 0 to 60. The plot compares experimental data (red solid line) with simulation results (black dashed line). A shaded region indicates the $n < 0$ regime. A red arrow points to the experimental peak with a 'x4' magnification label.</p>

Ref. #	MTM Structure	Operating Freq. [GHz]
[2.33]		<p>a) T for Fixed $a_{ch}=1.59\text{mm}$, varying L</p>  <p>b) Γ for Fixed $a_{ch}=1.59\text{mm}$, varying L</p> 

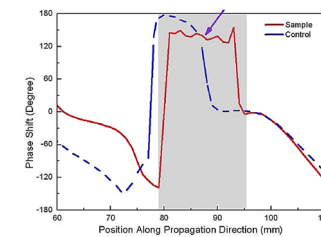
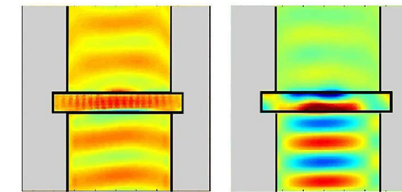
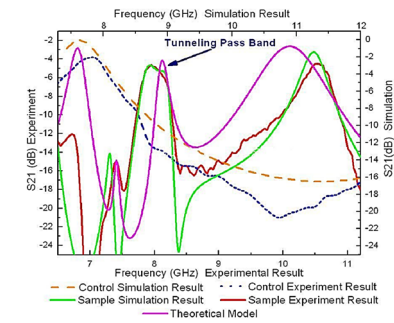
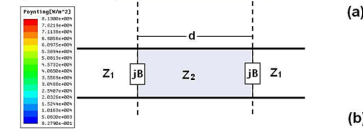
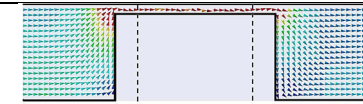
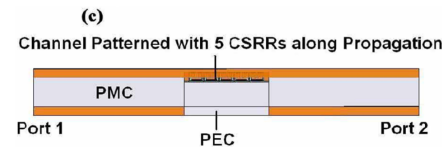
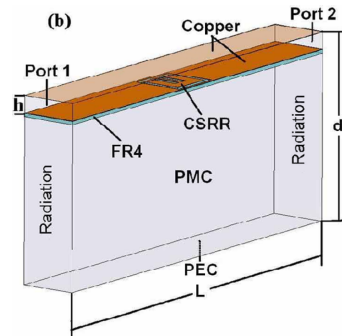
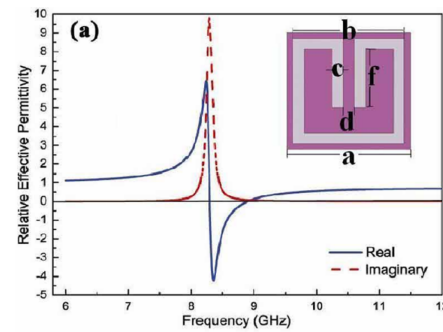
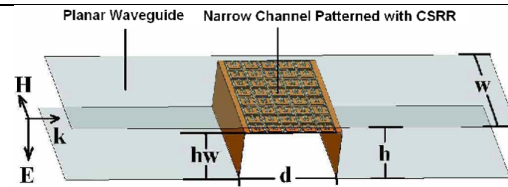
Ref. #

MTM Structure

Operating Freq.

[GHz]

[2.34]

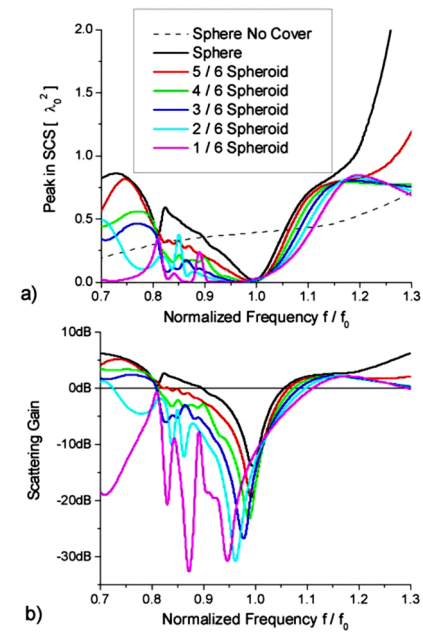
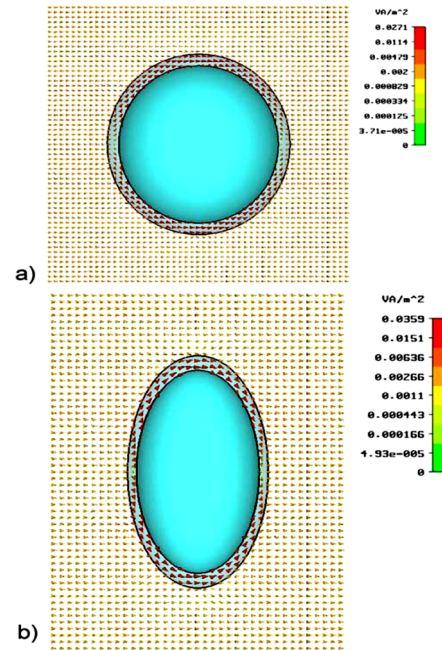


Ref. #

MTM Structure

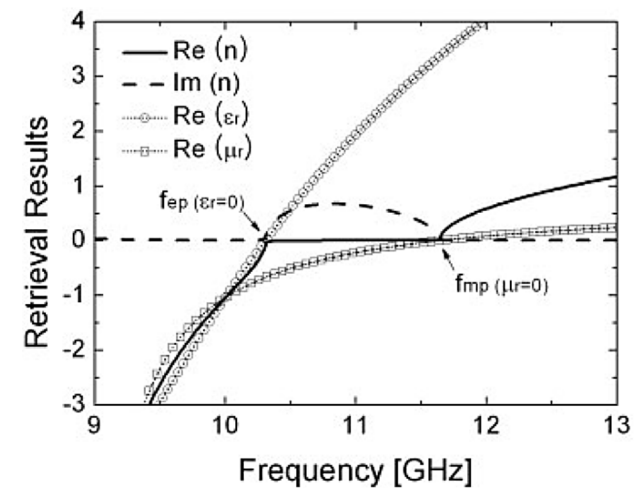
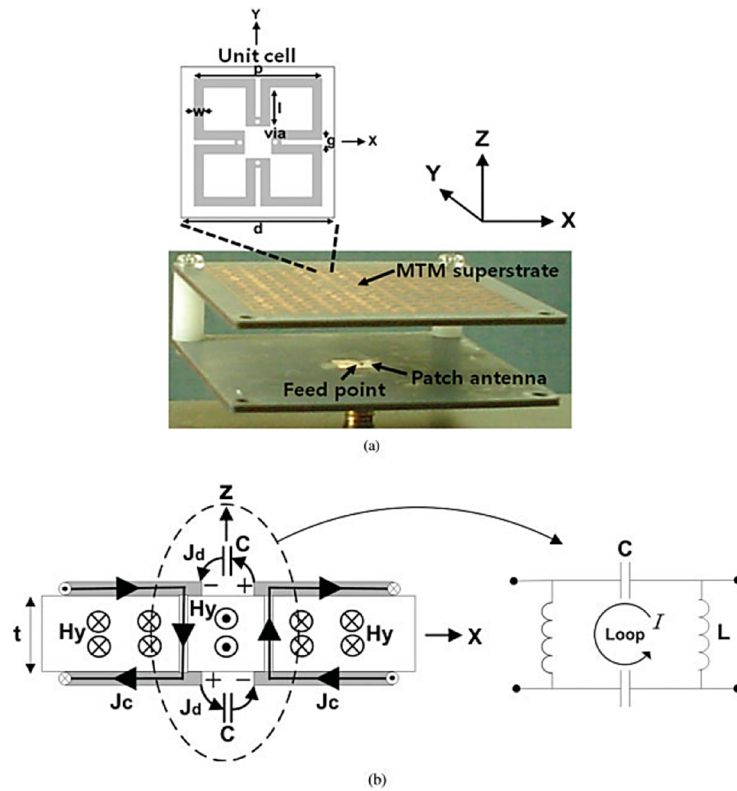
Operating Freq.
[GHz]

[2.36]



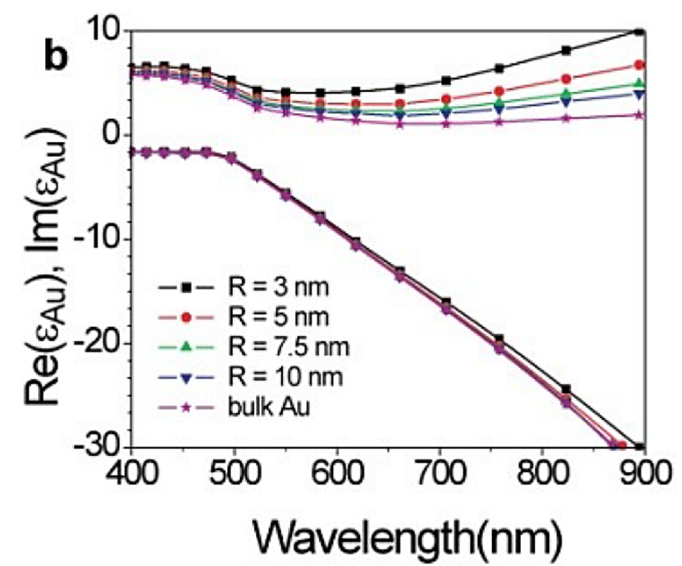
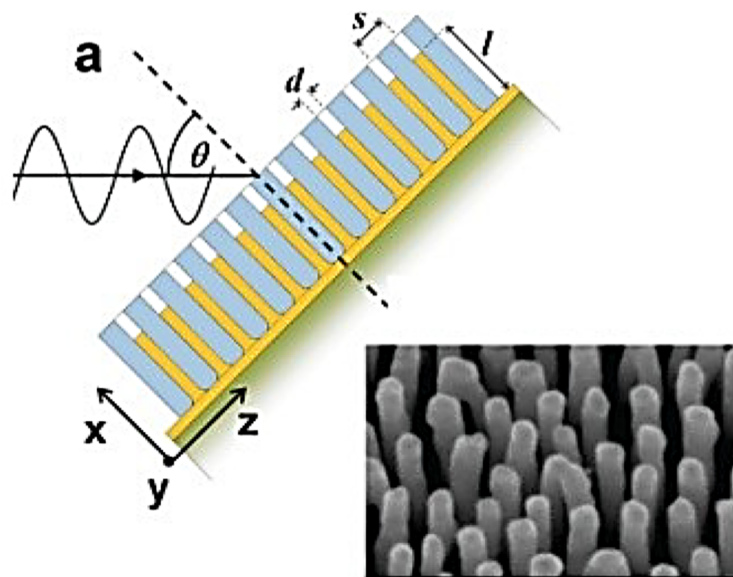
Ref. #	MTM Structure	Operating Freq. [GHz]
--------	---------------	--------------------------

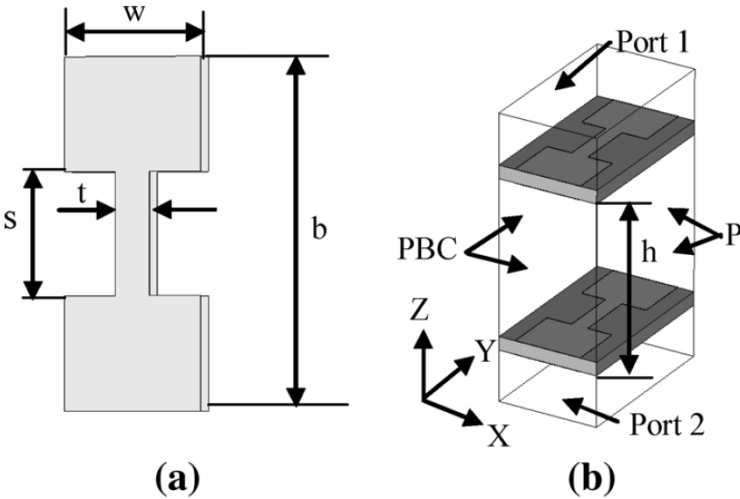
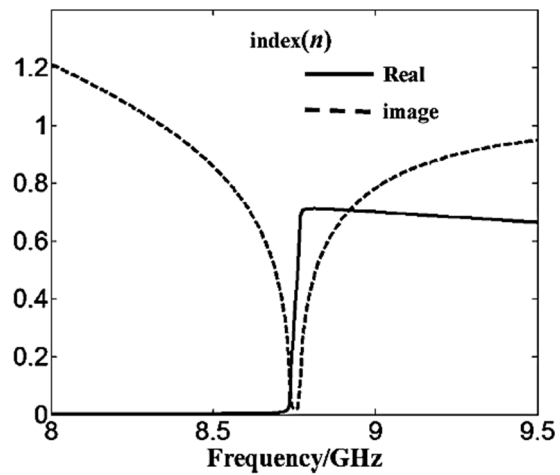
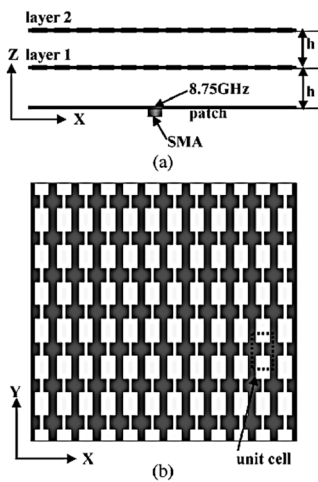
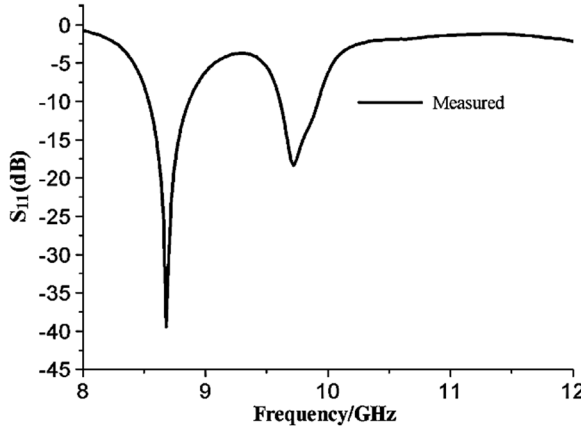
[2.37]

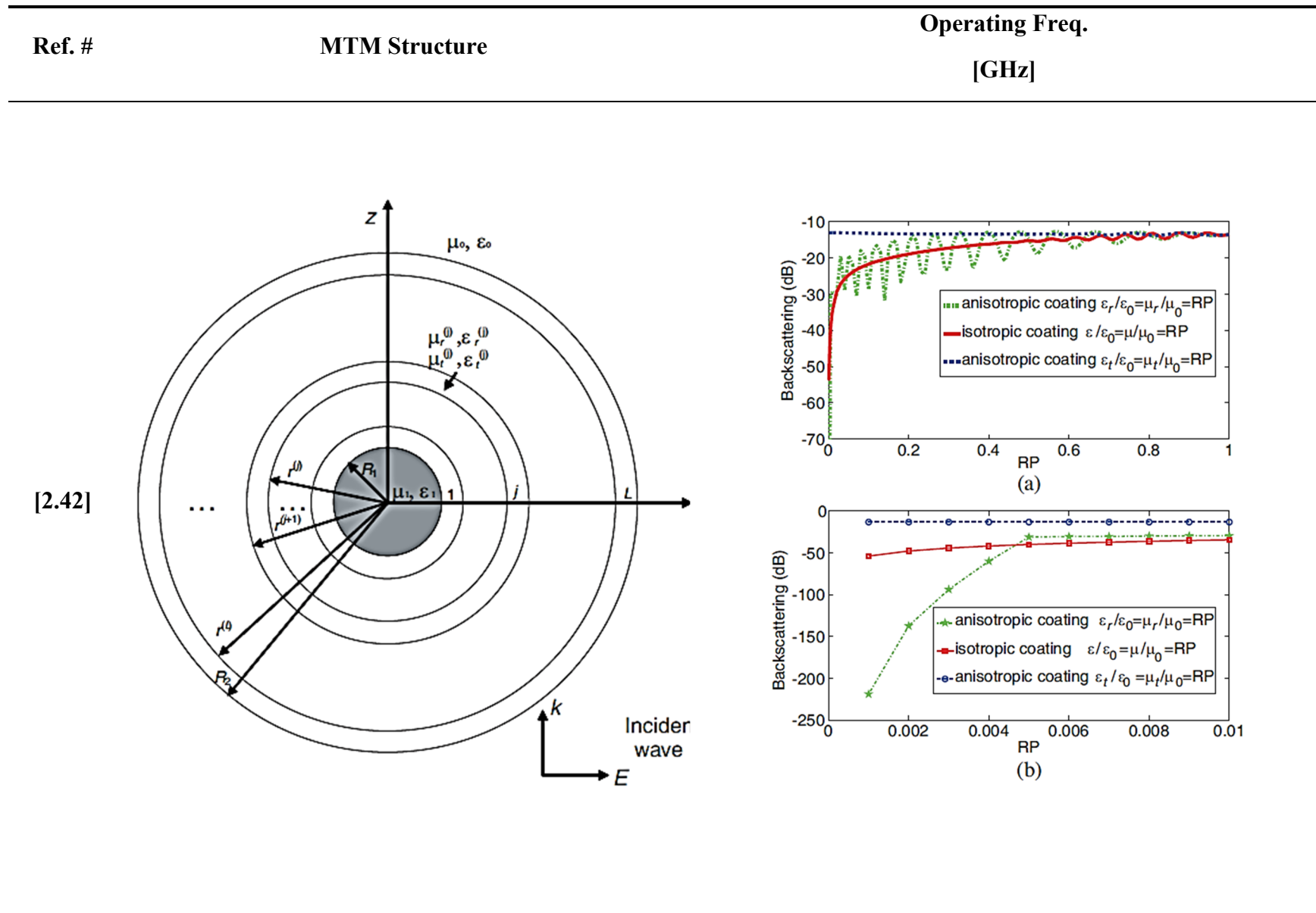


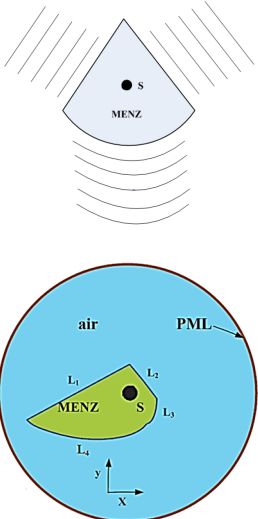
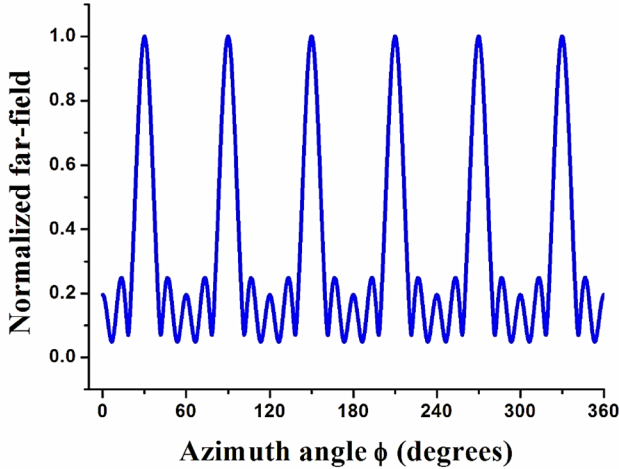
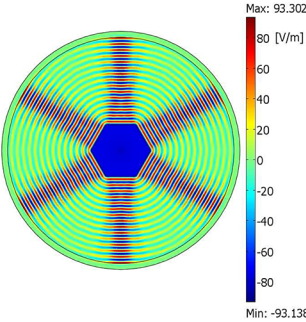
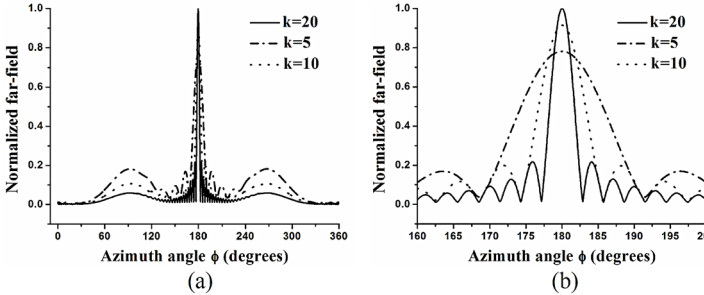
Ref. #	MTM Structure	Operating Freq. [GHz]
--------	---------------	--------------------------

[2.38]



Ref. #	MTM Structure	Operating Freq. [GHz]
[2.40]	 <p>(a) (b)</p>	
	 <p>(a) (b)</p>	



Ref. #	MTM Structure	Operating Freq. [GHz]																		
[2.43]																				
																				
	Table 1. Scales of the boundaries.																			
	<table><tr><td></td><td>L_1</td><td>L_2</td><td>L_3</td><td>L_4</td><td>Total</td></tr><tr><td>Length (m)</td><td>0.81</td><td>0.36</td><td>0.35</td><td>0.91</td><td>2.43</td></tr><tr><td>Proportion</td><td>33.33%</td><td>14.82%</td><td>14.40%</td><td>37.45%</td><td>100%</td></tr></table>		L_1	L_2	L_3	L_4	Total	Length (m)	0.81	0.36	0.35	0.91	2.43	Proportion	33.33%	14.82%	14.40%	37.45%	100%	
	L_1	L_2	L_3	L_4	Total															
Length (m)	0.81	0.36	0.35	0.91	2.43															
Proportion	33.33%	14.82%	14.40%	37.45%	100%															

Ref. #

MTM Structure

Operating Freq.
[GHz]

[2.44]

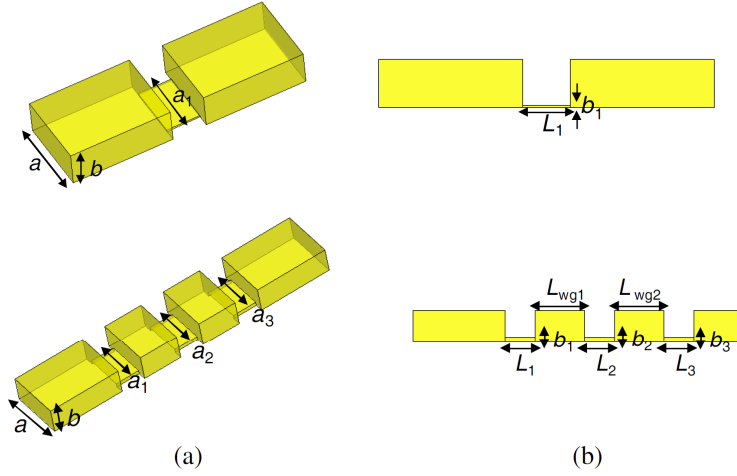
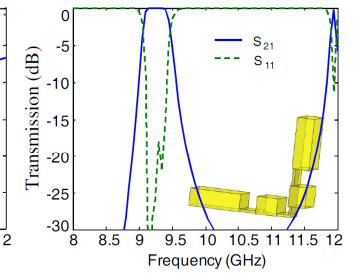
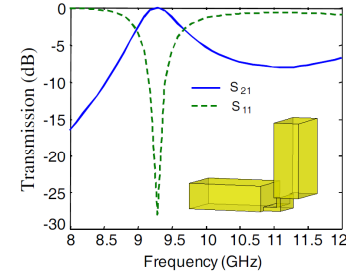
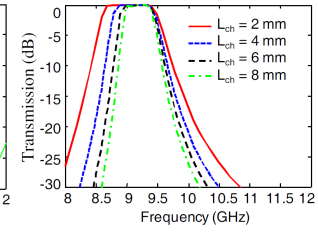
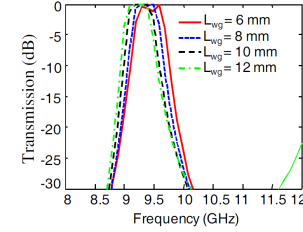
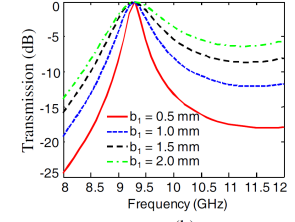
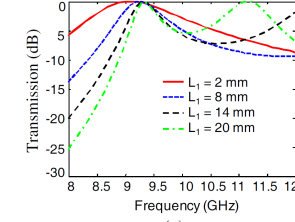
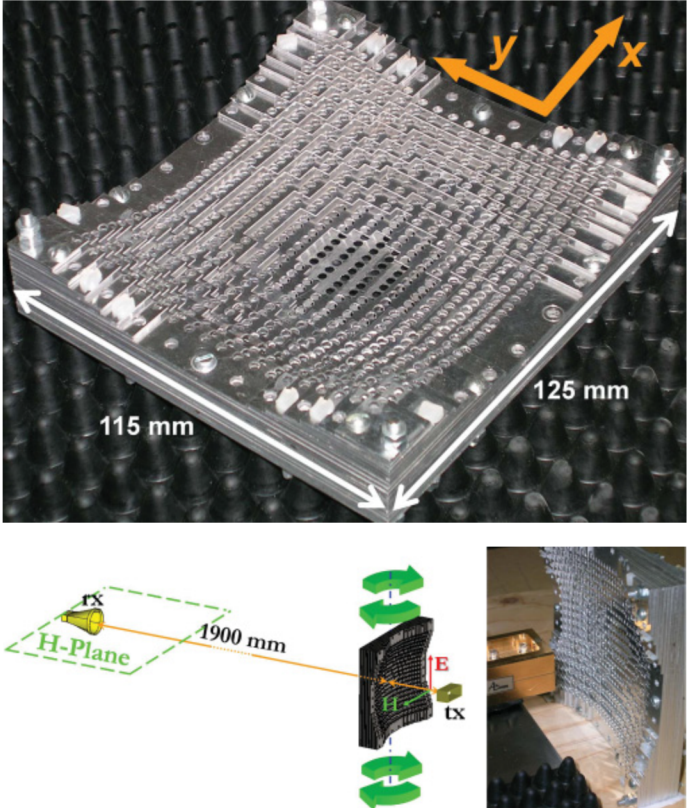
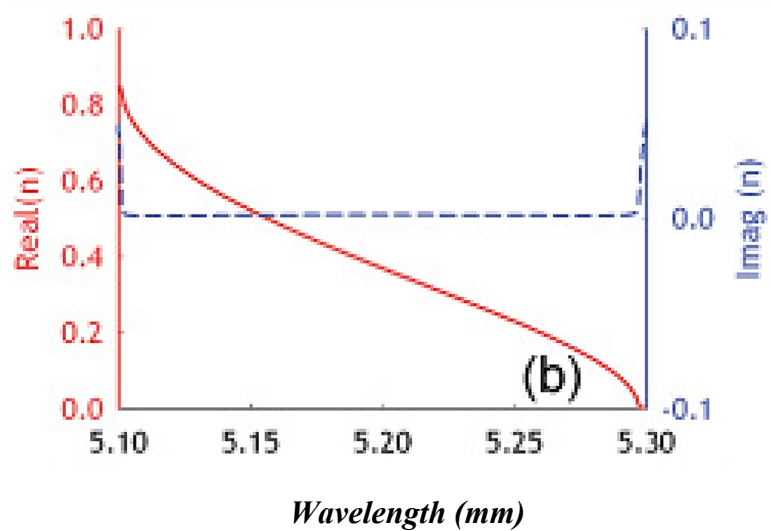


Table 1. The geometric parameters for the one-stage and cascaded three-stage ENZ super-tunneling structure (unit: mm).

a	b	a_1, a_2, a_3	b_1, b_2, b_3	L_{wg1}, L_{wg2}	L_1, L_2, L_3
22.86	10.16	16	1.5	12	8



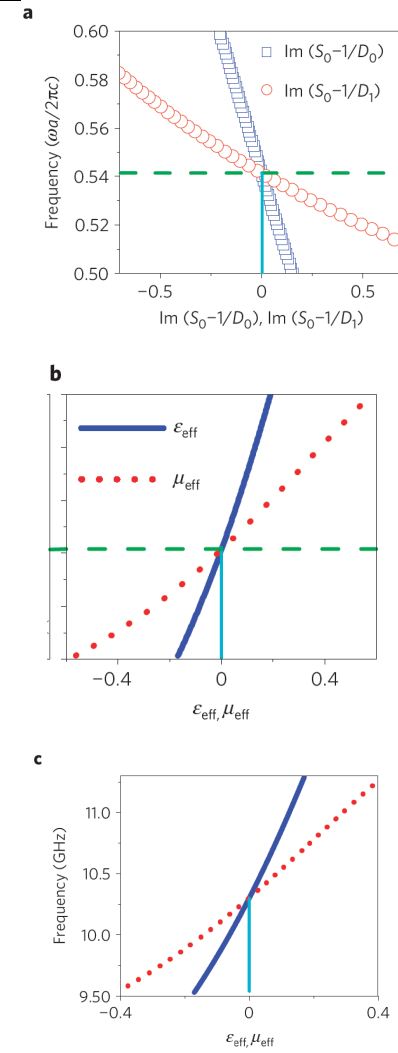
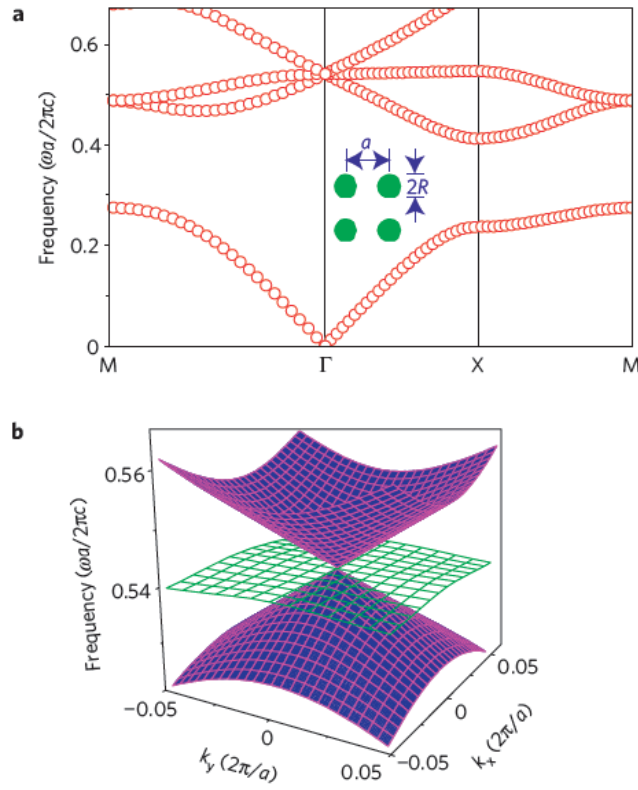
Ref. #	MTM Structure	Operating Freq. [GHz]
[2.47]		

Ref. #

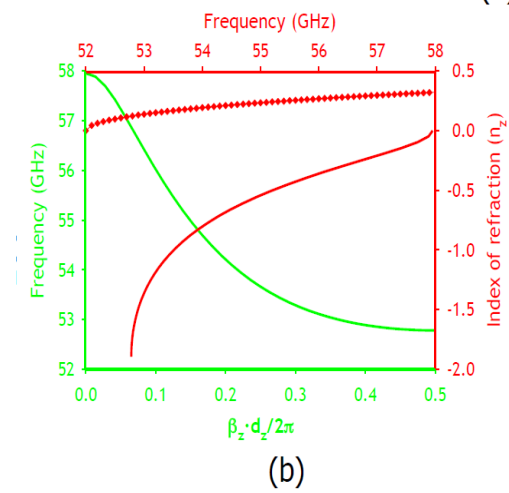
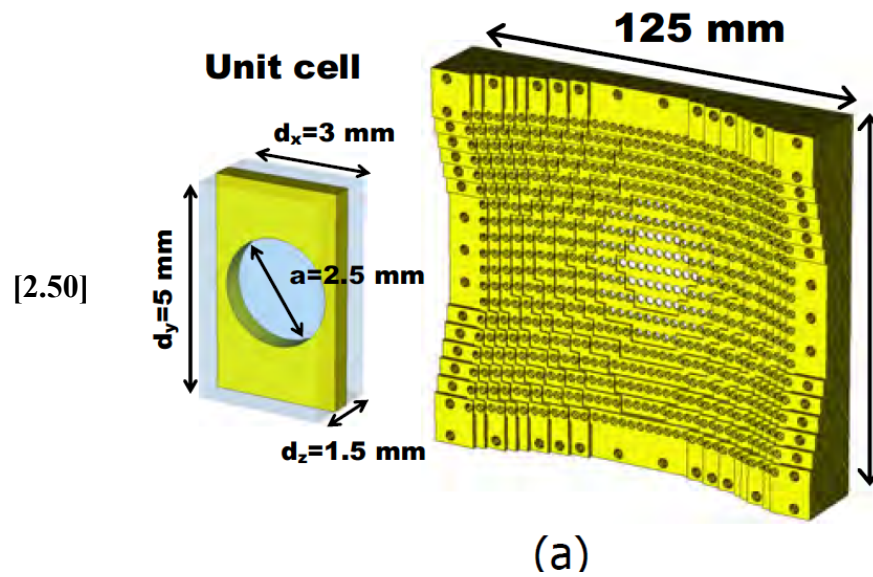
MTM Structure

Operating Freq.
[GHz]

[2.49]



Ref. #	MTM Structure	Operating Freq. [GHz]
--------	---------------	--------------------------

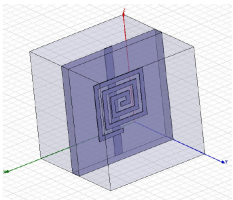


Ref. #

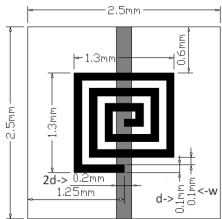
MTM Structure

Operating Freq.
[GHz]

[2.51]

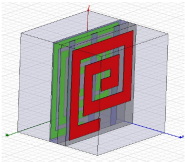


(a)

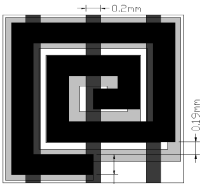


(b)

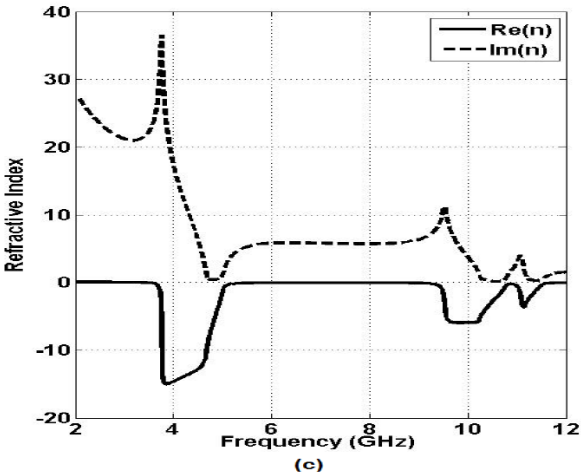
Fig. 1. Initial structure(a,b) of the proposed metamaterial



(a)



(b)

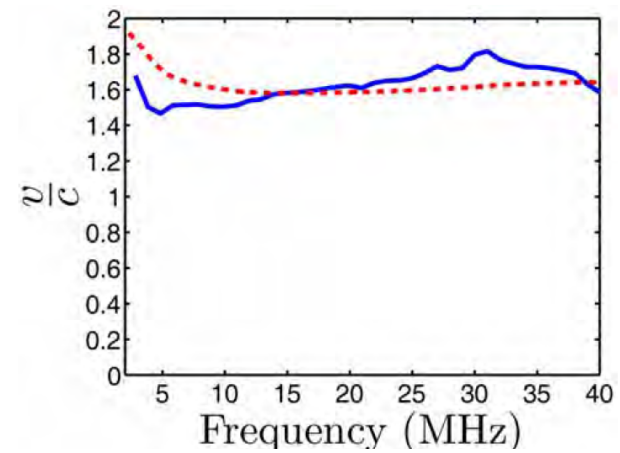
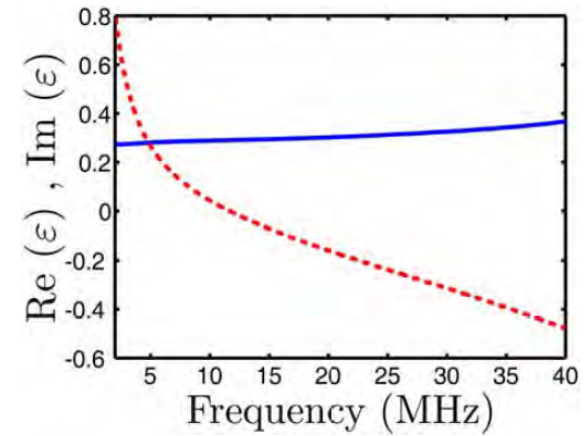
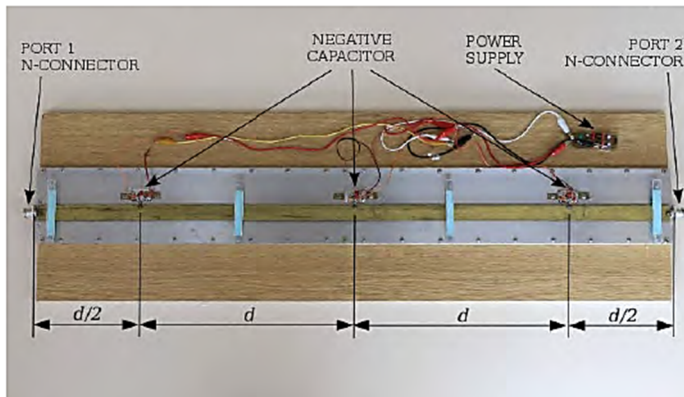
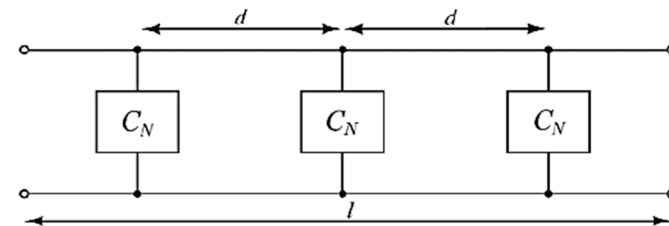


Ref. #

MTM Structure

Operating Freq.
[GHz]

[2.52]

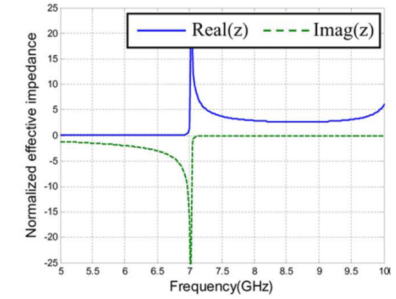
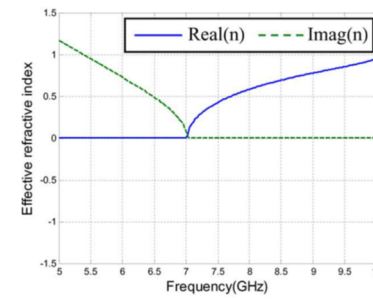
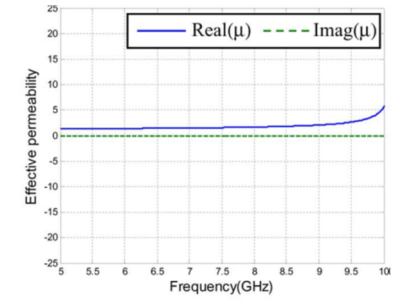
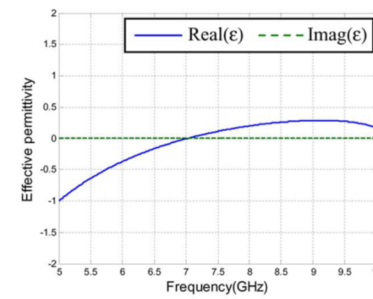
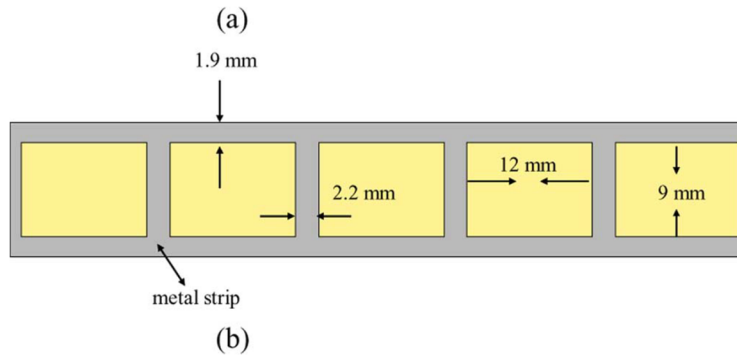
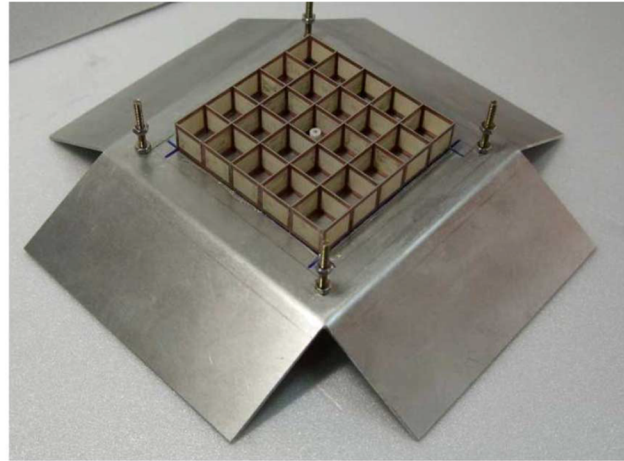


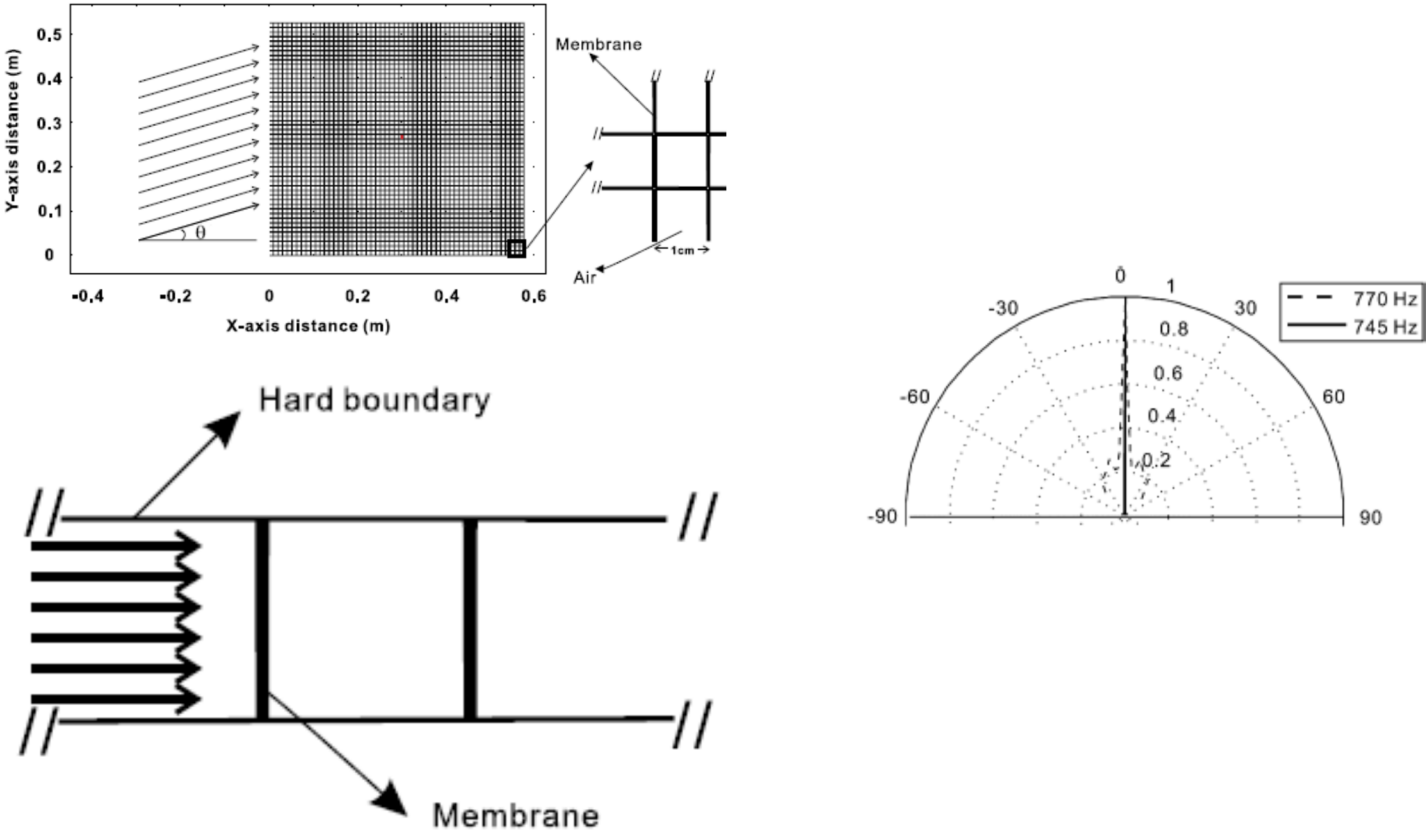
Ref. #

MTM Structure

Operating Freq.
[GHz]

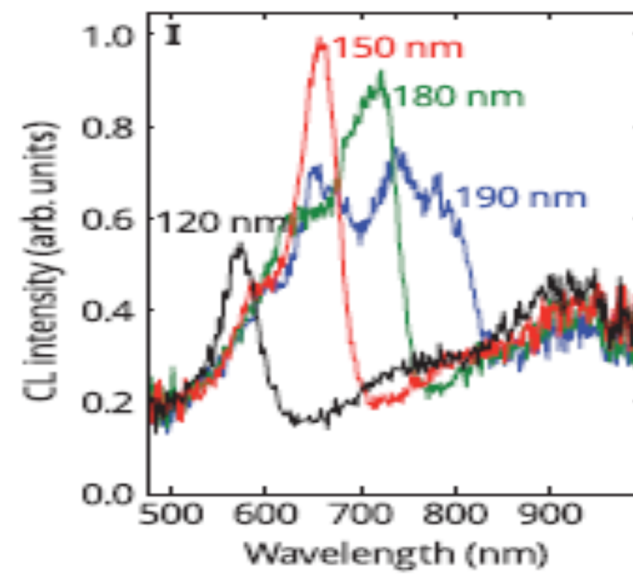
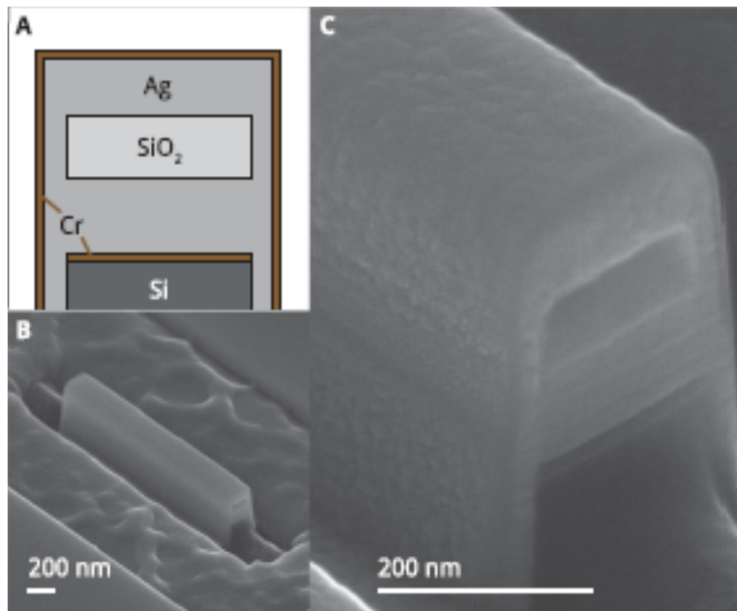
[2.53]



Ref. #	MTM Structure	Operating Freq. [GHz]
[2.54]	 <p>The figure illustrates the design and radiation characteristics of a metamaterial (MTM) structure. The top-left plot shows a 2D grid of the MTM structure in the X-Y plane, with an incident wave at an angle θ. The X-axis ranges from -0.4 to 0.6 m, and the Y-axis ranges from 0 to 0.5 m. A detailed view of the structure shows a grid of vertical and horizontal lines, with a 'Membrane' layer and 'Air' regions. The bottom-left diagram shows a cross-section of the structure, highlighting a 'Hard boundary' and a 'Membrane'. The right plot is a polar radiation pattern showing the radiation intensity for two frequencies: 770 Hz (dashed line) and 745 Hz (solid line). The plot is a semi-circle from -90 to 90 degrees, with radial lines at 30-degree intervals and concentric circles representing intensity levels from 0.2 to 0.8. The 770 Hz pattern shows a main lobe at 0 degrees, while the 745 Hz pattern shows a main lobe at approximately 30 degrees.</p>	

Ref. #	MTM Structure	Operating Freq. [GHz]
--------	---------------	--------------------------

[2.58]

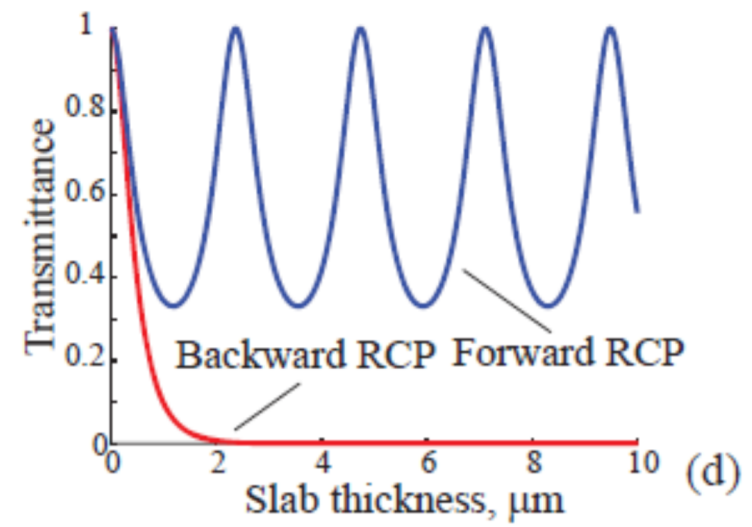
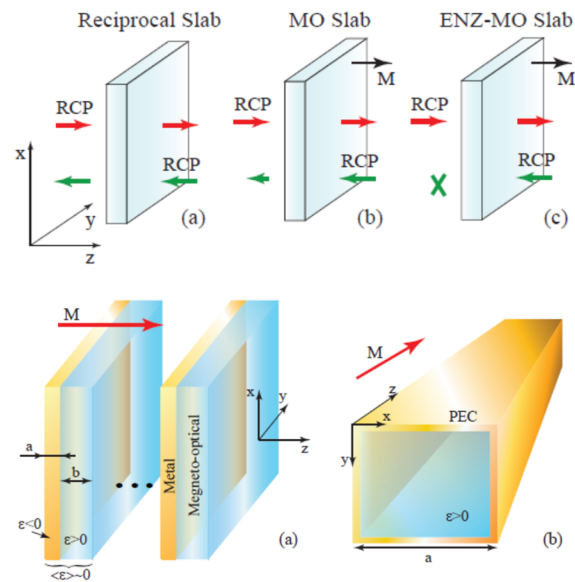


Ref. #

MTM Structure

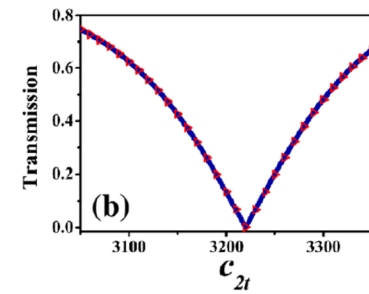
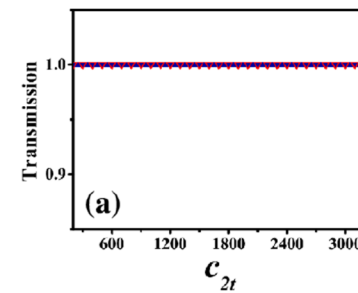
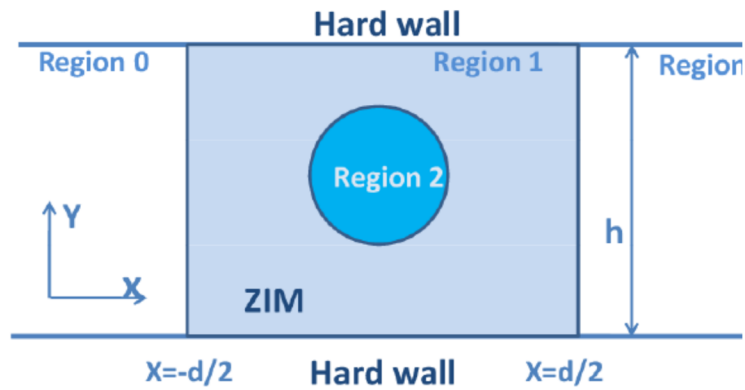
Operating Freq.
[GHz]

[2.59]



Ref. #	MTM Structure	Operating Freq. [GHz]
--------	---------------	--------------------------

[2.61]



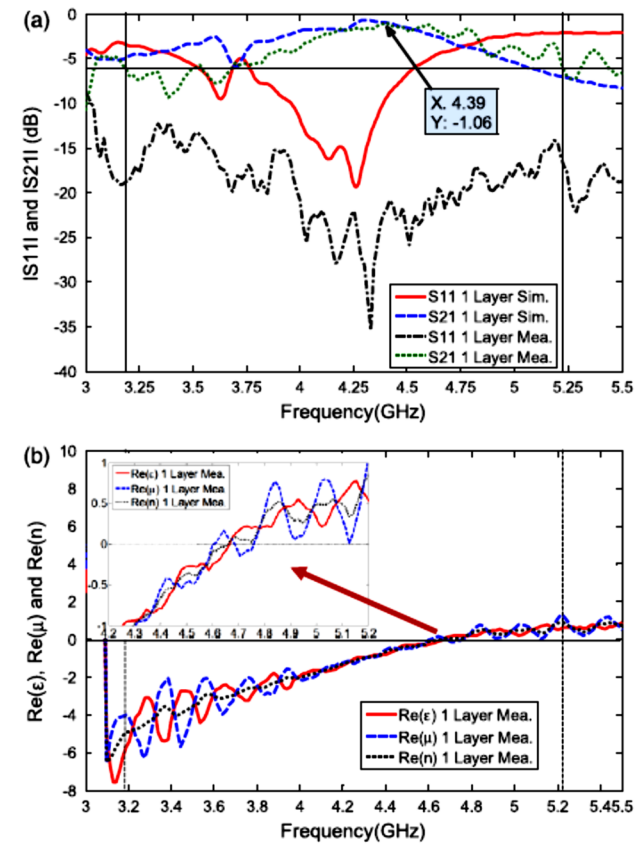
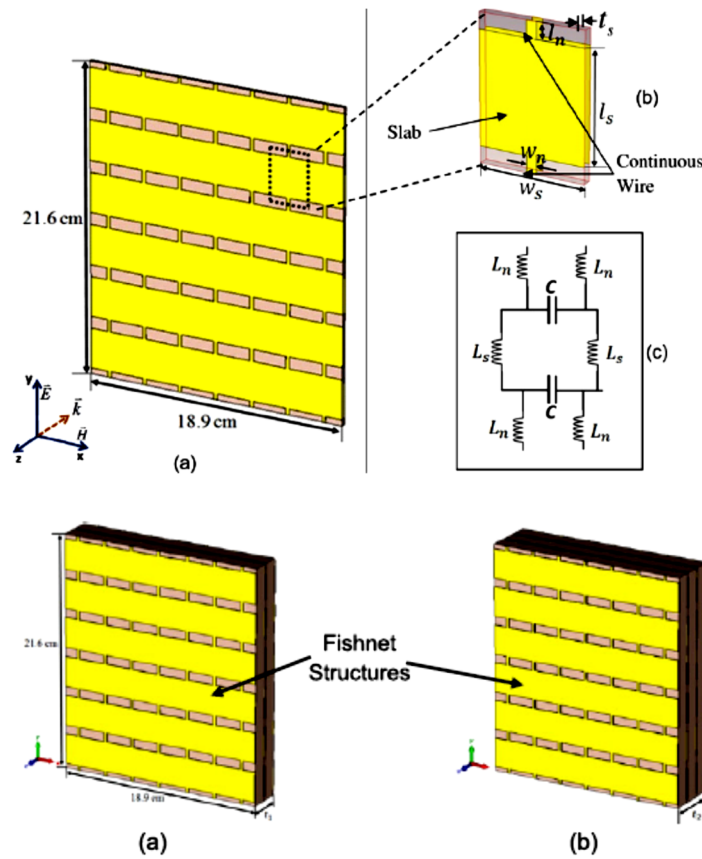
Ref. #

MTM Structure

Operating Freq.

[GHz]

[2.62]



CHAPTER III

RESEARCH METHODOLOGY

3.1: Design of Near-Zero Refractive Index Metamaterials (NZRIM)

In order to better understand and be able to design NZRIM, let us recall Snell's law.

When an incident wave touches the surface of ordinary right-handed (RH) materials, the refracted wave will propagate forward, thus creating a positive angle of refraction. In artificial EM media, when the same incident wave touches the surface of a left-handed (LH) material, the refracted wave will propagate backwards, creating a negative angle of refraction.

Negative Refractive Index

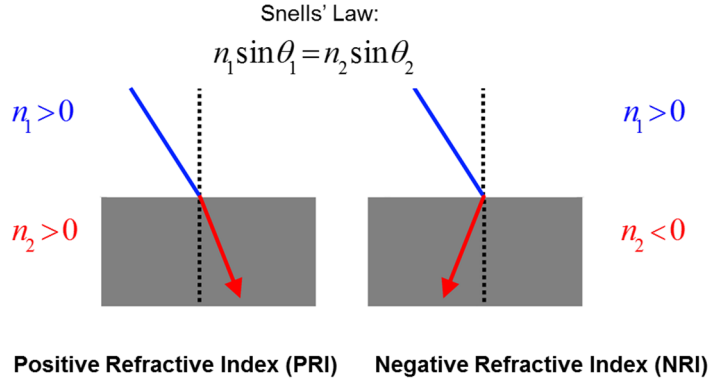


Fig. 3.1.1: Illustration of Negative Refractive Index (NRI).

Fig. 3.1.1 serves as an illustration of what we just explained regarding NRI compared with ordinary PRI, where n_1 denotes the refractive index of the incident wave with its angle θ_1 , while n_2 denotes the refractive index of the refracted wave with its angle θ_2 . Now let us consider

how Snell's law applies to near-zero refractive index materials (NZRIM). When an incident wave touches the surface of NRIM, the refracted wave will propagate normal to the surface of the material, as shown in Fig. 3.1.2, regardless of the angle of the incident wave.

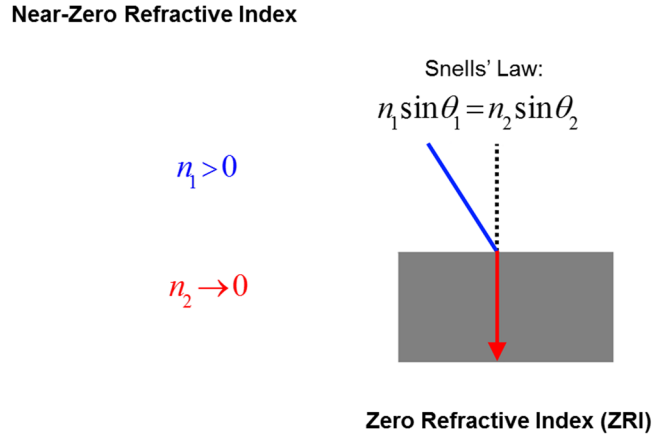


Fig. 3.1.2: Illustration of Zero Refraction Index (ZRI).

The refractive index is directly related to permittivity (ϵ) and permeability (μ) by the relationship $n = \sqrt{\epsilon\mu}$. From this relationship, we may draw a conclusion as to what cases will yield NZRI for our MTM design. There are three essential cases for NZRI:

- i.* $\epsilon \rightarrow 0$
- ii.* $\mu \rightarrow 0$
- iii.* $\epsilon \rightarrow 0$ and $\mu \rightarrow 0$.

Before we select from these three cases which one will be the most optimal for our NZRIM design, there is another important factor to consider which is impedance. The

impedance, denoted by z , is related to ε and μ by the relationship $z = \sqrt{\frac{\mu}{\varepsilon}}$. From the three cases for NZRI, this is how impedance factors into the design considerations:

$$i. \varepsilon \rightarrow 0 \Rightarrow z \rightarrow \infty$$

$$ii. \mu \rightarrow 0 \Rightarrow z \rightarrow 0$$

$$iii. \varepsilon \rightarrow 0 \text{ and } \mu \rightarrow 0.$$

In the first case, due to the high impedance, we will get high electric loss. For the second case, due to the low impedance, we will get high magnetic loss. In the third case, when both permittivity and permeability are near-zero simultaneously, then we get a matched impedance. This way, both electric and magnetic losses are suppressed. For this reason, the third case will be our optimal choice for the NZRIM design.

Another consideration is to define when the refractive index is “near” zero. From [3.1] we may see that refractive index, n , is near-zero when $|n| < 1$. A specific important factor desirable for our NZRIM design is minimize losses. There are two methods to determine LF : figure of merit (FOM) and loss factor (LF). The following equations define each of these methods:

$$FOM = \left| \frac{\text{Re}(n)}{\text{Im}(n)} \right| \quad (3.1)$$

$$LF = \frac{\text{Im}(n)}{\text{Re}(n)}. \quad (3.2)$$

In the case of FOM , a high value is desired. As for LF , a low value is the goal, where the condition to be satisfied is $LF < 1$. For our NZRIM, we will be utilizing LF to evaluate low loss of the design.

3.2: Simulation Setup

3.2.1: 2D with Substrate

For our NZRIM, we will be utilizing the EM commercial software package CST Studio Suite 2015[®] [3.2], and most specifically, the Microwave Studio Suite module within CST. For our 2D MTM structure design setup, Figs. 3.2.1 – 3.2.42 demonstrate the setup steps for the modeling, simulation and analysis in CST.

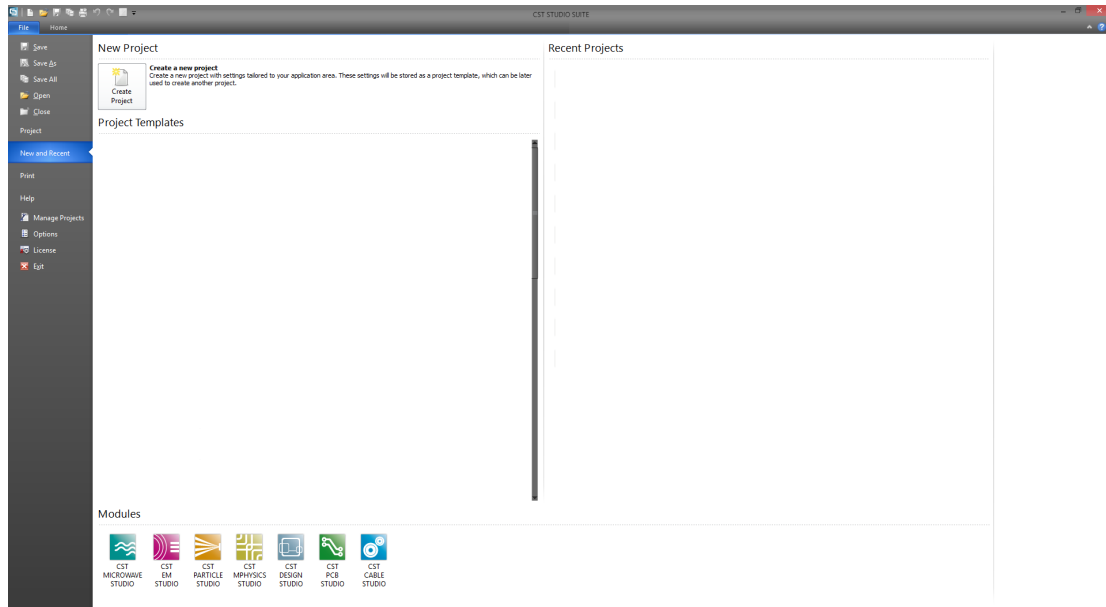


Fig. 3.2.1: Step 1 – Run CST STUDIO SUITE. Once loaded, this is the start screen.

New Project



Create a new project

Create a new project with settings tailored to your application area. These settings will be stored as a project template, which can be later used to create another project.

Fig. 3.2.2: Step 2 – Click “Create a new project” button.

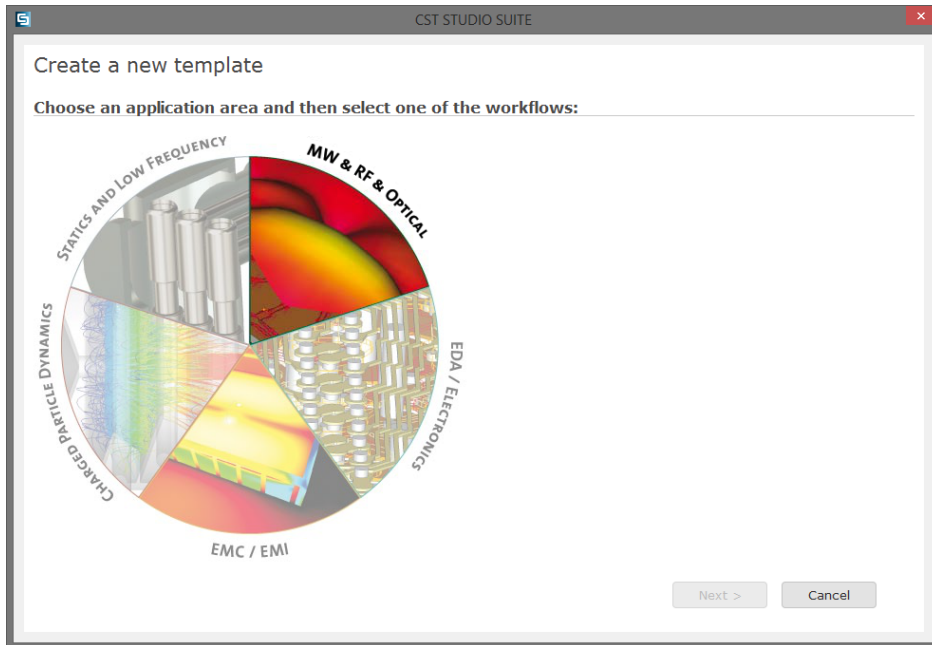


Fig. 3.2.3: Step 3 – From the “Create a new template” screen, select “MW & RF & Optical”.

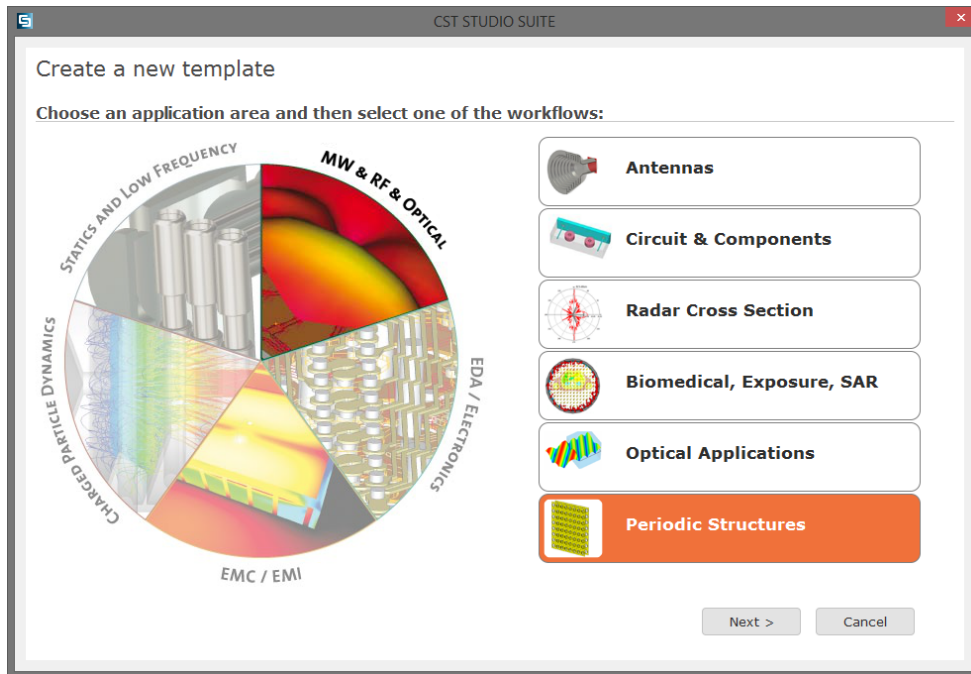


Fig. 3.2.4: Step 4 – Select the “Periodic Structures” workflow.

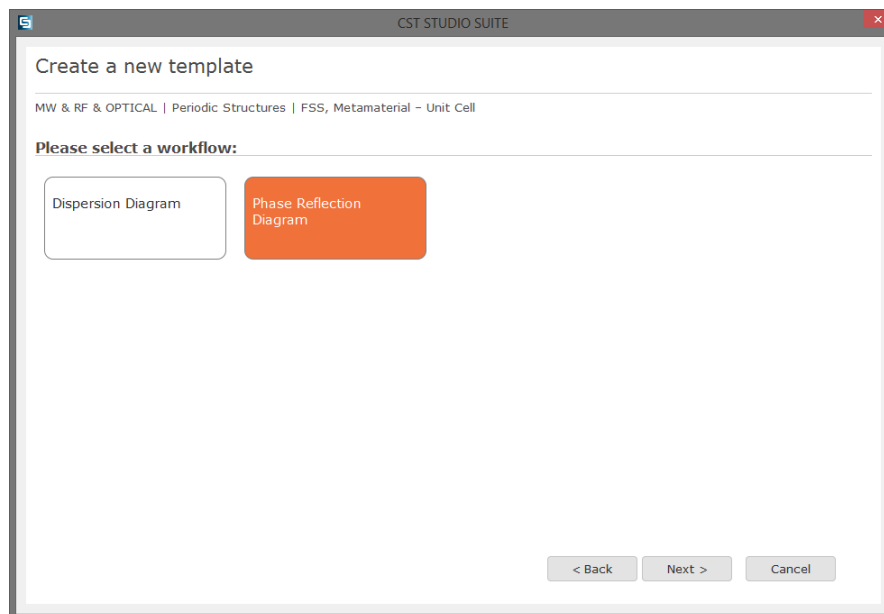


Fig. 3.2.5: Step 5 – Select “Phase Reflection Diagram” workflow.

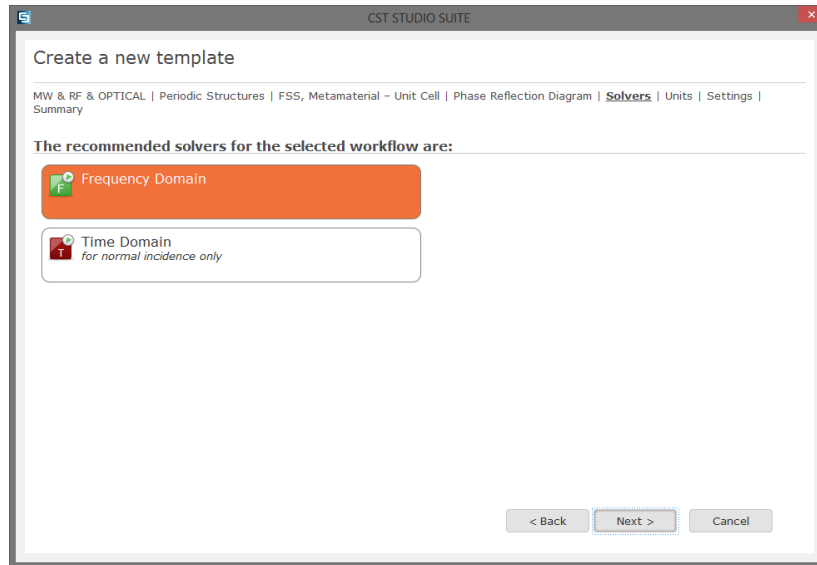


Fig. 3.2.6: Step 6 – Select “Frequency Domain” solver.

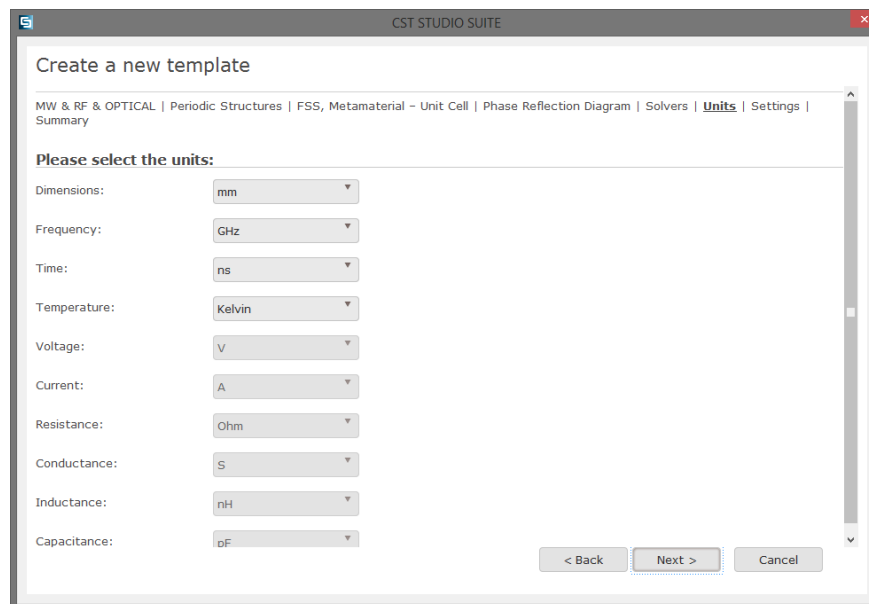


Fig. 3.2.7: Step 7 – Select the appropriate units. The default settings are set for microwave applications.

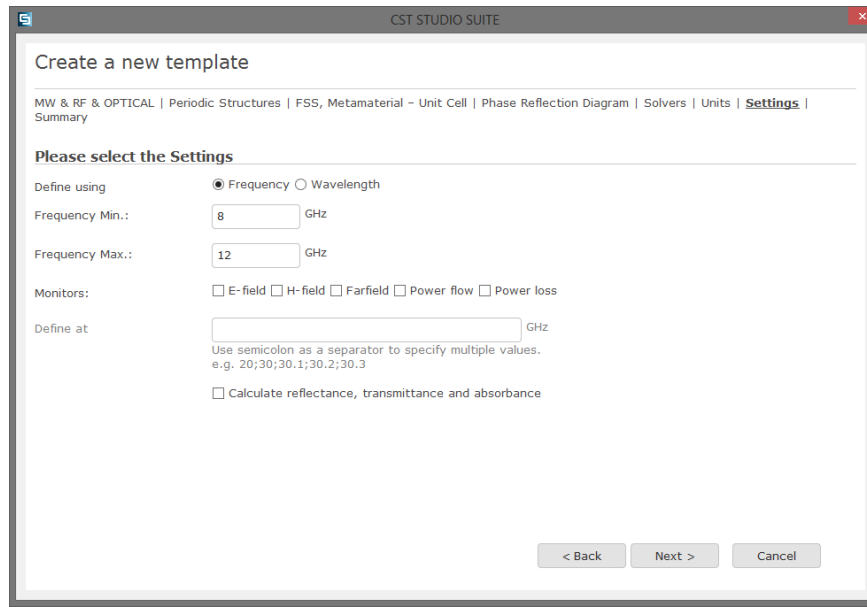


Fig. 3.2.8: Step 8 – Configure additional settings such as frequency range and monitors (optional at this point).

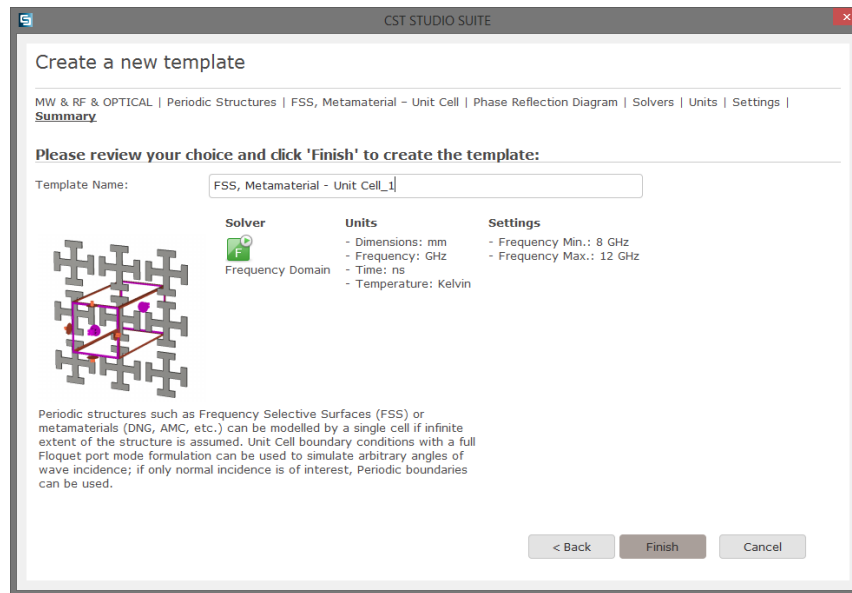


Fig. 3.2.9: Step 9 – Name template appropriately for future use.

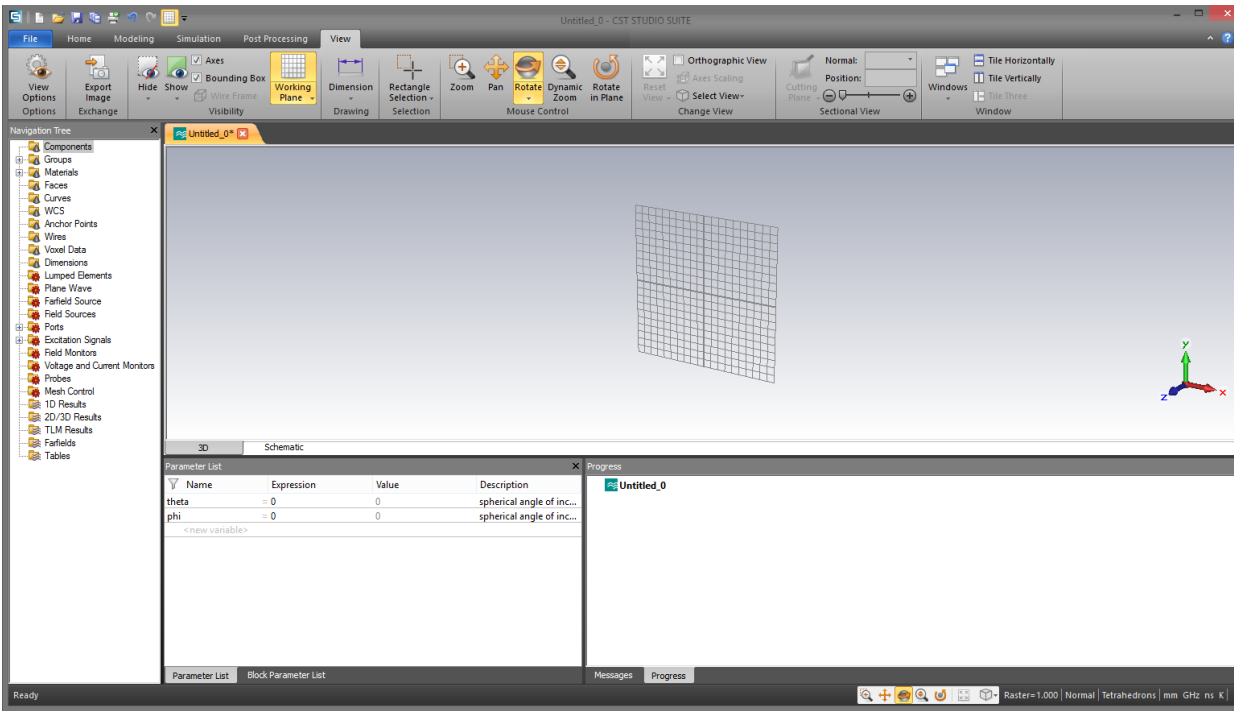


Fig. 3.2.10: CST Microwave Studio Workspace.

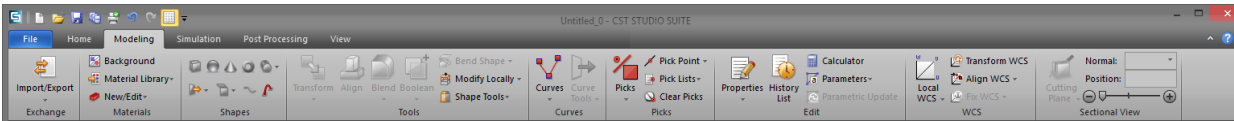


Fig. 3.2.11: “Modeling” tab ribbon.

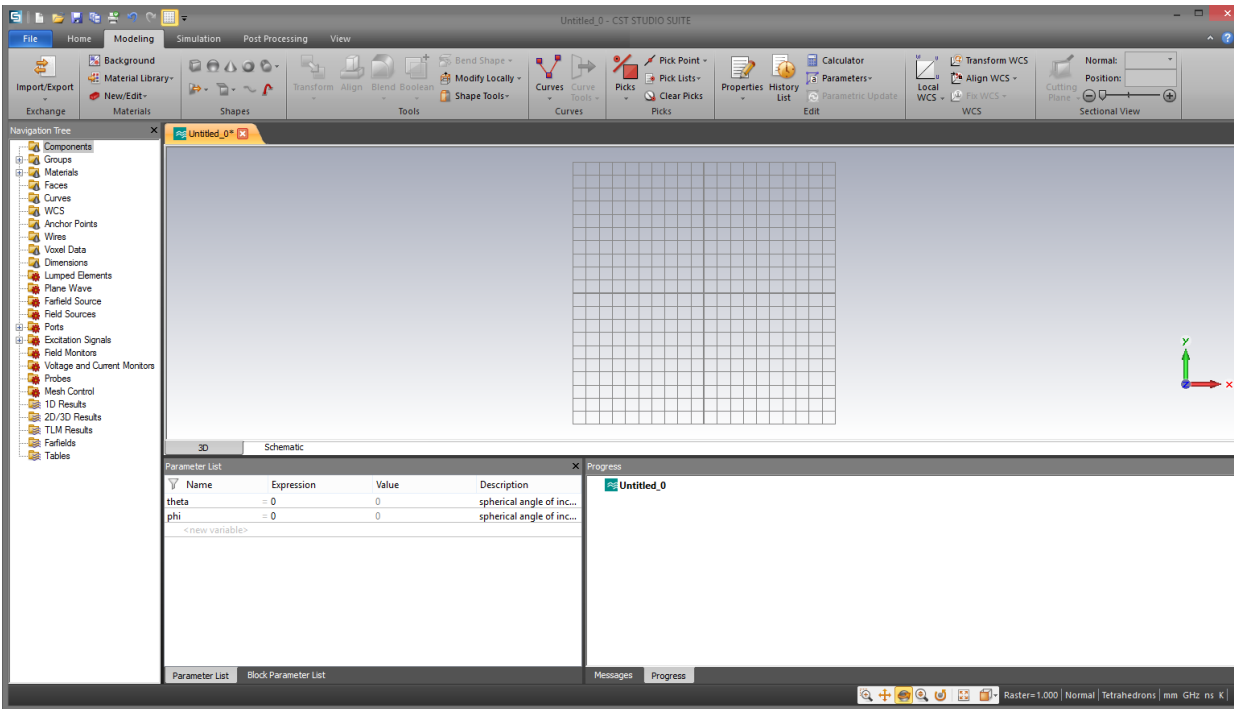


Fig. 3.2.12: Step 10 – Click the “Modeling” tab at the top, then click the “Brick” button.

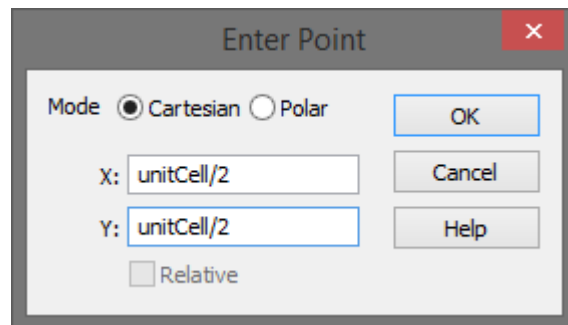


Fig. 3.2.13: Step 11 – After clicking the “Brick” button, press the Tab key on the keyboard. Although one may manually select the points for the structure, it is more efficient to assign aptly-named variables for these. This prompt is for the x -max and y -max coordinates of the structure.

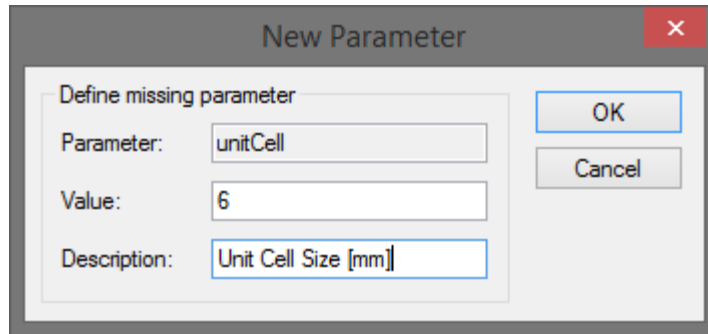


Fig. 3.2.14: Step 12 – After clicking OK on the previous step, this “New Parameter” window will pop up. In our case, the Unit Cell is 6×6 mm. Don’t forget the description (optional).

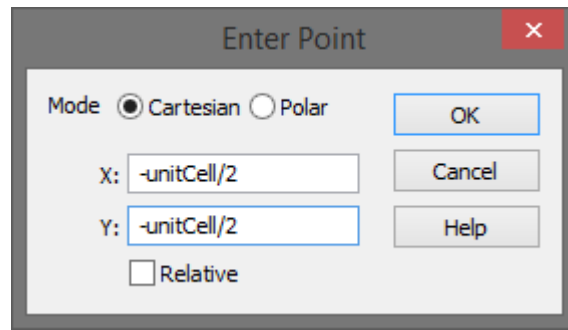


Fig. 3.2.15: Step 13 – Next, just as in Step 11, this window prompts for the x -min and y -min coordinates of the structure.

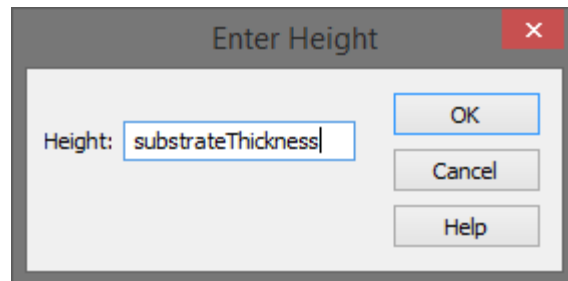


Fig. 3.2.16: Step 14 – After entering the coordinates for the length and width of the structure, CST will prompt for the “height” of the structure. By default, the software allows the user to manually select the points in the Workspace. Simply hit the Tab key to enter a variable name instead as shown.

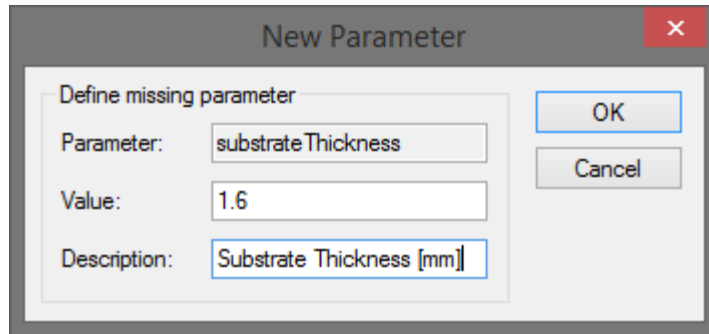


Fig. 3.2.17: Step 15 – After clicking OK on the previous step, this “New Parameter” window will pop up. In our case, the substrate thickness for FR-4 is 1.6 mm. Don’t forget the description (optional).

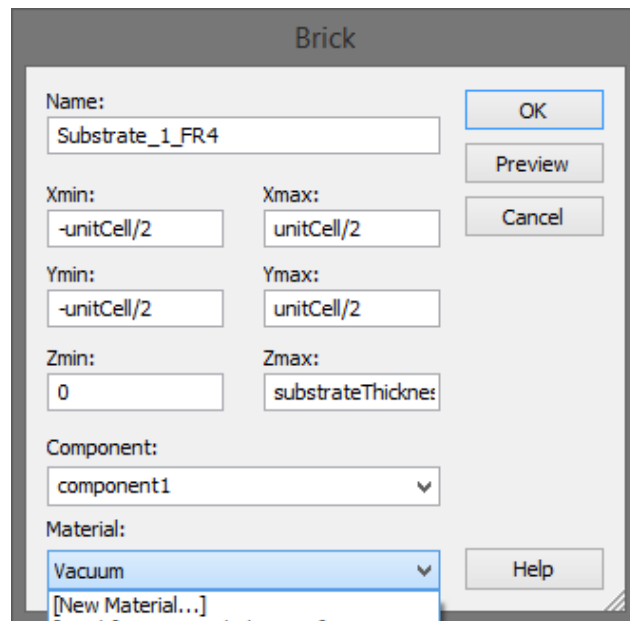


Fig. 3.2.18: Step 15 – Once finished with the size parameters, this confirmation window will pop up. Here you may name this structure, readjust parameters, and select the material. Click the drop-down for the “Materials” and select either from the default materials or, in our case, “[Load material from library...]” to select FR-4.

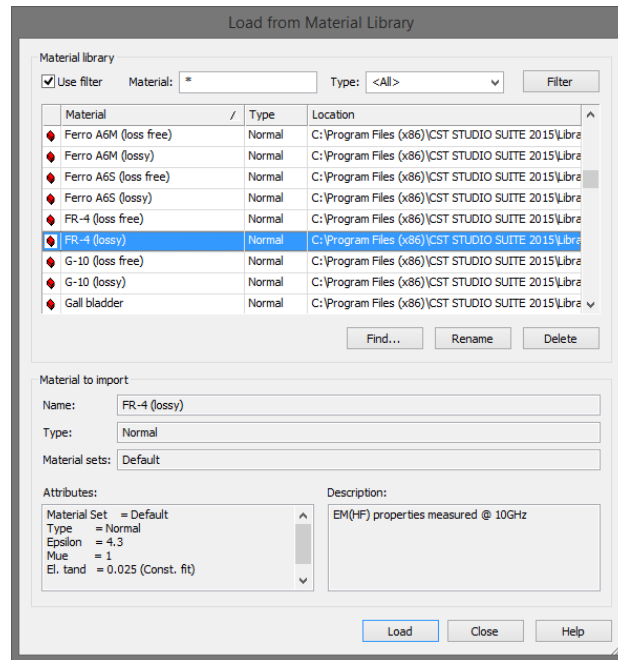


Fig. 3.2.19: Step 16 – Select the desired material from the Material Library, in our case, FR-4 (lossy) was selected.

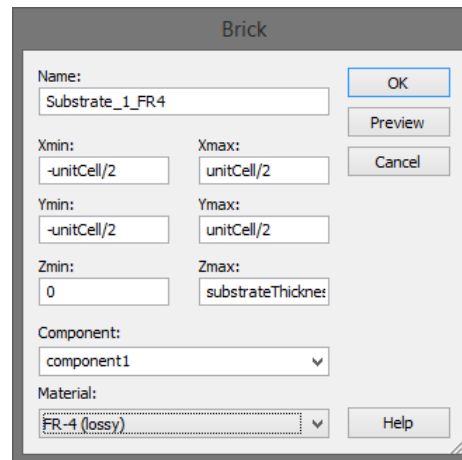


Fig. 3.2.20: Step 17 –CST will prompt the user to confirm all the parameters for the structure.

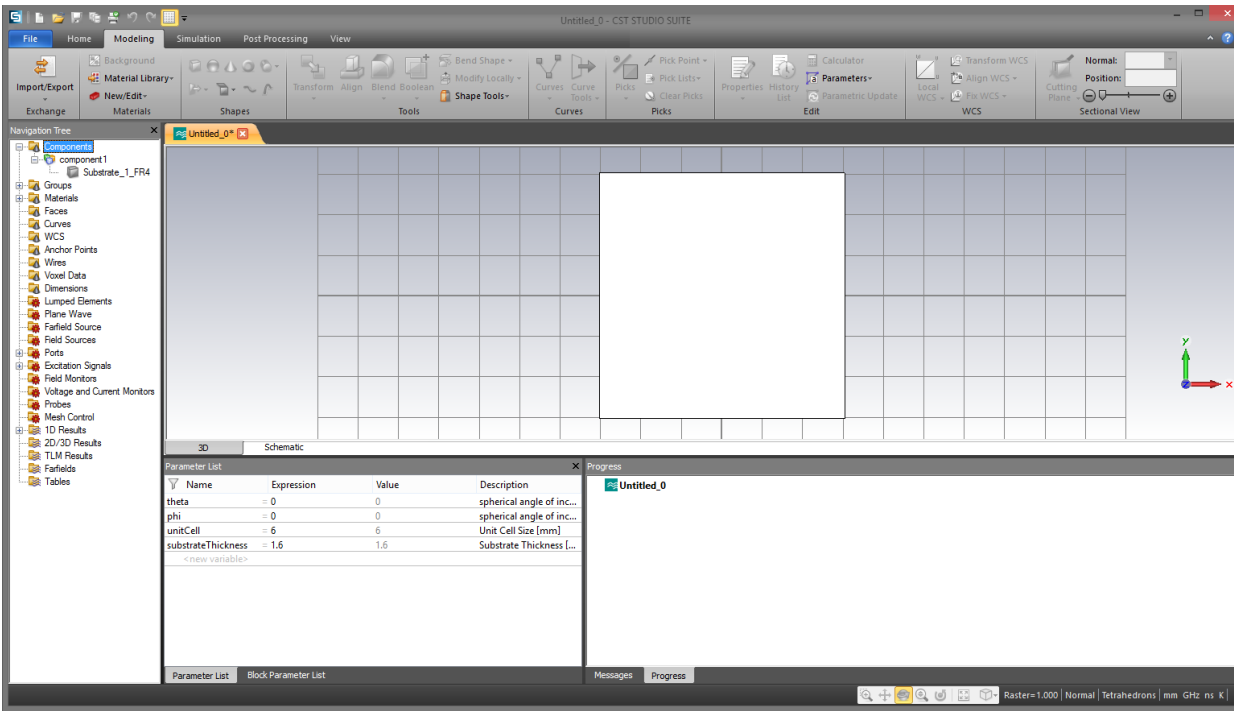


Fig. 3.2.21: FR-4 (lossy) substrate structure in CST Workspace.

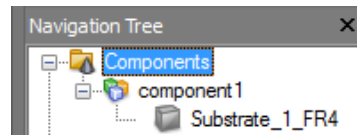


Fig. 3.2.22: Components for the design will be displayed at the top-left column under “Navigation Tree.”

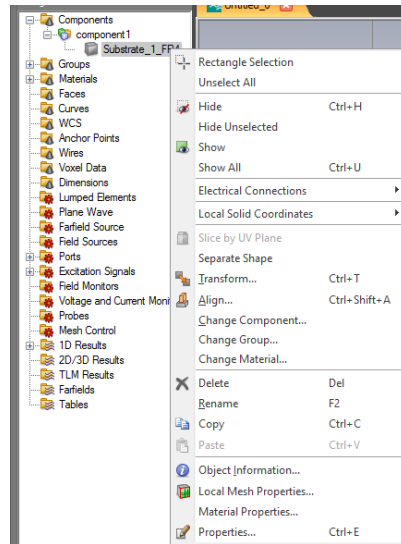


Fig. 3.2.23: Step 18 – (optional) In case the design requires different values for ϵ_r and μ_r , these may be modified by right-clicking the structure from the component list, then select “Material Properties”.

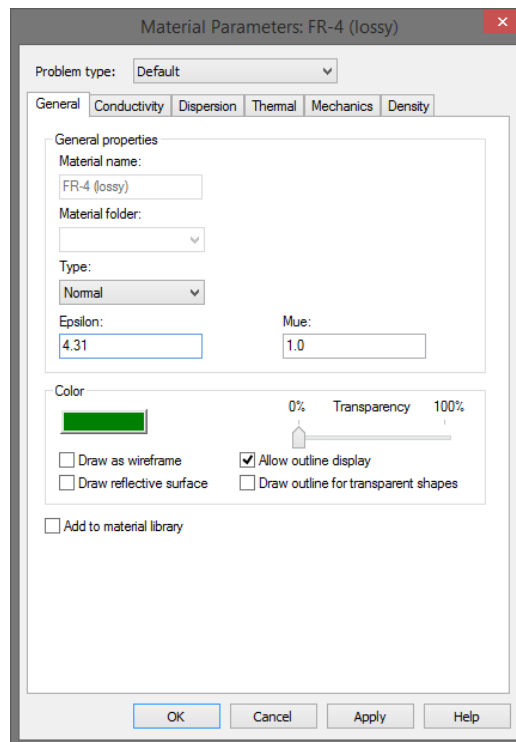


Fig. 3.2.24: Step 19 – (optional) From the “Material Parameters” General tab, one may change the value for Epsilon, Mue, color, etc.

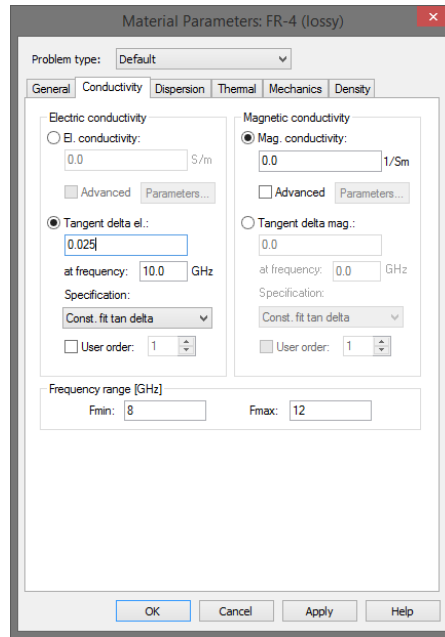


Fig. 3.2.25: Step 20 – (optional) From the “Material Parameters” Conductivity tab, one may change the value for loss tangent, etc.

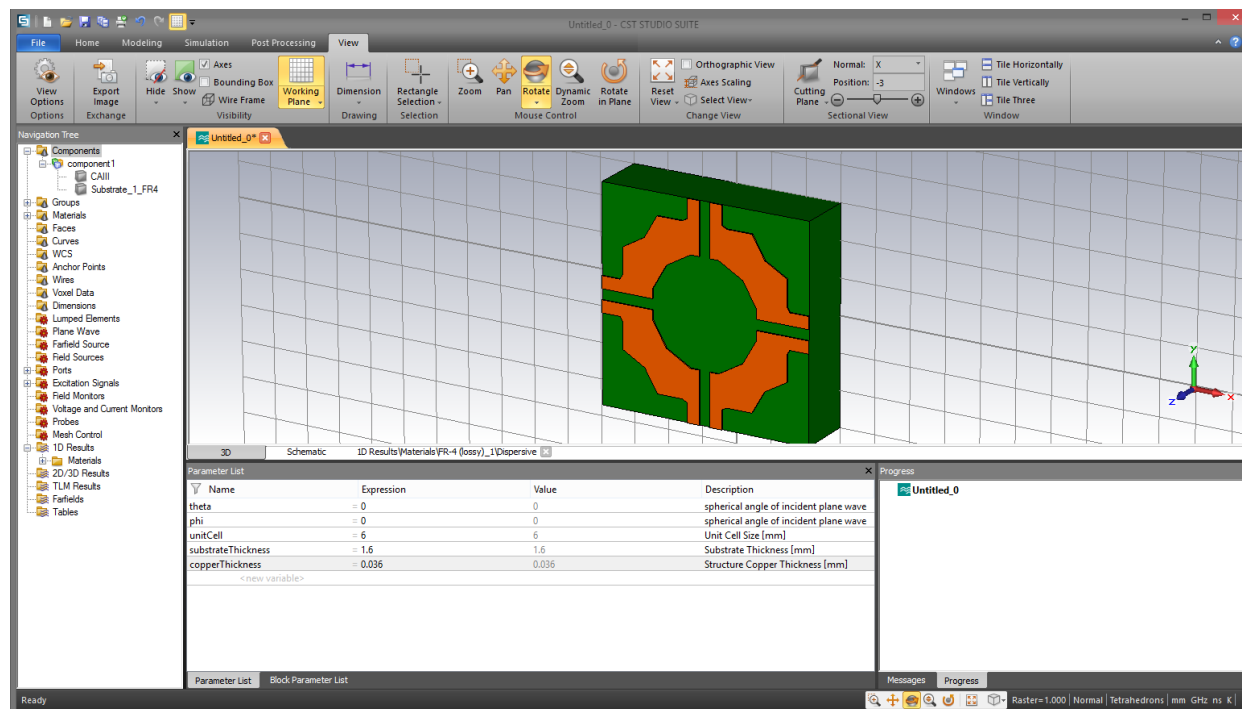


Fig. 3.2.26: Substrate and MTM structure CAIII. The same steps for apply for the MTM structure.

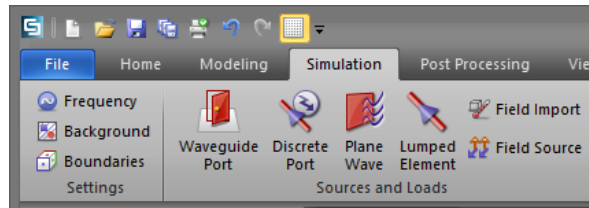


Fig. 3.2.27: Step 21 – From the “Simulation” tab, select the Frequency  button.

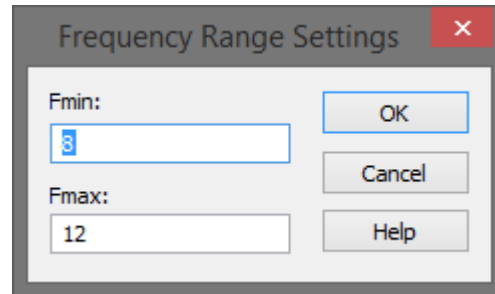


Fig. 3.2.28: Step 22 – Input the desired frequency range min and max values to be simulated.

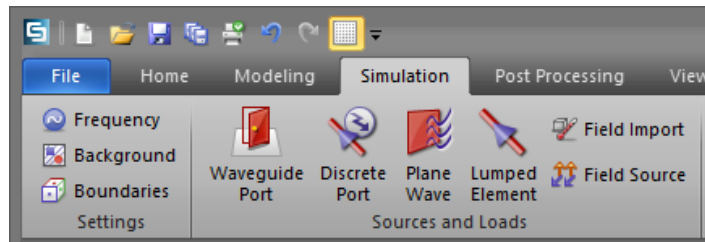
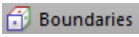


Fig. 3.2.29: Step 23 – From the “Simulation” tab, once more, select the “Boundaries”  button.

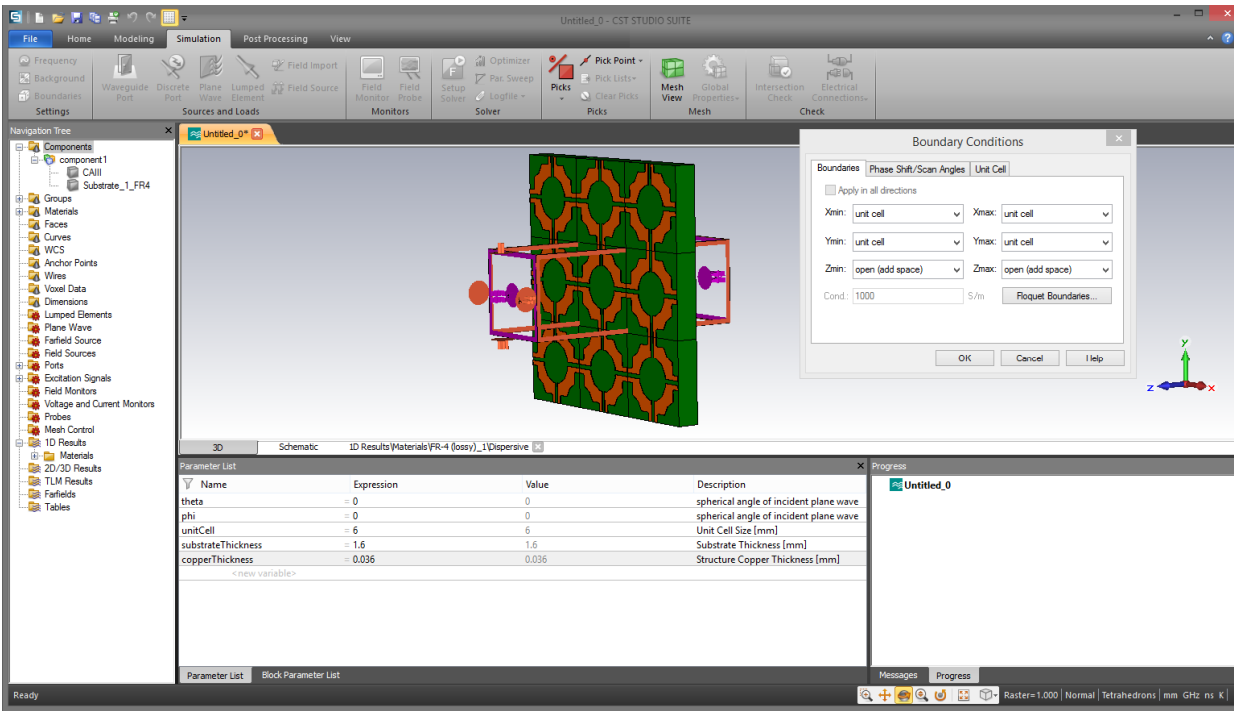


Fig. 3.2.30: Step 24 – Since we are working with periodic structures, set x -min, y -min, x -max, y -max to “unit cell”, and z -min and z -max (the propagation direction) set to “open (add space)” which allows for CST to evaluate the best spacing for the location of Port-1 and Port-2 with respect to the MTM structure “slab.”

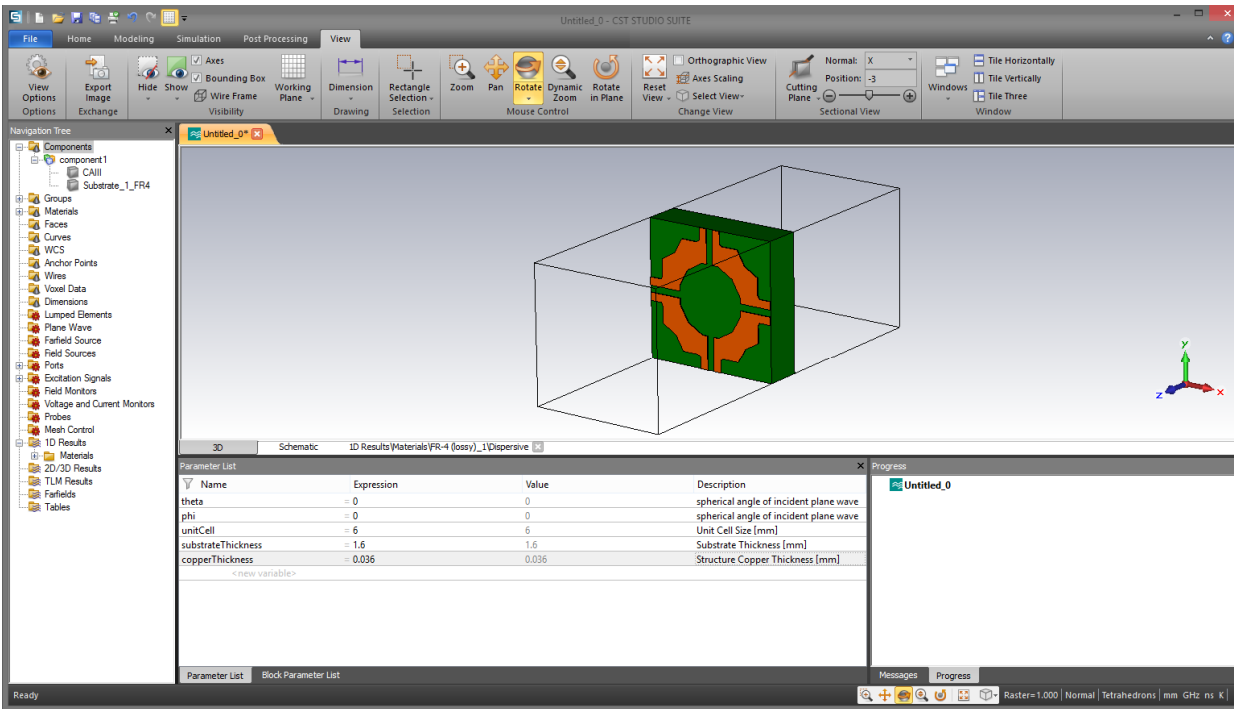


Fig. 3.2.31: MTM structure in Unit Cell configuration with Bounding Box, which appears after setting Boundary Conditions.

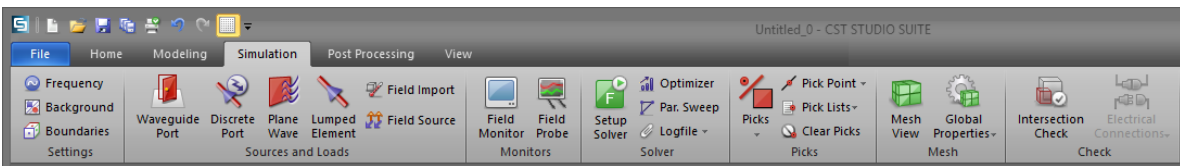


Fig. 3.2.32: Step 25 – From the “Simulation” tab, click “Setup Solver.”

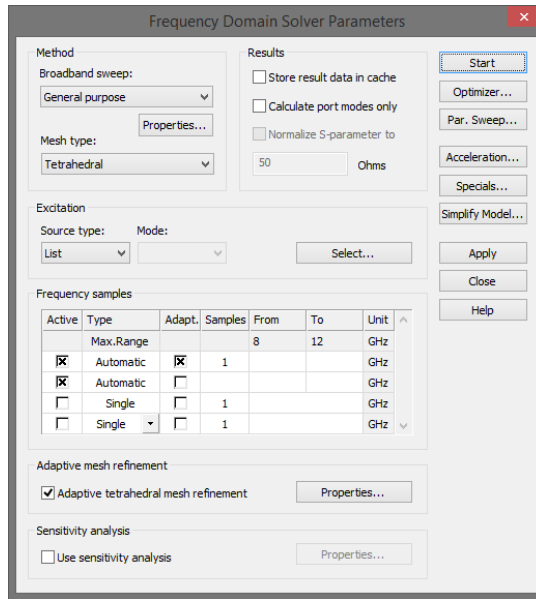


Fig. 3.2.33: Step 26 – From the Frequency Solver, click the “Select...” button to configure the excitation.

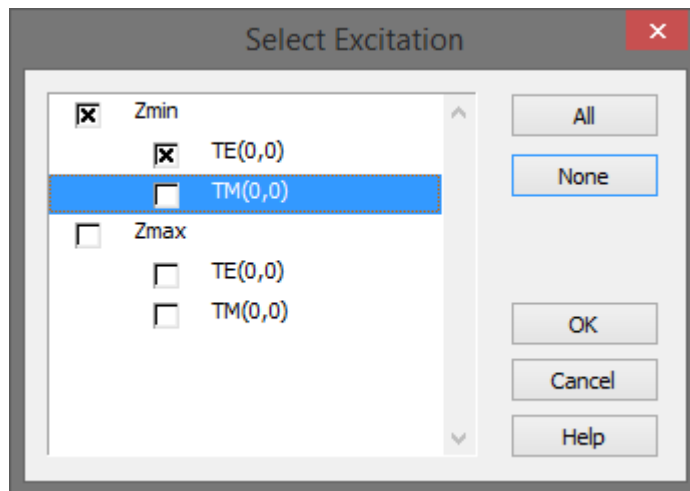


Fig. 3.2.34: Step 27 – Select excitation source from z-min, and TE(0,0) mode.

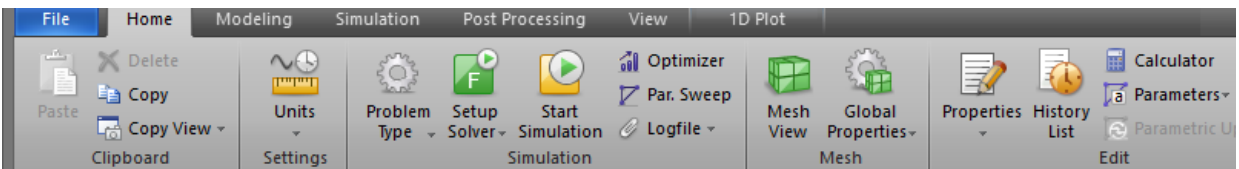


Fig. 3.2.35: Step 28 – To start the simulation, you may either click “Start” from within the Frequency Solver, or from the “Home” tab, click the “Start Simulation” button.

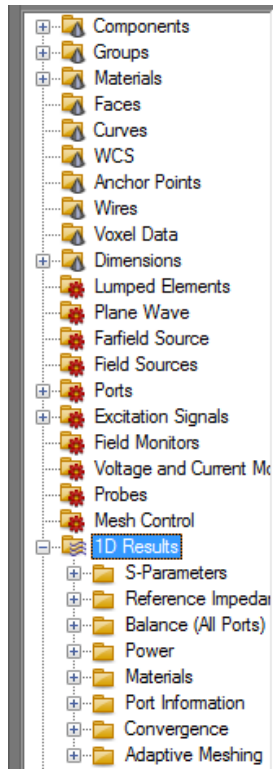


Fig. 3.2.36: Step 28 – After the simulation has completed, you may view the various results by selecting 1D, 2D/3D Results in the Navigation Tree. In our case, we are interested in the *S*-Parameters for further investigation, so click on “1D Results”, then “*S*-Parameters”, where you may view either individual *S*-Parameters or all at once.

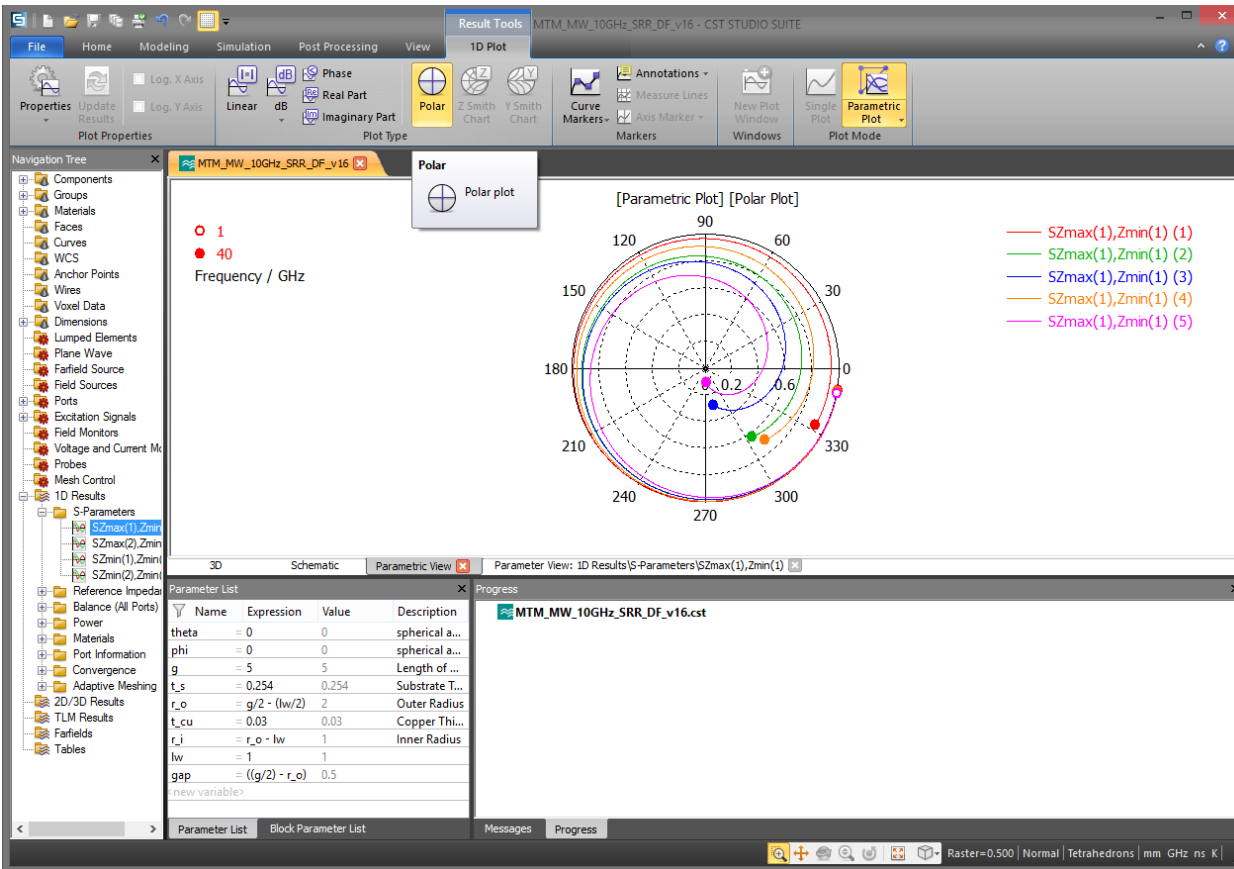



Fig. 3.2.37: Step 29 – In order to export the S-Parameter data, you must click on the individual S-Parameter, (which will enable the “1D plot” tab to appear), then select the “Polar”  button (which contains frequency, magnitude and phase data of each of the samples).

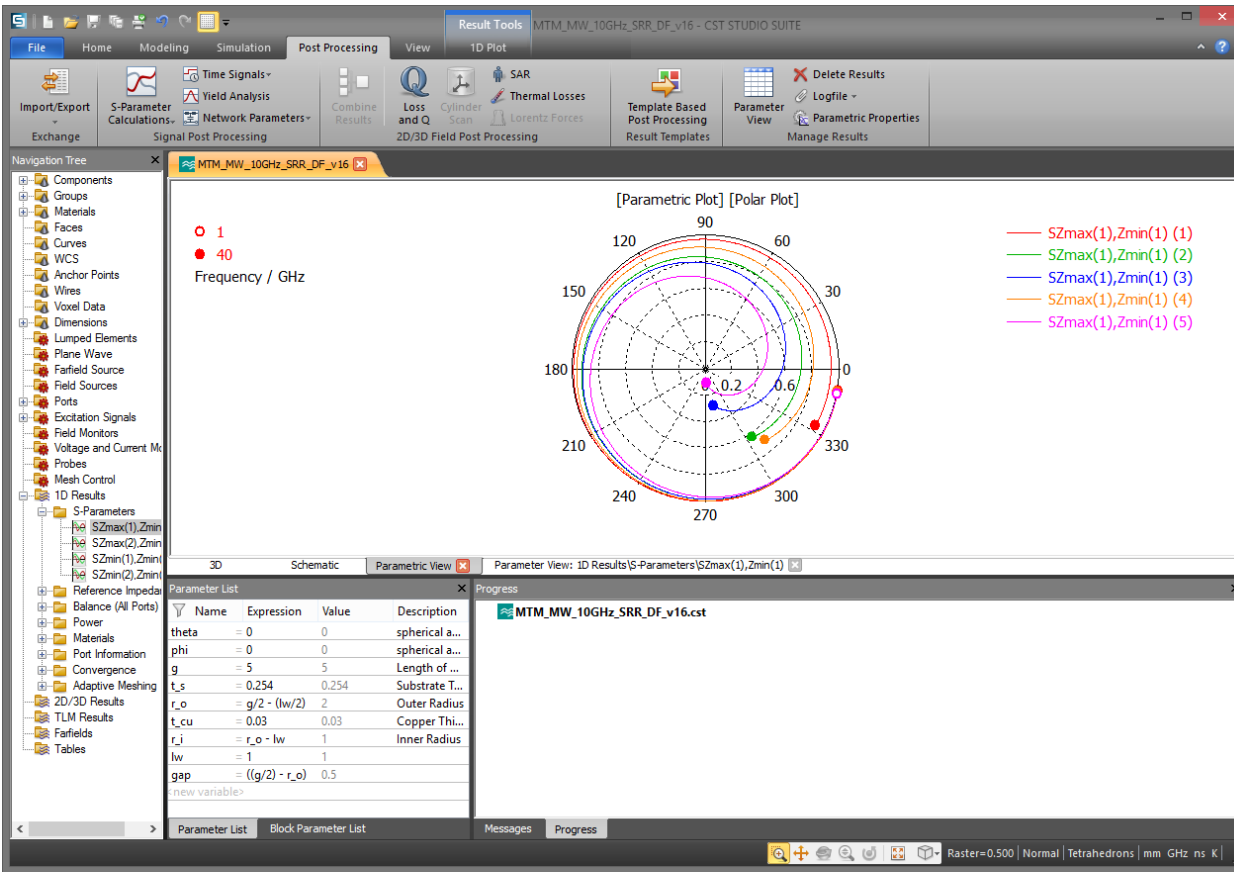


Fig. 3.2.38: Step 30 – Once the S -Parameter is set to Polar, select the “Post Processing” tab.

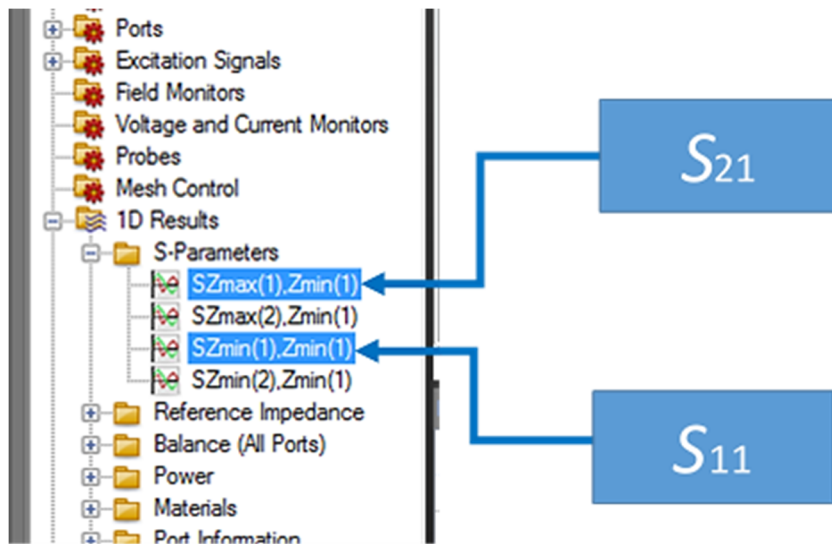


Fig. 3.2.39: By default, CST labels the S_{11} and S_{21} S -Parameters $SZmin(1),Zmin(1)$ and $SZmax(1),Zmin(1)$, respectively, according to the configured excitation and ports from Step 27.

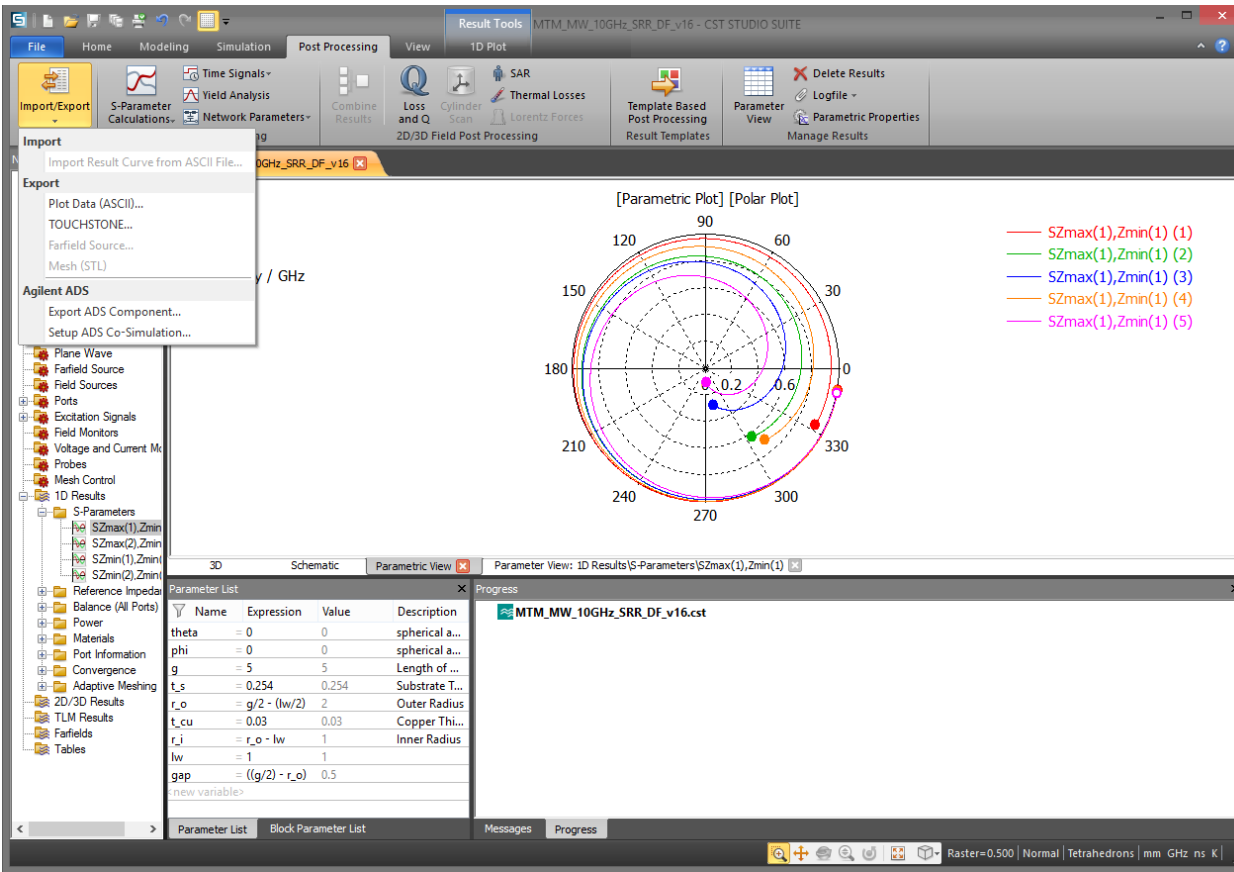


Fig. 3.2.40: Step 31 – From the “Post Processing” tab, click the “Import/Export” button, then select “Plot Data (ASCII)...”.

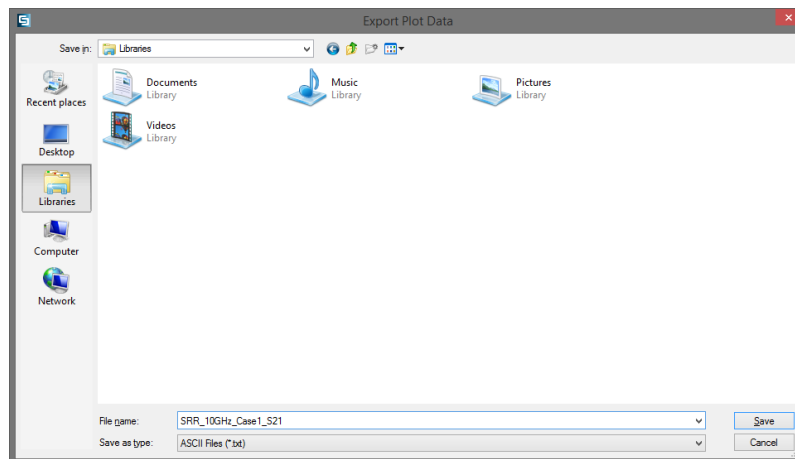


Fig. 3.2.41: Step 32 – The user is prompted to select a location and filename for the S -Parameter data. It is highly encouraged to properly name the data with case names, etc., rather than “ $S21.txt$ ”.

Frequency / GHz	SZmax(1),Zmin(1)/abs,linear	SZmax(1),Zmin(1)/arg,degrees
1	0.99786653	347.17914
1.039	0.99770069	346.67814
1.078	0.99752798	346.17696
1.117	0.99734837	345.67559
1.156	0.99716182	345.17403
1.195	0.99696833	344.67228
1.234	0.99676785	344.17033
1.273	0.99656036	343.66817
1.312	0.99634584	343.16579
1.351	0.99612424	342.6632
1.39	0.99589555	342.16039

Fig. 3.2.42: ASCII representation of the exported S-Parameter data.

After obtaining *S*-Parameter data, as shown in Fig. 3.2.42, one may then utilize other software tools, such as MATLAB, by developing a tool with which implements the proper method to extract the effective complex parameters ϵ , μ , z , n and compute LF . In our case, we implemented the “Robust method for effective parameter extraction” discussed in Chapter 2.3.

3.2.2: 3D Structure

After designing and optimizing our 2D MTM structure, we then want to synthesize a 3D MTM as this is the selected design which will contain the desired characteristics we have thus achieved as far as NZRIM. Figs. 3.2.43 – 3.2.52 demonstrate the basic process for such synthesis.

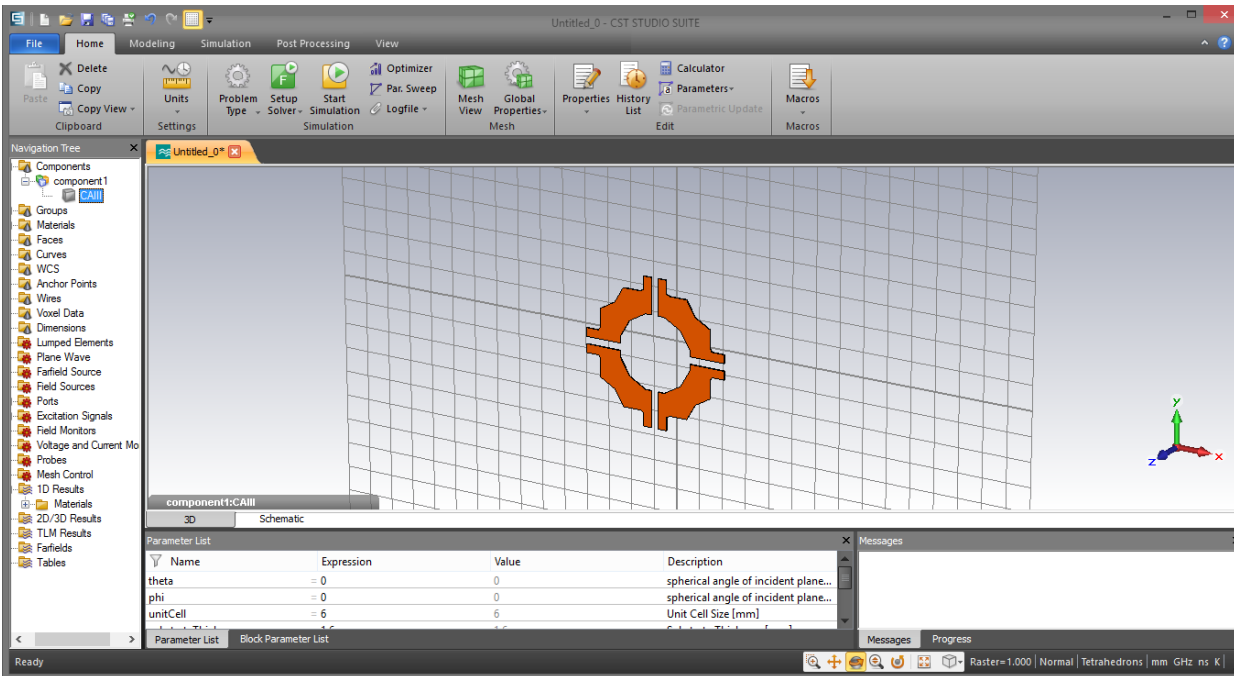


Fig. 3.2.43: Step 1 – Building from the foundation for Section 3.2.1, we start with our 2D MTM structure. Click to select the MTM structure name under the “Components” folder, top-left column. In our case, the MTM is called “CAIII.”

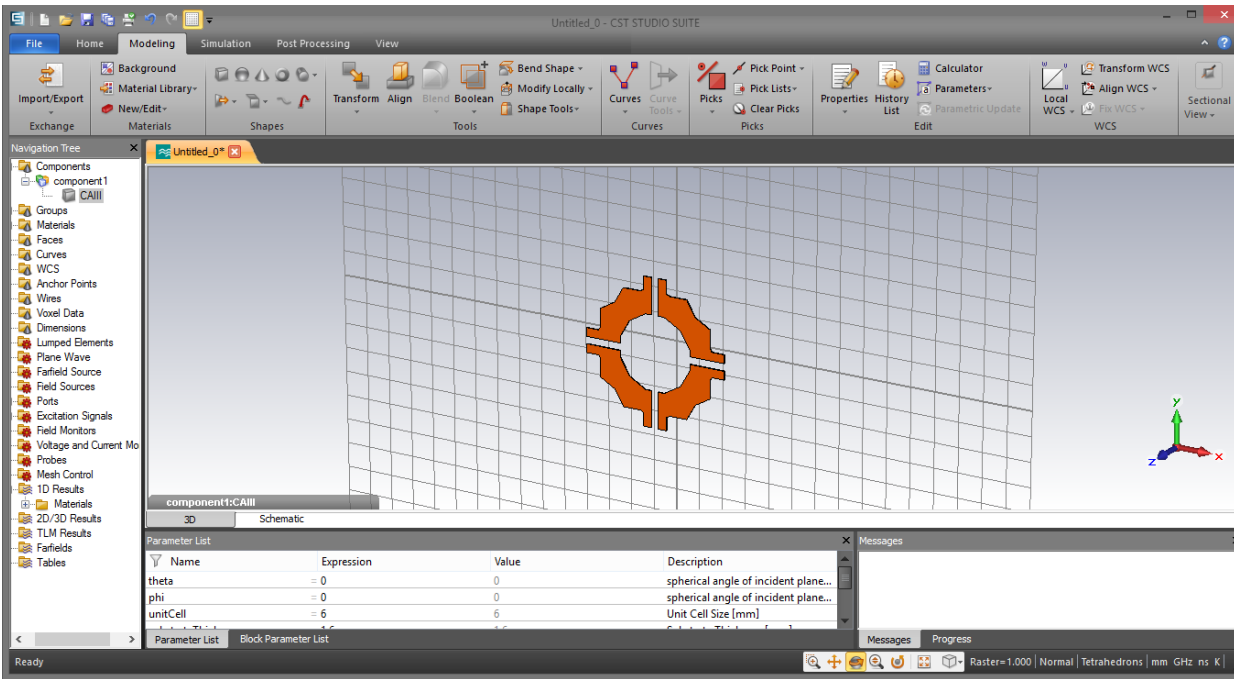


Fig. 3.2.44: Step 2 – Once the MTM structure is selected, click on the “Modeling” tab.

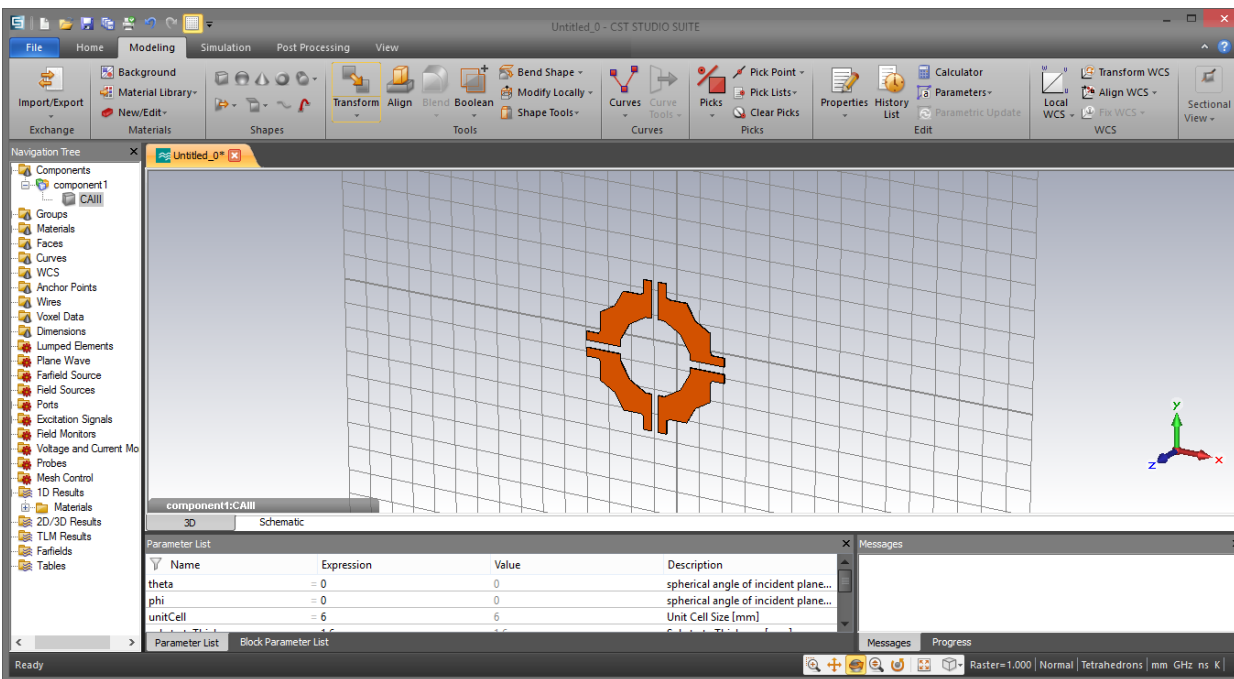
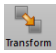


Fig. 3.2.45: Step 3 – From the “Modeling” tab, select the “Transform”  button.

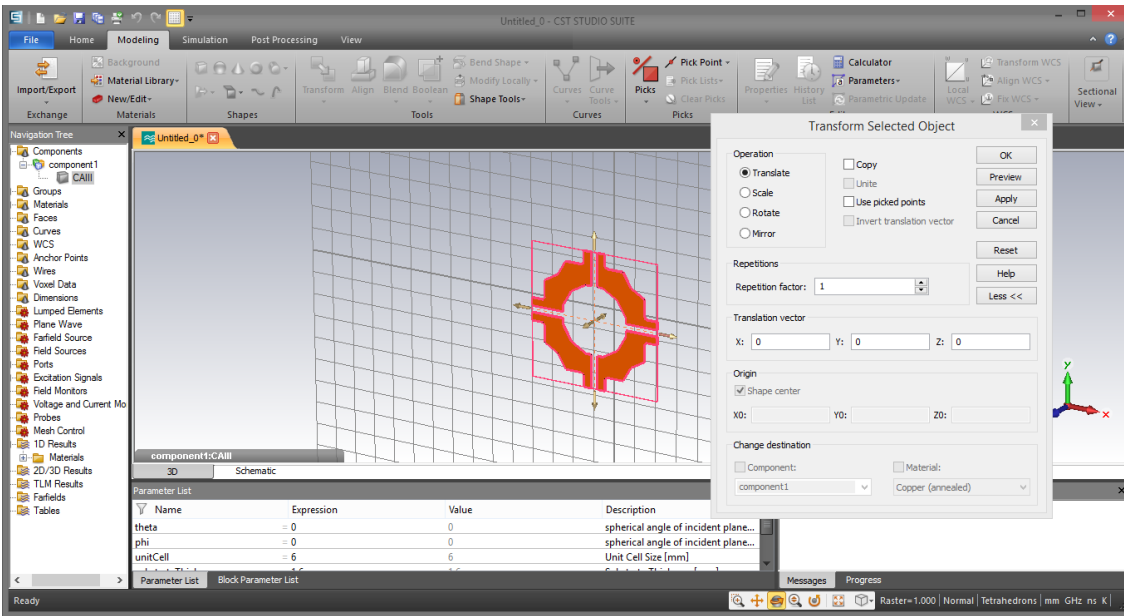


Fig. 3.2.46: The Transform button will prompt to either Translate (Move), Scale, Rotate or Mirror the selected structure.

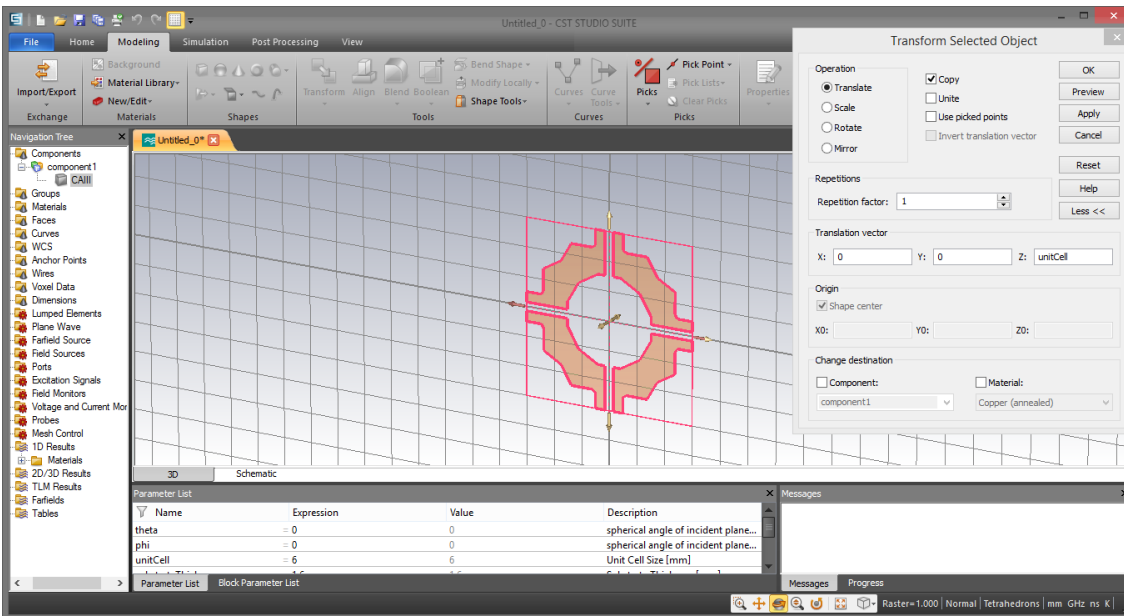


Fig. 3.2.47: Step 4 – Since we are designing a “cube” structure from the 2D MTM selected, click the “Copy” box, and fill the desired length to copy the 2D structure in the desired direction.

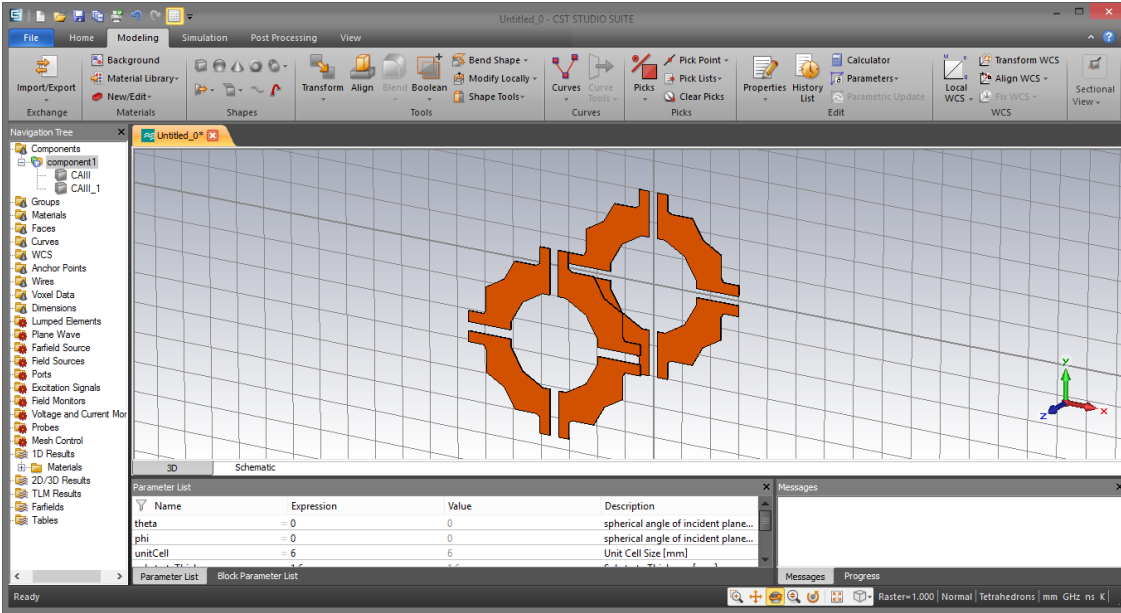


Fig. 3.2.48: “Front” and “Back” sides of the cube in the z-direction. After “copying” and moving the 2D MTM structure, we have two structures under “component1.”

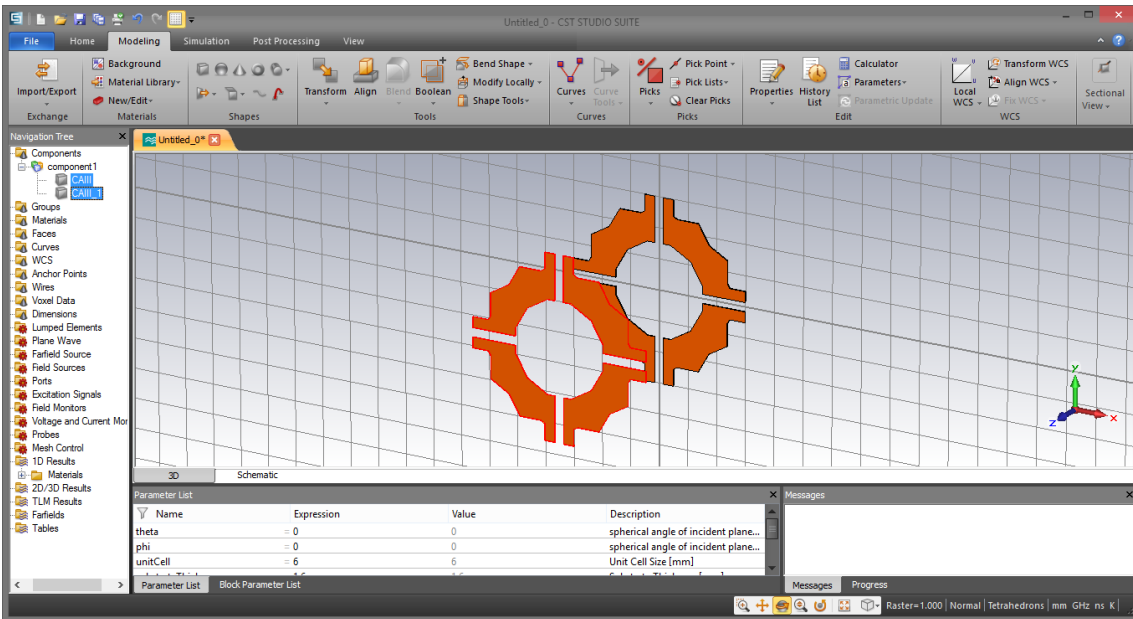


Fig. 3.2.49: Step 5 – Select both the original and new 2D structures, then click the “Transform” button once again.

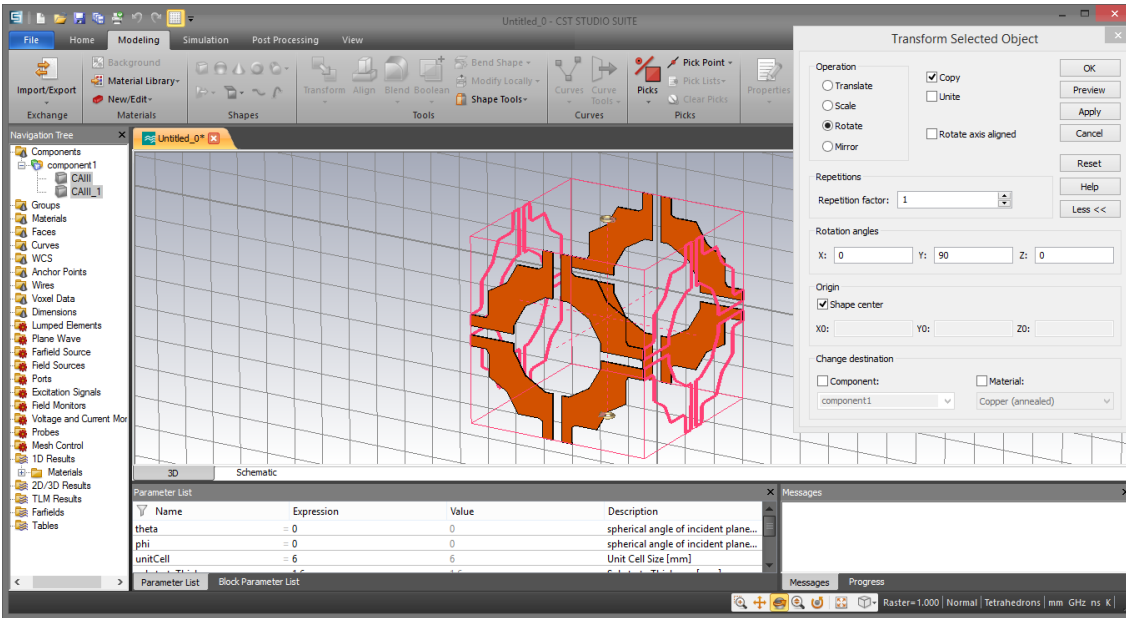


Fig. 3.2.50: Step 6 – Select to “Rotate” the structure, check the “Copy” box, fill the Rotation angle 90° in the y-axis, and choose the Origin to be the center of the shape.

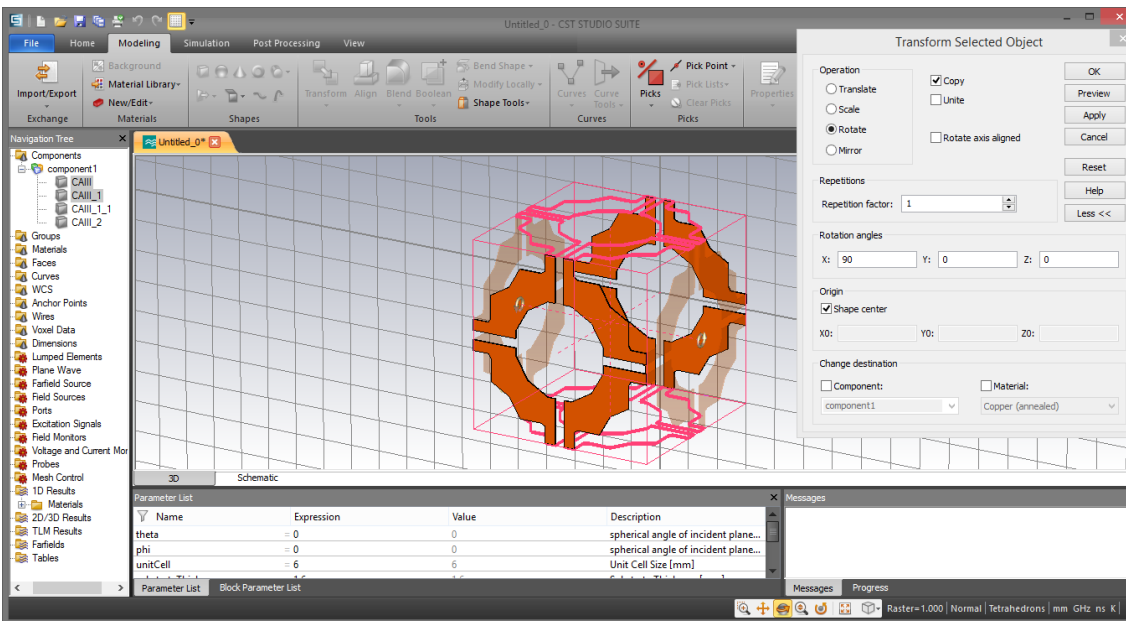


Fig. 3.2.51: Step 7 – We repeat Steps 5 and 6, however, select the Rotation angle 90° in the x-axis to complete the cube structure.

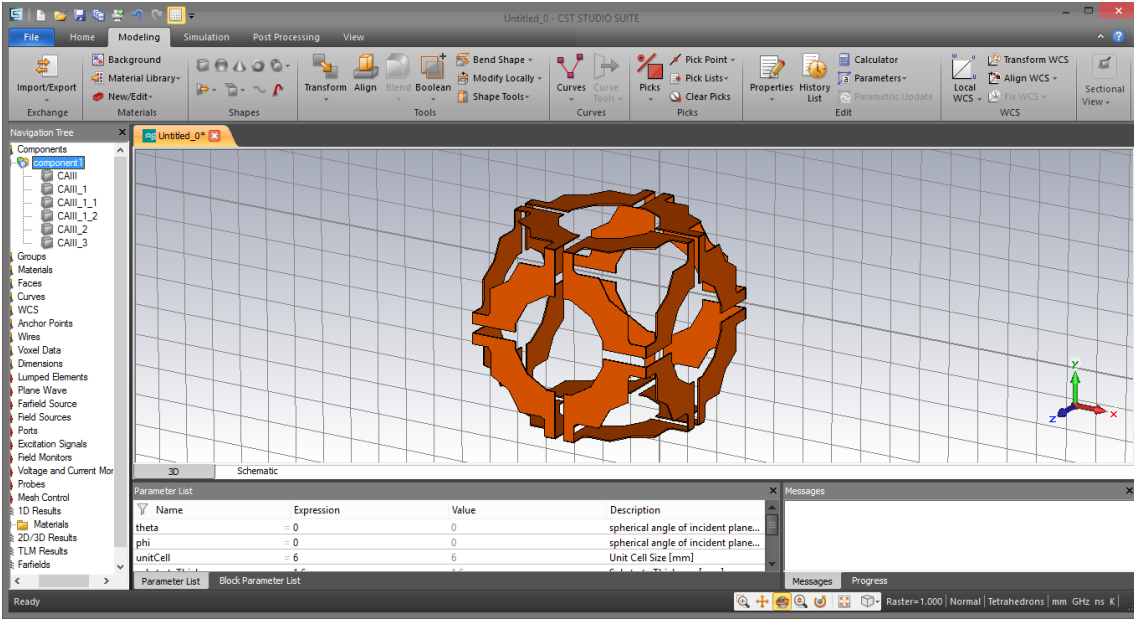


Fig. 3.2.52: Completed 3D CAIII MTM Structure.

At this point, in Fig. 3.2.52, we are still not done. There are other items to consider such as the thickness of the MTM will double as a periodic structure. Therefore, since our design is continuous, we may need to consider halving the thickness from the sides of the structure not parallel to the propagation direction. In our case, the front and back sides are left intact, but the top, bottom and side structure thicknesses need to be cut in half. Once all this is complete, we may then add all the structures into a single unit with the “Boolean” button from the “Modeling” tab.

3.3: Metamaterial Structure Validation

Two articles were utilized in order to validate numerical studies for this research. Applied Physics paper (2004) from Katsarakis’ group on the electric coupling to magnetic resonance of SRRs served as a validation for CST simulations. Katsarakis studied both theoretical and experimentally the transmission properties of a lattice of split ring resonators (SRRs) for different electromagnetic (EM) field polarizations and propagation directions. They discovered unexpectedly that the incident electric field \mathbf{E} couples to the magnetic resonance of the SRR when the EM waves propagate perpendicular to the SRR plane and the incident \mathbf{E} is parallel to the gap-bearing sides of the SRR [3.3].

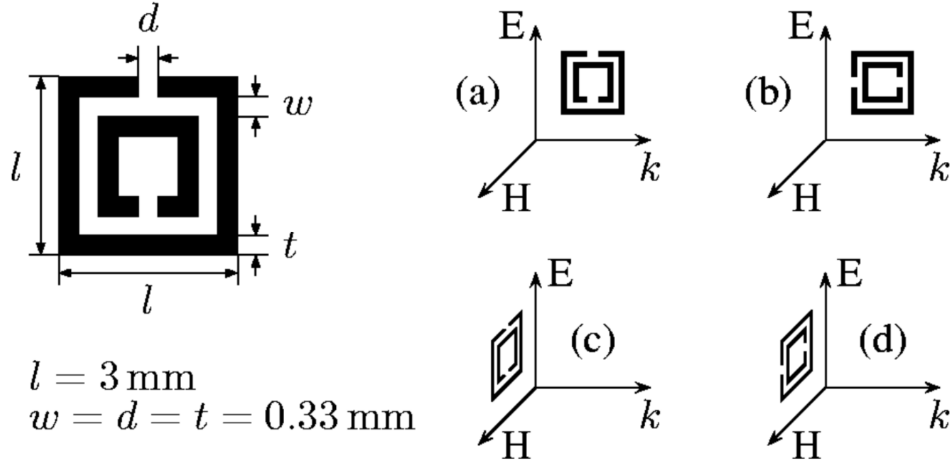


Fig. 3.3.1: From Katsarakis et al. [3.3], the left-hand side depicts the MTM structure studied. The right-hand side shows the four orientations for the SRR with respect to the “triad” \mathbf{k} , \mathbf{E} , and \mathbf{H} of the incident EM field.

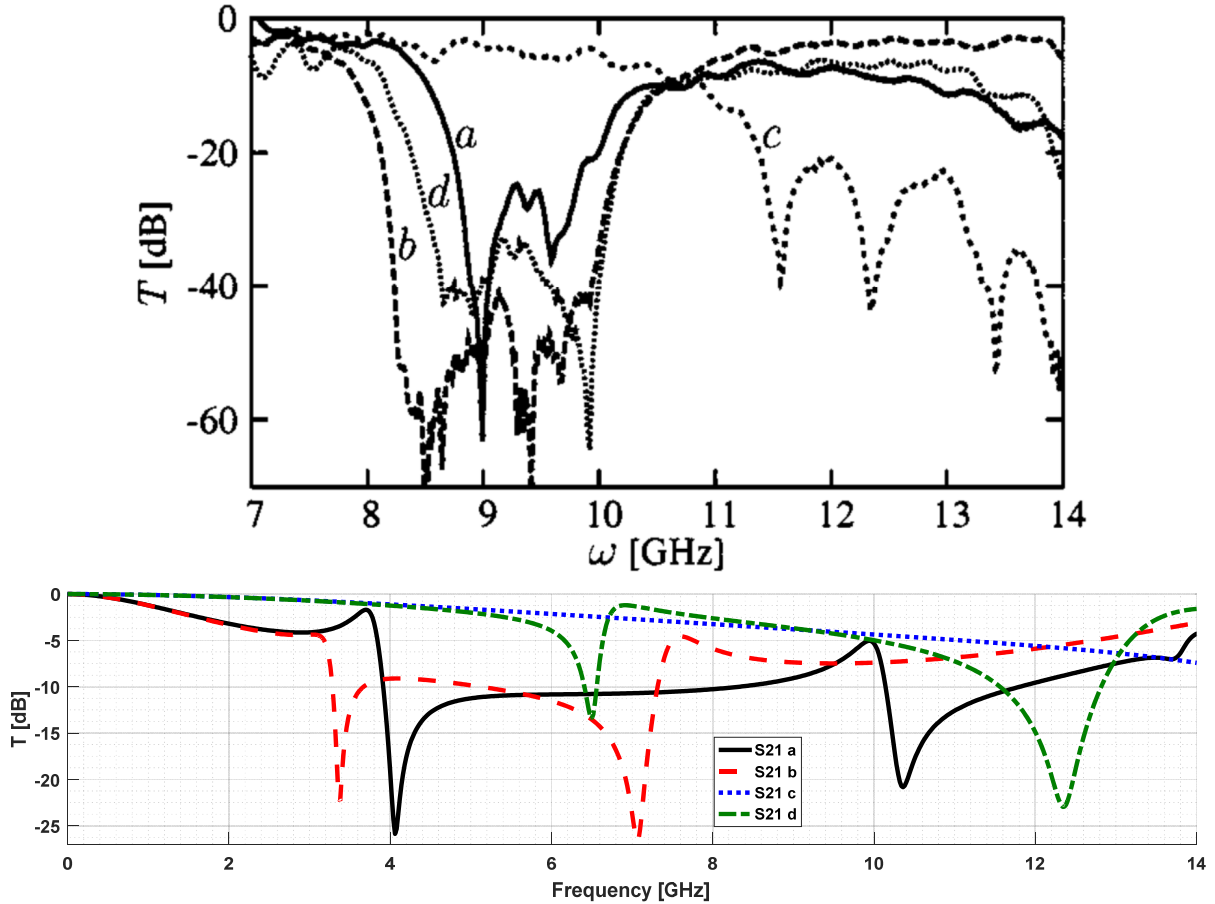


Fig. 3.3.2: From Katsarakis et al. [3.3], the top plot shows the measured transmission spectra of a lattice of SRRs for the four different orientations shown in Fig. 3.3.1. The bottom plot demonstrates the plotted (MATLAB) transmission spectra from the S -Parameter data obtained from CST simulation to validate CST setup.

For the experimental study, Katsarakis [3.3] fabricated using a conventional printed circuit board (PCB) process with $30\text{ }\mu\text{m}$ thick copper patterns on one side of a 1.6 mm thick FR-4 dielectric substrate. The FR-4 board has a dielectric constant of 4.8 and a dissipation factor of 0.017 at 1.5 GHz. The design and dimensions of the SRR, are described in Fig. 3.3.1. The composite metamaterial (CMM) was then constructed by stacking together the SRR structures in a periodic arrangement. The unit cell contains one SRR and has the dimensions 5 mm (parallel to the cut sides), 3.63 mm (parallel to the continuous sides), and 5.6 mm (perpendicular to the SRR plane).

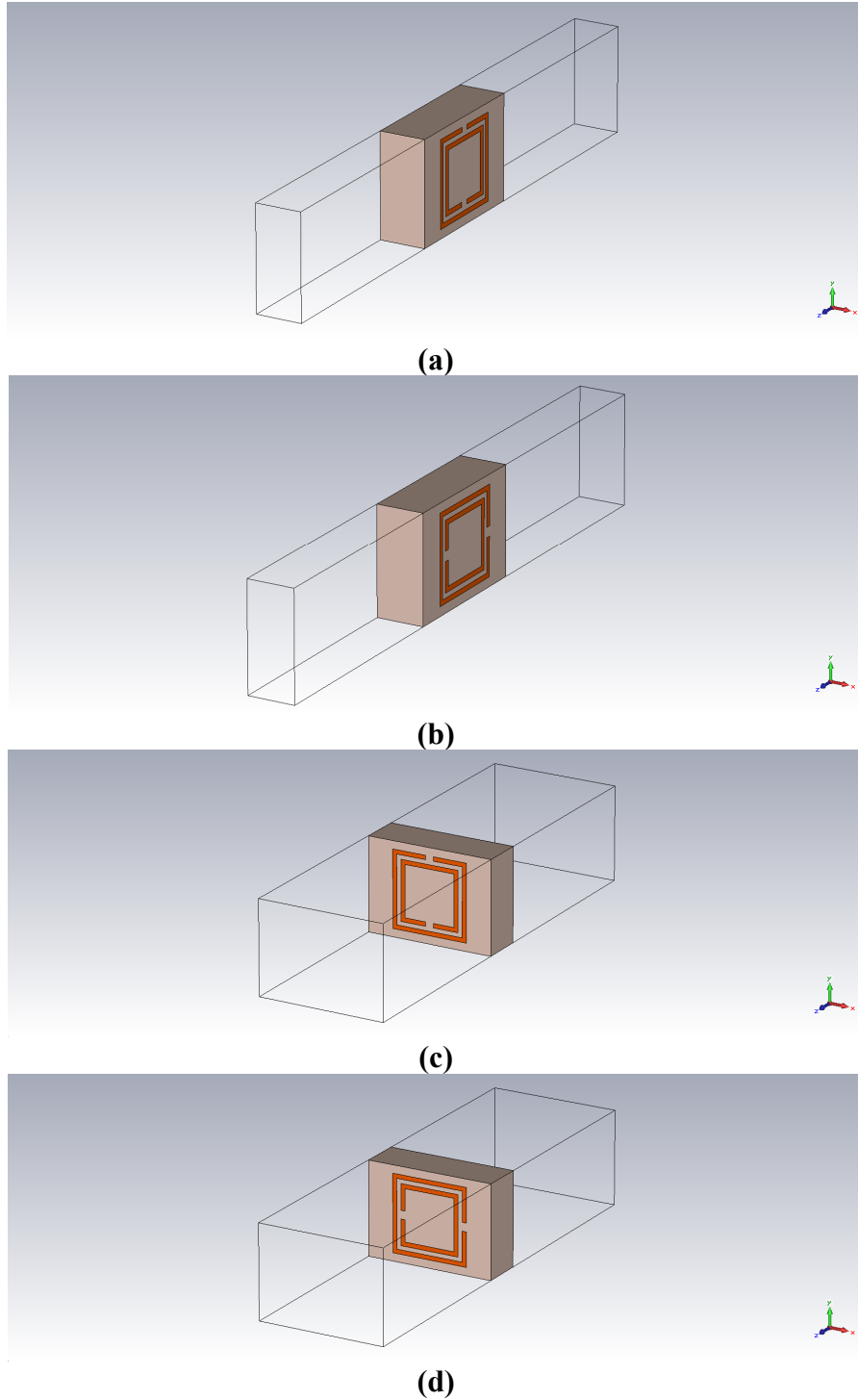


Fig. 3.3.3: CST simulation of cases *a – d* from Katsarakis study Fig. 3.3.1 [3.3], to validate CST setup.

Journal of Optics (2005) paper from Kafesakis' group on detailed numerical studies of the transmission properties of LH MTMs was utilized to validate robust method for parameter

extraction MATLAB code. Kafesaki utilized numerical simulation techniques and commercially available CST Microwave Studio Suite[®] to study the transmission properties of left-handed (*LH*) metamaterials and arrays of split-ring resonators (SRRs). They examined the dependence of the transmission through single- and double-ring SRRs on parameters of the system such as the size and shape of the SRRs, size of the unit cell, dielectric properties of the embedding medium where the SRRs reside and SRR orientation relative to the incoming electromagnetic field [3.4].

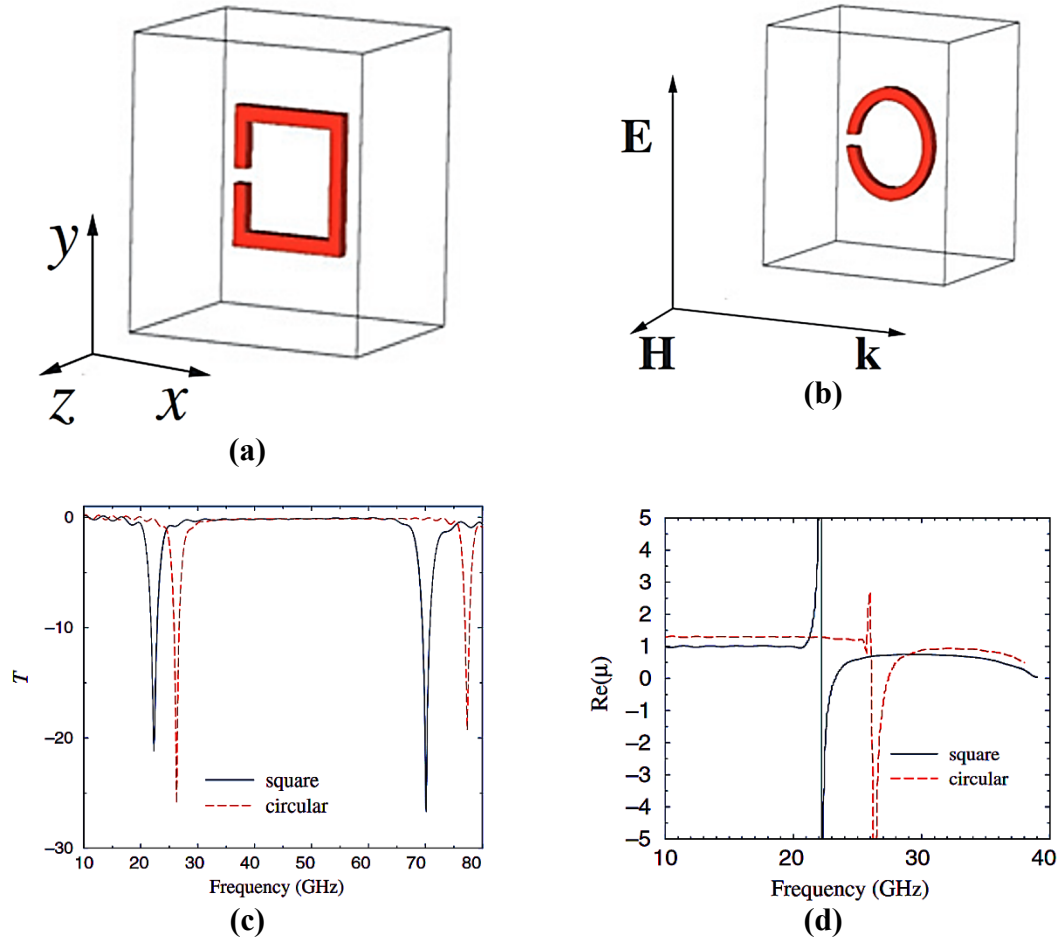


Fig. 3.3.4: From Kafesaki et al. [3.4], (a). – (b). corresponding designs studied square and circular single SRR, (c). transmission, (T , in dB) as a function of frequency (GHz) for the structures (a) and (b), (d). magnetic permeability as a function of frequency for structures (a) and (b).

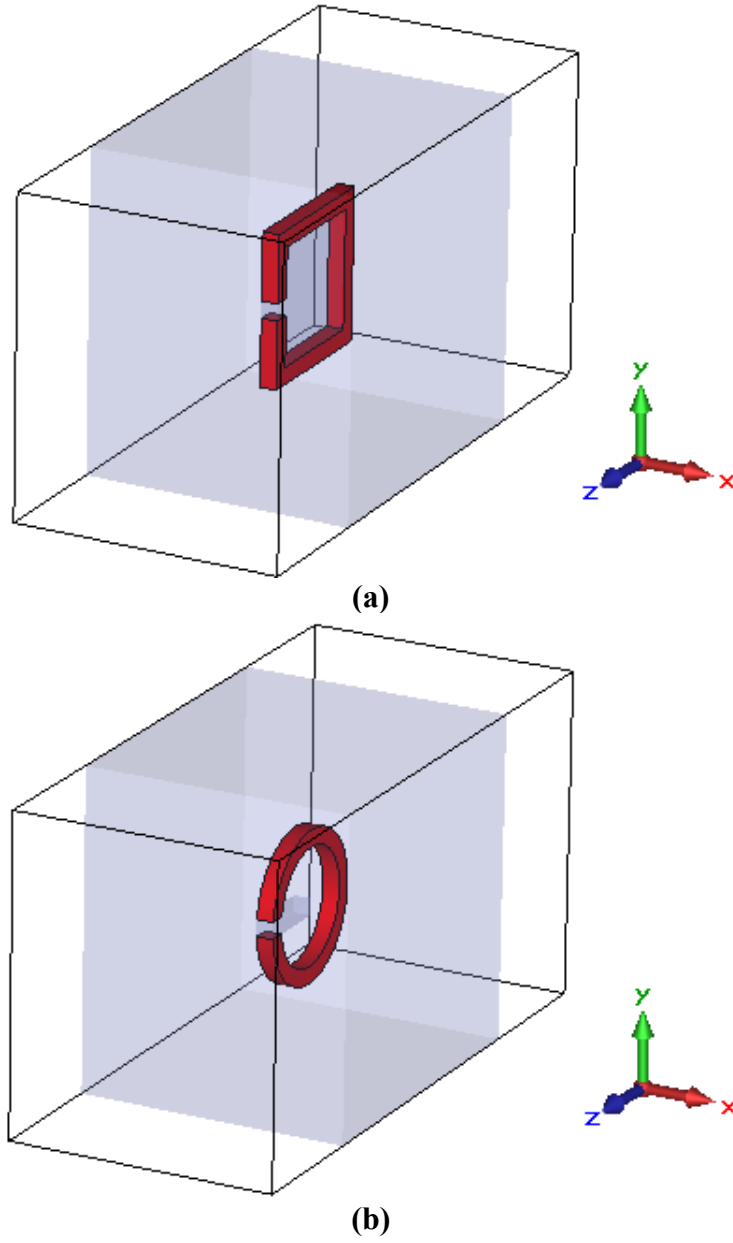


Fig. 3.3.5: CST simulation of Single-ring SRR structures from Kafesaki's study Fig. 3.3.2 [3.4], in order to validate Robust Method for Extraction of Effective Parameters MATLAB code: (a). squared, (b). circular.

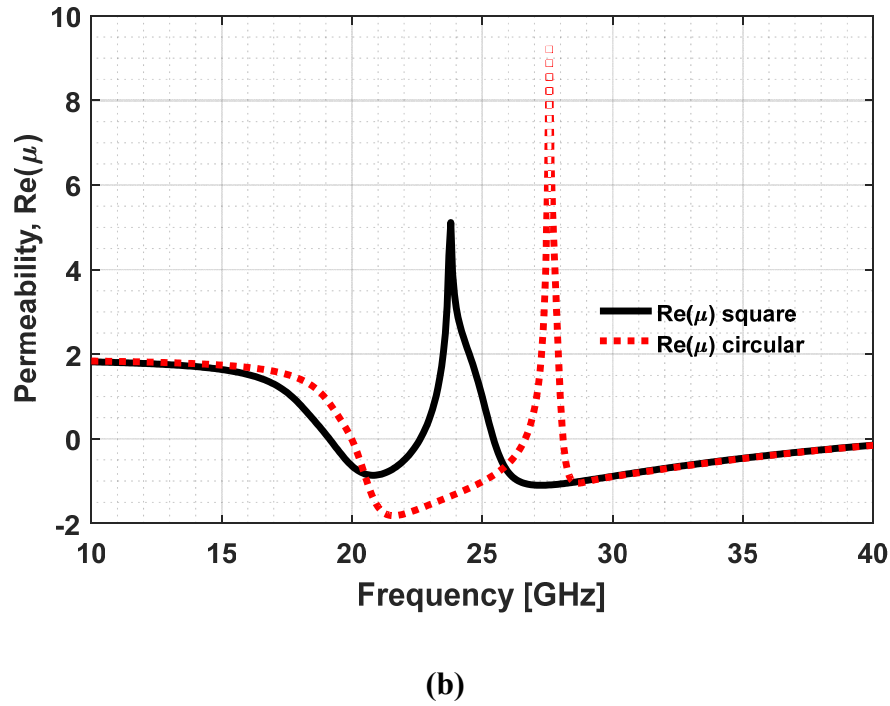
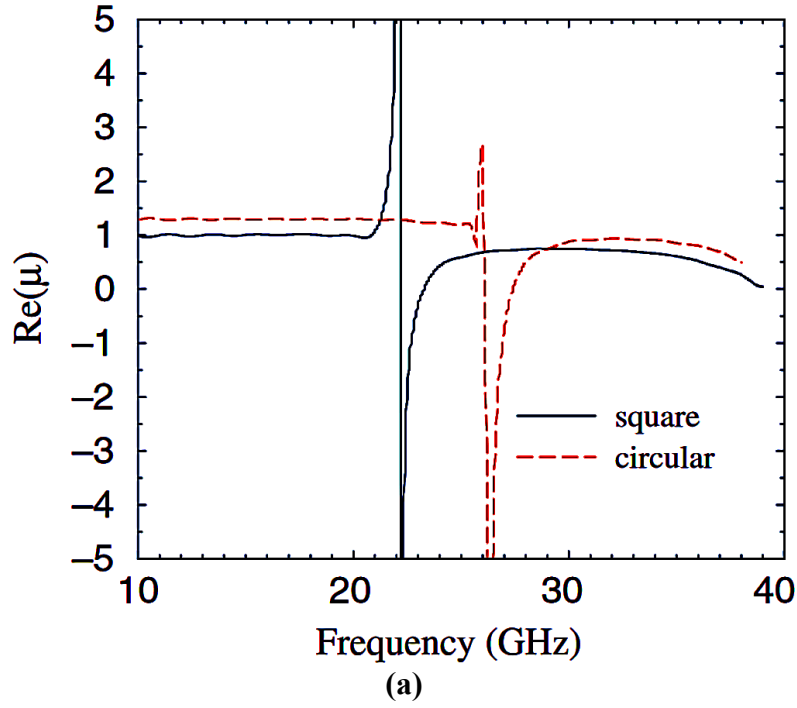


Fig. 3.3.6: Comparison of extraction for magnetic permeability as a function of frequency for structures square and circular SRR [3.4], in order to validate Robust Method for Extraction of Effective Parameters MATLAB code: (a). Kafesaki's result for $\text{Re}(\mu)$, (b). Extracted $\text{Re}(\mu)$ using Robust Method.

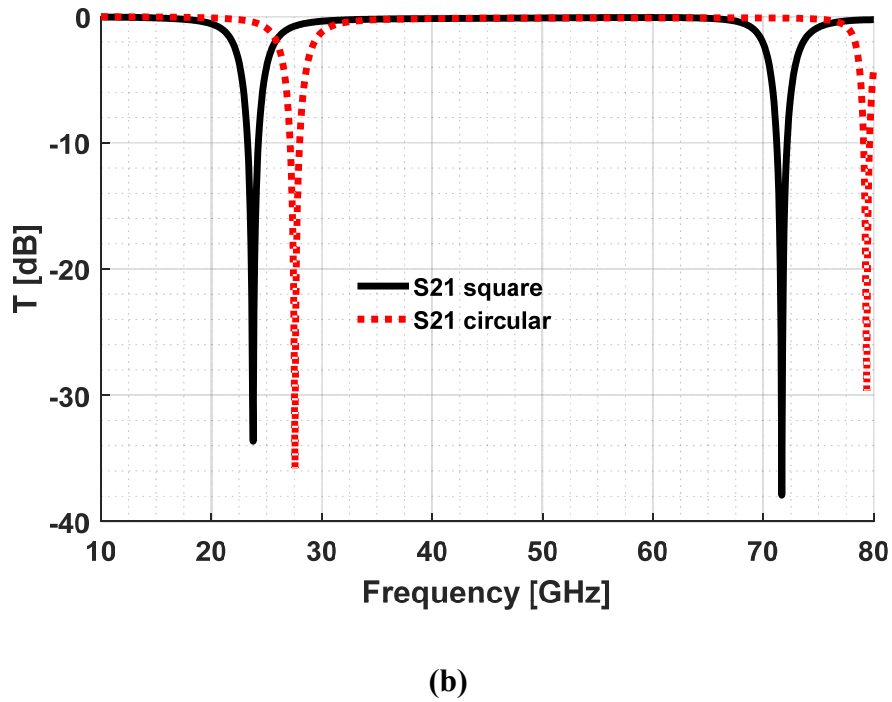
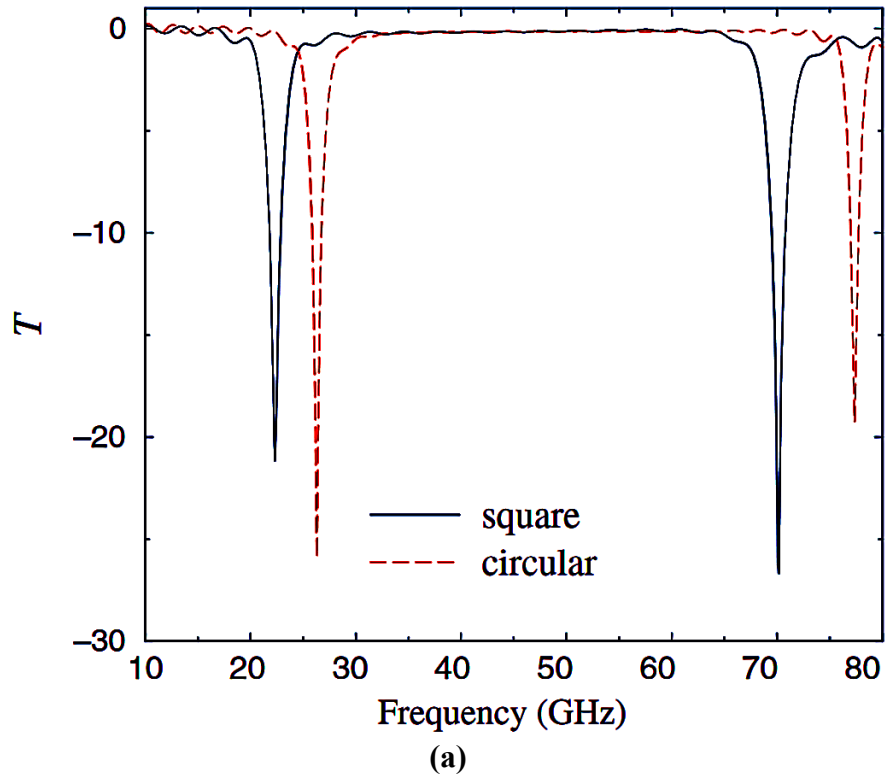


Fig. 3.3.7: Comparison of transmission (T , in dB) as a function of frequency: (a). Kafesaki's result [3.4], (b). obtained S_{21} data from CST simulation and plotted via MATLAB.

CHAPTER IV

DESIGN AND NUMERICAL STUDIES

4.1: Introduction

In Chapter 4, the focus is to study the 3D fishnet metamaterial (MTM) structure in a step-by-step fashion by modeling, simulating and analyzing the electromagnetic properties, i.e., permittivity (ϵ), permeability (μ), refractive index (n), impedance, and loss factor (LF) of fundamental structures which are: 1) circular closed-ring resonator (CCRR), 2) circular split-ring resonator (CSRR) and then a modification to the CSRR which will be referred in this thesis as the “Omega” structure. There are two types of the Omega structures: 1) Disconnected Omegas and 2) Connected Omega or “Omeganets.” After optimizing for the n near-zero (NNZ) and low LF bands, they will be implemented for 3D NNZ structure design. By varying the physical parameters of the structure within the unit cell, one may observe the behavior of permittivity and permeability. The unit cell parameters which will be varied in the 2D cases include the linewidth of the structure, the spacing between the periodic structures and the split within the structure itself. These MTM structures serve as the building blocks for the 2D Omeganet structure which will then be transformed into a 3D metamaterial structure with the goal of yielding near-zero refractive index material (NZRIM). Commercial software CST Microwave Studio® 2015 is utilized to synthesize and simulate the MTM structures for this study. Given that the desired frequency for the design is in X -band regime, the selected operating center frequency is 10 GHz.

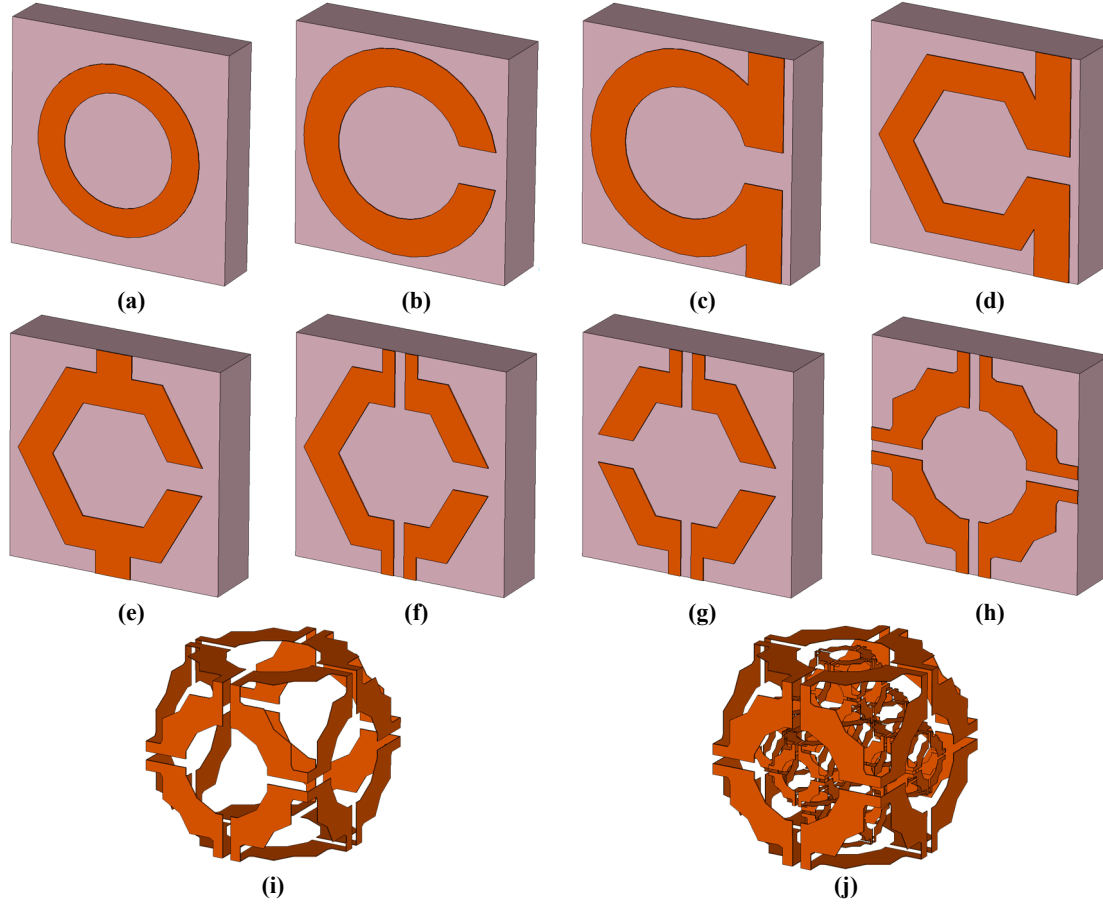


Fig. 4.1.1: Progression of 3D Omega-net MTM Design from its Fundamental Structure to the End Product: (a) Circular Closed-Ring Resonator (CCRR), (b) Circular Split-Ring Resonator (CSRR), (c) Omeganet structure derived from the CSRR, (d) Hexagonalized Omeganet, (e)-(h) Selected Optimizations Performed on Hexagonal Omeganet, (i) “Single Shell” Cubic Hexagonal Omeganet derived from Optimized Hexagonal Omeganet Structure, (j) “Octahedral Double-Shell” Cubic Hexagonal Omeganet derived from Optimized 2D Hexagonal Omeganet Structure.

4.2: Circular Closed-Ring Resonator (CCRR) Structures

In order to better comprehend the behavior of MTMs, one may want to start by digesting the rudimentary structure of the end product. Fig.4.1.1 demonstrates the progression of our design from its fundamental structure until the realization of the 3D design. For this research, the end product is a 3D Ω -shaped fishnet we call “Omeganet” as shown in Fig. 4.1.1(j). A single 2D Omeganet unit cell structure is derived from the CSRR, depicted in Fig. 4.1.1(b). The CSRR is derived from a very basic structure, the circular closed-ring resonator (CCRR), seen in Fig.

4.1.1(a). The SRR structure proposed by Pendry and his research group [4.1] is commonly used left-handed (*LH*) material studies [4.2,4.3]. The magnetic resonance of the SRR structure is induced by the splits within the rings and by the spacing between structures [4.1]. The ambiguity in the reasoning for the spacing gaps of periodic CSRR can be lifted by using a CCRR structure in which the splits are not present, then we will observe that the CCRR structure will destroy the magnetic resonance but keep the electric resonance [4.4].

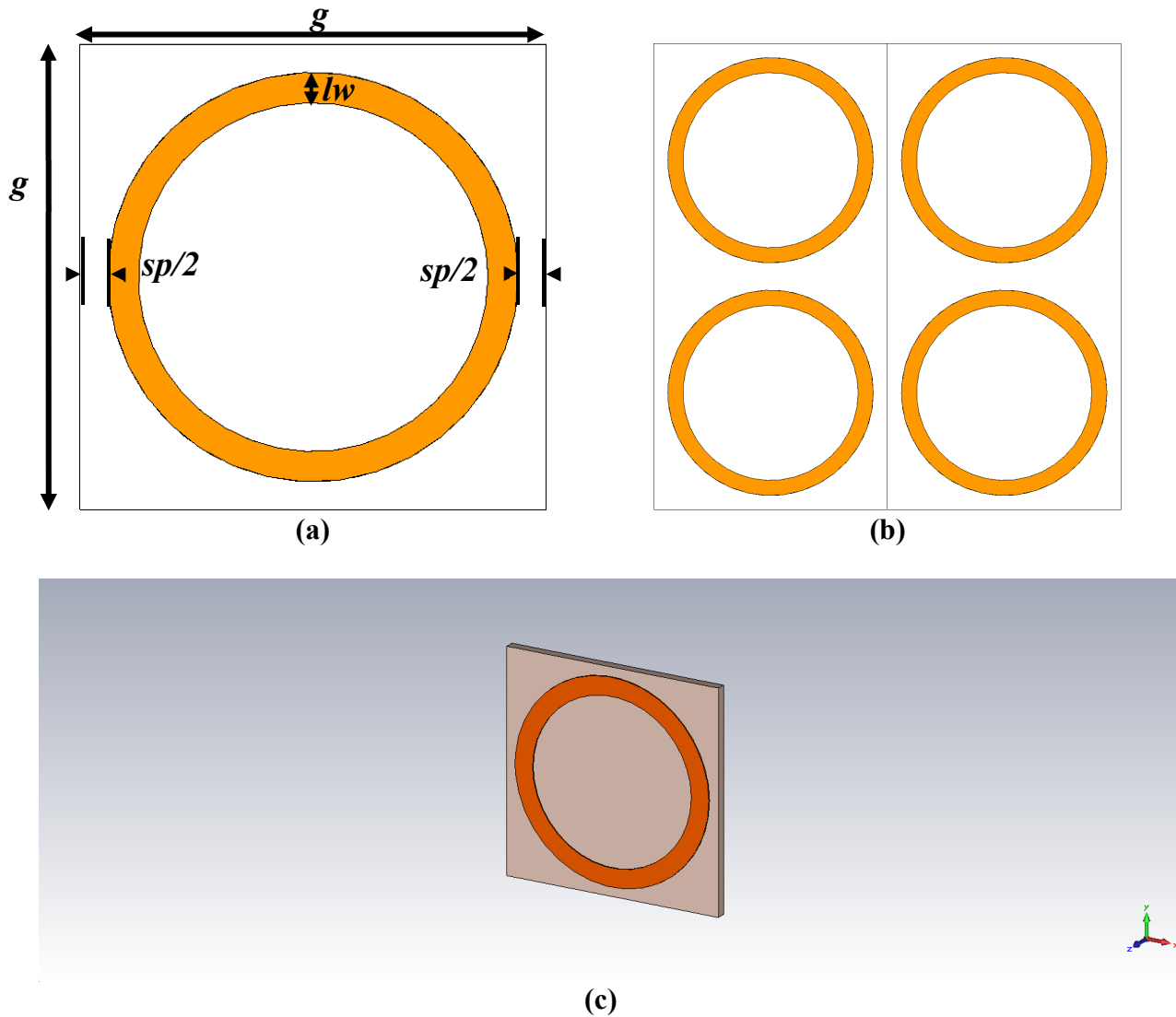


Fig. 4.2.1: Circular Closed-Ring Resonator (CCRR) Structure: (a). CCRR in unit cell with parameters g (unit cell size), lw (structure linewidth), sp (spacing between periodic structures), (b). Representation of periodic array with 2×2 CCRR unit cells, (c). CCRR in unit cell with propagation direction in the z -direction.

The substrate utilized for this design is a 0.254 mm thick double copper-clad Arlon Di 880 board with thickness 0.254 mm, permittivity $\epsilon_r = 2.2$, loss tangent $\tan\delta = 0.0001$. The copper thickness for the structure is 0.03 mm.

The behavior observed by this type of structure is mainly of magnetic nature. Hence, a resonant frequency is obtained. By varying the parameters mentioned one may either increase or decrease the resonant frequency. There are four cases studied with respect to varying g the unit cell sizes: (4 mm \times 4 mm), (5 mm \times 5 mm), (6 mm \times 6 mm) and (8 mm \times 8 mm). Within each of the unit cell sizes the linewidth, lw , and the spacing between structures, sp , was varied.

4.2.1: CCRRs in 4 mm \times 4 mm Unit Cell

The first unit cell size studied is the 4 mm \times 4 mm. Table 4.2.1 shows the results for the eight cases employed for the CCRR structure and Fig. 4.2.2 is a visual representation acquired from synthesized structures via CST. From CST, we obtain the input reflection coefficient data (S_{11}) and the forward transmission (insertion) gain data (S_{21}) in polar form which retains the frequency, magnitude and phase information of each sample point within the specified frequency range. With the S_{11} and S_{21} data, we then employ the robust method for extracting the complex effective parameters described in Chapter 2.3.

One may notice that as we decrease the spacing between the structures, and thus occupying more real estate within the unit cell, the resonant frequency is shifted down. The specific order of the case varying is essentially halving from the previous case. In Fig. 4.2.3(a) we may also observe the magnetic resonances of Cases 4 – 8 depicted in green, gray, purple, teal and orange dotted lines.

TABLE 4.2.1
CCRR Structure Linewidth and Spacing Variations for 4 mm × 4 mm Unit Cell

Case	Linewidth, (lw) [mm]	Spacing, (sp) [mm]	Resonant frequency [GHz]	Tx, S21 [dB]
1	1.0	2.0	63.49	-44.15
2	1.0	1.0	60.96	-55.36
3	0.5	1.0	44.61	-51.27
4	0.5	0.5	35.09	-54.89
5	0.25	0.5	28.34	-51.94
6	0.125	0.25	21.87	-49.53
7	0.0625	0.125	18.51	-47.08
8	0.03125	0.0625	16.60	-45.08

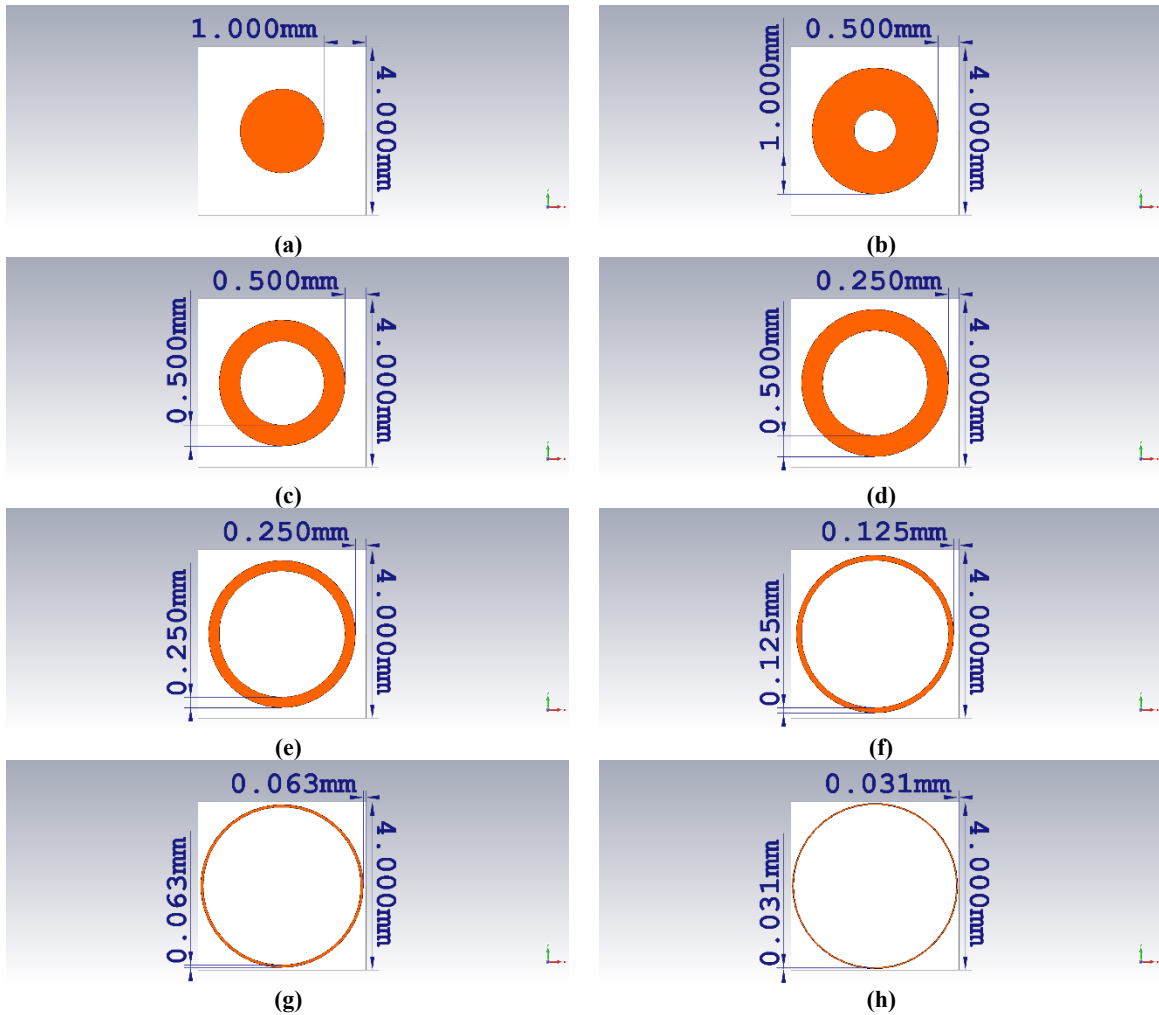


Fig. 4.2.2: CCRR Designs for Unit Cell Size 4 mm × 4 mm Varying Parameters for Linewidth, lw , and Spacing Between Periodic Structures, sp : (a). $lw = 1$ mm, $sp = 2$ mm, (b). $lw = 1$ mm, $sp = 1$ mm, (c). $lw = 0.5$ mm, $sp = 1$ mm, (d). $lw = 0.5$ mm, $sp = 0.5$ mm, (e). $lw = 0.25$ mm, $sp = 0.5$ mm, (f). $lw = 0.125$ mm, $sp = 0.25$ mm, (g). $lw = 0.0625$ mm, $sp = 0.125$ mm, (h). $sp = 0.03125$ mm, $sp = 0.0625$ mm.

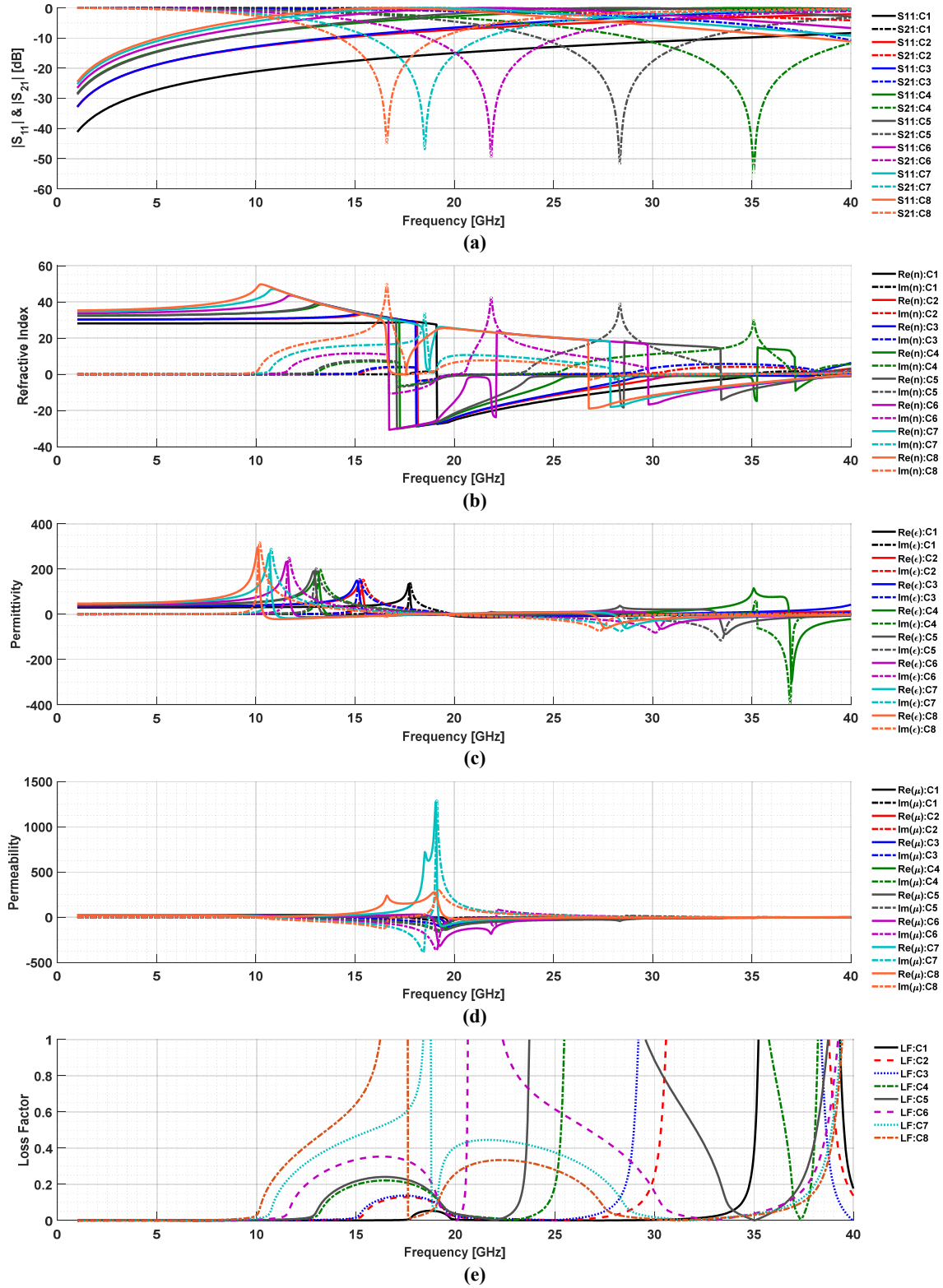


Fig. 4.2.3: Effective Parameter Extraction from Simulation Results for 4 mm × 4 mm Unit Cell CCRR Cases 1 – 8: (a) S -Parameters, (b) Real and imaginary parts of n , (c) Real and imaginary parts of ϵ , (d) Real and imaginary parts of μ , (e) Loss Factor.

Fig. 4.2.3 shows the transmission and reflection coefficients as well as the simulation results for refractive index, permittivity, permeability and loss factor. We may observe that by the resonant frequency shifts down as we decrease the linewidth of the structure as well as the spacing between the periodic structures, thus occupying more of the real estate of the unit cell. We may see from Fig. 4.3.2(a), that the resonant behavior for Cases 1 and 2 are out of the simulated specified frequency range. This is since the size of the structure is much smaller than the unit cell. Similarly, we will observe Case 1 and 3 for the $5\text{ mm} \times 5\text{ mm}$ unit cell size are out of the specified range. However, to be accurate, these cases were later simulated individually in order to obtain the exact resonant frequency and include it in our study.

4.2.2: CCRRs in $5\text{ mm} \times 5\text{ mm}$ Unit Cell

The second unit cell size studied is the $5\text{ mm} \times 5\text{ mm}$. Table 4.2.2 shows the results for the eight cases employed for the CCRR structure and Fig. 4.2.4 is a visual representation acquired from synthesized structures via CST. In addition to Cases 4 – 8, we may now appreciate the magnetic resonance of Case 3, depicted in Fig. 4.2.5(a) in blue, due not only to occupying more real estate from the larger unit cell but also by reducing the gap between periodic structures.

TABLE 4.2.2
CCRR Structure Linewidth and Spacing Variations for $5\text{ mm} \times 5\text{ mm}$ Unit Cell

Case	Linewidth, (lw) [mm]	Spacing, (sp) [mm]	Resonant frequency [GHz]	Tx, S21 [dB]
1	1.0	2.0	49.59	-51.78
2	1.0	1.0	42.32	-53.71
3	0.5	1.0	30.68	-52.50
4	0.5	0.5	24.28	-54.55
5	0.25	0.5	20.66	-51.91
6	0.125	0.25	16.37	-49.30
7	0.0625	0.125	14.07	-46.45
8	0.03125	0.0625	12.54	-44.31

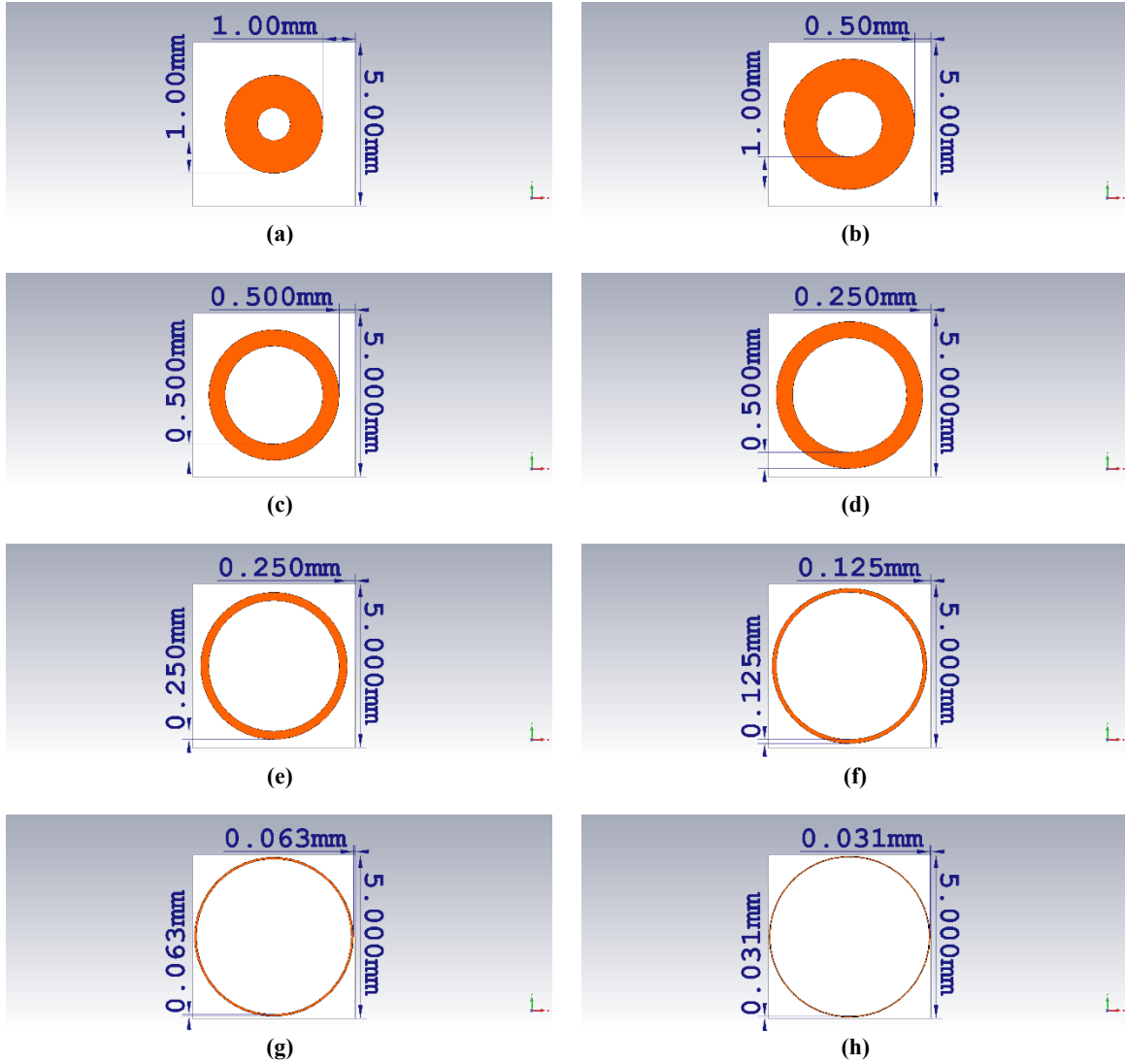


Fig. 4.2.4: CRR Designs for Unit Cell Size $5 \text{ mm} \times 5 \text{ mm}$ Varying Parameters for Linewidth, lw , and Spacing Between Periodic Structures, sp : (a). $lw = 1 \text{ mm}$, $sp = 2 \text{ mm}$, (b). $lw = 1 \text{ mm}$, $sp = 1 \text{ mm}$, (c). $lw = 0.5 \text{ mm}$, $sp = 1 \text{ mm}$, (d). $lw = 0.5 \text{ mm}$, $sp = 0.5 \text{ mm}$, (e). $lw = 0.25 \text{ mm}$, $sp = 0.5 \text{ mm}$, (f). $lw = 0.125 \text{ mm}$, $sp = 0.25 \text{ mm}$, (g). $lw = 0.0625 \text{ mm}$, $sp = 0.125 \text{ mm}$, (h). $lw = 0.03125 \text{ mm}$, $sp = 0.0625 \text{ mm}$.

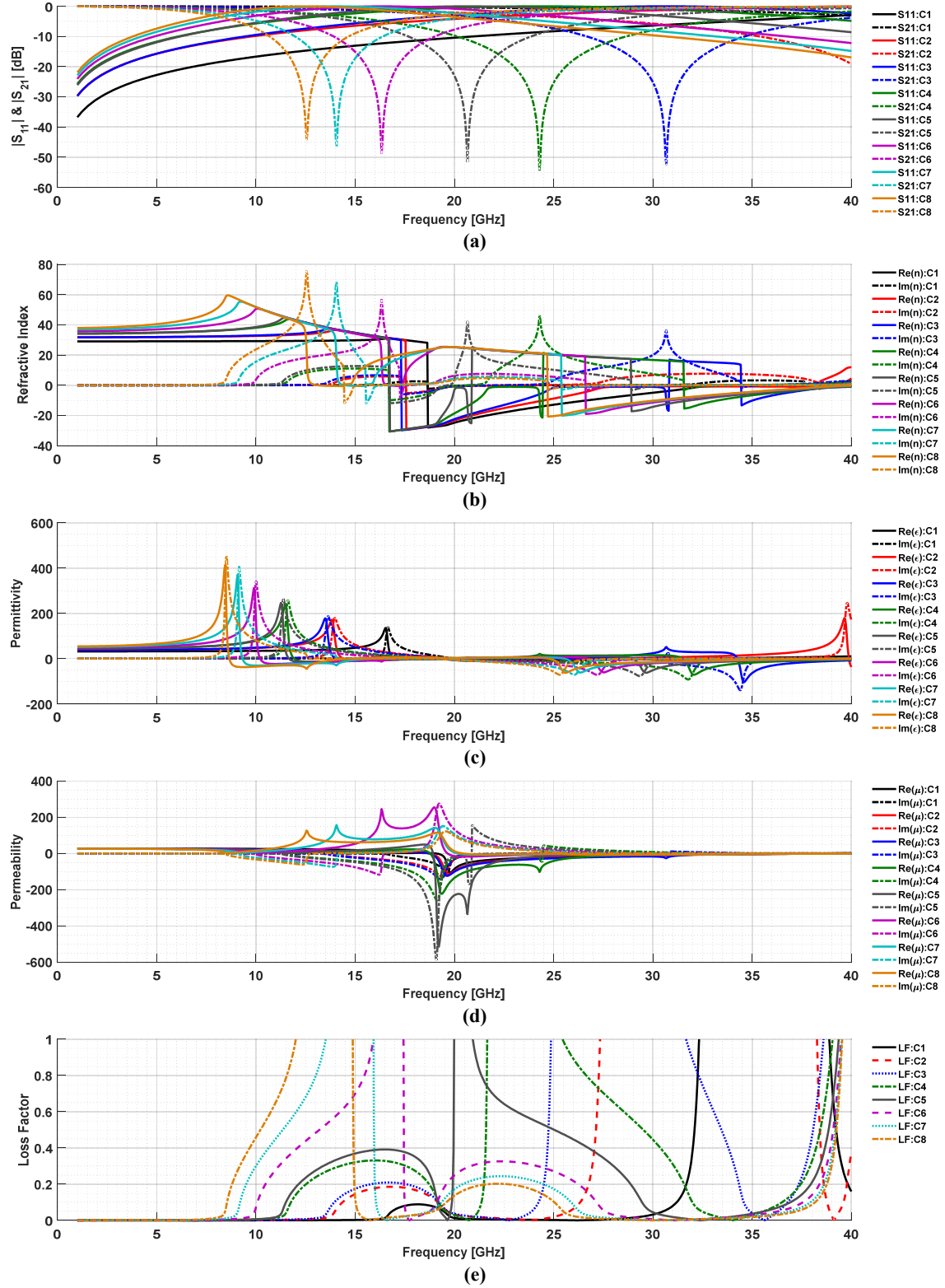


Fig. 4.2.5: Effective Parameter Extraction from Simulation Results for 5 mm × 5 mm Unit Cell CCRR Cases 1 – 8: (a) S -Parameters, (b) Real and imaginary parts of n , (c) Real and imaginary parts of ϵ , (d) Real and imaginary parts of μ , (e) Loss Factor.

4.2.3: CCRRs in 6 mm × 6 mm Unit Cell

The third unit cell size studied is the 6 mm × 6 mm. Table 4.2.3 shows the results for the eight cases employed for the CCRR structure and Fig. 4.2.6 is a visual representation acquired from synthesized structures via CST. In addition to Cases 3 – 8, we may now appreciate the magnetic resonances of Cases 1 and 2 depicted in Fig. 4.2.7(a) in red and black dotted lines, respectively.

TABLE 4.2.3
CCRR Structure Linewidth and Spacing Variations for 6 mm × 6 mm Unit Cell

Case	Linewidth, (lw) [mm]	Spacing, (sp) [mm]	Resonant frequency [GHz]	Tx, S21 [dB]
1	1.0	2.0	38.87	-54.17
2	1.0	1.0	30.09	-56.01
3	0.5	1.0	22.49	-53.60
4	0.5	0.5	18.63	-55.44
5	0.25	0.5	16.21	-48.74
6	0.125	0.25	13.36	-48.12
7	0.0625	0.125	11.99	-45.38
8	0.03125	0.0625	11.01	-43.77

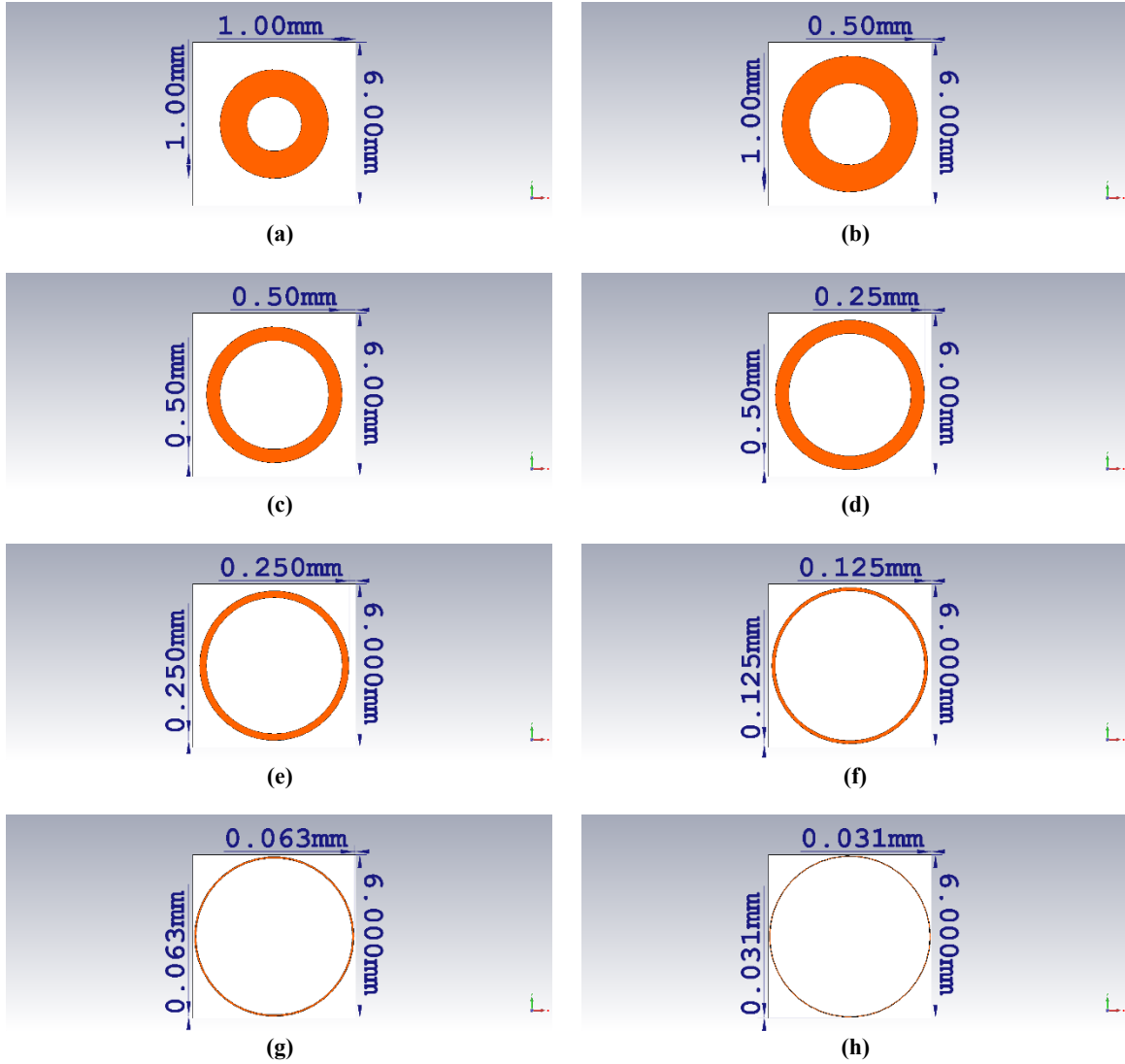


Fig. 4.2.6: CCRR Designs for Unit Cell Size $6 \text{ mm} \times 6 \text{ mm}$ Varying Parameters for Linewidth, lw , and Spacing Between Periodic Structures, sp : (a). $lw = 1 \text{ mm}$, $sp = 2 \text{ mm}$, (b). $lw = 1 \text{ mm}$, $sp = 1 \text{ mm}$, (c). $lw = 0.5 \text{ mm}$, $sp = 1 \text{ mm}$, (d). $lw = 0.5 \text{ mm}$, $sp = 0.5 \text{ mm}$, (e). $lw = 0.25 \text{ mm}$, $sp = 0.5 \text{ mm}$, (f). $lw = 0.125 \text{ mm}$, $sp = 0.25 \text{ mm}$, (g). $lw = 0.0625 \text{ mm}$, $sp = 0.125 \text{ mm}$, (h). $lw = 0.03125 \text{ mm}$, $sp = 0.0625 \text{ mm}$.

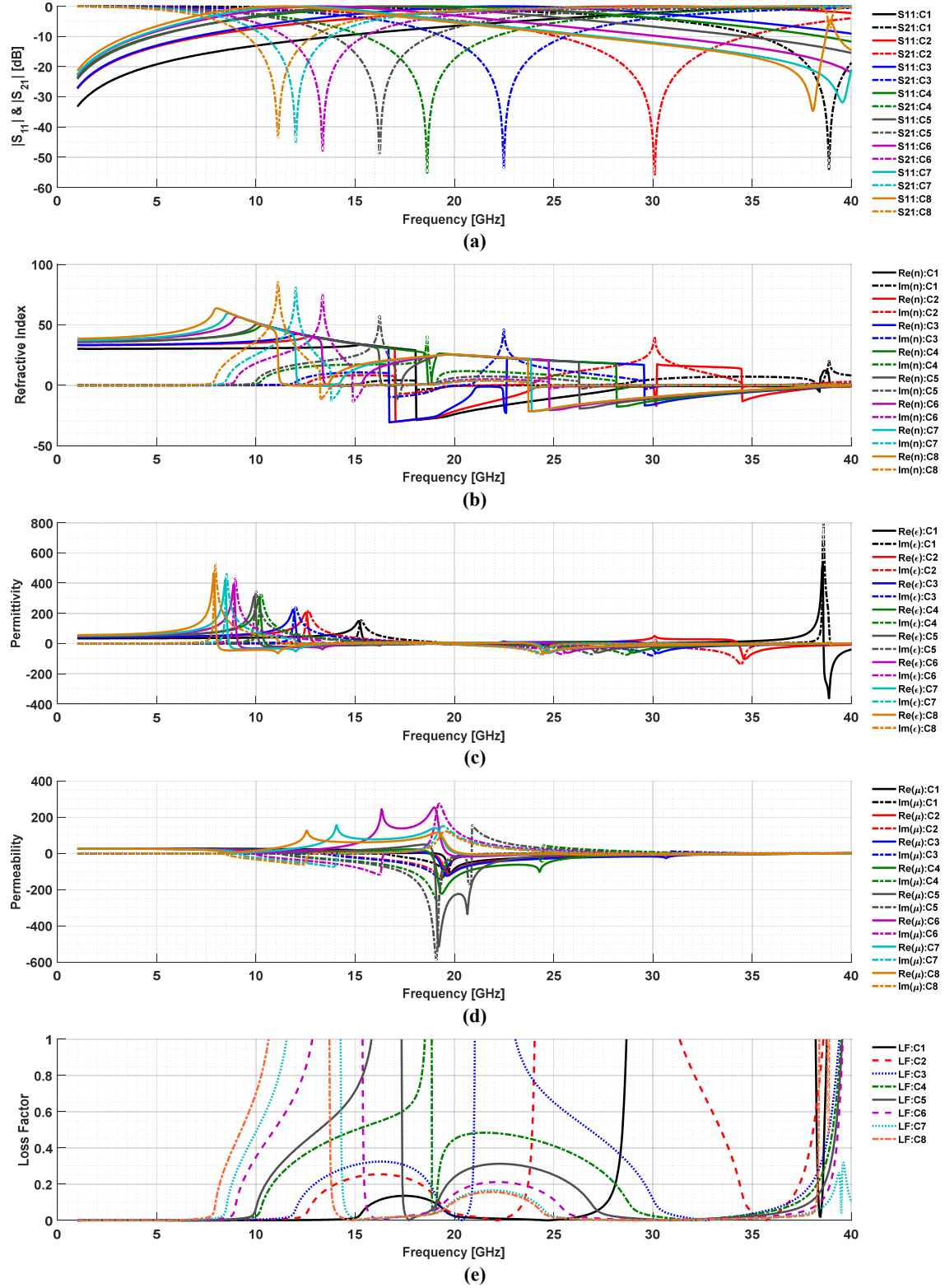


Fig. 4.2.7: Effective Parameter Extraction from Simulation Results for 6 mm × 6 mm Unit Cell CCRR Cases 1 – 8: (a) S -Parameters, (b) Real and imaginary parts of n , (c) Real and imaginary parts of ϵ , (d) Real and imaginary parts of μ , (e) Loss Factor.

4.2.4: CCRRs in 8 mm × 8 mm Unit Cell

The fourth and final case of CCRR unit cell sizes studied is the 8 mm × 8 mm. Table 4.2.4 shows the results for the eight cases employed for the CCRR structure and Fig. 4.2.8 is a visual representation acquired from synthesized structures via CST. In Fig. 4.2.7(a) we may notice that the magnetic resonances of Cases 1 – 8 have all shifted down the frequency spectra compared with the frequency response of CCRR in unit cell size 6 mm × 6 mm.

TABLE 4.2.4
CCRR Structure Linewidth and Spacing Variations for 8 mm × 8 mm Unit Cell

Case	Linewidth, (<i>lw</i>) [mm]	Spacing, (<i>sp</i>) [mm]	Resonant frequency [GHz]	Tx, S21 [dB]
1	1.0	2.0	23.15	-54.87
2	1.0	1.0	18.20	-55.83
3	0.5	1.0	14.96	-52.31
4	0.5	0.5	12.66	-51.25
5	0.25	0.5	11.26	-51.30
6	0.125	0.25	9.31	-47.31
7	0.0625	0.125	8.61	-44.36
8	0.03125	0.0625	8.02	-41.53

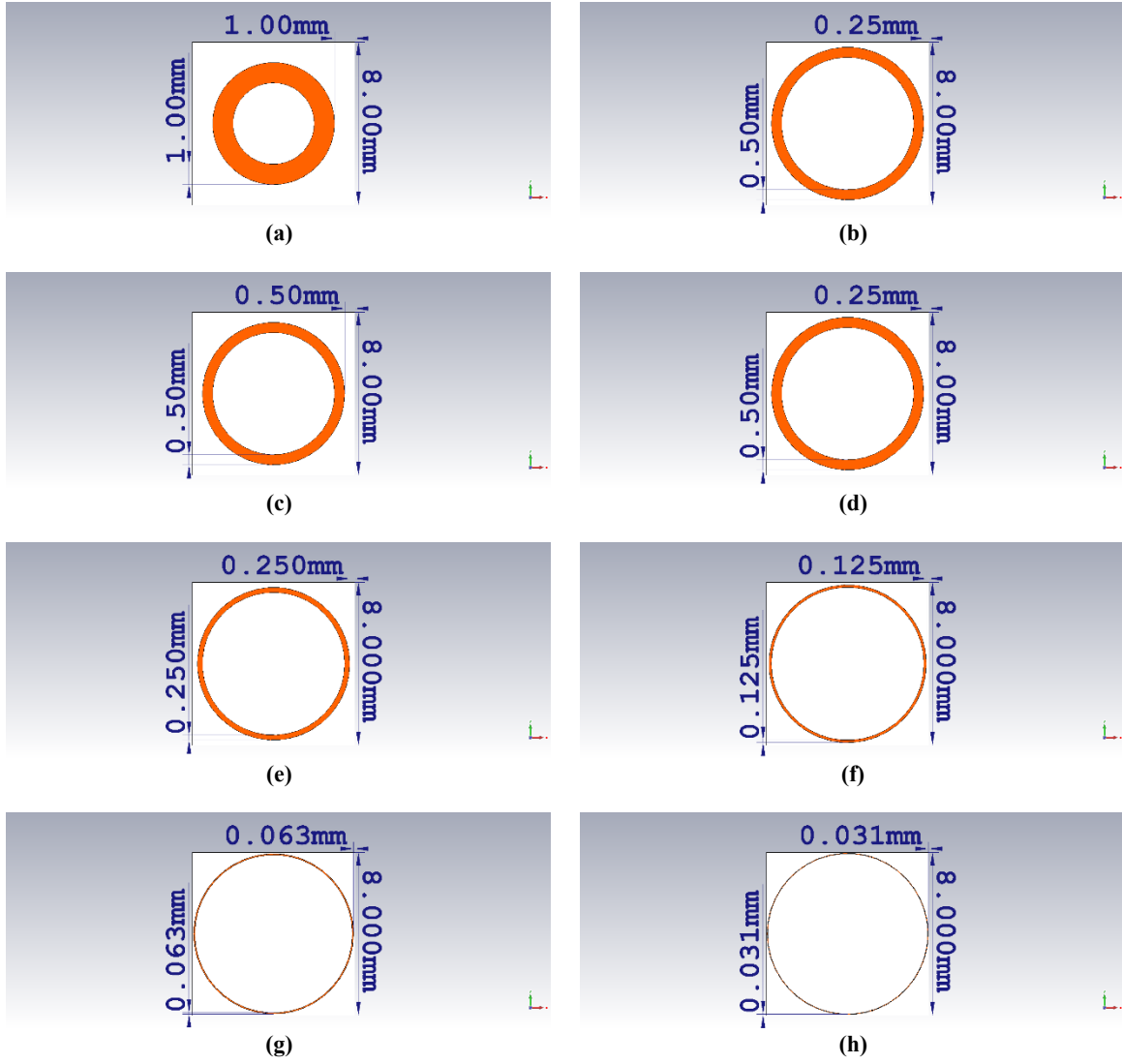


Fig. 4.2.8: CCRR Designs for Unit Cell Size $8 \text{ mm} \times 8 \text{ mm}$ Varying Parameters for Linewidth, lw , and Spacing Between Periodic Structures, sp : (a). $lw = 1 \text{ mm}$, $sp = 2 \text{ mm}$, (b). $lw = 1 \text{ mm}$, $sp = 1 \text{ mm}$, (c). $lw = 0.5 \text{ mm}$, $sp = 1 \text{ mm}$, (d). $lw = 0.5 \text{ mm}$, $sp = 0.5 \text{ mm}$, (e). $lw = 0.25 \text{ mm}$, $sp = 0.5 \text{ mm}$, (f). $lw = 0.125 \text{ mm}$, $sp = 0.25 \text{ mm}$, (g). $lw = 0.0625 \text{ mm}$, $sp = 0.125 \text{ mm}$, (h). $lw = 0.03125 \text{ mm}$, $sp = 0.0625 \text{ mm}$.

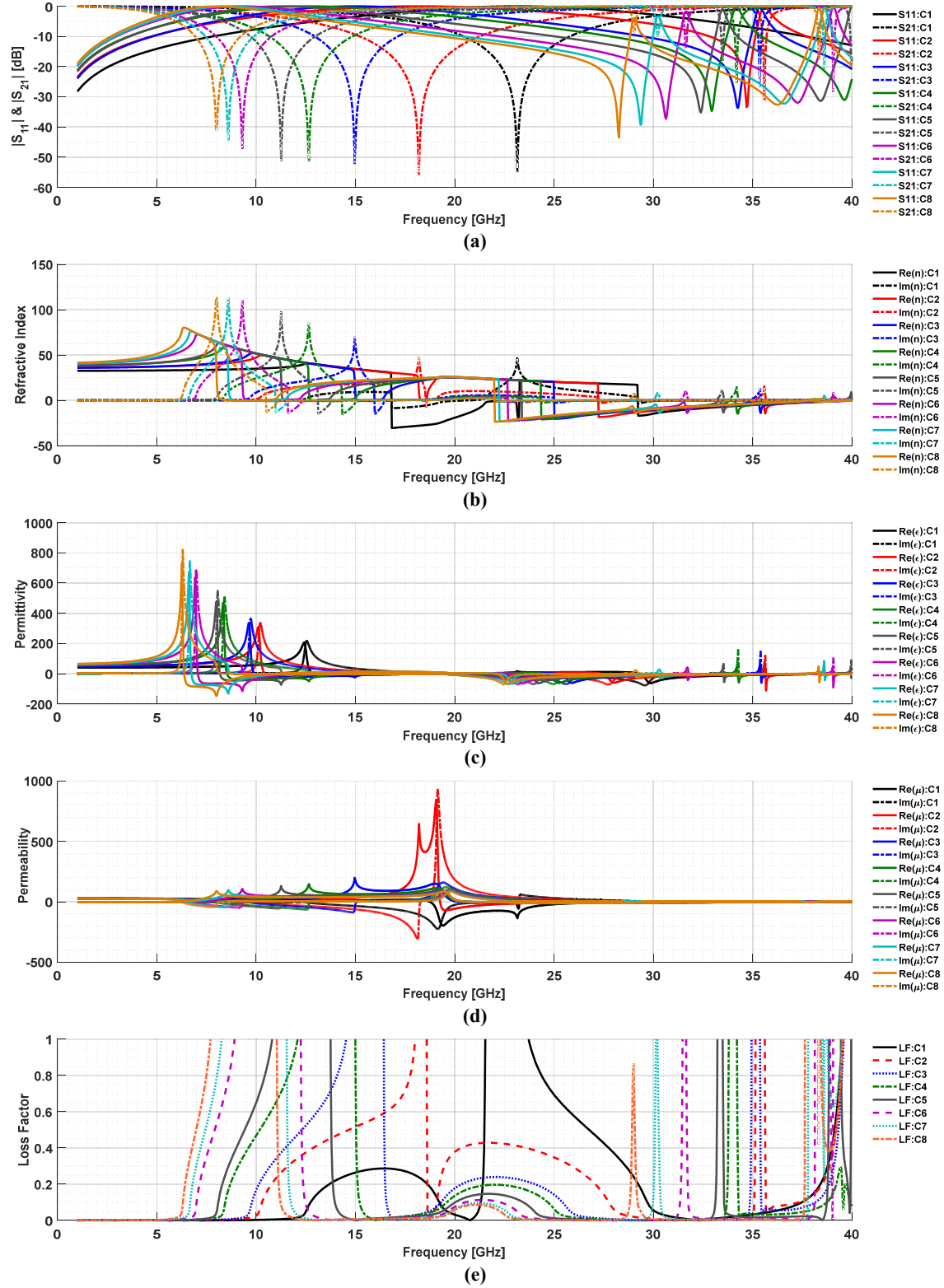


Fig. 4.2.9: Effective Parameter Extraction from Simulation Results for 8 mm × 8 mm Unit Cell CCRR Cases 1–8: (a) S -Parameters, (b) Real and imaginary parts of n , (c) Real and imaginary parts of ϵ , (d) Real and imaginary parts of μ , (e) Loss Factor.

4.3: Split-Ring Resonator (SRR) Structures

The second structure studied is the circular split-ring resonator (CSRR), seen in Fig.

4.3.2. From Smith's research of the SRR [4.5], by introducing a *split* within the ring one may control and vary the magnetic resonance response of the MTM, shown in Fig. 4.3.1(a).

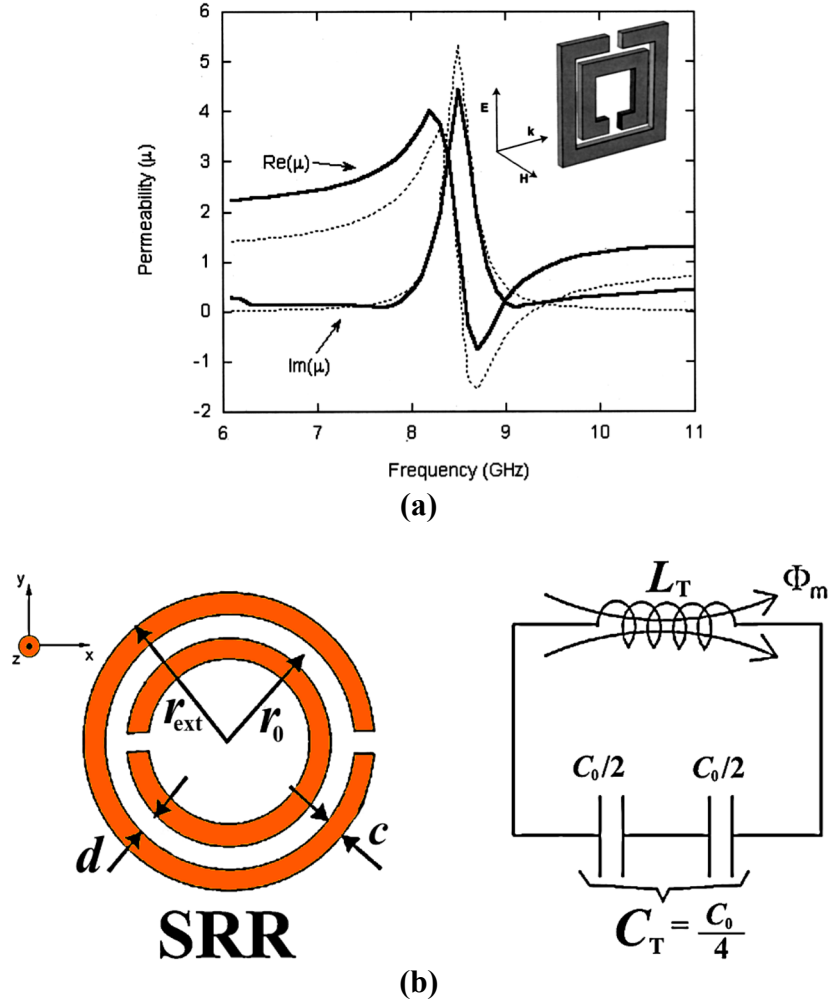


Fig. 4.3.1: SRR Reference Studies on EM Response and Equivalent-Circuit: (a) From [4.5], permeability as a function of frequency for a square SRR. Solid dark lines correspond to the real and imaginary parts of the permeability determined using transfer matrix method (TMM) from simulation data; (b) From [4.6], SRR topology (left) and its equivalent-circuit model (right) (ohmic losses can be taken into account by including series resistance in the model).

The approach introduced by Baena et. al. [4.6] is very useful when considering a design involving SRRs. In their research, they demonstrate that SRRs behave as an LC resonator [4.7]. Fig. 4.3.1(b) shows the geometrical topology and equivalent-circuit model. In this figure, C_T denotes the total capacitance between the rings, i.e., $C_T = 2\pi r_0 C_{pul}$, where C_{pul} is the per-unit length capacitance between the rings that compose the resonator. $C_0/2$ represents the capacitance related to each individual SRR halve. L_T denotes the SRR total self-inductance, which can be approximated to the inductance of a single ring with averaged radius of the resonator r_0 and width of the ring c . By considering the equivalent-circuit model of the SRR, its resonance frequency f_0 can be calculated as:

$$f_0 = \frac{1}{\sqrt{L_T C_T}} \quad (4.1)$$

Furthermore, by varying the length of the split in conjunction with the spacing between periodic structures and the linewidth of the MTM, we are able to tailor the resonant frequency to the desired location along the frequency domain as the SRR controls the magnetic resonance, thus controlling the direction of the \mathbf{H} field for magnetic coupling.

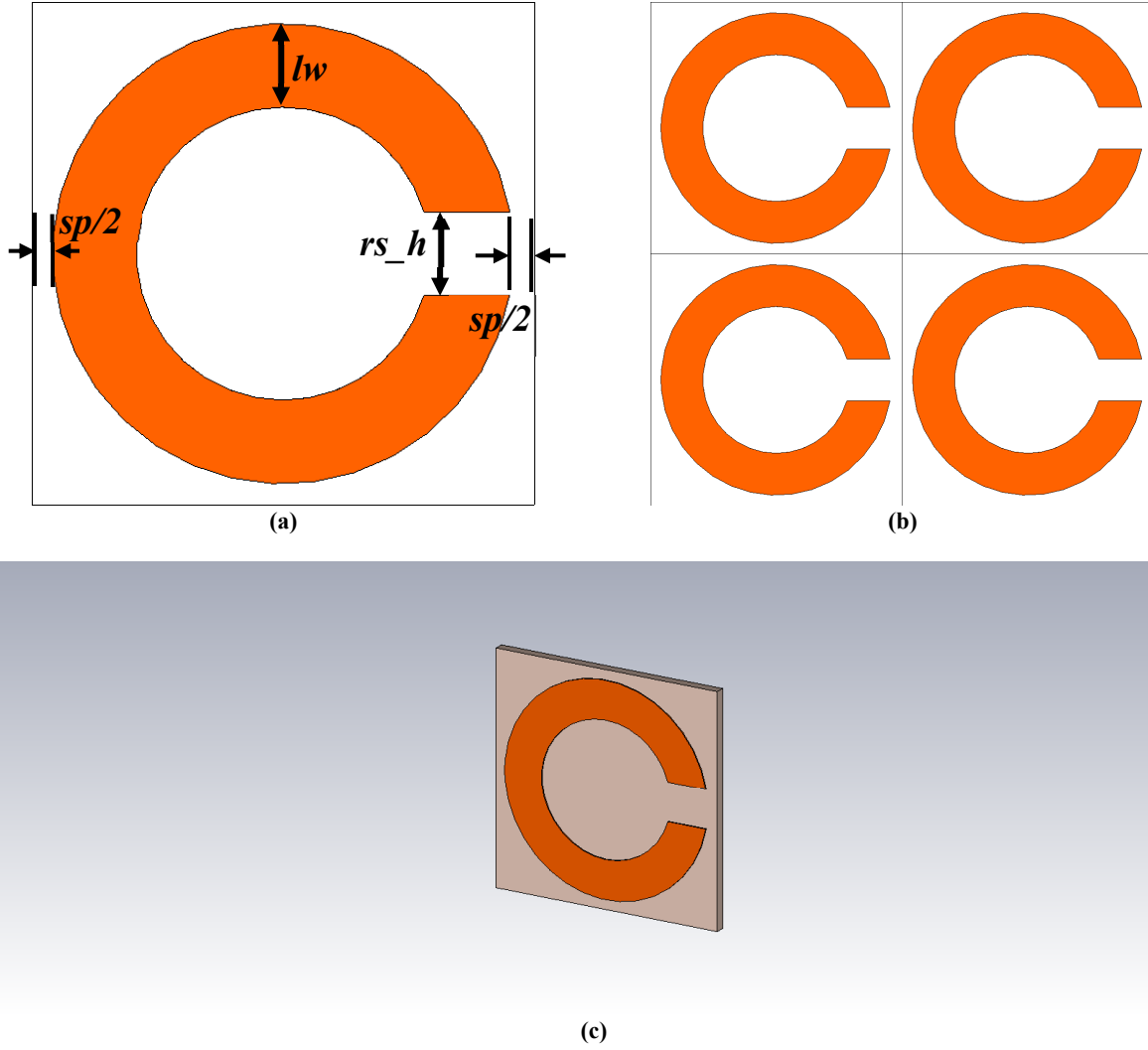


Fig. 4.3.2: Circular Split Ring Resonator (CSRR) Metamaterial Structure: (a). CSRR in unit cell with varying parameters linewidth of structure lw , spacing between periodic structures sp , and horizontal ring split rs_h , (b). Representation of periodic array with 2×2 CSRR unit cells, (c). CSRR in unit cell with propagation in the z -direction.

For this study, two unit cell sizes were explored: $6 \text{ mm} \times 6 \text{ mm}$ and $8 \text{ mm} \times 8 \text{ mm}$. A variable was introduced which controlled the horizontal ring split inclusion, rs_h . With fabrication in mind, the spacing between structures, sp , would be fixed to 0.5 mm for three linewidth variations: 1.0 mm , 0.5 mm and 0.25 mm . For each linewidth variation, four cases were explored in the following order:

i) $\text{Ring Split} = \text{Linewidth} \times 2$

ii) $\text{Ring Split} = \text{Linewidth}$

iii) $\text{Ring Split} = \text{Linewidth} / 2$

iv) $\text{Ring Split} = \text{Linewidth} / 4$

A total of twelve cases were studied for the CSRR. Just as in the CCRR cases, the simulation boundary frequency range selected for the CSRR was selected to be from 0 – 40 GHz for the 6 mm \times 6 mm study and 0 – 30 GHz for the 8 mm \times 8 mm. Table 4.3.1 reflects the results obtained for the 6 mm \times 6 mm. One noticeable and desirable difference between the CCRR and the CSRR is that in the case of the CSRR we may observe a response similar to a bandpass filter while we only see a single resonance with the CCRR. Exploiting this behavior of the CSRR will prove useful to our EM MTM design.

4.3.1: SRRs in 6 mm × 6 mm Unit Cell

TABLE 4.3.1
Ring Split Variations for 6 mm × 6 mm Unit Cell (Boundary Range: 1 – 40 GHz)

(lw) [mm]	(sp) [mm]	(rs_h) [mm]	RF1 [GHz]	S21 _{RF1} [dB]	RF3 [GHz]	S11 _{RF3} [dB]	RF2 [GHz]	S21 _{RF2} [dB]
1.0	0.5	2.0	11.06	-43.22	18.63	-44.90	32.98	-48.10
1.0	0.5	1.0	10.05	-46.22	14.85	-48.84	31.69	-49.84
1.0	0.5	0.5	9.39	-45.14	12.86	-55.86	30.95	-53.54
1.0	0.5	0.25	8.84	-39.60	11.53	-62.85	30.37	-54.58
0.5	0.5	1.0	8.80	-41.81	13.91	-50.46	26.97	-46.31
0.5	0.5	0.5	8.41	-43.15	12.35	-56.18	25.96	-49.73
0.5	0.5	0.25	8.10	-35.76	11.30	-54.98	25.18	-50.82
0.5	0.5	0.125	7.83	-40.08	10.56	-54.17	24.56	-48.82
0.25	0.5	0.5	7.98	-37.82	12.23	-54.70	23.82	-45.68
0.25	0.5	0.25	7.67	-39.23	11.18	-55.97	22.92	-46.83
0.25	0.5	0.125	7.55	-38.30	10.71	-56.08	22.61	-47.38
0.25	0.5	0.0625	7.40	-36.48	10.20	-59.36	22.22	-47.85

For clarity, the simulation results for all twelve cases were divided into two figures with Fig. 4.3.3 showing the simulation results of Cases 1 – 8, while Fig. 4.3.4 shows the remaining Cases 9 – 12 for the 6 mm × 6 mm unit cell size. Similarly, Fig. 4.3.5 and Fig. 4.3.6 depict the results for Cases 1 – 8 and Cases 9 – 12 respectively. We may observe that as the linewidth and the horizontal split are decreased, the passband resonance is equally shifted to a lower frequency.

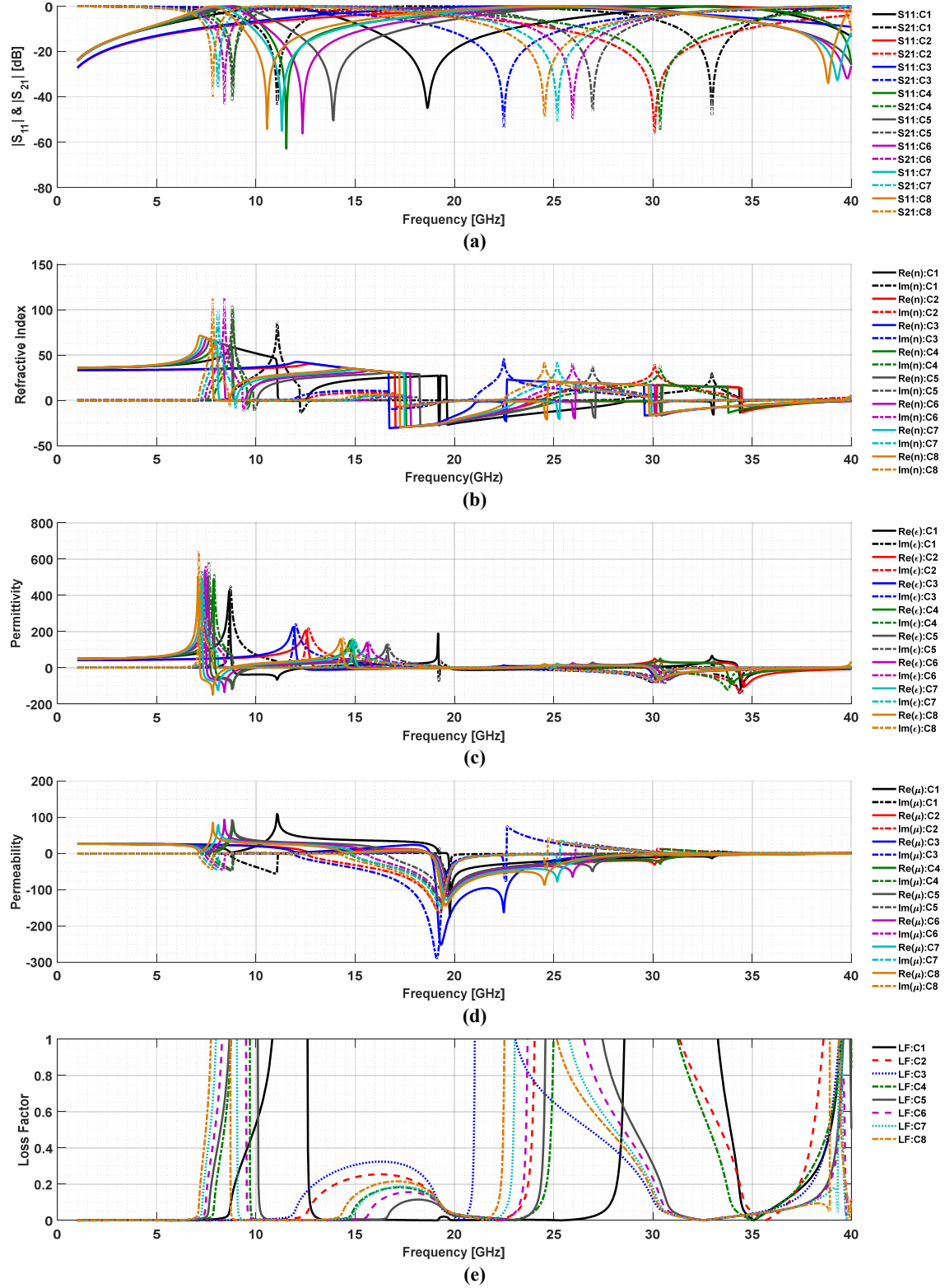


Fig. 4.3.3: Effective Parameter Extraction from Simulation Results for 6 mm × 6 mm Unit Cell CSRR Cases 1–8: (a) S -Parameters, (b) Real and imaginary parts of n , (c) Real and imaginary parts of ϵ , (d) Real and imaginary parts of μ , (e) Loss Factor.

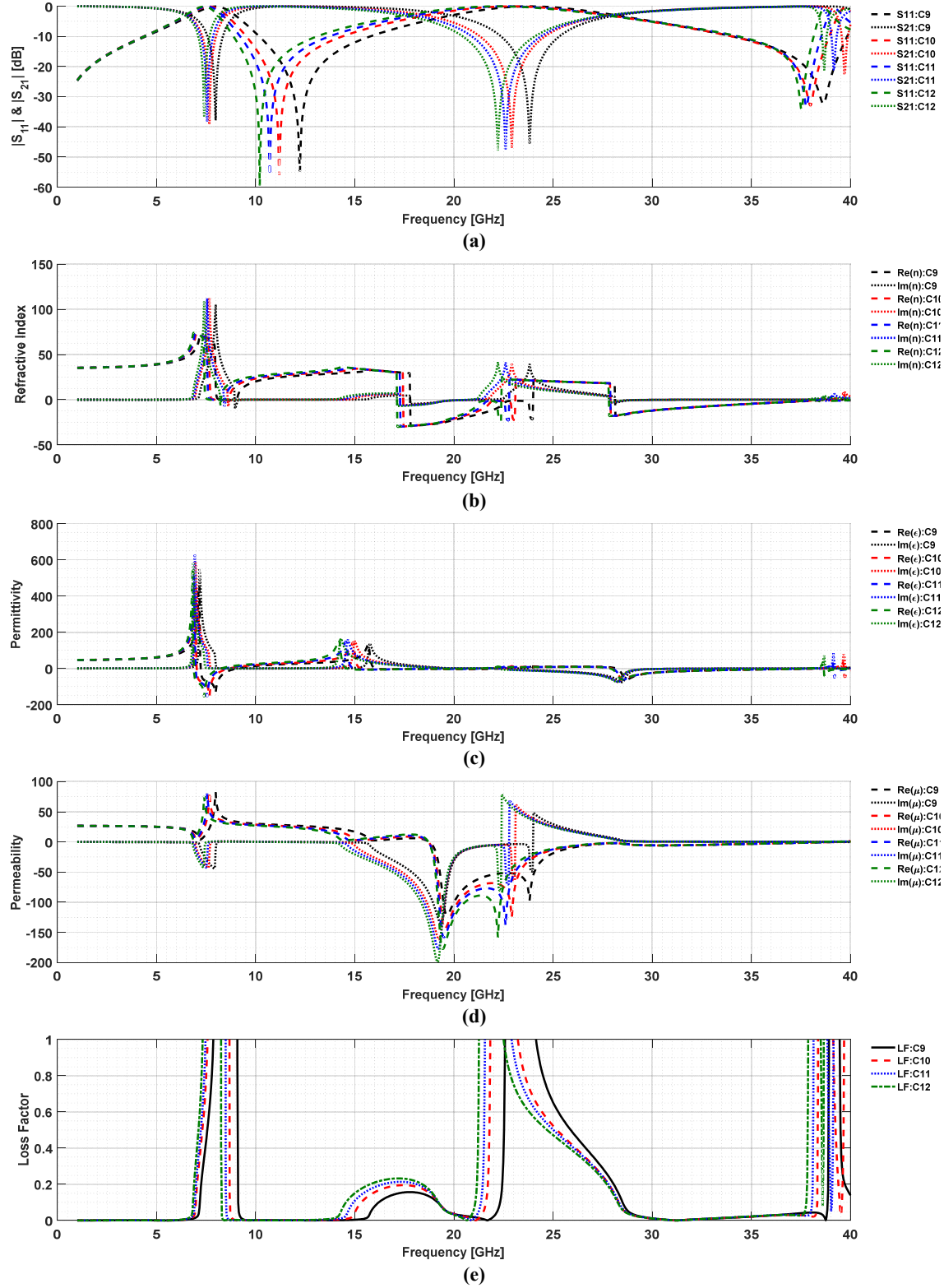


Fig. 4.3.4: Effective Parameter Extraction from Simulation Results for 6 mm × 6 mm Unit Cell CSRR Cases 9–12: (a) S -Parameters, (b) Real and imaginary parts of n , (c) Real and imaginary parts of ϵ , (d) Real and imaginary parts of μ , (e) Loss Factor.

4.3.2: SRRs in 8 mm × 8 mm Unit Cell

TABLE 4.3.2
Ring Split Variations for 8 mm × 8 mm Unit Cell (Boundary Range: 1 – 30 GHz)

(lw) [mm]	(sp) [mm]	(rs_h) [mm]	RF1 [GHz]	S21_{RF1} [dB]	RF3 [GHz]	S11_{RF3} [dB]	RF2 [GHz]	S21_{RF2} [dB]
1.0	0.5	2.0	7.21	-42.3	11.9	-51.86	22.14	-48.34
1.0	0.5	1.0	6.77	-40.41	10.1	-55.78	21.16	-52.78
1.0	0.5	0.5	6.42	-45.36	9.00	-52.98	20.46	-51.04
1.0	0.5	0.25	6.13	-36.80	8.22	-48.82	19.97	-54.59
0.5	0.5	1.0	6.19	-40.24	9.79	-58.42	18.57	-46.08
0.5	0.5	0.5	5.99	-37.19	8.95	-52.70	17.94	-48.09
0.5	0.5	0.25	5.84	-38.83	8.31	-52.69	17.41	-48.66
0.5	0.5	0.125	5.61	-38.22	7.76	-54.60	16.86	-48.64
0.25	0.5	0.5	5.67	-37.04	8.71	-53.41	16.63	-45.39
0.25	0.5	0.25	5.61	-35.59	8.40	-65.35	16.43	-44.85
0.25	0.5	0.125	5.52	-38.46	8.02	-51.83	16.11	-46.53
0.25	0.5	0.0625	5.44	-36.17	7.70	-51.43	15.82	-45.48

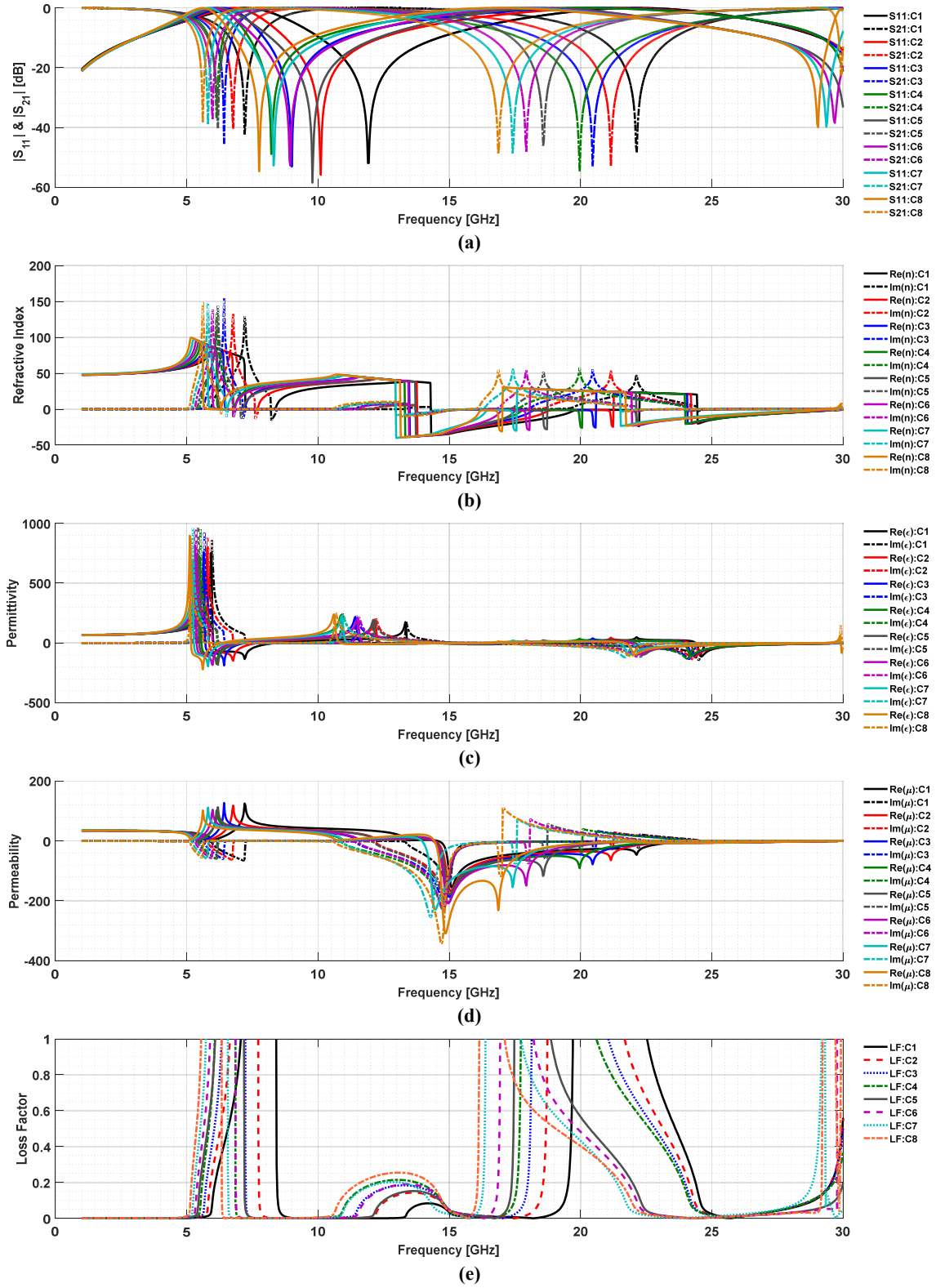


Fig. 4.3.5: Effective Parameter Extraction from Simulation Results for 8 mm × 8 mm Unit Cell CSRR Cases 1–8: (a) S -Parameters, (b) Real and imaginary parts of n , (c) Real and imaginary parts of ϵ , (d) Real and imaginary parts of μ , (e) Loss Factor.

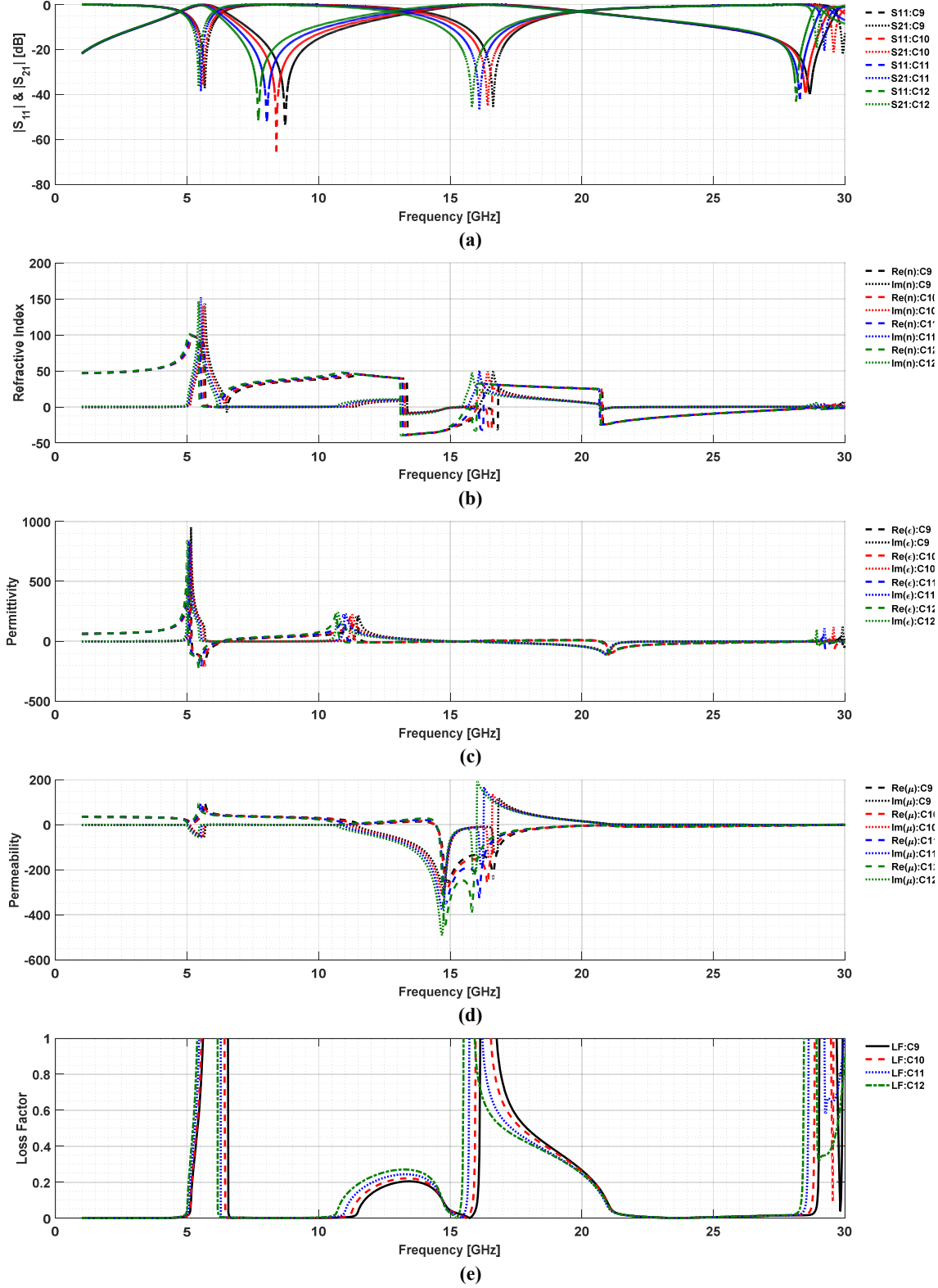


Fig. 4.3.6: Effective Parameter Extraction from Simulation Results for 8 mm × 8 mm Unit Cell CSRR Cases 9–12: (a) S-Parameters, (b) Real and imaginary parts of n , (c) Real and imaginary parts of ϵ , (d) Real and imaginary parts of μ , (e) Loss Factor.

Given these preliminary results, Case 2 ($lw = 1.0$ mm, $sp = 0.25$ mm, $rs_h = 1.0$ mm) and Case 3 ($lw = 1.0$ mm, $sp = 0.25$ mm, $rs_h = 0.5$ mm) were selected for further investigation for our next structures, the “Omega” and “Omeganet”, due to the passband resonance in the X -band frequency range and for potential manufacturability.

4.4: Omeganet and Omega MTM Structures

The following study builds up on the foundation from previous CCRR and CSRRs structures. Now that we know how to control the resonance from the CSRR study, with this structure we are introducing a wire-type inclusion into the CSRR forming the Greek letter “ Ω ” shape. Omega and Omeganet MTM structures are shown in Fig. 4.4.3. These structures were simulated on to different substrates: Arlon Di 880 (lossy) and FR4 (lossy), with substrate thickness of 0.254 mm and 1.6 mm respectively.

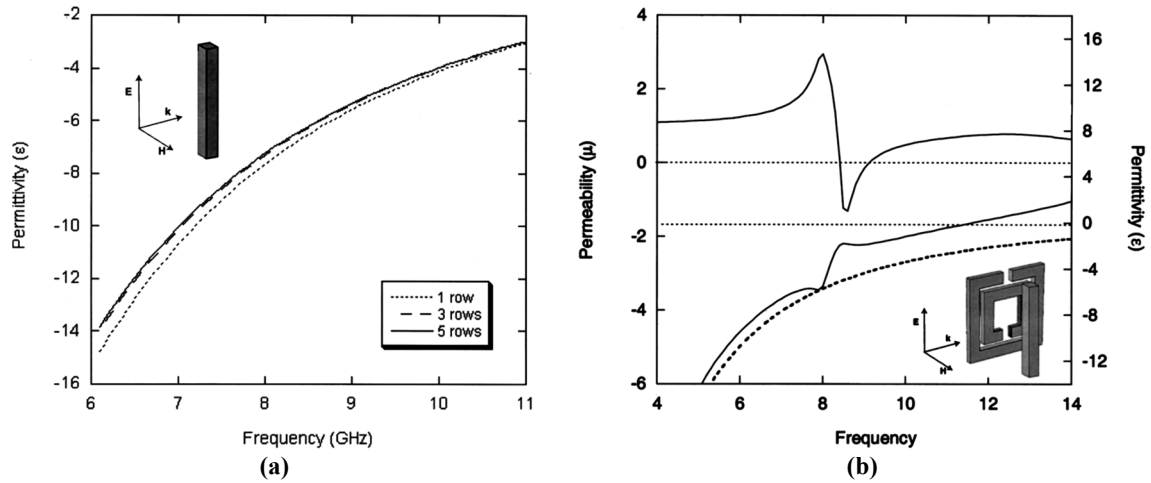


Fig. 4.4.1: From [4.5], (a). Real part of the permittivity as a function of frequency for a wire medium, (b). Real part of permeability and real part of permittivity as a function of frequency for the combination of SRR/wire medium.

From Smith’s research of the SRR, besides introducing a *split* within the ring to control and vary the magnetic resonance response of the MTM, introducing a wire medium, shown in

Fig. 4.4.1(a), will allow for the control of the permittivity, thus tailoring the direction of the \mathbf{E} field for electric coupling. The permittivity is related with stopband while the permeability is related with the magnetic resonance. By combining a wire medium with a SRR medium, shown in Fig. 4.4.1(b), one may now overlap the stopband and the resonance [4.5], and thus control the refractive index as the latter is directly related to the permeability and permittivity by the relationship $n = \sqrt{\epsilon\mu}$. For the rest of this study we refer to this wire medium as the *Epsilon*-controlling bar (ECB).

From Kafesaki's research on fishnet structures and their variations, it was concluded that after observing the surface current distribution and magnetic and electric fields for a particular fishnet structure, one may draw a simple effective LC circuit model describing the fishnet structure close to the magnetic resonance regime. Fig. 4.4.2 shows such a model for a single unit cell of a fishnet structure. Fig. 4.4.2(a) provides a schematic representation directly related to the geometry of the structure with L_s and L_n representing the inductance arising for the loop-like currents at the slabs and the necks, respectively and C the capacitance between the two slabs. By considering and taking into account the periodicity of the MTM structure, the equivalence of the points A (B) and A' (B'), the model from Fig. 4.4.2(a) can be transformed into a simpler and more appropriate model that may be employed in calculations shown in Fig. 4.4.2(b) [4.9].

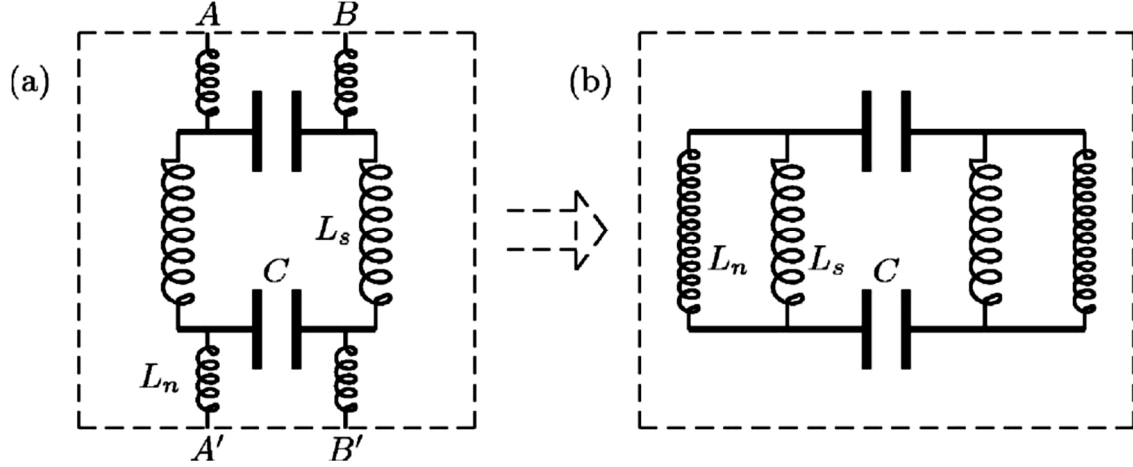


Fig 4.4.2: From [4.9], an LC circuit model for the fishnet structure where L_s and L_n denote the loop inductances at the slabs and necks, respectively, and C the capacitance of the structure.

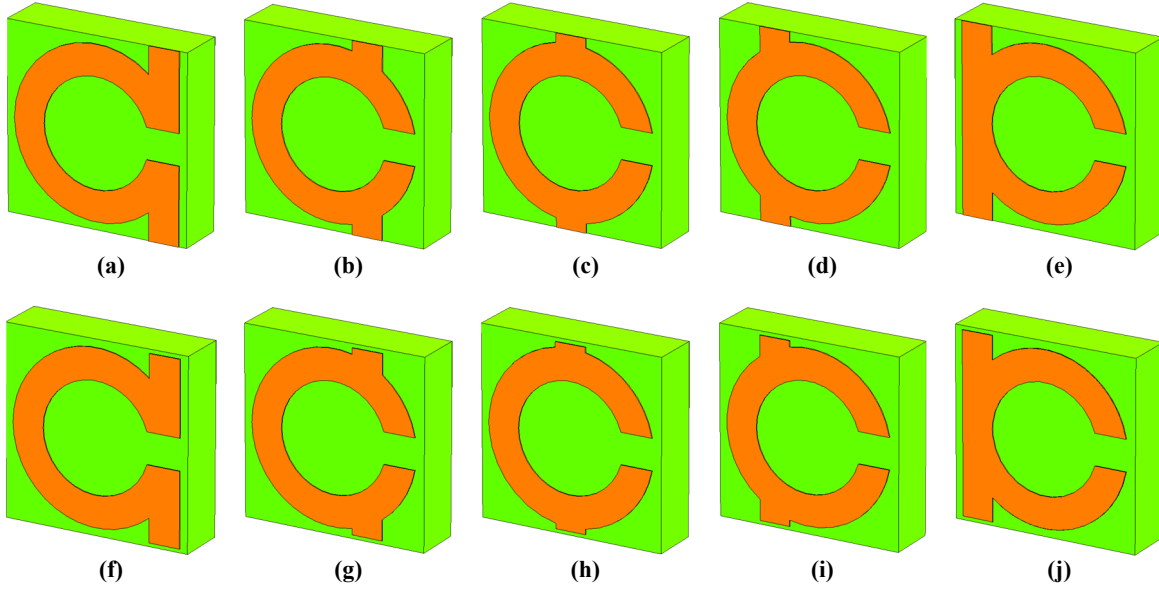


Fig. 4.4.3: Progression of the 2D Omeganets (top row) and Omegas (bottom row) in FR-4 Substrate varying the location of the ECB: (a). Omeganet Right ECB Case, (b). Omeganet Right-Middle ECB Case, (c). Omeganet Middle ECB Case, (d). Omeganet Left-Middle ECB Case, (e). Omeganet Left ECB Case, (f). Omega Right ECB Case, (g). Omega Right-Middle ECB Case, (h). Omega Middle ECB Case, (i). Omega Left-Middle ECB Case, (j). Omega Left ECB Case.

In Fig. 4.4.3, we demonstrate that the idea behind this study is to vary the location of the *Epsilon*-controlling bar (ECB) and observe the EM response on a single 2D layer, improving from the structure in 4.4.1(b), which has the wire medium as a separate layer from the SRR. By

varying dx and thus shifting the ECB, the L_s and L_n for the Omeganets, related to the equivalent-circuit model from Fig. 4.4.2, will also change. It is important to note that for the Omega structures, Figs. 4.4.3(f) – 4.4.3(j), there will be an added capacitance at the top and bottom of their respective ECBs as these are not continuous in the periodic sense.

4.4.1: Omeganet MTM Structures Over Arlon Di 880 (lossy) Substrate

The first case studied for Omegas is with the Arlon Di 880 substrate. For both cases of the substrates, the dimensions regarding the Omega structures remain the same with the exception of the substrate thickness. Here with the Arlon Di 880, a thinner substrate thickness of 0.254 mm was employed with permittivity $\epsilon_r = 2.2$, loss tangent $\tan\delta = 0.0009$ and the MTM structure's copper thickness equal to 0.03 mm. Fig. 4.4.4 depicts the unit cell for each of the two structures. On the left side is the Omeganet MTM structure, Fig. 4.4.4(a), which has its name for the fact that the periodic structure is continually connected with the wire-type inclusion as seen with other fishnet MTM designs. On the right hand is the Omega structure which is disconnected from the periodic unit cells. As in the CSRR case, we may see the spacing between structures as a variable and the horizontal ring split as well. From the preliminary results obtained from the CSRR investigation, the spacing between structures of length 0.5mm was selected, and remains fixed for the rest of the Omegas study. However, there is an additional variable introduced, dx , which is the location of the ECB. This variable is bounded the outer radius of the Omega structure. There were five cases investigated by varying dx into a possibility of five equally spaced locations along the x -axis: Right ($dx = 2.25$), Right-Middle ($dx = 1.125$), Middle ($dx = 0$), Left-Middle ($dx = -1.125$) and Left ($dx = -2.25$).

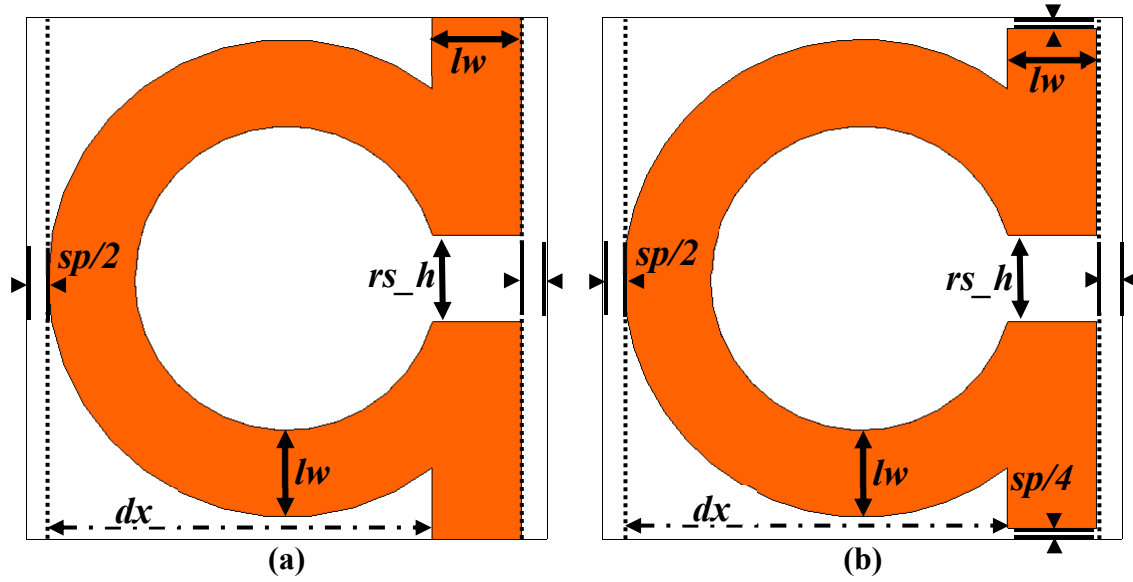


Fig. 4.4.4: Modified CSRR 6 mm \times 6 mm “Omega” Metamaterial Structure with the *Epsilon*-Controlling Bar (ECB) at the Right Side Position with parameters $lw = rs_h = 1$ mm, $sp = 0.5$ mm, and variable dx : (a) Omeganet Unit Cell with Connected End-to-End ECB, (b) Omega Unit Cell with Disconnected ECB.

Figs. 4.4.5 – 4.4.9 correspond to the 2D Omeganets in Arlon Di 880 substrate varying the location of the ECB from the *right* sub-structure case, where $dx = 2.25$ to the *left* sub-structure case, where $dx = -2.25$, for a total of five cases. As discussed earlier, one may observe that as dx is shifted to a different location, the length of the top and bottom of the ECBs will change with respect to the periodic MTM structures.

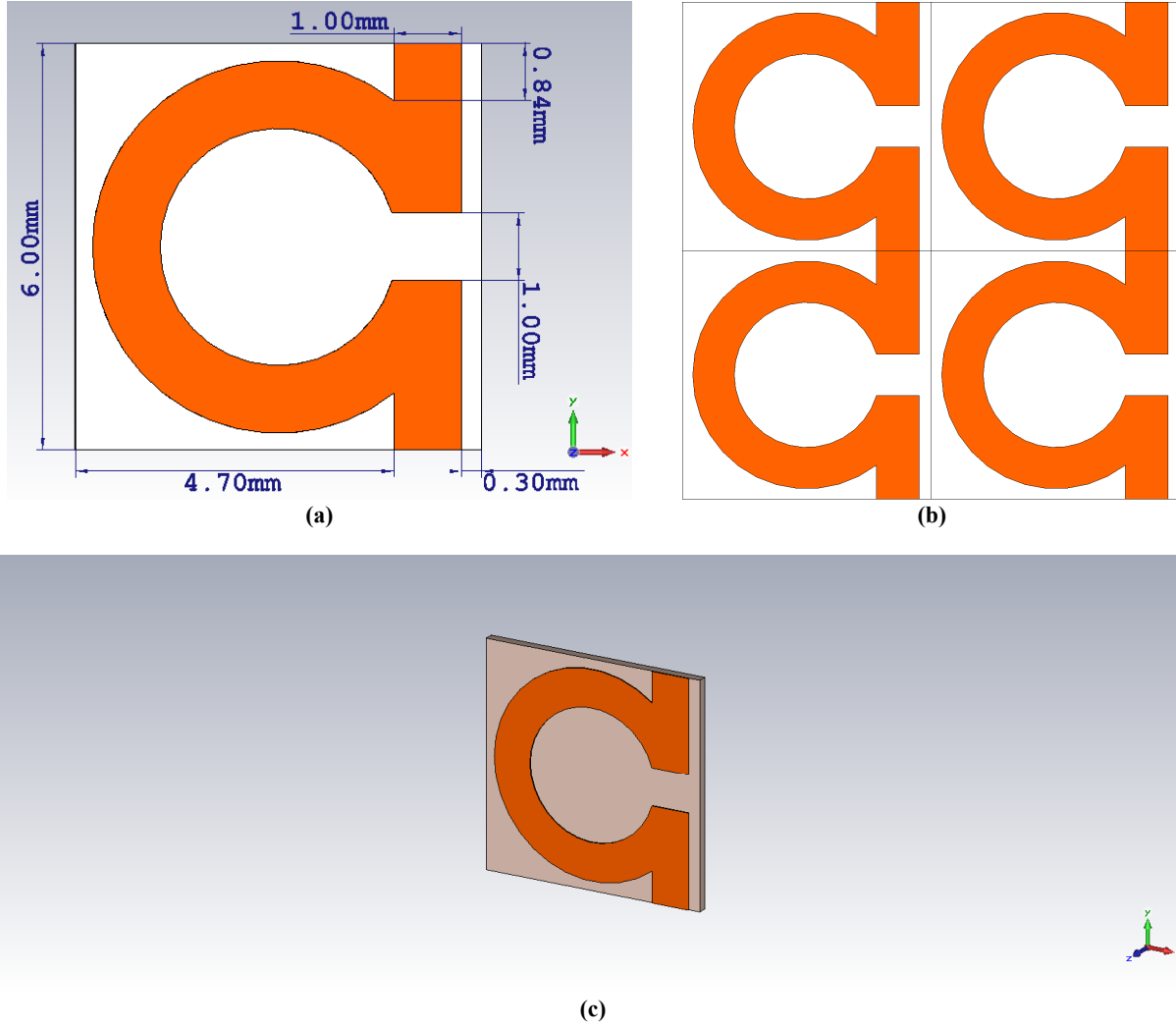


Fig. 4.4.5: Omeganet MTM Structure in $6 \text{ mm} \times 6 \text{ mm}$ Unit Cell Size: (a). Omeganet Structure displaying the design dimensions in unit cell with fixed parameters linewidth, $lw = 1.0 \text{ mm}$, spacing between structures, $sp = 0.5 \text{ mm}$, and the ECB is located on the Right case ($dx = 2.25$), (b). Representation of periodic array with 2×2 Omeganet unit cells, (c). Omeganet Structure in Unit Cell with propagation in the z -direction.

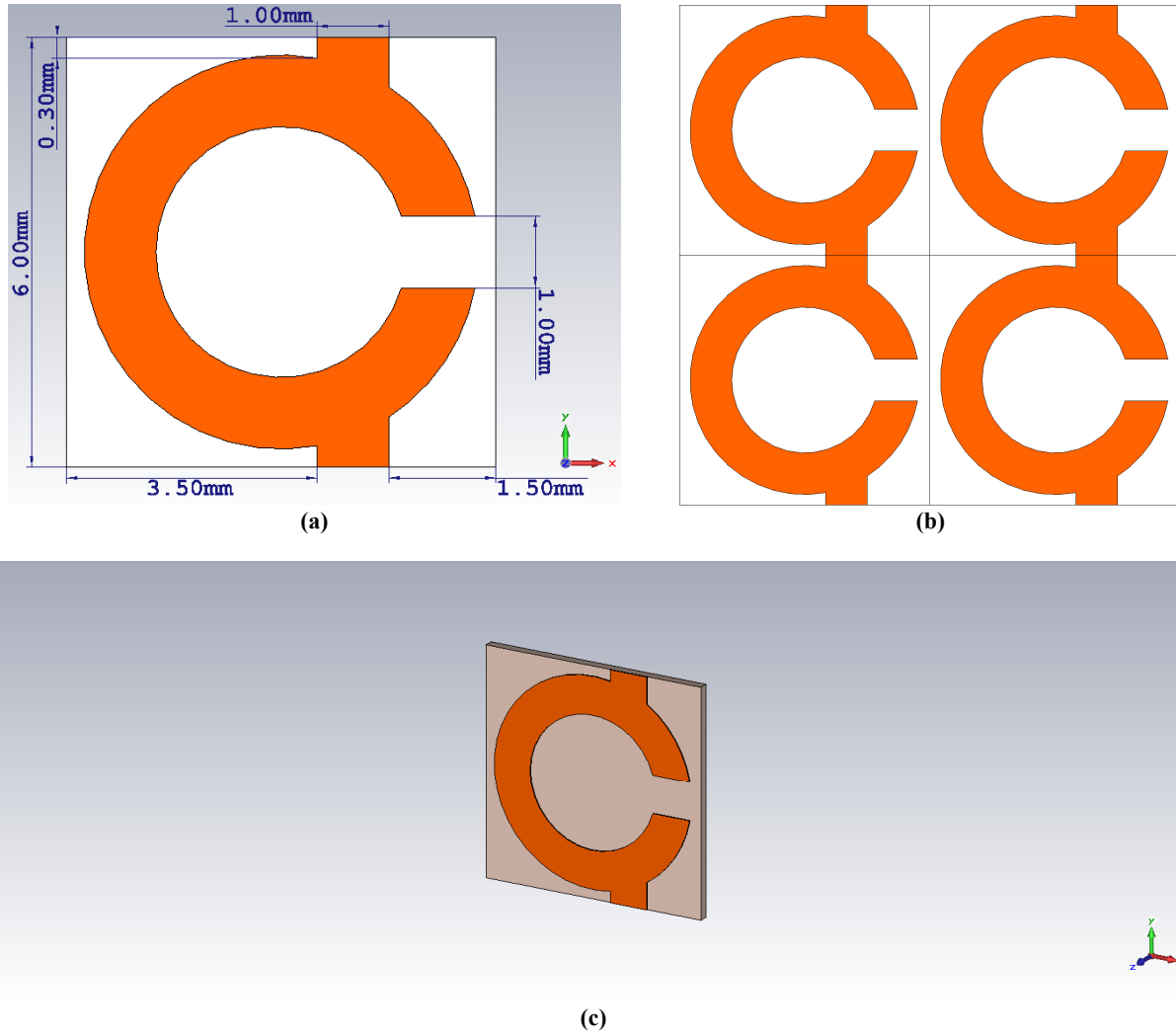


Fig. 4.4.6: Omeganet MTM Structure in $6\text{ mm} \times 6\text{ mm}$ Unit Cell Size: (a). Omeganet Structure displaying the design dimensions in unit cell with fixed parameters linewidth, $l_w = 1.0\text{ mm}$, spacing between structures, $sp = 0.5\text{ mm}$, and the ECB is located on the Right-Middle case ($dx = 1.125$), (b). Representation of periodic array with 2×2 Omeganet unit cells, (c). Omeganet Structure in Unit Cell with propagation in the z -direction.

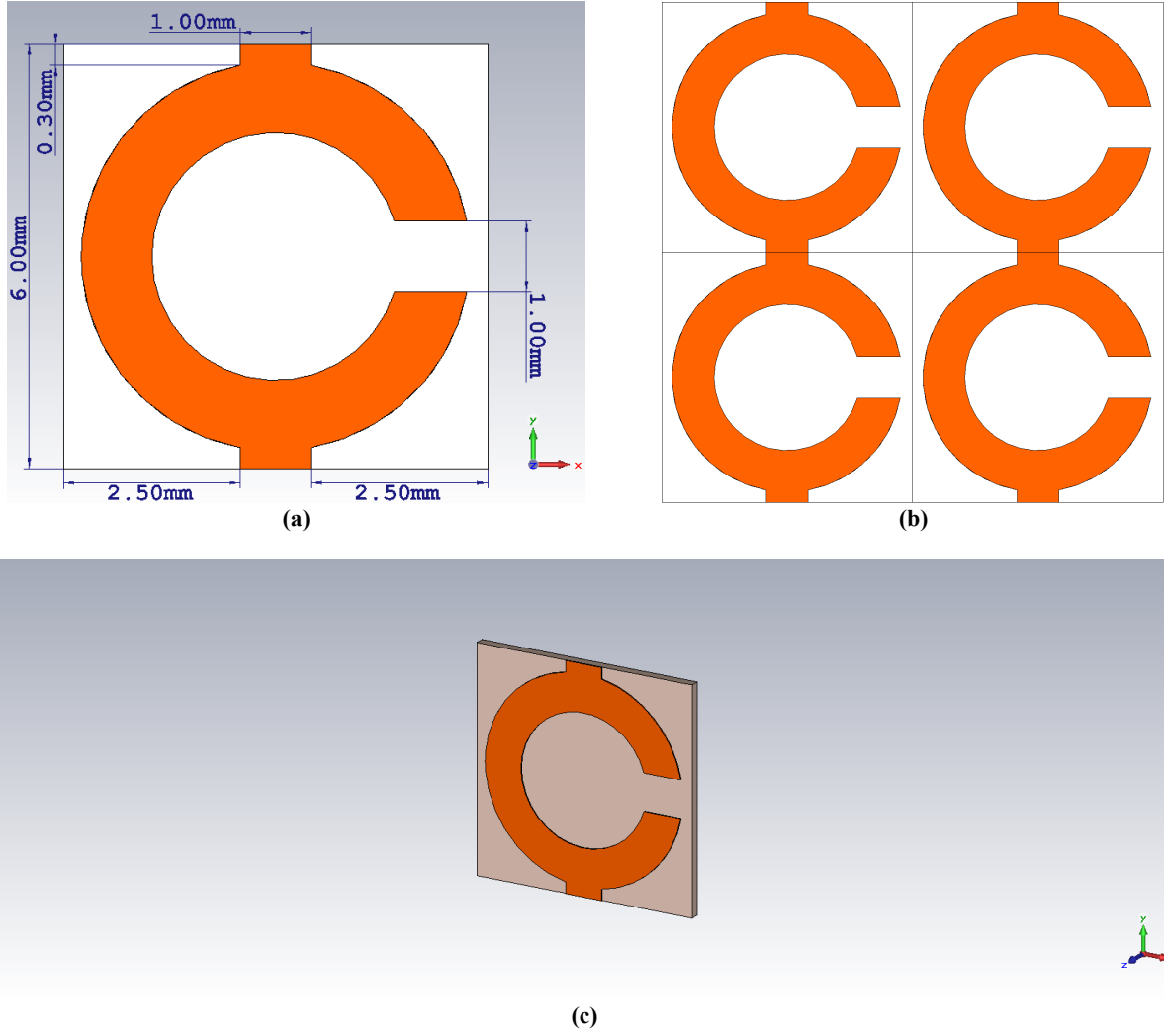
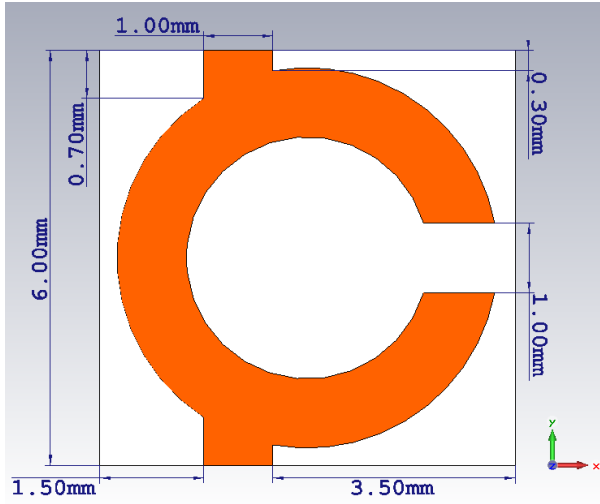
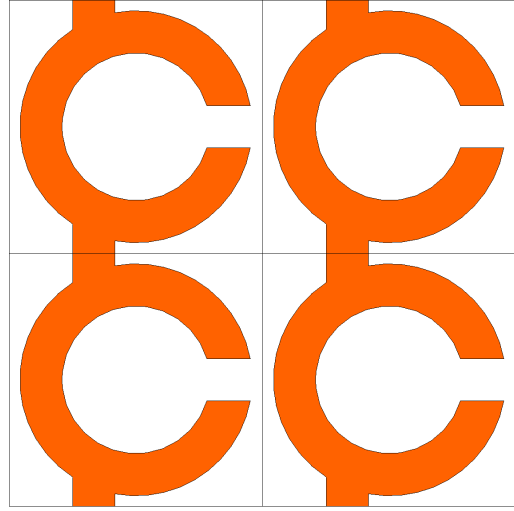


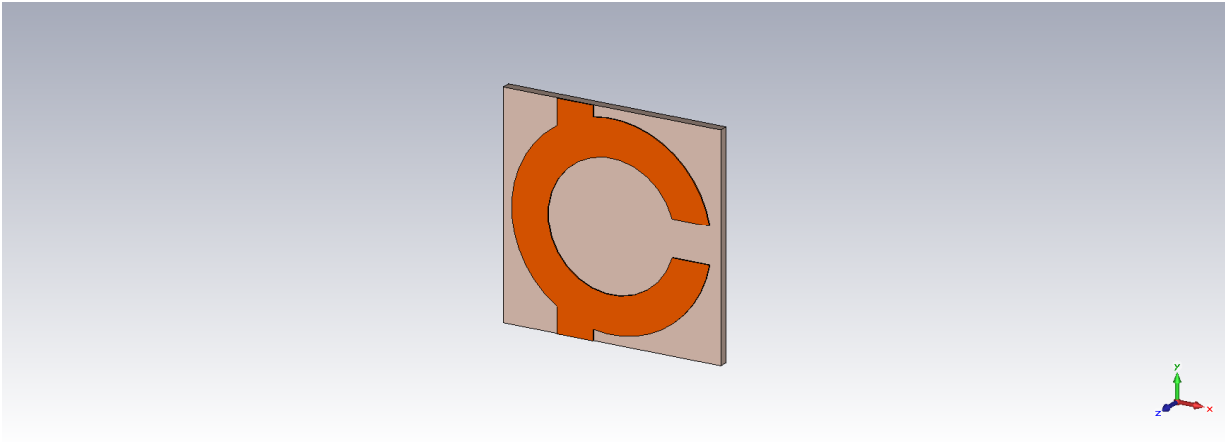
Fig. 4.4.7: Omeganet MTM Structure in $6\text{ mm} \times 6\text{ mm}$ Unit Cell Size: (a). Omeganet Structure displaying the design dimensions in unit cell with fixed parameters linewidth, $l_w = 1.0\text{ mm}$, spacing between structures, $sp = 0.5\text{ mm}$, and the ECB is located on the Middle case ($dx = 0$), (b). Representation of periodic array with 2×2 Omeganet unit cells, (c). Omeganet Structure in Unit Cell with propagation in the z -direction.



(a)



(b)



(c)

Fig. 4.4.8: Omeganet MTM Structure in $6\text{ mm} \times 6\text{ mm}$ Unit Cell Size: (a). Omeganet Structure displaying the design dimensions in unit cell with fixed parameters linewidth, $lw = 1.0\text{ mm}$, spacing between structures, $sp = 0.5\text{ mm}$, and the ECB is located on the Left-Middle case ($dx = -1.125$), (b). Representation of periodic array with 2×2 Omeganet unit cells, (c). Omeganet Structure in Unit Cell with propagation in the z -direction.

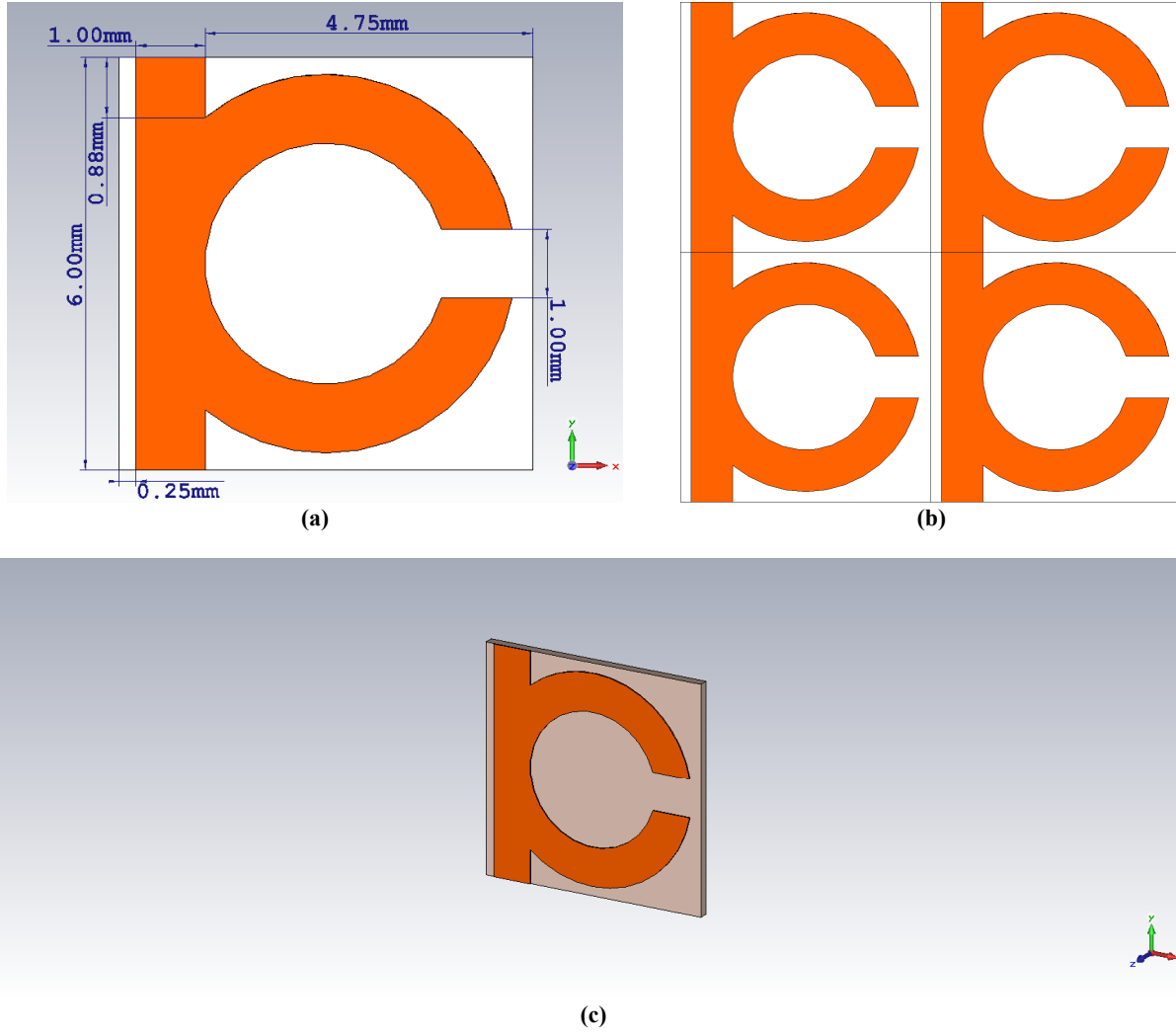


Fig. 4.4.9: Omeganet MTM Structure in $6\text{ mm} \times 6\text{ mm}$ Unit Cell Size: (a). Omeganet Structure displaying the design dimensions in unit cell with fixed parameters linewidth, $lw = 1.0\text{ mm}$, spacing between structures, $sp = 0.5\text{ mm}$, and the ECB is located on the Left case ($dx = -2.25$), (b). Representation of periodic array with 2×2 Omega unit cells, (c). Omeganet Structure in Unit Cell with propagation in the z -direction.

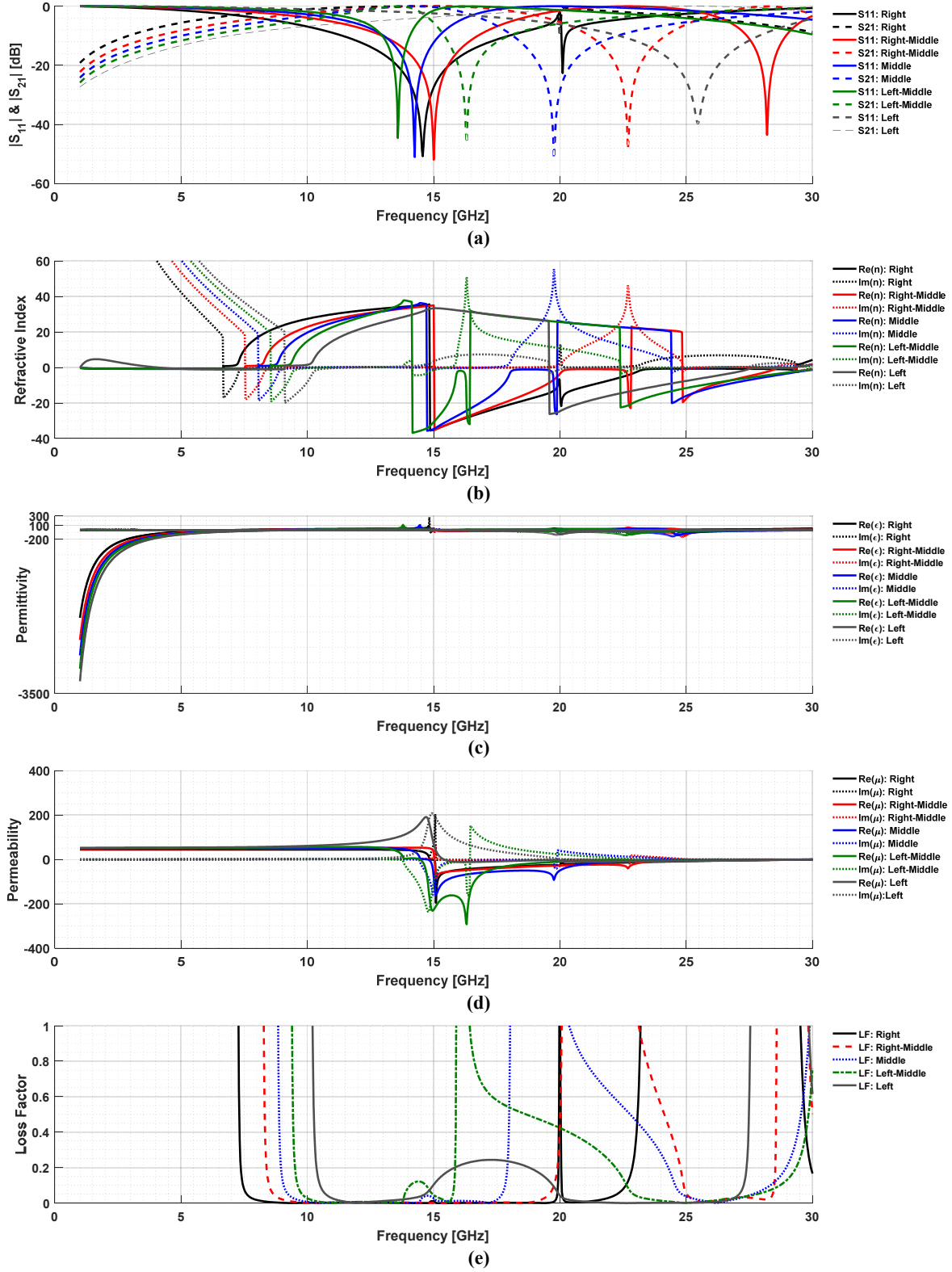


Fig. 4.4.10: Effective Parameter Extraction from Simulation Results for $6 \text{ mm} \times 6 \text{ mm}$ Unit Cell 2D Omeganet in Arlon Di 880 Substrate: (a) S -Parameters, (b) Real and imaginary parts of n , (c) Real and imaginary parts of ϵ , (d) Real and imaginary parts of μ , (e) Loss Factor.

TABLE 4.4.1
Summary of Low Loss NZRIM Bands for 2D Omeganet Structures in Arlon Di 880 Substrate

Sub-Structure	Frequency Range for $ n < 1.0$ [GHz]	Frequency Range where $ n < 1.0$ and $LF < 1$ [GHz]				Bandwidth (BW) [%]		Total BW where $ n < 1.0$ and $LF < 1$ [GHz]
		1st Band (From)	1st Band (To)	2nd Band (From)	2nd Band (To)	1st Band	2nd Band	Per Sub-Structure
Right	R1: 22.36-30	22.36	23.19	29.52	30.00	1.76	0.81	1.31
Right-Middle	R1: 27.2-30	27.20	28.58	29.83	30.00	2.36	0.28	1.55
Middle	R1: 28.01-29.89	28.01	29.89	-	-	3.05	-	1.88
Left-Middle	R1: 5-9.472	9.37	9.47	-	-	0.54	-	2.62
	R2: 27.48-30	27.48	30.00	-	-	4.03	-	
Left	R1: 10.21-10.31	10.21	10.31	-	-	0.48	-	2.02
	R2: 25.76-30	25.76	27.54	29.86	30.00	3.13	0.23	

Table 4.4.1 depicts the tabulation of low loss near-zero refractive index material (NZRIM) bands for the 2D Omeganet MTM structure studied from Figs. 4.4.5 to 4.4.9. R1 and R2, Range 1 and Range 2 respectively, denote that in some cases the sub-structures presented multi-range, multi-bands which satisfied the desired conditions of low loss and NNZ. For example, the case where the ECB is located on the left-middle position we may in Table 4.4.1 the lower Range 1 satisfied the condition $|n| < 1$ from 5.0 – 9.475 GHz. However, from this frequency range for NNZ, there is only a single band where the condition for loss factor < 1 is satisfied from 9.37 – 9.47 GHz. In contrast, we can observe that for the case where the ECB is located on the left position, the higher Range 2 where $|n| < 1$ extends from 25.76 – 30.0 GHz

while having two low loss bands: the first low loss band ranges from 25.76 – 27.54 GHz and the second low loss band ranges from 29.86 – 30.0 GHz. The percent bandwidth (BW) was computed utilizing the fractional bandwidth equation

$$BW[\%] = \frac{f_{high} - f_{low}}{f_{center}} \times 100. \quad (4.2)$$

The 1st low loss band of Range 2 thus has a computed percent BW of 3.13% while the second low loss band has a percent BW of 0.23 %. The last column on the right side of Table 4.4.1 shows the arithmetic sum of all bands for a sub-structure where $|n| < 1$ and $LF < 1$. In this case, for the *left* sub-structure we were just discussing the sum of all low loss NNZ bands for all ranges is 2.02 GHz.

4.4.2: Omega MTM Structures Over Arlon Di 880 (lossy) Substrate

Just as for the Omeganet study, all dimensions apply here for the Omega MTM structure in Arlon Di 880 substrate. However, the difference with this MTM structure than the Omeganet is the additional split introduced at the top and bottom ends of the *Epsilon*-controlling bar (ECB), rendering the structure a non-fishnet in the conventional sense as the structure stands disconnected from the other periodic unit cell structures. The split between vertical unit cells is fixed at a quarter of the horizontal spacing, such that it is equal to 0.25 mm.

Once more, the location of the ECB, dx , will be varied in the same fashion for five cases: Right ($dx = 2.25$), Right-Middle ($dx = 1.125$), Middle ($dx = 0$), Left-Middle ($dx = -1.125$) and Left ($dx = -2.25$). Figs. 4.4.11 – 4.4.15 correspond to the 2D Omegas in Arlon Di 880 substrate varying dx .

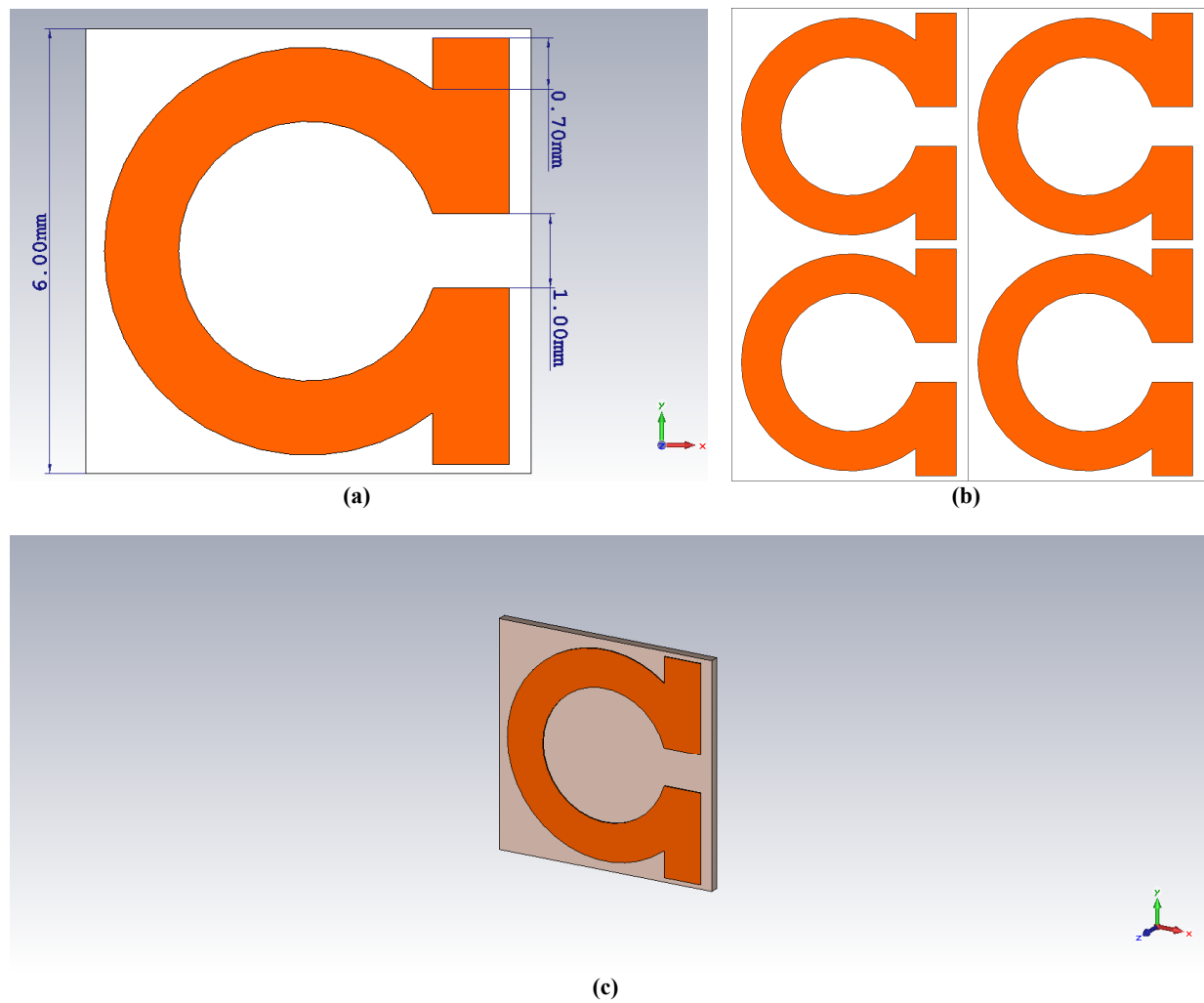


Fig. 4.4.11: Omega MTM Structure in $6 \text{ mm} \times 6 \text{ mm}$ Unit Cell Size: (a). Omega Structure displaying the design dimensions in unit cell with fixed parameters linewidth, $lw = 1.0 \text{ mm}$, spacing between structures, $sp = 0.5 \text{ mm}$, and the ECB is located on the Right case ($dx = 2.25$), (b). Representation of periodic array with 2×2 Omega unit cells, (c). Omega Structure in Unit Cell with propagation in the z -direction.

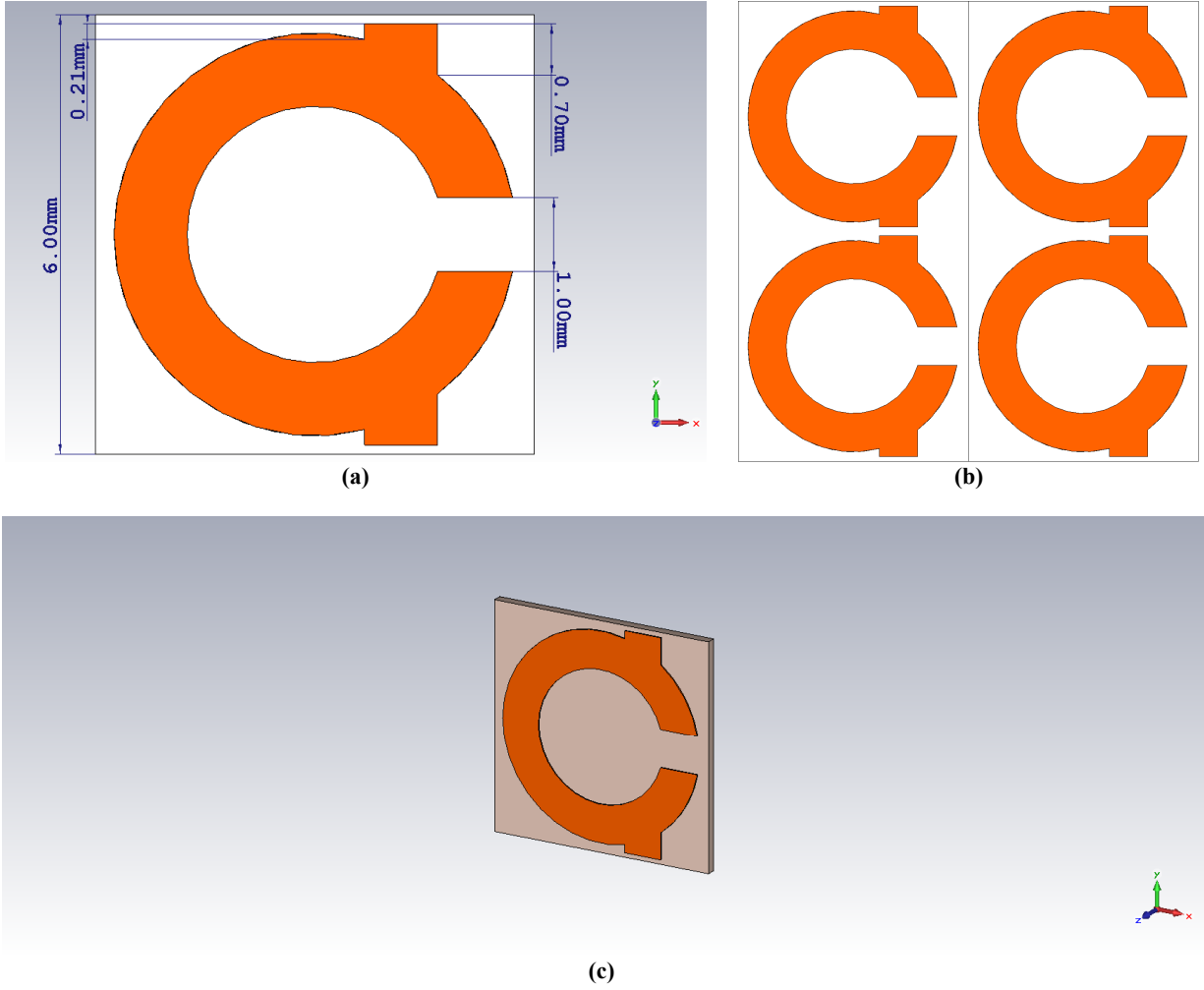


Fig. 4.4.12: Omega MTM Structure in $6\text{ mm} \times 6\text{ mm}$ Unit Cell Size: (a). Omega Structure displaying the design dimensions in unit cell with fixed parameters linewidth, $l_w = 1.0\text{ mm}$, spacing between structures, $sp = 0.5\text{ mm}$, and the ECB is located on the Right-Middle case ($dx = 1.125$), (b). Representation of periodic array with 2×2 Omega unit cells, (c). Omega Structure in Unit Cell with propagation in the z -direction.

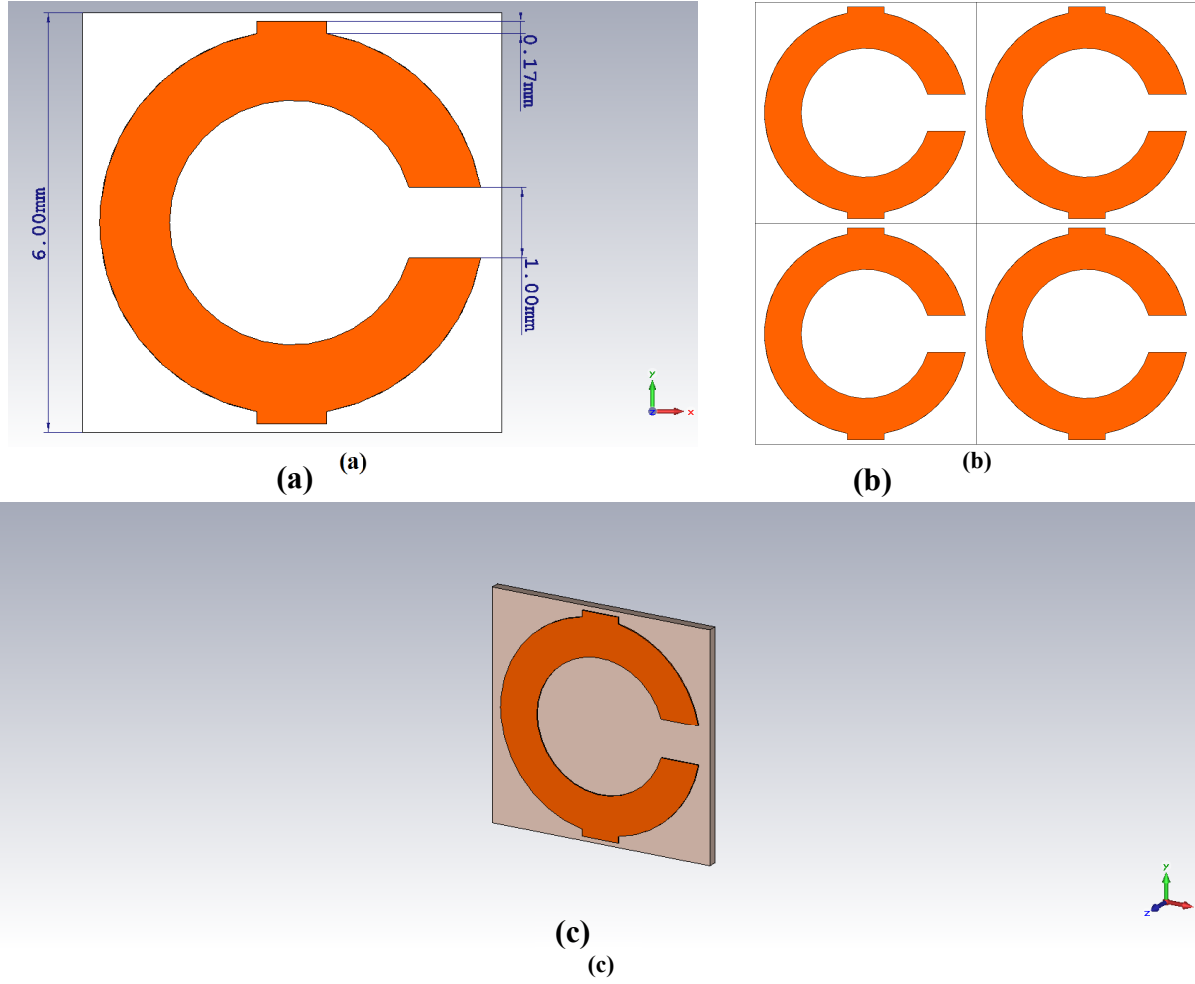


Fig. 4.4.13: Omega MTM Structure in $6\text{ mm} \times 6\text{ mm}$ Unit Cell Size: (a). Omega Structure displaying the design dimensions in unit cell with fixed parameters linewidth, $lw = 1.0\text{ mm}$, spacing between structures, $sp = 0.5\text{ mm}$, and the ECB is located on the Middle case ($dx = 0$), (b). Representation of periodic array with 2×2 Omega unit cells, (c). Omega Structure in Unit Cell with propagation in the z -direction.

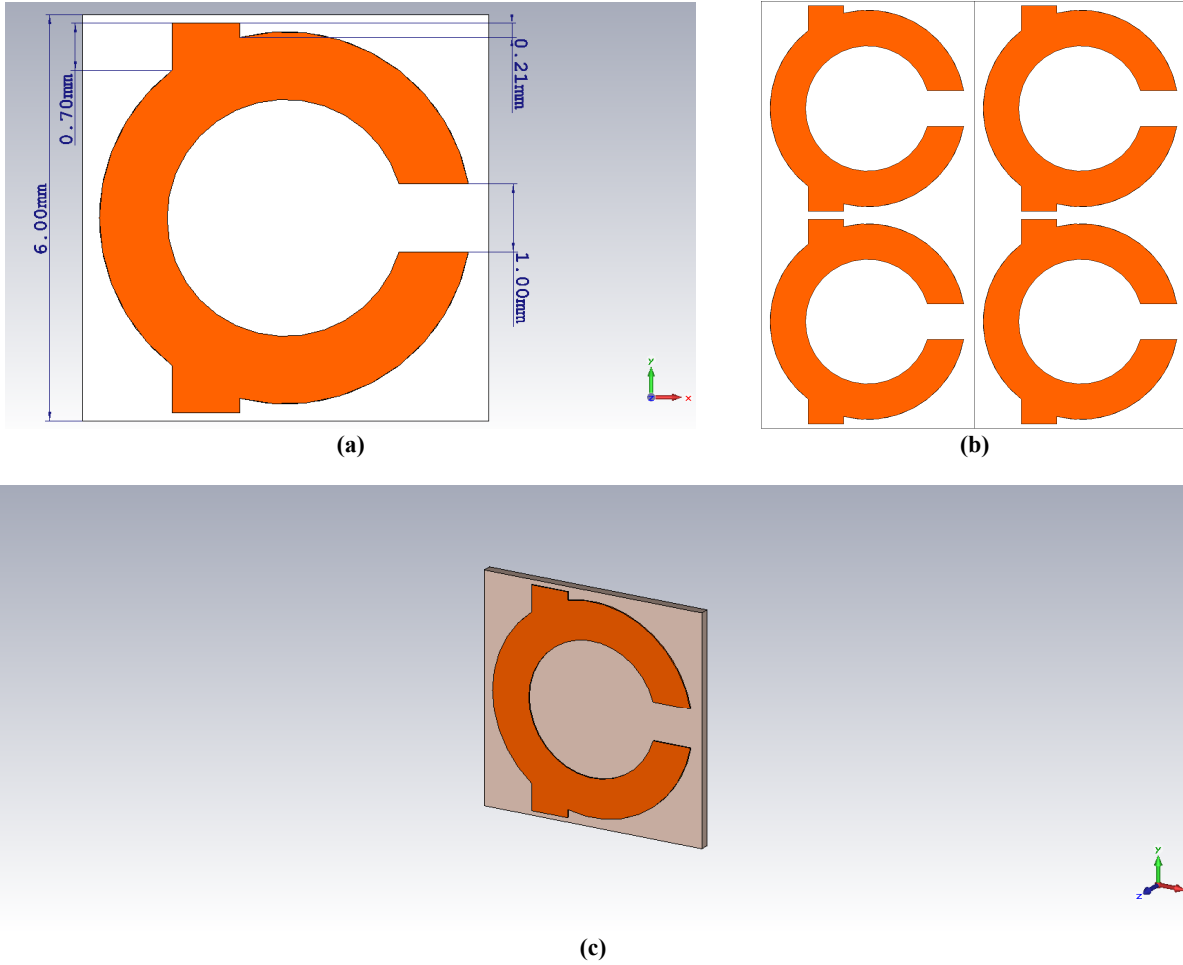


Fig. 4.4.14: Omega MTM Structure in $6 \text{ mm} \times 6 \text{ mm}$ Unit Cell Size: (a). Omega Structure displaying the design dimensions in unit cell with fixed parameters linewidth, $lw = 1.0 \text{ mm}$, spacing between structures, $sp = 0.5 \text{ mm}$, and the ECB is located on the Left-Middle case ($dx = -1.125$), (b). Representation of periodic array with 2×2 Omega unit cells, (c). Omega Structure in Unit Cell with propagation in the z -direction.

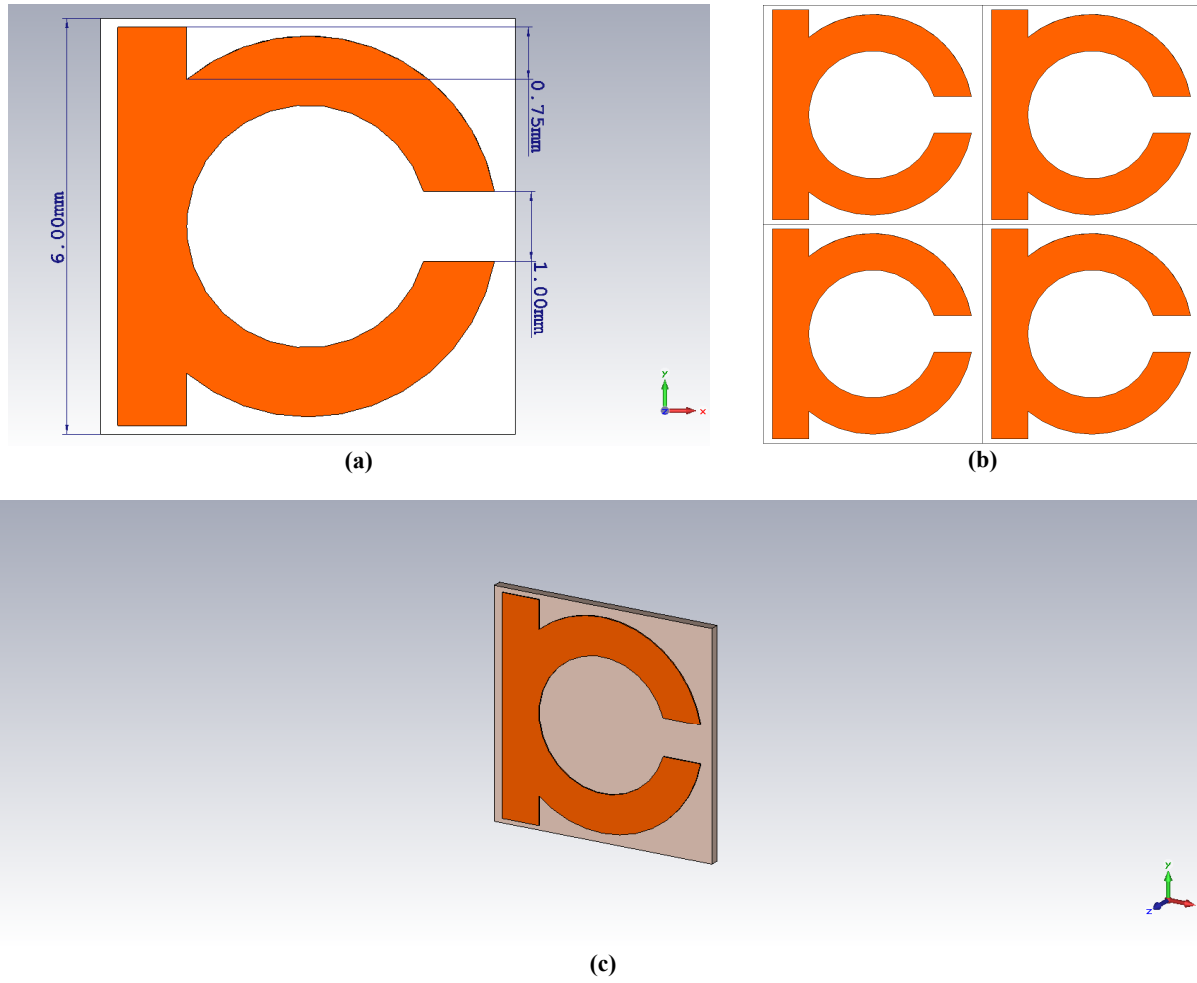


Fig. 4.4.15: Omega MTM Structure in $6\text{ mm} \times 6\text{ mm}$ Unit Cell Size: (a). Omega Structure displaying the design dimensions in unit cell with fixed parameters linewidth, $l_w = 1.0\text{ mm}$, spacing between structures, $sp = 0.5\text{ mm}$, and the ECB is located on the Left case ($dx = -2.25$), (b). Representation of periodic array with 2×2 Omega unit cells, (c). Omega Structure in Unit Cell with propagation in the z -direction.

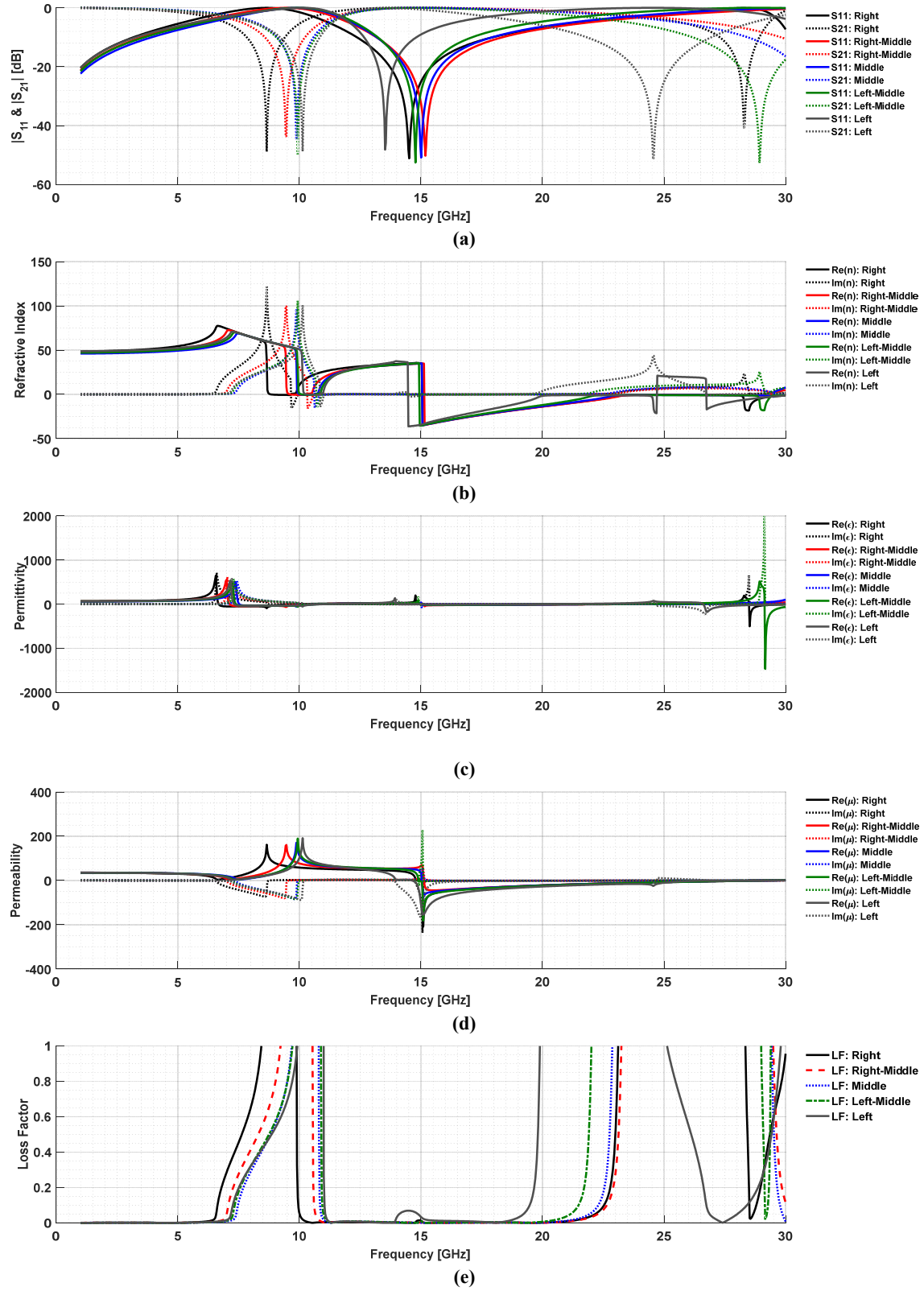


Fig. 4.4.16: Effective Parameter Extraction from Simulation Results for 6 mm × 6 mm Unit Cell 2D Omega in Arlon Di 880 Substrate: (a) S -Parameters, (b) Real and imaginary parts of n , (c) Real and imaginary parts of ϵ , (d) Real and imaginary parts of μ , (e) Loss Factor.

TABLE 4.4.2
Summary of Low Loss NZRIM Bands for 2D Omega Structures in Arlon Di 880 Substrate

Sub-Structure	Frequency Range for $ n < 1.0$ [GHz]	Frequency Range where $ n < 1.0$ and $LF < 1$ [GHz]				Bandwidth (BW) [%]		Total BW where $ n < 1.0$ and $LF < 1$ [GHz]
		1st Band (From)	1st Band (To)	2nd Band (From)	2nd Band (To)	1st Band	2nd Band	
Right	R1: 9.888-9.915	9.89	9.92	-	-	0.14	-	2.50
	R2: 22.29-28.28	22.29	23.11	-	-	1.74	-	
	R3: 28.35-30	28.35	30.00	-	-	2.68	-	
Right-Middle	R1: 9.481-10.57	10.54	10.57	-	-	0.14	-	1.41
	R2: 22.37-30	22.37	23.24	29.49	30.00	1.84	0.86	
Middle	R1: 9.905-10.82	10.80	10.82	-	-	0.09	-	1.15
	R2: 22.11-29.8	22.11	22.87	29.43	29.80	1.63	0.62	
Left-Middle	R1: 9.959-10.91	10.89	10.91	-	-	0.09	-	0.69
	R2: 21.44-28.91	21.44	22.01	-	-	1.28	-	
	R3: 29.29-30	29.29	29.39	-	-	0.17	-	
Left	R1: 10.16-11.01	11.00	11.01	-	-	0.05	-	1.68
	R2: 19.6-24.54	19.60	19.89	-	-	0.72	-	
	R3: 28.42-30	28.42	29.80	-	-	2.26	-	

4.4.3: Omeganet MTM Structures Over FR-4 (lossy) Substrate

The second case studied for Omegas is with the FR-4 substrate. With the exception of the substrate thickness, the dimensions regarding the Omega structures remain the same as with the Arlon case. With the FR-4 substrate, a thickness of 1.6 mm was employed with permittivity $\epsilon_r = 4.3$, loss tangent $\tan\delta = 0.025$ and structure copper thickness is 0.03 mm. The same five cases of varying dx were investigated. Fig. 4.4.17 shows the progression of the cases for both Omeganets, Fig. 4.4.17(a)-(e) and Omegas, Fig. 4.4.17(f)-(j).

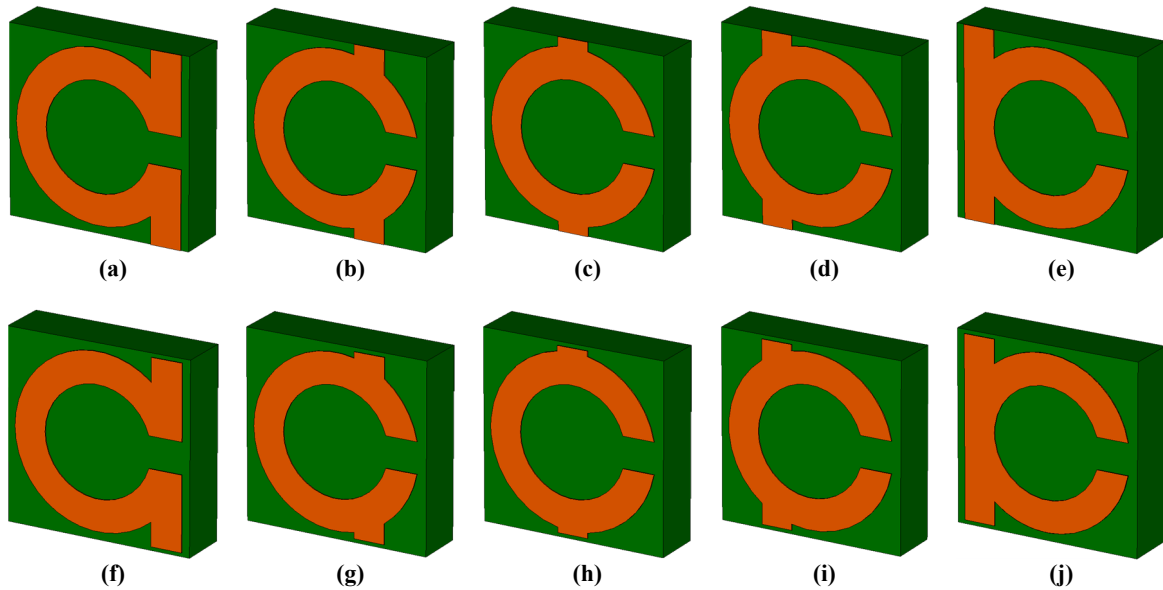


Fig. 4.4.17: Progression of the 2D Omeganets (top row) and Omegas (bottom row) in FR-4 Substrate: (a). Omeganet Right Case, (b). Omeganet Right-Middle Case, (c). Omeganet Middle Case, (d). Omeganet Left-Middle Case, (e). Omeganet Left Case, (f). Omega Right Case, (g). Omega Right-Middle Case, (h). Omega Middle Case, (i). Omega Left-Middle Case, (j). Omega Left Case.

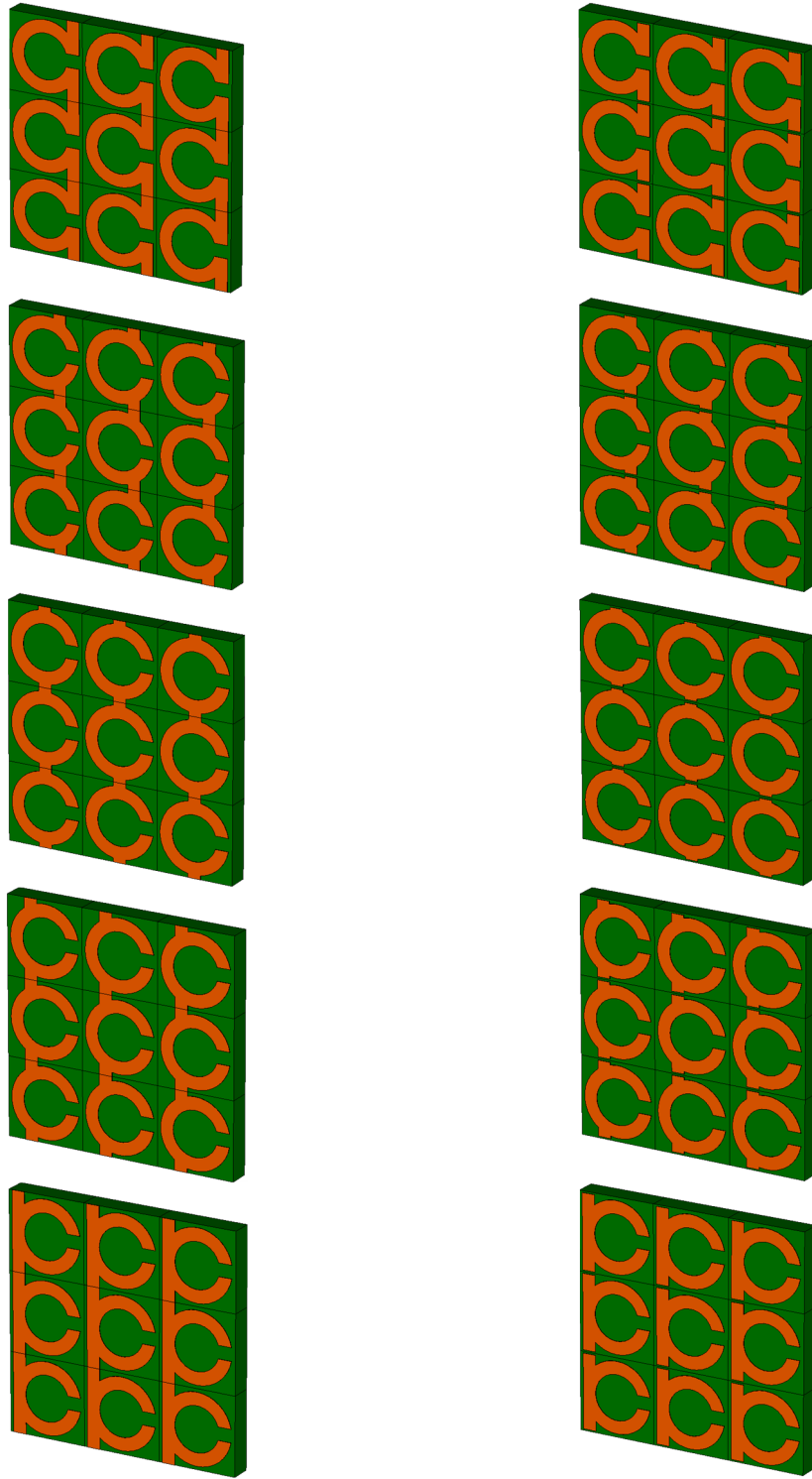


Fig. 4.4.18: 3×3 Unit Cells Array View of the 2D Omeganets (left column.) and 2D Omegas (right column.) in FR-4 (lossy) Substrate.

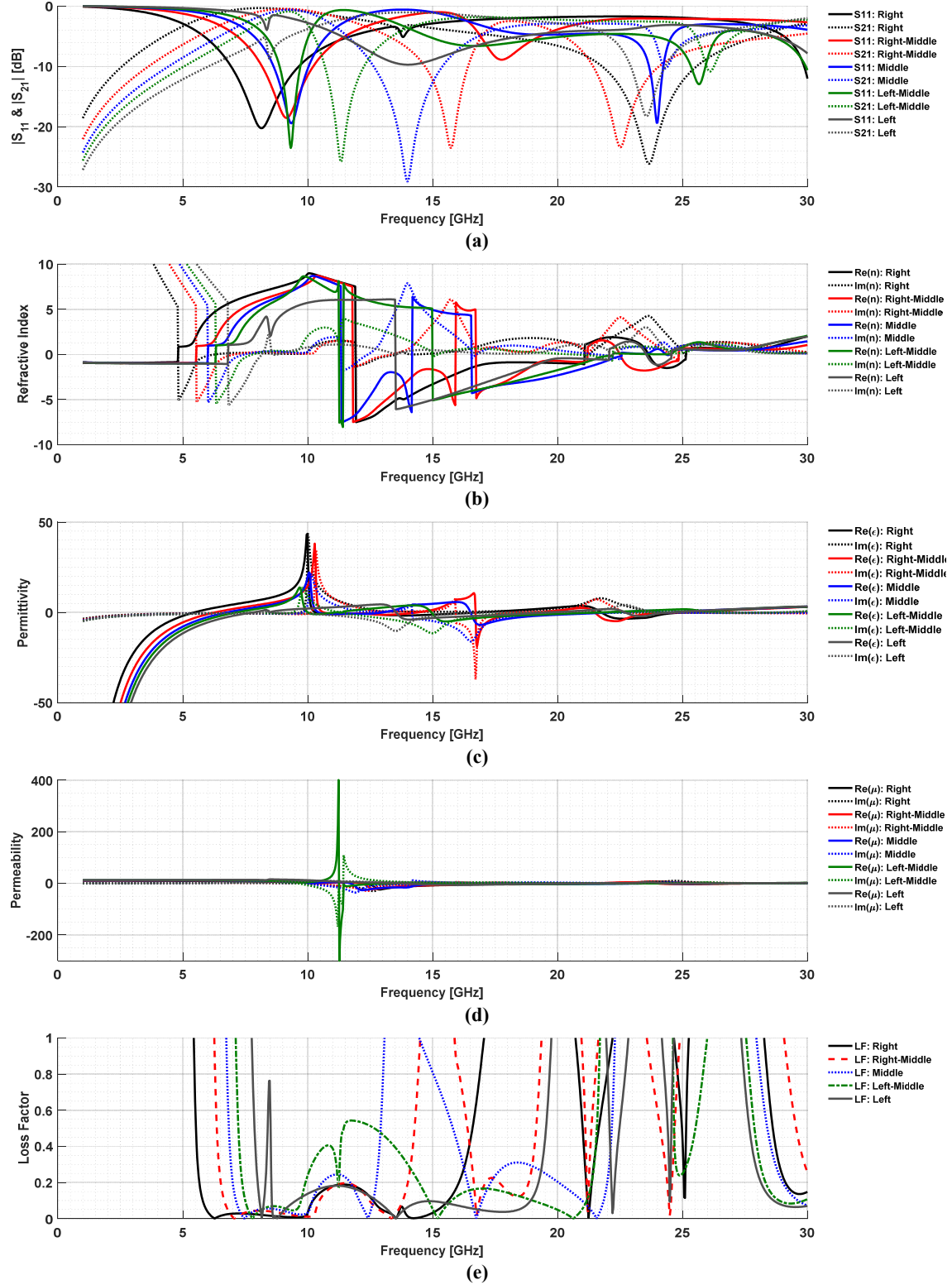


Fig. 4.4.19: Effective Parameter Extraction from Simulation Results for 6 mm × 6 mm Unit Cell 2D Omeganet in FR-4 (lossy) Substrate 5 Cases: (a) S -Parameters, (b) Real and imaginary parts of n , (c) Real and imaginary parts of ϵ , (d) Real and imaginary parts of μ , (e) Loss Factor.

TABLE 4.4.3
Summary of Low Loss NZRIM Bands for 2D Omeganet Structures in FR-4 Substrate

Sub-Structure	Frequency Range for $ n <1.0$ [GHz]	Frequency Range where $ n <1.0$ and $LF<1$ [GHz]				Bandwidth (BW) [%]		Total BW where $ n <1.0$ and $LF<1$ [GHz]
		1st Band (From)	1st Band (To)	2nd Band (From)	2nd Band (To)	1st Band	2nd Band	Per Sub-Structure
Right	R1: 24.9-28.76	24.90	25.25	28.27	28.76	0.69	0.86	0.84
Right-Middle	R1: 19.16-22.71	19.16	19.36	20.96	21.29	0.51	0.78	1.84
	R2: 24.43-29.92	24.43	24.89	29.07	29.92	0.92	1.44	
Middle	R1: 21.67-28.99	21.67	22.30	27.96	28.99	1.39	1.81	1.66
Left-Middle	R1: 20.97-25.15	20.97	21.70	24.62	25.15	1.65	1.06	1.26
Left	R1: 19.29-22.36	19.29	19.75	21.95	22.36	1.15	0.93	2.09
	R2: 24.23-28.15	24.23	24.65	27.35	28.15	0.84	1.44	

4.4.4: Omega MTM Structure Over FR-4 (lossy) Substrate

This portion of our study is a continuation of the second case studied for Omegas with the FR-4 substrate. With the exception of the substrate thickness, the dimensions regarding the Omega structures remain the same as with the Arlon case. With the FR-4 substrate, a thickness of 1.6 mm was employed with permittivity $\epsilon_r = 4.3$, loss tangent $\tan\delta = 0.025$ and structure copper thickness equal to 0.03 mm. The same five cases of varying dx were investigated. Fig. 4.4.20 shows the progression of the cases for the 2D Omegas in 3×3 unit cell array configuration (individual unit cell size 6 mm \times 6 mm), to appreciate the periodicity of the

structure. From this view, one may observe the split between the vertical unit cells, fixed at a quarter of the spacing, equals 0.25 mm.

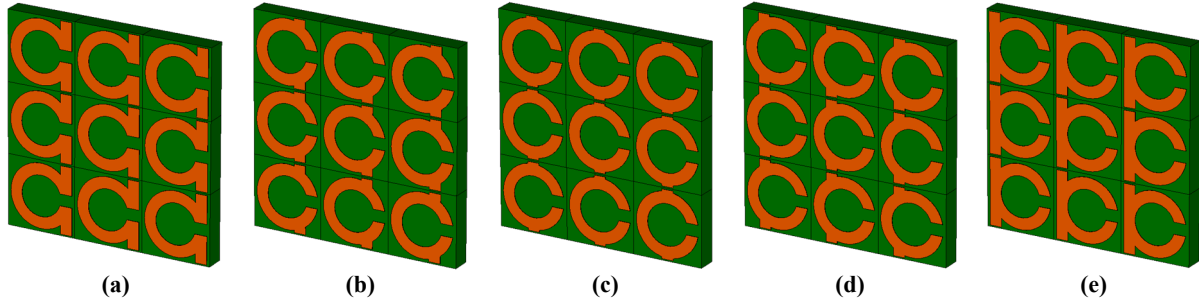


Fig. 4.4.20: 3×3 Unit Cells Array View of the 2D Omegas in FR-4 (lossy) Substrate: (a). Omega Right Case, (b). Omega Right-Middle Case, (c). Omega Middle Case, (d). Omega Left-Middle Case, (e). Omega Left Case.

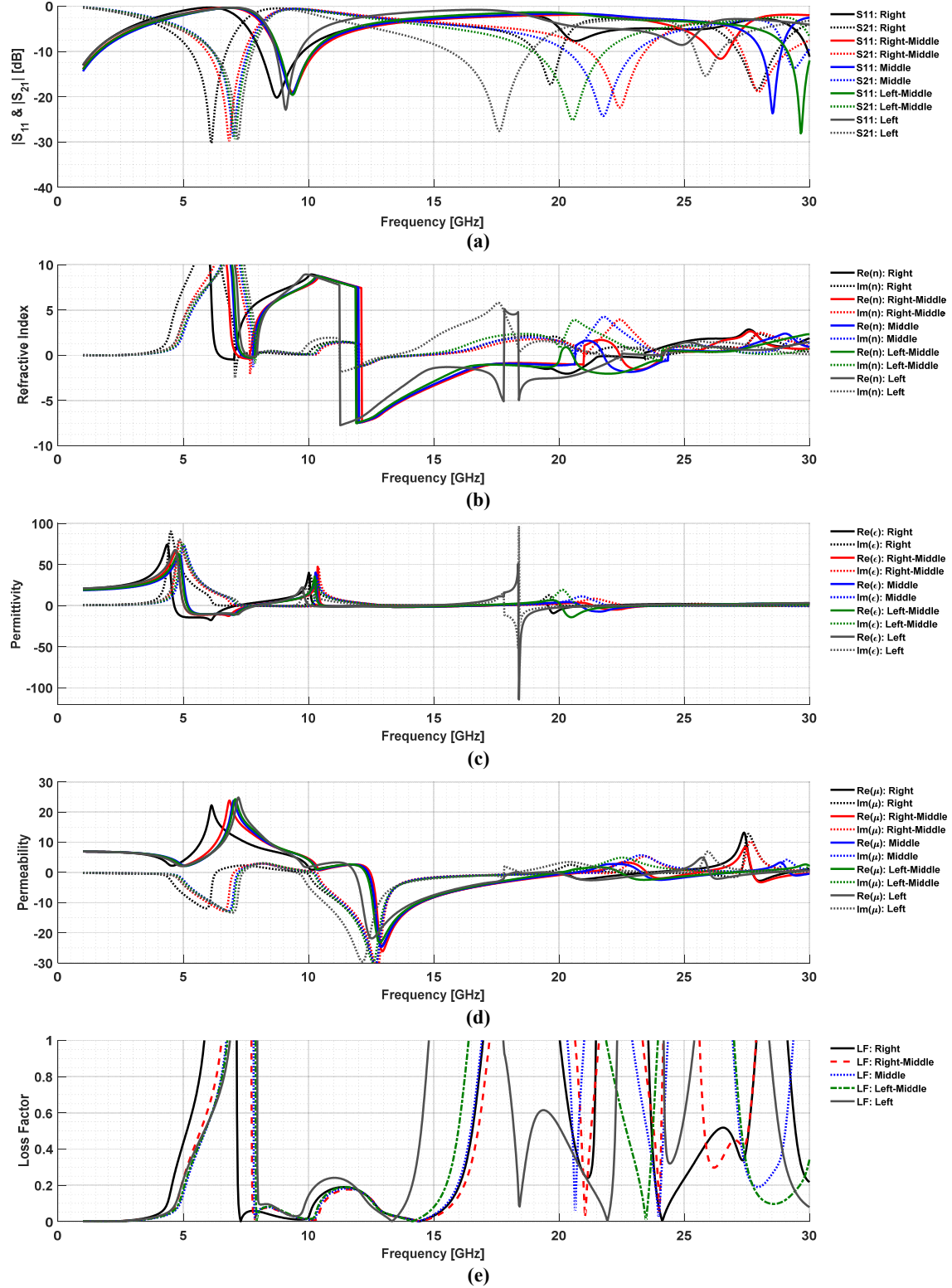


Fig. 4.4.21: Effective Parameter Extraction from Simulation Results for $6 \text{ mm} \times 6 \text{ mm}$ Unit Cell 2D Omega FR-4 (lossy) 5 Cases: (a) S -Parameters, (b) Real and imaginary parts of n , (c) Real and imaginary parts of ϵ , (d) Real and imaginary parts of μ , (e) Loss Factor.

TABLE 4.4.4
Summary of Low Loss NZRIM Bands for 2D Omega Structures in FR-4 Substrate

Sub-Structure	Frequency Range for $ n <1.0$ [GHz]	Frequency Range where $ n <1.0$ and $LF<1$ [GHz]				Bandwidth (BW) [%]		Total BW where $ n <1.0$ and $LF<1$ [GHz]
		1st Band (From)	1st Band (To)	2nd Band (From)	2nd Band (To)	1st Band	2nd Band	Per Sub-Structure
Right	R1: 21.13-24.27	21.13	21.47	23.56	24.27	0.79	1.48	1.05
Right-Middle	R1: 20.98-21.01	20.98	21.01	-	-	0.07	-	0.78
	R2: 23.79-25.99	23.79	24.16	25.61	25.99	0.76	0.74	
Middle	R1: 12.12-12.01	12.00	12.01	-	-	0.04	-	1.17
	R2: 20.55-20.66	20.55	20.66	-	-	0.27	-	
	R3: 23.87-27.5	23.87	24.35	26.93	27.50	0.98	1.05	
Left-Middle	R1: 23.41-27.8	23.41	23.95	26.98	27.80	1.11	1.50	1.36
Left	R1: 18.38-18.39	18.38	18.39	-	-	0.03	-	0.94
	R2: 21.81-24.6	21.81	22.32	24.18	24.60	1.13	0.86	

4.4.5: Hexagonal Two-Dimensional Omeganet Over FR-4 (lossy) Substrate

Inspired by the design of fractal geometry, radomes, honeycombs and soccer ball plus the idea of weaving our 2D Omeganet into a 3D Omeganet, our investigation considered exploring “hexagonalized” Omeganets MTM structures. The progression of the varying for the ECB in the five original cases may be observed in Fig. 4.4.22.

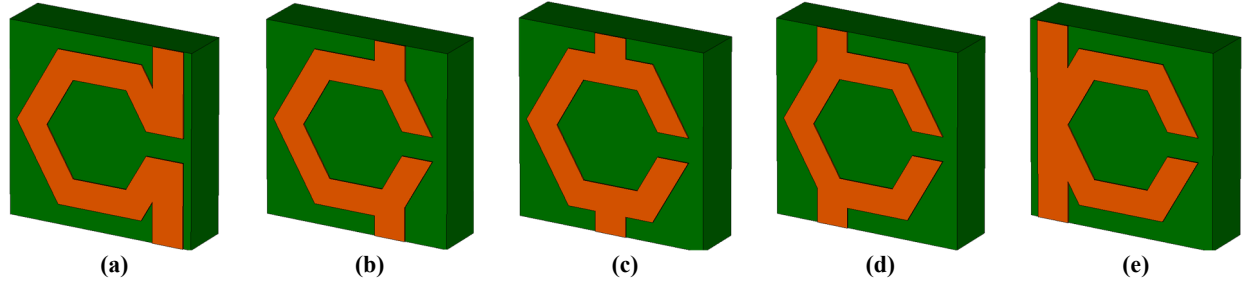


Fig. 4.4.22: Progression of the 2D Hexagonal Omeganets in FR-4 Substrate: (a). Hex. Omeganet Right Case, (b). Hex. Omeganet Right-Middle Case, (c). Hex Omeganet Middle Case, (d). Hex. Omeganet Left-Middle Case, (e) Hex. Omeganet Left Case.

Similar to the previous Omeganet cases, the substrate employed here is FR-4 with substrate thickness equal to 1.6 mm, permittivity $\epsilon_r = 4.3$ and loss tangent $\tan\delta = 0.025$. However, this study involved some minor differences such as the structure copper thickness of 0.036 mm, the linewidth lw was fixed at 1 mm, unit cell $6\text{ mm} \times 6\text{ mm}$, the spacing between structures sp was fixed at 0.5 mm as well as the horizontal ring split which was fixed at 0.75 mm. The location of the ECB, dx , continued to be variable, as shown in Fig. 4.4.23.

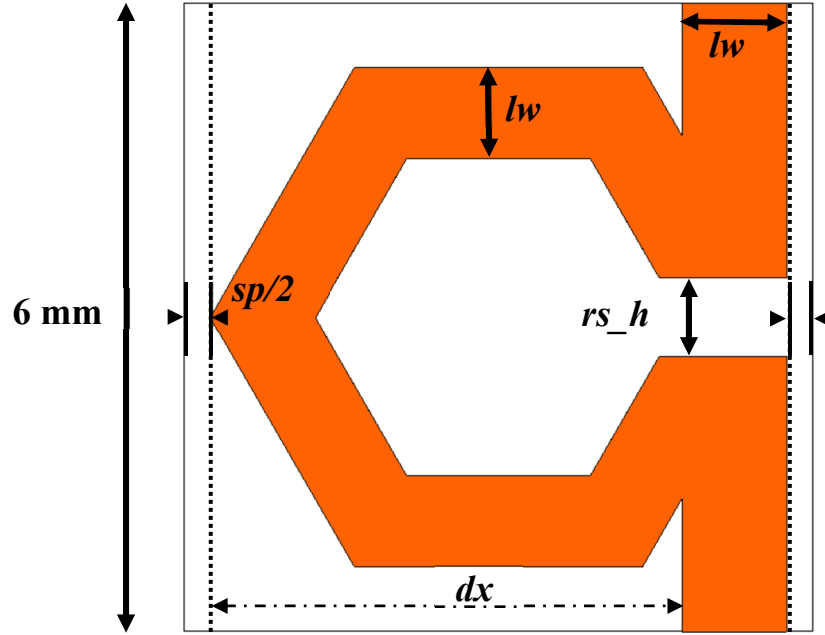


Fig. 4.4.23: Hexagonal 2D Omeganet MTM Structure in $6\text{ mm} \times 6\text{ mm}$ Unit Cell with the *Epsilon*-Controlling Bar (ECB) at the Right Side Position and structure parameters $lw = 1\text{ mm}$, $rs_h = 0.75\text{ mm}$, $sp = 0.5\text{ mm}$, and variable dx .

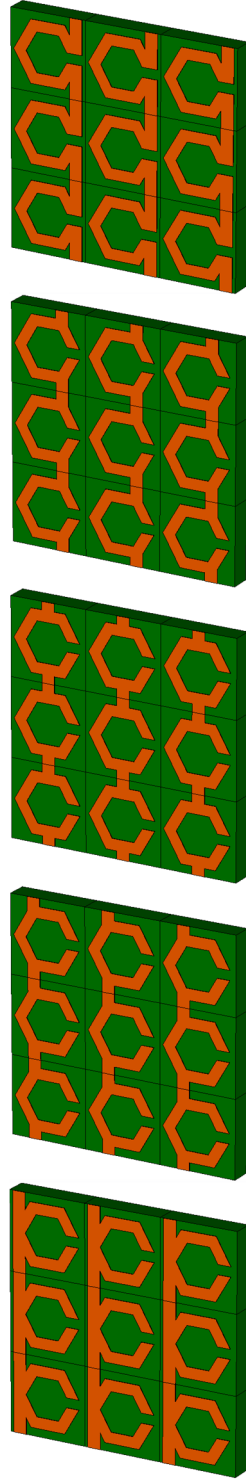


Fig. 4.4.24: 3×3 Unit Cells Array View of the 2D Hexagonal Omeganets Five Cases in FR-4 (lossy) Substrate.

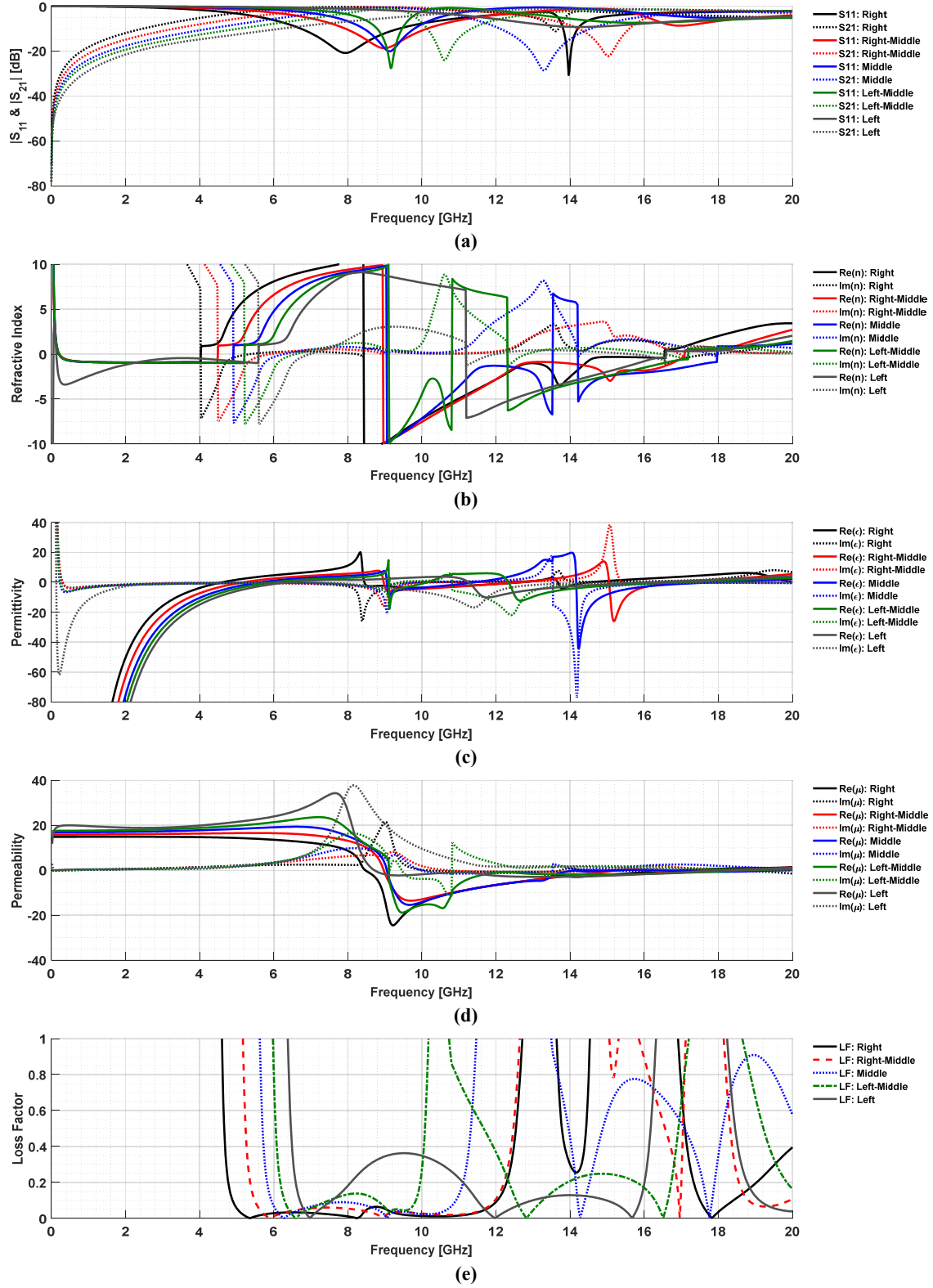


Fig. 4.4.25: Effective Parameter Extraction from Simulation Results for $6 \text{ mm} \times 6 \text{ mm}$ Unit Cell 2D Hexagonal Omeganet in FR-4 (lossy) Substrate: (a) S -Parameters, (b) Real and imaginary parts of n , (c) Real and imaginary parts of ϵ , (d) Real and imaginary parts of μ , (e) Loss Factor.

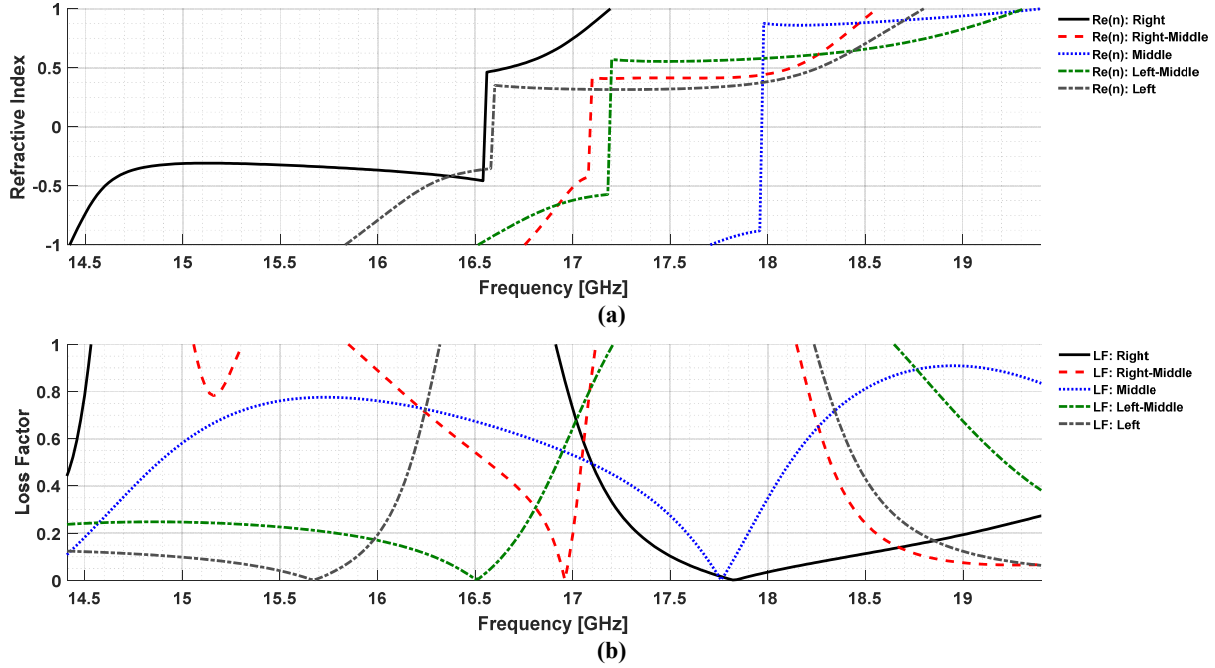


Fig. 4.4.26: Comparison and Evaluation of Effective Parameter Extraction for 6 mm \times 6 mm Unit Cell 2D Hexagonal Omeganet in FR-4 (lossy) Substrate: (a). Refractive index and (b) Loss Factor of the Hexagonal Omeganet Structures Focusing on the NNZ Frequency Range.

Fig. 4.4.26 shows a focused view of where we notice the hexagonal Omeganet NNZ band plus the loss factor which corresponds to this same frequency. Evaluating the results obtained from the hexagonal Omeganet, from Fig. 4.4.26 (blue dotted line) and Table 4.4.5, the substructure with ECB in the middle position ($dx = 0$) appears to have the most desired qualities and is then selected for further investigation. Specifically, this structure contains the broadest NNZ with low LF .

TABLE 4.4.5
Summary of Low Loss NZRIM Bands for 2D Hexagonal Omeganet Structures in FR-4 Substrate

Sub-Structure	Frequency Range for $ n < 1.0$ [GHz]	Frequency Range where $ n < 1.0$ and $LF < 1$ [GHz]				Bandwidth (BW) [%]		Total BW where $ n < 1.0$ and $LF < 1$ [GHz]
		1st Band (From)	1st Band (To)	2nd Band (From)	2nd Band (To)	1st Band	2nd Band	Per Sub-Structure
Right	R1: 8.429-8.431	8.43	8.43	-	-	0.01	-	0.38
	R2: 14.42-17.19	14.42	14.53	16.92	17.19	0.38	0.79	
Right-Middle	R1: 8.949-8.951	8.95	8.95	-	-	0.01	-	0.77
	R2: 16.76-18.56	16.76	17.12	18.15	18.56	1.04	1.12	
Middle	R1: 9.049-9.051	9.05	9.05	-	-	0.01	-	1.68
	R2: 17.71-19.39	17.71	19.39	-	-	4.15	-	
Left-Middle	R1: 9.109-9.111	9.11	9.11	-	-	0.01	-	1.35
	R2: 16.52-19.31	16.52	17.21	18.65	19.31	1.97	1.74	
Left	R1: 15.84-18.8	15.84	16.32	18.24	18.80	1.45	1.51	1.04

4.4.6: Select Cases Derived from 2D Hexagonal Omeganet Over FR-4 (lossy) Substrate

In this last section, the previously mentioned “Middle” case from hexagonal Omeganet was further investigated and many experimental designs were explored, however, here are three selected structures derived from optimizations on Case 3 of the hexagonal Omeganet structure.

Fig 4.4.27(b) – 4.4.27(c) show the select MTM structure designs discussed.

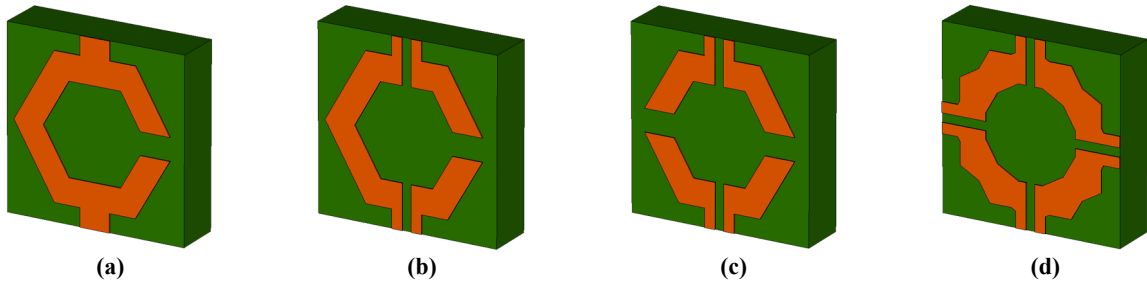


Fig. 4.4.27: Selected Designs Derived from Hexagonal Omeganet MTM Structure with Optimization Design Names: (a). C3, (b). C3a, (c). C3ai, (d). C3aiii.

Included is the original Case 3 (Fig. 4.4.27(a)) which is the third case from the hexagonal Omeganet (“Middle” Sub-structure from Table 4.4.5 where $dx = 0$) and will serve as a benchmark to compare with, as we present its optimizations.

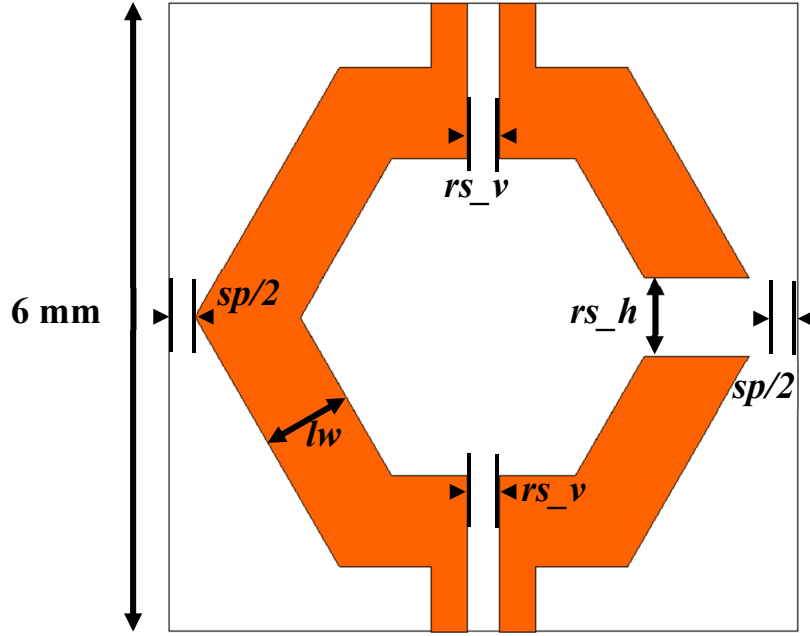


Fig. 4.4.28: MTM Design “C3a” Hexagonal 2D Omeganet Structure in $6\text{ mm} \times 6\text{ mm}$ Unit Cell with the *Epsilon*-Controlling Bar (ECB) Position $dx = 0$ and structure parameters $lw = 1\text{ mm}$, $rs_h = 0.75\text{ mm}$, $rs_v = 0.3\text{ mm}$, $sp = 0.5\text{ mm}$.

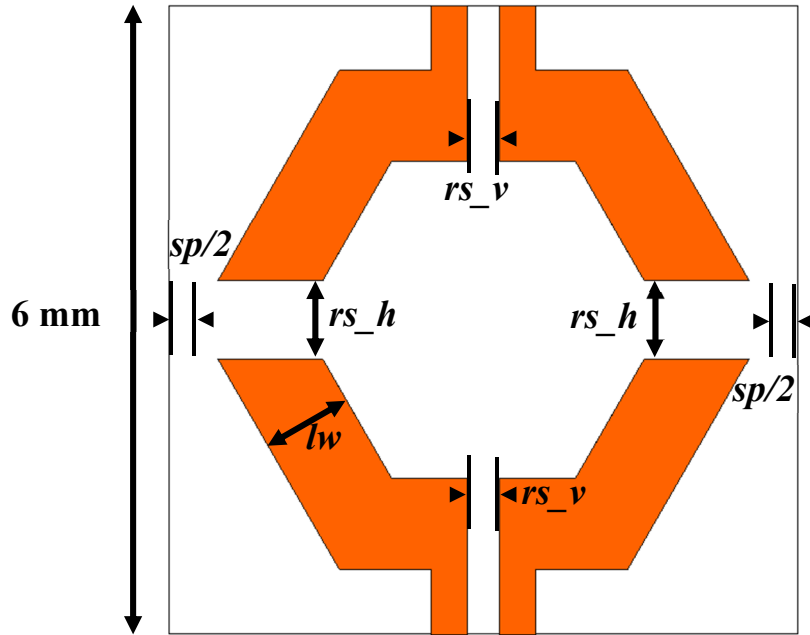


Fig. 4.4.29: MTM Design “C3ai” Hexagonal 2D Omeganet Structure in $6\text{ mm} \times 6\text{ mm}$ Unit Cell with the *Epsilon*-Controlling Bar (ECB) Position $dx = 0$ and structure parameters $lw = 1\text{ mm}$, $rs_h = 0.75\text{ mm}$, $rs_v = 0.3\text{ mm}$, $sp = 0.5\text{ mm}$.

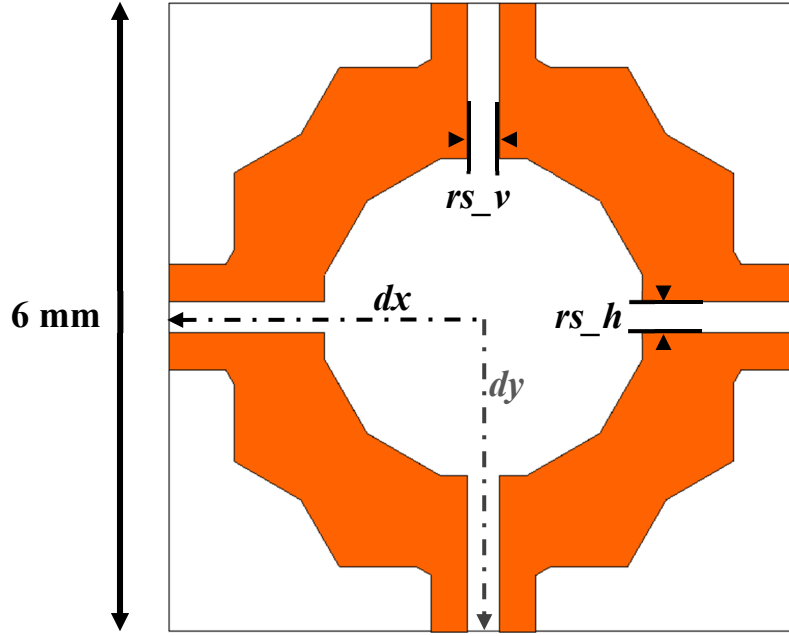


Fig. 4.4.30: MTM Design “C3aiii” Hexagonal 2D Omeganet Structure in $6\text{ mm} \times 6\text{ mm}$ Unit Cell with the *Epsilon*-Controlling Bar (ECB) Position $dx = dy = 0$ and structure parameters $lw = 1\text{ mm}$, $rs_h = rs_v = 0.3\text{ mm}$.

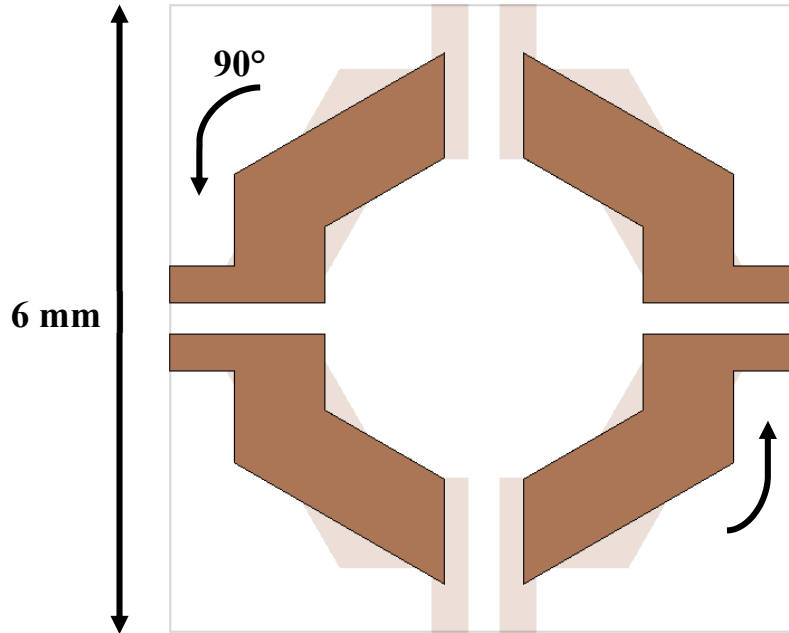
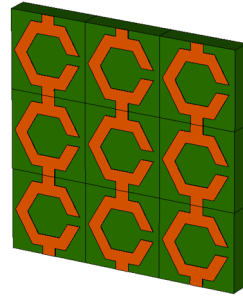
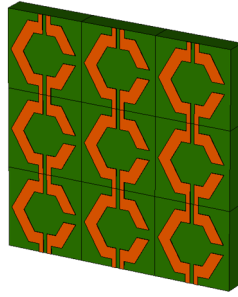


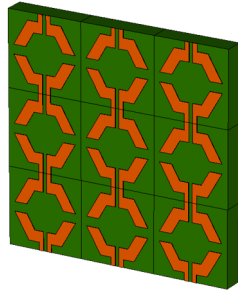
Fig. 4.4.31: 2D Hexagonal Omeganet MTM Design “C3aiii” Derivation from Design “C3ai” by 90-degree rotation and overlaying.



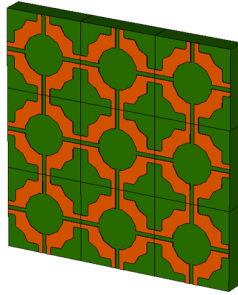
(a)



(b)



(c)



(d)

Fig. 4.4.32: 3×3 Unit Cells Array Configuration of the Selected 2D Hexagonal Omeganets MTM Design Optimizations: (a). C3, (b). C3a, (c). C3ai, (d). C3aiii.

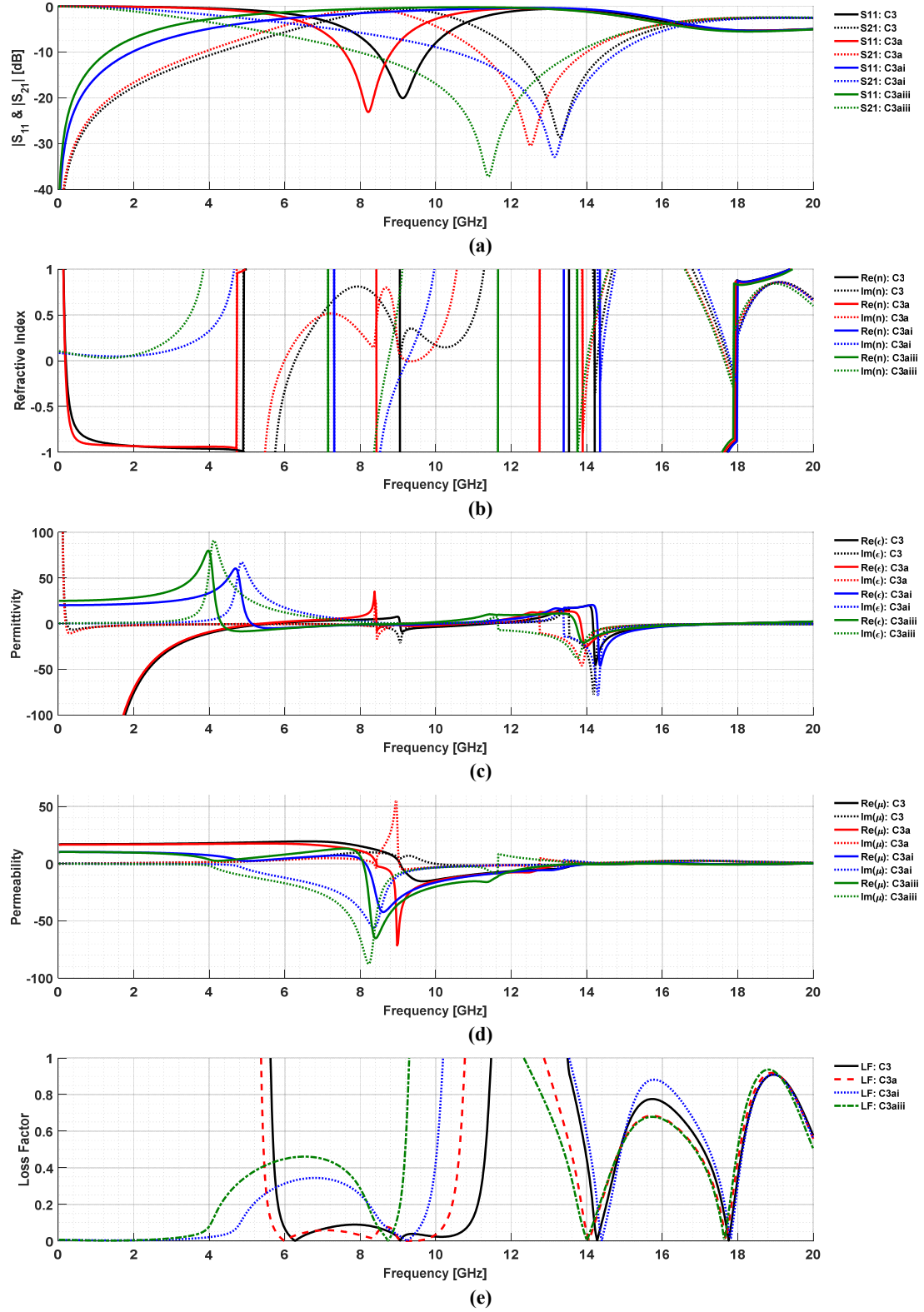


Fig. 4.4.33: Effective Parameter Extraction from Simulation Results for $6 \text{ mm} \times 6 \text{ mm}$ Unit Cell Select Optimizations for 2D Hexagonal Omeganet in FR4 (lossy) Substrate: (a) S -Parameters, (b) Real and imaginary parts of n , (c) Real and imaginary parts of ϵ , (d) Real and imaginary parts of μ , (e) Loss Factor.

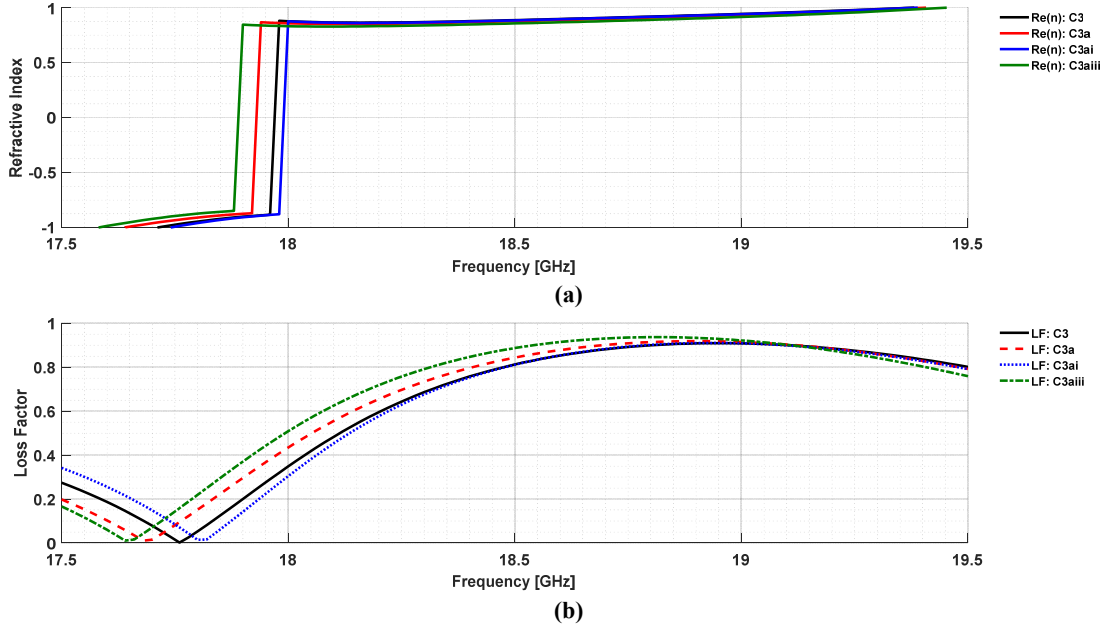


Fig. 4.4.34: Select 2D Omeganet MTM Structure: (a). Refractive index and (b) Loss Factor of the Hexagonal Omeganet Structures Focusing on the NNZ Frequency Range.

TABLE 4.4.6

Summary of Low Loss NZRIM Bands for Select 2D Hexagonal Omeganet Structures in FR-4 Substrate

Sub-Structure	Frequency Range for $ n <1.0$	Frequency Range where $ n <1.0$ and $LF<1$		Band- width (BW)	Total BW where $ n <1.0$ and $LF<1$
	[GHz]	[GHz]		[%]	[GHz]
		1st Band (From)	1st Band (To)	1st Band	Per Sub-Structure
C3	R1: 9.049-9.051	9.05	9.05	0.01	1.68
	R2: 17.71-19.39	17.71	19.39	4.15	
C3A	R1: 8.429-8.431	8.43	8.43	0.01	1.77
	R2: 17.64-19.41	17.64	19.41	4.36	
C3AI	R1: 17.74-19.38	17.74	19.38	4.06	1.64
C3AIII	R1: 17.59-19.45	17.59	19.45	4.56	1.86

By inspection, we may observe in Fig. 4.4.34 that the four designs display well over 1 GHz range NNZ and exhibit low loss. With the exception of the case C3ai, the other two designs are optimizations derived from the C3 hexagonal Omeganet. One observation to note is that both

of those structures, C3a and C3aiii, contain the 0.3 mm split along the ECB. In more detail, Table 4.4.6 shows the specific range where the band of each structure is both near-zero and low loss. Case C3AIII contains a broader range of NNZ and low loss, therefore, we select this 2D sub-structure design for its desirable qualities for further investigation and to synthesize into 3D.

4.5: Three-Dimensional Omeganet Metamaterial Structures

Armed now with an arsenal of optimized 2D MTM designs for NNZ and low loss, we may now proceed to synthesize our selection into 3D. In our case, we continue to employ the selected structure material copper (annealed) at a thickness of 0.036 mm. Fig. 4.5.1 demonstrates the progression of our 3D Omeganet design from a single-shell, an embedded miniaturized single-shell within another single-shell (called “double-shell”), an expansion of embedded miniaturized single-shells along the propagation direction that form a diamond shape (called “diamond double-shell”) and an expansion of two embedded diamond double-shells which form an octahedral structure (called “octahedral double-shell”). One important note is that the miniaturized embedded shell is a scale-down of Fig. 4.5.1(a), which is $6 \times 6 \times 6 \text{ mm}^3$, by a factor of one-third, making them $2 \times 2 \times 2 \text{ mm}^3$.

Since we are working with periodic structures, in CST Microwave Studio® one issue encountered is that some of the sides of the structure will be sandwiched periodically and thus doubled, completely modifying the desired EM response. In order to overcome this issue, the thickness of the sides of our structure which will be stacked periodically must be halved. These would include: the top, bottom, left and right faces of our structure which would otherwise be considered normal to the propagation in the z direction.

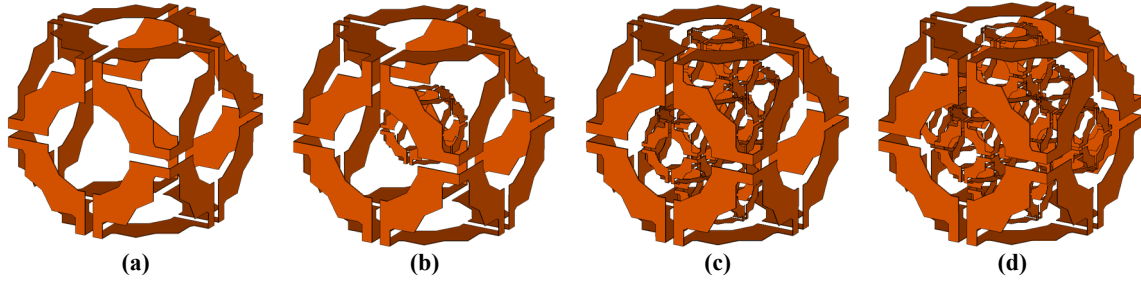


Fig. 4.5.1: Synthesized 3D Omeganet Structures Derived from the Select Optimized 2D Hexagonal Omeganet Structure CAIII: (a). Single-Shell (SS), (b). Double-Shell (DS), (c). Diamond Double-Shell (DDS), (d). Octahedral Double-Shell (ODS).

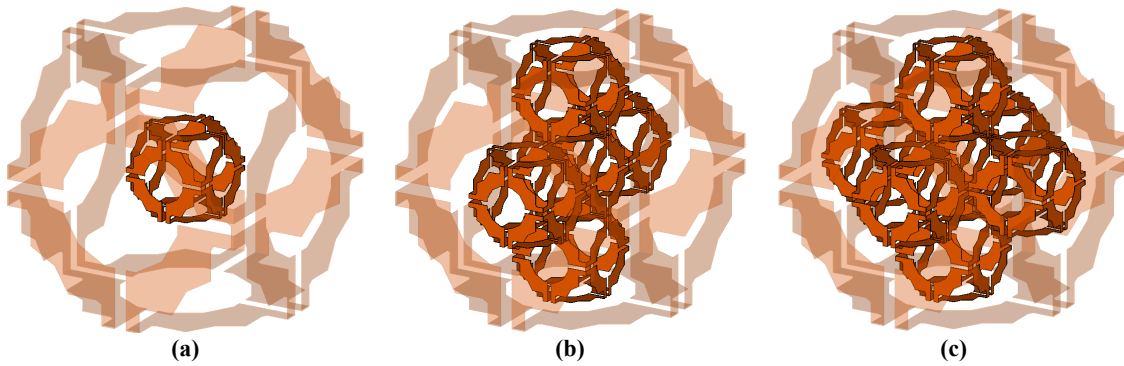


Fig. 4.5.2: Inner View of the Double-Shell 3D Omeganet Designs: (a). Double-Shell (DS), (b). Diamond Double-Shell (DDS), (c). Octahedral Double-Shell (ODS).

Fig. 4.5.2 shows the inner view of the trio of 3D Omeganet MTM structures designed to contain miniaturized inclusions of the base structure form Fig. 4.5.1(a). We classify this group as a double-shell (DS) structure group. Although we see the inner shell of the single DS Omeganet “floating” in the middle, this structure may be filled with a foam or gel which may contain the EM characteristics which are that of air. This inner shell for the DS trio is a scale-down of the SS by a factor of one-third. In the cases of the DDS and ODS, the inner portions which reach out are flush with the outer shell.

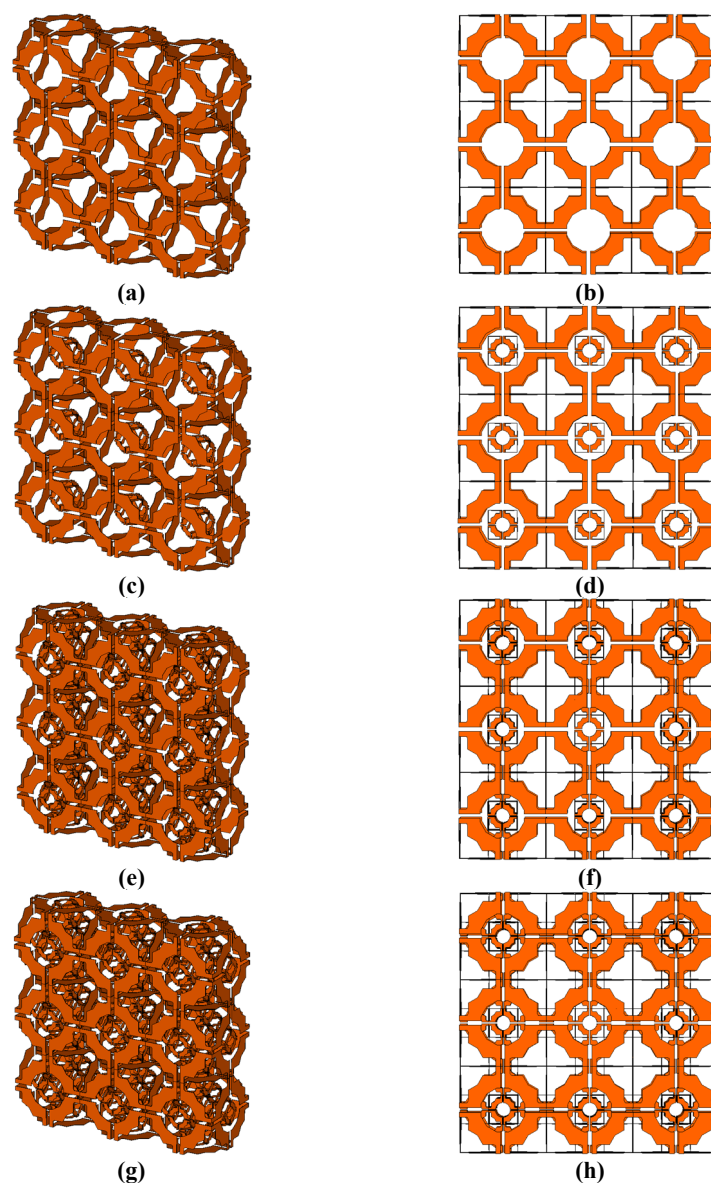


Fig. 4.5.3: 3×3 Unit Cells Array View of the 3D Hexagonal Omeganets where Left Colum are in Perspective View and Right Colum are Frontal View: (a) & (b). Single-Shell (SS), (c) & (d). Double-Shell (DS), (e) & (f). Diamond Double-Shell (DDS), (g) & (h). Octahedral Double-Shell (ODS).

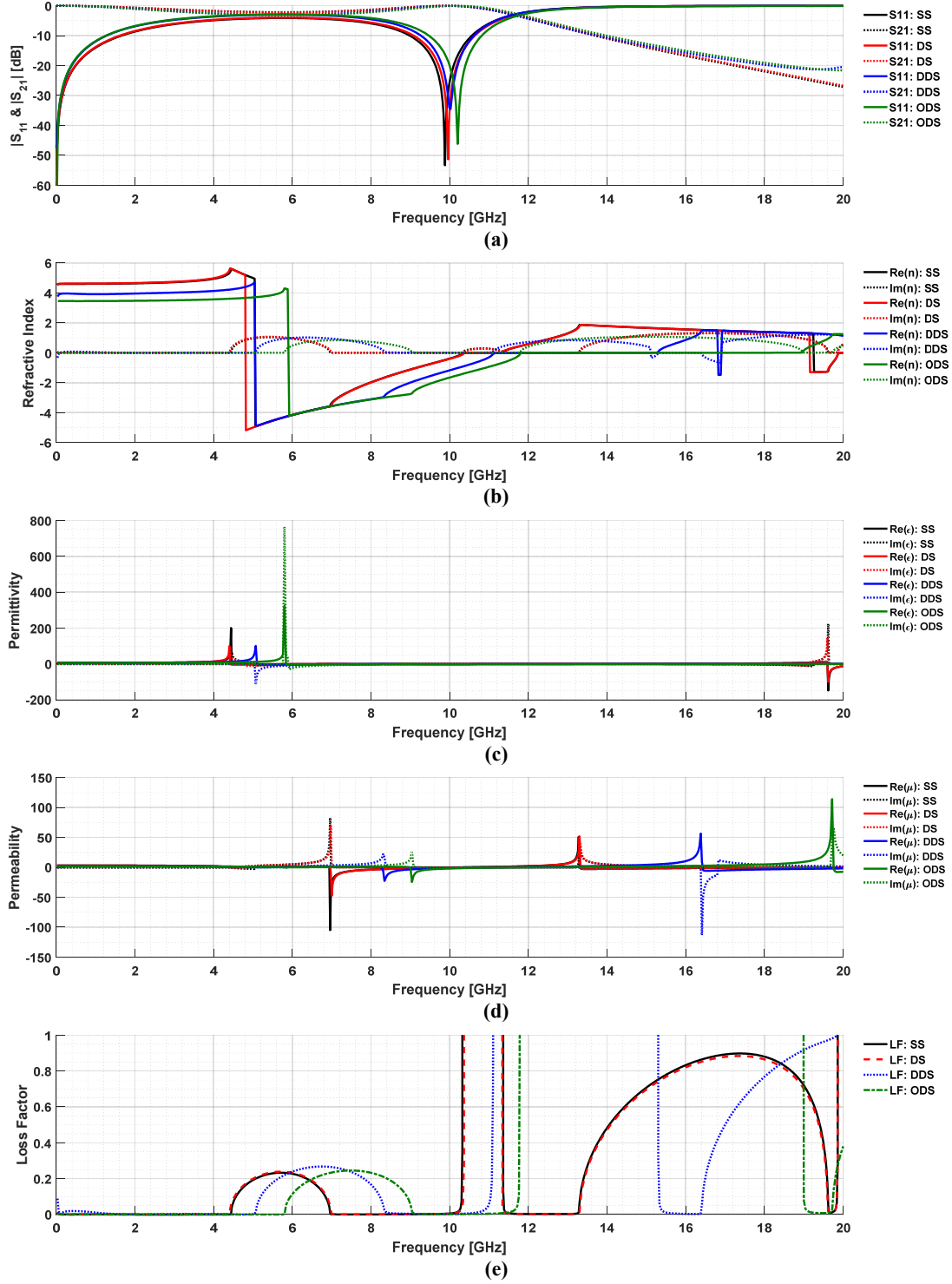


Fig. 4.5.4: Effective Parameter Extraction from Simulation Results for 3D Hexagonal Omegagnet MTM Structures: (a) Magnitude [dB] of S -Parameters, (b) Real and imaginary parts of n , (c) Real and imaginary parts of ϵ , (d) Real and imaginary parts of μ , (e) Loss Factor.

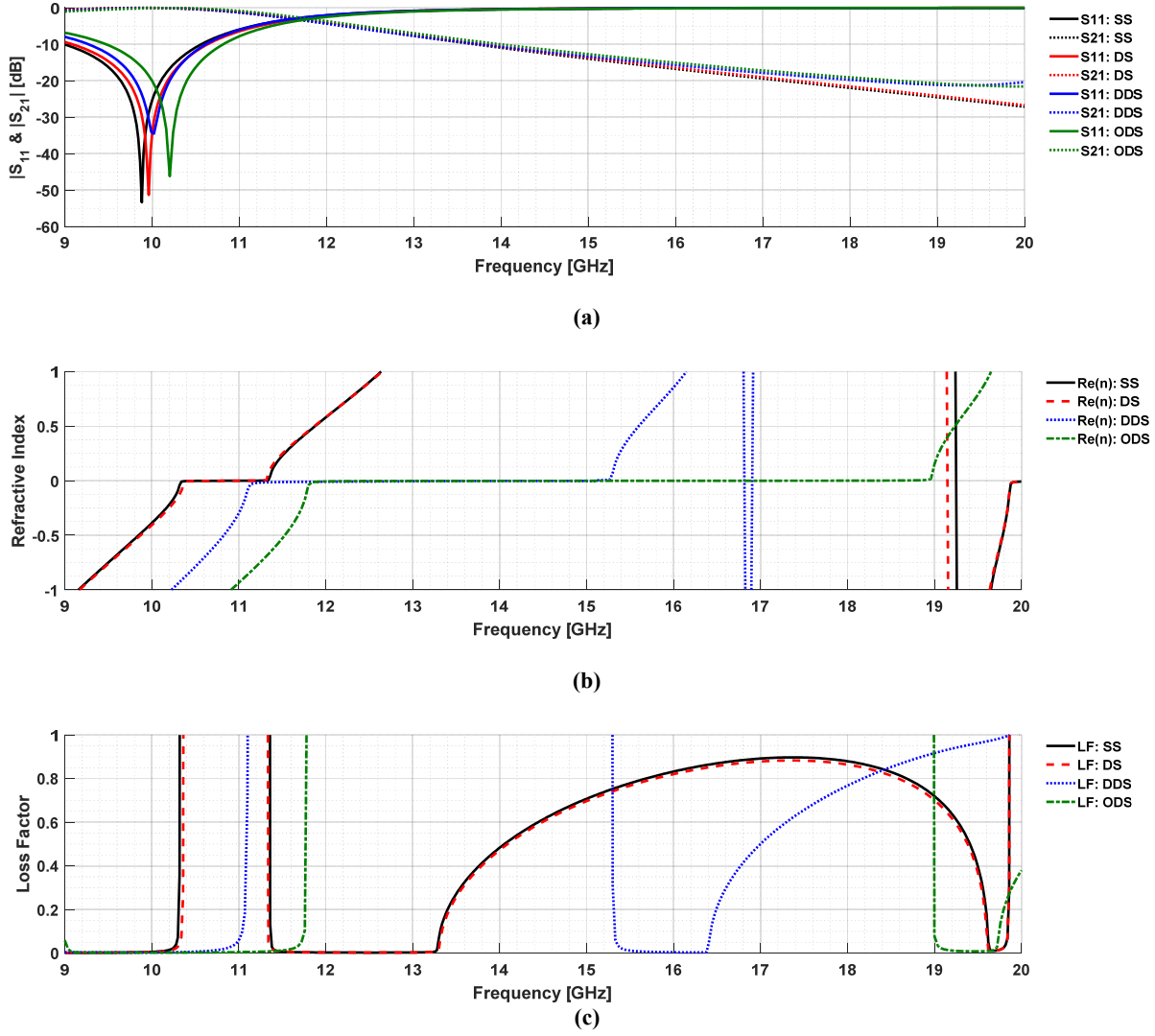


Fig. 4.5.5: Evaluation of Effective Parameter Extraction Results for 3D Hexagonal Omeganet MTM Structures Focusing on the NNZ Frequency Range in General: (a). Magnitude [dB] of S -Parameters, (b). Refractive index and (c) Loss Factor.

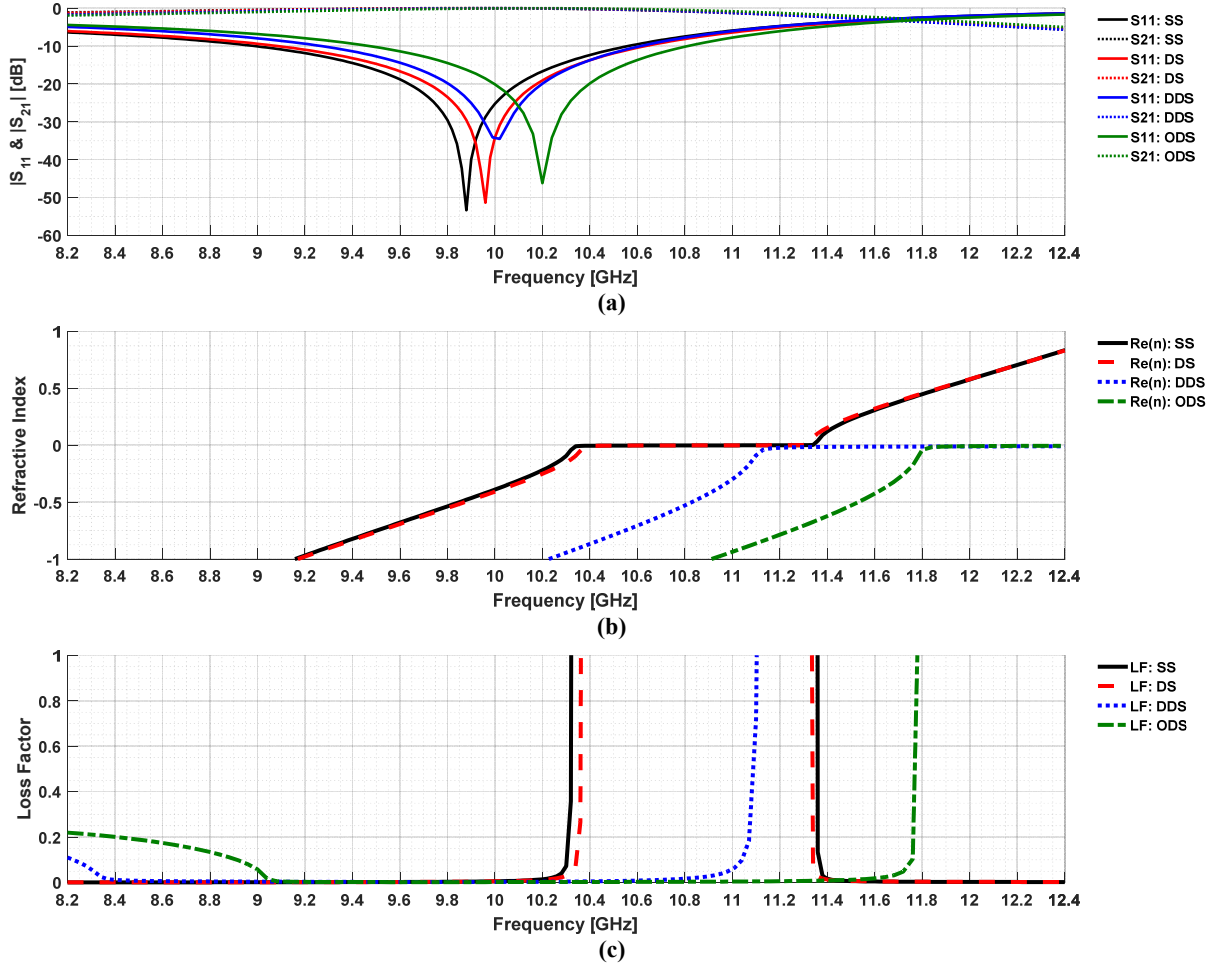


Fig. 4.5.6: Evaluation of Effective Parameter Extraction Results for 3D Hexagonal Omeganet MTM Structures Focusing on the NNZ Frequency Range in the *X*-band Frequency Range: (a). Magnitude [dB] of *S*-Parameters, (b). Refractive index and (c) Loss Factor.

TABLE 4.5.1
Summary of Low Loss NZRIM Bands for 3D Omeganet Structures

Sub-Structure	Frequency Range for $ n < 1.0$ [GHz]	Frequency Range where $ n < 1.0$ and $LF < 1$ [GHz]				Bandwidth (BW) [%]		Total BW where $ n < 1.0$ and $LF < 1$ [GHz]
		1st Band (From)	1st Band (To)	2nd Band (From)	2nd Band (To)	1st Band	2nd Band	
SS	R1: 9.157-12.64	9.16	10.32	11.36	12.59	5.33	5.14	2.60
	R2: 19.65-19.86	19.65	19.86	-	-	0.53	-	
DS	R1: 4.808-4.812	4.81	4.81	-	-	0.04	-	2.66
	R2: 9.213-12.63	9.21	10.36	11.34	12.63	5.25	5.38	
	R3: 19.64-19.86	19.64	19.86	-	-	0.55	-	
DDS	R1: 5.052-5.058	5.05	5.06	-	-	0.06	-	1.79
	R2: 10.23-16.15	10.23	11.10	15.30	16.15	3.77	2.70	
	R3: 16.8-16.83	16.80	16.83	-	-	0.09	-	
	R4: 16.89-16.92	16.89	16.92	-	-	0.09	-	
ODS	R1: 5.895-5.905	5.90	5.91	-	-	0.08	-	1.54
	R2: 10.91-19.65	10.91	11.78	18.99	19.65	3.56	1.71	

By inspection, we may observe in Fig. 4.5.6 that the SS and DS 3D MTM structures exhibit a broad NNZ, low loss frequency range. We may observe that overall, with the 3D designs of our optimized hexagonal Omeganet MTM, we are able to obtain NNZ and even $n = 0$ which would be interesting to bring forth for further investigation. In more detail, Table 4.5.1 shows the specific range where the band of each structure is both near-zero and low loss. Design DS contains a broadest range of NNZ and low loss, while the SS design is very much of a close

magnitude. For *X*-band, both SS and DS designs would be suitable for both military and medical sensor applications as well as microwave and optical lenses.

CHAPTER V

CONCLUSIONS AND DISCUSSION

5.1: Conclusion

Theoretical analysis, computer modeling and simulation are steps taken in the design of metamaterials (MTMs). A computational tool based on the robust method for effective parameter extraction is successfully developed and validated in order to examine the effective material parameters. This tool is also employed as a preliminary test for the design of MTMs. Novel two-dimensional (2D) and three-dimensional (3D) MTM designs which exhibit desirable near-zero refractive index (NZI) with relatively low loss factor (*LLF*) are developed. These MTMs are:

2D:

C3A (pp. 148 – 154):

- Percent Bandwidth (BW) of 4.36 % and a total NZI + LLF BW of 1.77 GHz.

C3AI (pp. 149 – 154):

- Percent Bandwidth of 4.06 % and a total NZI + LLF BW of 1.64 GHz.

C3AIII (pp. 150 – 154):

- Percent Bandwidth of 4.56 % and a total NZI + LLF BW of 1.86 GHz.

3D:

Single-Shell (pp. 156 – 162):

- Percent Bandwidth of 10.47 % (Dual Band) and a total NZI + LLF BW of 2.39 GHz.

Double-Shell (pp. 156 – 162):

- Percent Bandwidth of 10.63 % (Dual Band) and a total NZI + LLF BW of 2.44 GHz.

Diamond Double-Shell (pp. 156 – 162):

- Percent Bandwidth of 6.47 % (Dual Band) and a total NZI + LLF BW of 1.72 GHz.

Octahedral Double-Shell (pp. 156 – 162):

- Percent Bandwidth of 5.27 % (Dual Band) and a total NZI + LLF BW of 1.53 GHz.

The inner-workings of a circular closed ring resonator (CCRR) allows us to evaluate the magnetic resonance, the robust research on the split ring resonator (SRR) and equivalent-circuit groundwork allow us to design a MTM structure based on SRR for a specific frequency range as the inclusion of the split provides us the ability to control μ , and by integrating an *Epsilon*-controlling bar (ECB) that forms a fishnet into our design, the Omeganet, we can control both ε and μ . From our optimized MTM design CAIII, we may now build a 3D structure. From the tools and techniques at our disposal via CST Microwave Studio[®], we synthesized a progression of cubic structures. Essentially, we are deliberately omitting the substrate, and utilizing the MTM itself to form the 3D structure.

5.2: Discussion

Through simulations, the proposed 2D and 3D structures were proved to have zero or near-zero refractive index, including very low imaginary part of the refractive index in the *X*-band microwave regimes.

5.3: Future Work

Based on the results presented in this thesis, further studies can be conducted as suggested in the following sections.

5.3.1: Fabrication and Measurements

Due to time constraints, it was not feasible to fabricate any of our 2D or 3D designs. Some methods have been proposed such as 3D printing and sputtering techniques that grow material on a substrate.

5.3.2: Further Optimizations

Another consideration would be to optimize the existing designs further by introducing curvature along the sharp edges of the MTMs, and therefore allowing for a smoother current density response.

5.3.3: Application Approach

A wide range of applications may be explored from these designs such as medical or military/industrial sensors, and microwave and optical lenses.

REFERENCES

- [1.1] Kshetrimayum, R. S. A brief intro to metamaterials. *Potentials, IEEE* **23**, 44–46 (2004).
- [2.1]. R. A. Shelby, D. R. Smith, and S. Schultz, “Experimental verification of a negative index of refraction,” *Science*, vol. 292, no. 5514, pp. 77–79, 6 Apr. 2001.
- [2.2]. J. B. Pendry, “Negative refraction makes a perfect lens,” *Phys. Rev. Lett.*, vol. 85, no.18, pp. 3966–3969, Oct. 2000.
- [2.3]. J. B. Pendry, A. J. Holden, D. J. Robbins, and W. J. Stewart, “Magnetism from conductors and enhanced nonlinear phenomena,” *Microwave Theory and Techniques, IEEE Transactions on*, vol. 47, no. 11, pp. 2075–2084, 1999.
- [2.4]. J. Pendry, D. Schurig, and D. R. Smith, “Metamaterial Electromagnetic Cloak at Microwave Frequencies,” *Science*, **314**, 5810, 2006, pp. 977-980.
- [2.5]. Li, Y. *et al.* On-chip zero-index metamaterials. *Nature Photonics* **9**, 738–742 (2015).
- [2.6]. Matra, K. & Wongkasem, N. Left-handed chiral isotropic metamaterials: analysis and detailed numerical study. *Journal of Optics A: Pure and Applied Optics* **11**, 074011 (2009).
- [2.7]. Panpradit, W., Sonsilphong, A., Soemphol, C. & Wongkasem, N. High negative refractive index in chiral metamaterials. *Journal of Optics* **14**, 075101 (2012).
- [2.8]. M. Silveirinha, N. Engheta, “Tunneling of Electromagnetic Energy through Subwavelength Channels and Bends using ϵ -Near-Zero Materials”, *Phys. Rev. Lett.* 97, 157403 (2006)
- [2.9]. Vehmas, J., Alitalo, P. & Tretyakov, S. A. Experimental demonstration of antenna blockage reduction with a transmission-line cloak. *Microwaves, Antennas & Propagation, IET* **6**, 830–834 (2012).
- [2.10]. Ziolkowski, R. W. Propagation in and scattering from a matched metamaterial having a zero index of refraction. *Physical Review E* 70, (2004).
- [2.11]. J. C. Bose, “On the rotation of plane of polarisation of electric waves by a twisted structure,” *Proc. Roy. Soc.*, vol. 63, pp. 146–152, 1898.

- [2.12]. I. V. Lindell, A. H. Sihvola, and J. Kurkijarvi, "Karl F. Lindman: The last Hertzian, and a Harbinger of electromagnetic chirality," *IEEE Antennas Propag. Mag.*, vol. 34, no. 3, pp. 24–30, 1992.
- [2.13]. W. E. Kock, "Metallic delay lenses," *Bell Sys. Tech. J.*, vol. 27, pp. 58–82, 1948.
- [2.14]. V. G. Veselago, "The electrodynamics of substances with simultaneously negative values of ϵ and μ ," *Sov. Phys. Uspekhi*, vol. 10, no. 4, pp. 509–514, 1968. [*Usp. Fiz.Nauk*, vol. 92, pp. 517–526, 1967.]
- [2.15]. J. B. Pendry, A. J. Holden, W. J. Stewart, and I. Youngs, "Extremely low frequency plasmons in metallic mesostructures," *Phys. Rev. Lett.* **76**, 4773(1996).
- [2.16]. D. R. Smith, W. J. Padilla, D. C. Vier, S. C. Nemat-Nasser, and S. Schultz, "Composite medium with simultaneously negative permeability and permittivity," *Phys. Rev. Lett.*, vol. 84, no. 18, pp. 4184–4187, May 2000.
- [2.17]. Sihvola, A. Metamaterials in electromagnetics. *Metamaterials* 1, 2–11 (2007).
- [2.18]. Shelby, R. A., D. R. Smith, and S. Schultz, "Experimental verification of a negative index of refraction," *Science*, Vol. 292, 77–79, Apr. 6, 2001.
- [2.19]. Chen, X., T. M. Grzegorzczuk, B.-I. Wu, J. Pacheco, and J. A. Kong, "Robust method to retrieve the constitutive effective parameters of metamaterials," *Physical Review E*, Vol. **70**, 016608, 2004.
- [2.20]. Nicolson, A. M. and G. F. Ross, "Measurement of the intrinsic properties of materials by time-domain techniques," *IEEE Transactions on Instrumentation and Measurement*, Vol. **19**, 377–382, 1970.
- [2.21]. Smith, D. R., S. Schultz, P. Marko, and C. M. Soukoulis, "Determination of effective permittivity and permeability of metamaterials from reflection and transmission coefficients," *Physical Review B*, Vol. **65**, 195104, 2002.
- [2.22]. Markos, P. and C. Soukoulis, "Transmission properties and effective electromagnetic parameters of double negative metamaterials," *Opt. Express*, Vol. **11**, 649–661, 2003.
- [2.23]. S. Arslanagic, T. V. Hansen, N. A. Mortensen, A. H. Gregersen, O. Sigmund, R. W. Ziolkowski, and O. Breinbjerg, "A review of the scattering-parameter extraction method with clarification of ambiguity issues in relation to metamaterial homogenization," *Antennas and Propagation Magazine, IEEE*, vol. **55**, no. 2, pp. 91–106, 2013.
- [2.24]. R. W. Ziolkowski, "Design, fabrication, and testing of double negative metamaterials," *IEEE Transactions on Antennas and Propagation*, vol. **51**, no. 7, pp. 1516–1529, Jul. 2003.

- [2.25]. A. Nuhman “Extraction of Material Parameters for Metamaterials Using a Full-Wave Simulator”, APM, 3013
- [2.26]. J. A. Kong, Electromagnetic Wave Theory (EMW, Cambridge, MA, 2000).
- [2.27]. J. A. Kong, Prog. Electromagn. Res. **35**, 1 (2002).
- [2.28]. Ziolkowski, R. W. Propagation in and scattering from a matched metamaterial having a zero index of refraction. *Physical Review E* **70**, (2004).
- [2.29]. Silveirinha, M. & Engheta, N. Tunneling of Electromagnetic Energy through Subwavelength Channels and Bends using ϵ -Near-Zero Materials. *Physical Review Letters* **97**, (2006).
- [2.30]. Silveirinha, M. & Engheta, N. Design of matched zero-index metamaterials using nonmagnetic inclusions in epsilon-near-zero media. *Physical Review B* **75**, (2007).
- [2.31]. Valentine, J. *et al.* Three-dimensional optical metamaterial with a negative refractive index. *Nature* **455**, 376–379 (2008).
- [2.32]. Alù, A., Silveirinha, M. G., Salandrino, A. & Engheta, N. Epsilon-near-zero metamaterials and electromagnetic sources: Tailoring the radiation phase pattern. *Physical Review B* **75**, 155410 (2007).
- [2.33]. Edwards, B., Alù, A., Young, M. E., Silveirinha, M. & Engheta, N. Experimental Verification of Epsilon-Near-Zero Metamaterial Coupling and Energy Squeezing Using a Microwave Waveguide. *Physical Review Letters* **100**, (2008).
- [2.34]. Liu, R. *et al.* Experimental Demonstration of Electromagnetic Tunneling Through an Epsilon-Near-Zero Metamaterial at Microwave Frequencies. *Physical Review Letters* **100**, (2008).
- [2.35]. Vehmas, J., Alitalo, P. & Tretyakov, S. A. Experimental demonstration of antenna blockage reduction with a transmission-line cloak. *Microwaves, Antennas & Propagation, IET* **6**, 830–834 (2012).
- [2.36]. Alù, A. & Engheta, N. Robustness in design and background variations in metamaterial/plasmonic cloaking: ROBUSTNESS OF METAMATERIAL CLOAKING. *Radio Science* **43**, (2008).
- [2.37]. Jang, S.-L., Wun, J.-Y., Liu, C.-C. & Juang, M.-H. A low power LC-tank SiGe BiCMOS injection locked frequency divider. *Microwave and Optical Technology Letters* **51**, 1970–1973 (2009).
- [2.38]. Podolskiy, V. A., *et. al.*, Optical nonlocalities and additional waves in epsilon-near-zero metamaterials, Podolskiy_Zayats, OSA--CLEO—IQEC (2009)
- [2.39]. Jang, S.-L., Wun, J.-Y., Liu, C.-C. & Juang, M.-H. A low power LC-tank SiGe BiCMOS injection locked frequency divider. *Microwave and Optical Technology Letters* **51**, 1970–1973 (2009).

- [2.40]. Hang Zhou *et al.* A Novel High-Directivity Microstrip Patch Antenna Based on Zero-Index Metamaterial. *IEEE Antennas and Wireless Propagation Letters* **8**, 538–541 (2009).
- [2.41]. Yang, J.-J., Huang, M. & Peng, J. Directive emission obtained by mu and epsilon-near-zero metamaterials. *Radioengineering* **18**, 124–128 (2009).
- [2.42]. Cheng, X., Chen, H., Zhang, X.-M., Zhang, B. & Wu, B.-I. Cloaking a perfectly conducting sphere with rotationally uniaxial nihility media in monostatic radar system. *Progress In Electromagnetics Research* **100**, 285–298 (2010).
- [2.43]. Wang, B. & Huang, K.-M. Shaping the radiation pattern with mu and epsilon-near-zero metamaterials. *Progress In Electromagnetics Research* **106**, 107–119 (2010).
- [2.44]. Bai, J., Shi, S. & Prather, D. W. Analysis of epsilon-near-zero metamaterial super-tunneling using cascaded ultra-narrow waveguide channels. *Progress In Electromagnetics Research M* **14**, 113–121 (2010).
- [2.45]. Jin, Y. & He, S. Enhancing and suppressing radiation with some permeability-near-zero structures. *Optics express* **18**, 16587–16593 (2010).
- [2.46]. Yang, J. J., Francescato, Y., Maier, S. A., Mao, F. & Huang, M. Mu and epsilon near zero metamaterials for perfect coherence and new antenna designs. *Optics Express* **22**, 9107 (2014).
- [2.47]. Navarro-Cía, M., Beruete, M., Campillo, I. & Sorolla, M. Enhanced lens by ϵ and μ near-zero metamaterial boosted by extraordinary optical transmission. *Physical Review B* **83**, (2011).
- [2.48]. Choi, M. *et al.* A terahertz metamaterial with unnaturally high refractive index. *Nature* **470**, 369–373 (2011).
- [2.49]. Huang, X., Lai, Y., Hang, Z. H., Zheng, H. & Chan, C. T. Dirac cones induced by accidental degeneracy in photonic crystals and zero-refractive-index materials. *Nature Materials* **10**, 582–586 (2011).
- [2.50]. Sorrolla, F.A. Novel Antennas Based Upon Extraordinary Transmission Metamaterial Lenses, FA_8655-10-1-3078-REPORT (2011)
- [2.51]. Naghipourfar, M. & Atlasbaf, Z. New dual-band DNG metamaterials. *Canadian Journal on Electrical and Electronics Engineering* **2**, 47–56 (2011).
- [2.52]. Hraba, S., Krois, I., Bonic, I., Kirichenko, A. & Munoz, E. U. *Broadband epsilon-near-zero (ENZ) and mu-near-zero (MNZ) active metamaterial.* (DTIC Document, 2011).
- [2.53]. Hwang, R.-B., Hsu, N.-C. & Chin, C.-Y. A Spatial Beam Splitter Consisting of a Near-Zero Refractive Index Medium. *IEEE Transactions on Antennas and Propagation* **60**, 417–420 (2012).
- [2.54]. Jing, Y., Xu, J. & Fang, N. X. Numerical study of a near-zero-index acoustic metamaterial. *Physics Letters A* **376**, 2834–2837 (2012).

- [2.55]. Cook, A. Dirac metamaterials: Electromagnetic epsilon-near-zero metamaterials that mimic relativistic quantum particles. (2012).
- [2.56]. Ehrenberg, I. M., Sarma, S. E. & Wu, B.-I. A three-dimensional self-supporting low loss microwave lens with a negative refractive index. *Journal of Applied Physics* **112**, 073114 (2012).
- [2.57]. Gao, J. *et al.* Experimental realization of epsilon-near-zero metamaterial slabs with metal-dielectric multilayers. *Applied Physics Letters* **103**, 051111 (2013).
- [2.58]. Vesseur, E. J. R., Coenen, T., Caglayan, H., Engheta, N. & Polman, A. Experimental Verification of $n = 0$ Structures for Visible Light. *Physical Review Letters* **110**, (2013).
- [2.59]. Davoyan, A. R., Mahmoud, A. M. & Engheta, N. Optical isolation with epsilon-near-zero metamaterials. *Optics express* **21**, 3279–3286 (2013).
- [2.61]. Wang, Z., *et. al.*, Total Transmission and Total Reflection by Zero Index Metamaterials with Defects, PACS 47.35.Rs, (2013)
- [2.62]. Soemphol, C., Sonsilphong, A. & Wongkasem, N. Metamaterials with near-zero refractive index produced using fishnet structures. *Journal of Optics* **16**, 015104 (2014).
- [3.1] S. Enoch, G. Tayeb, P. Sabouroux, N. Guérin, and P. Vincent, A metamaterial for directive emissions, *Phys. Rev. Lett.* **89**, 213902
- [3.2] CST Microwave Studio TM, CST of America, Inc., www.cst.com
- [3.3] N. Katsarakis, T. Koschny, M. Kafesaki, E. N. Economou, and C. M. Soukoulis, “Electric coupling to the magnetic resonance of split ring resonators,” *Applied Physics Letters*, vol. 84, no. 15, p. 2943, 2004.
- [3.4] M. Kafesaki, T. Koschny, R. S. Penciu, T. F. Gundogdu, E. N. Economou, and C. M. Soukoulis, “Left-handed metamaterials: detailed numerical studies of the transmission properties,” *Journal of Optics A: Pure and Applied Optics*, vol. 7, no. 2, pp. S12–S22, Feb. 2005.
- [4.1]. Pendry J B, Holden A J, Robbins D J and Stewart W J,” Low frequency plasmons in thin-wire structures “,1998, *J. Phys.: Condens. Matter* 10 4785
- [4.2]. D. R. Smith, W. J. Padilla, D. C. Vier, S. C. Nemat-Nasser, and S. Schultz, “Composite medium with simultaneously negative permeability and permittivity,” *Phys. Rev. Lett.*, vol. 84, no. 18, pp. 4184–4187, May 2000.
- [4.3]. R. A. Shelby, D. R. Smith, and S. Schultz, “Experimental verification of a negative index of refraction,” *Science*, vol. 292, no. 5514, pp. 77–79, 6 Apr. 2001.
- [4.4]. K. Aydin, I. Bulu, K. Guven, M. Kafesaki, C. M. Soukoulis, and E. Ozbay, “Investigation of magnetic resonances for different split-ring resonator parameters and designs,” *New Journal of Physics*, vol. 7, pp. 168–168, Aug. 2005.

- [4.5] Smith, D. R., Schultz, S., Markoš, P. & Soukoulis, C. M. Determination of effective permittivity and permeability of metamaterials from reflection and transmission coefficients. *Physical Review B* **65**, (2002).
- [4.6] Baena, J. D. *et al.* Equivalent-circuit models for split-ring resonators and complementary split-ring resonators coupled to planar transmission lines. *IEEE Transactions on Microwave Theory and Techniques* **53**, 1451–1461 (2005).
- [4.7] R. Marqués, F. Mesa, J. Martel, and F. Medina, “Comparative analysis of edge- and broadside-coupled split ring resonators for metamaterial design—Theory and experiment,” *IEEE Trans. Antennas Propag.*, vol. 51, no. 10, pp. 2572–2581, Oct. 2003.
- [4.8] Gil, M. *et al.* *Electrically small resonators for metamaterial and microwave circuit design*. (INTECH Open Access Publisher, 2010).
- [4.9] Kafesaki, M. *et al.* Left-handed metamaterials: The fishnet structure and its variations. *Physical Review B* **75**, (2007).

BIOGRAPHICAL SKETCH

David Flores III attended La Joya High School in La Joya, TX and graduated top five percent of his class. Mr. Flores attended The University of Texas at San Antonio (UTSA) and Texas State University – San Marcos. In the Spring of 2012 he transferred to The University of Texas Pan American (UTPA) in Edinburg, TX where he continued his undergraduate studies. In December 2013 he graduated with a Bachelor of Science degree in Electrical Engineering. Given the opportunity, he continued attending The University of Texas Rio Grande Valley (UTRGV) (formerly UTPA) as a graduate student in the Spring of 2014.

Mr. Flores served as a Graduate Research Assistant under the guidance of Dr. Yoonsu “Paul” Choi from the Department of Electrical Engineering. He also served as a Graduate Research Assistant under the guidance of Dr. Aaron T. Wilson in the Department of Mathematics. As his final assignment before completing his graduate studies, he served as a Teaching Assistant for the Department of Electrical Engineering from June 2015 to May 2016. His research interests include novel applied electromagnetics topics in fields such as metamaterials and radar as well as special topics in digital signal processing and robotics & control systems. He currently enjoys researching and design of electromagnetic metamaterials with refractive index near-zero under the guidance of Dr. Nantakan Wongkasem. In May 2016, Mr. Flores was awarded with a Master of Science degree in Electrical Engineering from UTRGV.

Email address: david.dx@me.com